TU Delft

Delft University of Technology

Fast and reliable multi-GNSS precise point positioning with integer ambiguity resolution

Psychas, D.V.

DOI
10.4233/uuid:1d046ff3-1065-4c94-a86c-f739166c69b6

Publication date
2022

Document Version
Final published version

Citation (APA)
Psychas, D. V. (2022). *Fast and reliable multi-GNSS precise point positioning with integer ambiguity resolution*. [Dissertation (TU Delft), Delft University of Technology]. https://doi.org/10.4233/uuid:1d046ff3-1065-4c94-a86c-f739166c69b6

Important note
To cite this publication, please use the final published version (if applicable).
Please check the document version above.

Copyright
Other than for strictly personal use, it is not permitted to download, forward or distribute the text or part of it, without the consent of the author(s) and/or copyright holder(s), unless the work is under an open content license such as Creative Commons.

Takedown policy
Please contact us and provide details if you believe this document breaches copyrights.
We will remove access to the work immediately and investigate your claim.

This work is downloaded from Delft University of Technology.
For technical reasons the number of authors shown on this cover page is limited to a maximum of 10.

Fast and reliable multi-GNSS precise point positioning with integer ambiguity resolution

Fast and reliable multi-GNSS precise point positioning with integer ambiguity resolution

Proefschrift

ter verkrijging van de graad van doctor
aan de Technische Universiteit Delft,
op gezag van de Rector Magnificus Prof.dr.ir. T.H.J.J. van der Hagen,
voorzitter van het College voor Promoties,
in het openbaar te verdedigen
op donderdag 20 januari 2022 om 12:30 uur

door

Dimitrios Vasileios PSYCHAS

Master of Science in Earth Oriented Space Science and Technology,
Technische Universität München, Duitsland,
geboren te Mytilini, Griekenland.

Dit proefschrift is goedgekeurd door de

promotor: Prof.dr.ir. P.J.G. Teunissen
copromotor: Dr.ir. A.A. Verhagen

Samenstelling promotiecommissie:

Rector Magnificus	voorzitter
Prof.dr.ir. P.J.G. Teunissen	Technische Universiteit Delft, promotor
Dr.ir. A.A. Verhagen	Technische Universiteit Delft, copromotor
Onafhankelijke leden:	
Prof.dr. T. Moore	University of Nottingham, Verenigd Koninkrijk
Prof.dr.sc.nat. C. Günther	Deutsches Zentrum für Luft- und Raumfahrt, Duitsland
Prof.dr. R.B. Langley	University of New Brunswick, Canada
Prof.dr.ir. P.N.A.M. Visser	Technische Universiteit Delft
Prof.dr.-ing. habil. R. Klees	Technische Universiteit Delft, reservelid
Overig lid:	
Dr.ir. D. Odijk	Fugro, Nederland

This research was funded by the European Union's Horizon 2020 research and innovation program under the Marie Skłodowska-Curie Grant Agreement No 722023, and also partially supported by Fugro.

Keywords: Global navigation satellite systems (GNSS), Precise point positioning (PPP), Integer ambiguity resolution (IAR), PPP-RTK, Fast convergence, Ionospheric corrections, Multi-GNSS, Multi-frequency, Stochastic model, Generalized Kalman-filter

Printed by: Ridderprint

Cover design: Elena Sotiri

Copyright © 2021 by D.V. Psychas

ISBN: 978-94-6458-027-3 e-ISBN: 978-94-6458-035-8

An electronic version of this dissertation is available at
http://repository.tudelft.nl/.

Credit for Galileo satellites used on the cover: ESA artist's concept

As you set out for Ithaka,
hope your road is a long one.
Keep Ithaka always in your mind.
Arriving there is what you're destined for.
But don't hurry the journey at all.
Ithaka gave you the marvelous journey.

C.P. Cavafy, *Collected Poems*
(translation: E. Keeley)

Contents

Summary **xi**

Samenvatting (in Dutch) **xv**

1 Introduction **1**
1.1 Background . . . 1
1.2 Literature review . . . 3
1.3 Thesis objectives . . . 7
1.4 Outline of the thesis . . . 9
References . . . 11

2 Assessment of ionospheric corrections for PPP-RTK **17**
2.1 Introduction . . . 18
2.2 Brief review of *S*-system theory . . . 20
2.3 Methodology . . . 21
2.3.1 PPP-RTK user design computation . . . 21
2.3.2 Ionosphere modeling . . . 25
2.4 Results and analysis . . . 26
2.4.1 Experimental setup . . . 26
2.4.2 Results of the design computation . . . 29
2.4.3 Results of the ionosphere VTEC modeling . . . 31
2.5 Conclusions . . . 39
References . . . 40

3 Ionosphere-weighted PPP-RTK user performances **45**
3.1 Introduction . . . 46
3.2 Methodology . . . 48
3.2.1 GNSS observation equations . . . 48
3.2.2 PPP-RTK network . . . 49
3.2.3 Prediction of ionospheric corrections . . . 50
3.2.4 PPP-RTK user . . . 52
3.3 Results and analysis . . . 54
3.3.1 Data and processing strategy . . . 54
3.3.2 PPP-RTK network corrections . . . 56
3.3.3 Real-time PPP-RTK performance . . . 59
3.4 Conclusions . . . 64
References . . . 66

4 Multi-GNSS multi-frequency PPP-RTK user performances: Part I **71**
4.1 Introduction . . . 72
4.2 Integer ambiguity resolution . . . 74
4.2.1 Mixed-integer GNSS model . . . 74
4.2.2 Ambiguity success rate . . . 75
4.2.3 Partial ambiguity resolution . . . 76
4.3 PPP-RTK processing strategy . . . 77
4.3.1 Full-rank observation model . . . 78
4.3.2 Performance measures . . . 80
4.3.3 Experimental setup . . . 81
4.4 Results and analysis . . . 82
4.4.1 Single-station analysis . . . 82
4.4.2 Global analysis . . . 90
4.4.3 Five-frequency Galileo PPP-RTK . . . 94
4.5 Conclusions . . . 96
References . . . 97

5 Multi-GNSS multi-frequency PPP-RTK user performances: Part II **101**
5.1 Introduction . . . 102
5.2 Processing strategy . . . 104
5.2.1 Observation model . . . 104
5.2.2 Experimental setup . . . 107
5.3 Experimental results and analysis . . . 109
5.3.1 Formal analysis . . . 109
5.3.2 Empirical analysis . . . 115
5.4 Conclusions . . . 121
References . . . 123

6 A generalized Kalman filter in case of a misspecified stochastic model **129**
6.1 Introduction . . . 130
6.2 Kalman filter and its assumptions . . . 132
6.2.1 Model assumptions . . . 132
6.2.2 The Kalman filter . . . 132
6.3 Generalized Kalman filter . . . 133
6.3.1 A relaxed dynamic model . . . 134
6.3.2 A reparametrized measurement model . . . 134
6.3.3 The filter for $\underline{z}_t$ . . . 135
6.3.4 The filter for $\underline{x}_t$ . . . 137
6.4 State-vector error-variance matrices . . . 137
6.4.1 Recursive error-variance matrices . . . 138
6.5 Predicted residuals . . . 142
6.5.1 The predicted residual defined . . . 142
6.5.2 Statistical testing . . . 142
6.5.3 On the precision of the predicted residuals . . . 143
6.5.4 Reliability analysis . . . 144

6.6 Summary and concluding remarks . . . 145
References . . . 148

7 Impact and mitigation of neglecting PPP-RTK correctional uncertainty 151
7.1 Introduction . . . 152
7.2 Observation model . . . 153
7.2.1 Single-station provider . . . 153
7.2.2 PPP-RTK user . . . 156
7.3 Experimental results and analysis . . . 159
7.3.1 Data selection and processing strategy . . . 159
7.3.2 Quality of individual and combined corrections . . . 160
7.3.3 PPP-RTK user performance . . . 161
7.3.4 Relevance to multi-station PPP-RTK . . . 170
7.4 Conclusions . . . 171
References . . . 172

8 Conclusions and recommendations 177
8.1 Conclusions . . . 177
8.2 Recommendations . . . 179
References . . . 181

Acknowledgements 183

Curriculum Vitæ 185

List of publications 187

Summary

Precise Point Positioning (PPP) is a Global Navigation Satellite Systems (GNSS) modelling and processing method that provides single-receiver users with high positioning accuracy anywhere on the globe, without the explicit dependence on reference receivers. The realization of PPP is based on undifferenced code and phase measurements, a priori correction models, as well as on precise satellite orbits and clocks. Although PPP delivers highly accurate positioning results, a relatively long timespan is needed to achieve such accurate results. This long convergence time is mainly due to the presence of the carrier-phase ambiguities and ionospheric delays, and can be significantly reduced if one can do away with these unknown parameters using integer-estimation and external corrections, respectively. The integer ambiguity resolution-enabled variant of PPP, namely PPP-RTK, is the GNSS positioning mode that is capable of delivering ambiguity-resolved parameter solutions on the basis of single-receiver user data and state-space corrections, which include, next to satellite orbits and clocks, information about the satellite phase and code biases. These corrections, when properly provided from either a multi- or a single-station setup, enable recovery of the integer property of the user ambiguities, thus enabling single-receiver integer ambiguity resolution and, therefore, reduced convergence times compared to those experienced with ambiguity-float PPP.

A considerable observational time span of 30-60 min is, however, still needed to integer-resolve the ambiguities with sufficiently large success rate in the presence of ionospheric delays, which cannot compete with that achieved with relative positioning techniques over short baselines. The lack of any ionospheric information necessitates that the user utilizes the ionosphere-float model – a model that treats the slant ionospheric delays as unknown parameters – that is known to be relatively weak in the sense of its ambiguity resolution capabilities. Faster ambiguity resolution and, therefore, improved convergence time are expected when such information can be provided to the user's model.

The augmentation with ionospheric information, though, requires dense network infrastructure that is often not available either because of spatial restrictions or due to the high-cost and complex operation requirements involved. In such cases, a user's model strengthening can be alternatively substantiated through the integration of multi-constellation multi-frequency measurements. The increased number of satellites and frequencies paves the way for accelerating successful ambiguity resolution and, therefore, convergence times.

Next to the rapid centimeter-level convergence that is of top priority to the users, positioning reliability is critical as well for the user performance. The commonly used practice in PPP-RTK to neglect the correctional uncertainty may have considerable effects not only on the ambiguity resolution performance but, most importantly, on the precision description the user is provided with to judge his real-time performance. To obtain the optimal positioning performance, the users need to incorporate the quality description of the corrections into their estimation process.

Obviously, the PPP-RTK user positioning convergence time and reliability are still open problems. In order to overcome the aforementioned limitations, three approaches are investigated in this PhD thesis.

The first method utilizes ionospheric information from regional multi-scale networks to aid the user model in increasing its redundancy, thus allowing for faster PPP-RTK ambiguity resolution. An extensive formal analysis revealed that such an acceleration would be possible only if the precision of the provided ionospheric corrections is equal to or better than 5 cm. It was observed, though, that this quality level may not be achieved with a function-based two-dimensional ionosphere model that considers a single-layer model and a slant-to-vertical mapping function. To overcome this, a methodology was introduced that uses the slant delays directly as estimated from the PPP-RTK network processing and predicts, by means of the best linear unbiased prediction framework, the slant ionospheric corrections per satellite and per epoch at the user's location. It was shown how the user's model needs to be extended to its ionosphere-weighted variant in order to incorporate these corrections, and how their quality can be reliably evaluated. The empirical analysis of a sufficiently large number of positioning solution samples showed that near-instantaneous centimeter-level positioning is feasible in case the corrections are provided by a small-scale network. Further analysis of networks with varying density revealed, for the first time in terms of PPP-RTK, the impact the network density has on the achieved convergence times and their linear relationship with the mean inter-station distance.

Then, the approach of integrating multi-GNSS multi-frequency data, as an alternative to the ionospheric corrections augmentation, was analyzed for improving PPP-RTK convergence. The advantage of this approach compared to the previous is that it dispenses with the stringent requirement of operating a dense network infrastructure and also the necessity for the user to be located within the network's operating range to utilize the provided ionospheric signals. A formal performance analysis of globally distributed user stations showed the impact of the increased number of satellites and frequencies on the expected ambiguity resolution and positioning performance. Although both factors bring considerable improvements, it was revealed that the satellite redundancy plays a more crucial role in speeding up the convergence time due to the improved geometry strength. Analysis of various simulated datasets revealed that the sensitivity of the user's performance, in response to changes in the measurement precision, becomes less pronounced for multi-GNSS multi-frequency models. In addition, the impact of the number and spacing of frequencies on the multi-frequency PPP-RTK user performance was investigated, for the first time in terms of PPP-RTK. It was both formally and empirically evidenced that frequency spacing contributes to a larger extent, compared to the number of frequencies, to the user ambiguity resolution and, therefore, to the convergence times. The role of the estimable satellite code biases in multi-frequency data processing was highlighted and their impact on the achieved performance was evaluated. The positioning results using multi-frequency Galileo-plus-GPS data showed that centimeter-level positioning can be achieved almost instantaneously, even in the absence of ionospheric information.

Finally, the PPP-RTK user positioning reliability was analyzed in terms of the precision description the user is provided with when the user stochastic model is misspecified. A generalized Kalman-filter was introduced that is capable of, first, rigorously processing dynamic systems when only a subset of the state-vector elements are linked in time and, second, recursively providing the actual precision in case of a misspecified stochastic model as is the case when neglecting the uncertainty of PPP-RTK corrections. Analysis of the behavior of the filter-precision indicated that the actual error-variance, in response to changes in the assumed stochastic model, is difficult to predict a priori. The effects of such a misspecification on the data quality control mechanisms was discussed and analyzed with illustrative examples. The impact of the neglected PPP-RTK correctional uncertainty on the user ambiguity resolution and positioning performance was empirically evaluated for nonzero correction latencies. It was evidenced that, apart from the reduced ambiguity success rates, the inconsideration of the corrections' quality may lead to significant deviation between the formal and empirical positioning errors, thereby misleading the users with incorrect standard deviations. Mitigation methods were developed and their performance was numerically demonstrated for varying latency and for both single- and multi-constellation models.

Samenvatting (in Dutch)

Precieze plaatsbepaling (in het Engels Precise Point Positioning - PPP) is een Globaal Navigatie Satelliet System (GNSS) modellerings- en verwerkingsmethode die gebruikers met één ontvanger overal ter wereld een hoge plaatsbepalingsnauwkeurigheid biedt, zonder de expliciete afhankelijkheid van referentieontvangers. De realisatie van PPP is gebaseerd op ongedifferentieerde code- en fasemetingen, a priori correctiemodellen, evenals op precieze satellietbanen en -klokken. Hoewel PPP zeer nauwkeurige plaatsbepalingsresultaten levert, is een relatief lange tijdspanne nodig om dergelijke nauwkeurige resultaten te bereiken. Deze lange convergentietijd is voornamelijk te wijten aan de aanwezigheid van de draaggolf fasemeerduidigheden en ionosferische vertragingen, en kan aanzienlijk worden verminderd als men deze onbekende parameters kan elimineren met behulp van respectievelijk geheeltallige meerduidigheidsschatting en externe correcties. De variant van PPP waarbij de geheeltallige meerduidigheden worden geschat, namelijk PPP-RTK, is de GNSS-plaatsbepalingsmodus die in staat is om parameteroplossingen te leveren op basis van gebruikersgegevens met één ontvanger en toestandsruimte- (state-space) correcties, waaronder, naast satellietbanen en -klokken, informatie over de satelliet fase en code biases. Deze correcties, indien correct geleverd vanuit een multi- of een enkele-station setup, maken herstel van de geheeltalligheids-eigenschap van de gebruikers fase meerduidigheden mogelijk, waardoor geheeltallige meerduidigheidsbepaling voor een enkele-ontvanger mogelijk wordt en daardoor de convergentietijden worden verminderd in vergelijking standaard PPP.

Er is echter nog steeds een aanzienlijke observatietijd van 30-60 minuten nodig om de meerduidigheden met een voldoende groot succespercentage op te lossen in de aanwezigheid van ionosferische vertragingen, die niet kunnen concurreren met die welke worden bereikt met relatieve plaatsbepalingstechnieken. Het ontbreken van enige ionosferische informatie vereist dat de gebruiker het ionosfeer-float-model gebruikt – een model dat de schuine ionosferische vertragingen als onbekende parameters behandelt – waarvan bekend is dat het relatief zwak is zodat succesvolle geheeltallige meerduidigheidsbepaling niet snel mogelijk is. Een snellere oplossing van de meerduidigheden en daardoor een verbeterde convergentietijd worden verwacht wanneer dergelijke informatie aan het model van de gebruiker kan worden verstrekt.

De toevoeging van ionosferische informatie vereist echter een dichte netwerkinfrastructuur die vaak niet beschikbaar is vanwege ruimtelijke beperkingen of vanwege de hoge kosten en complexe operationele vereisten. In dergelijke gevallen kan de modelversterking van een gebruiker alternatief worden onderbouwd door de integratie van multi-constellatie multi-frequentie metingen. Het toegenomen aantal satellieten en frequenties maakt de weg vrij voor het versnellen van succesvolle meerduidigheidsbepaling en dus convergentietijden.

Naast de snelle convergentie op centimeterniveau die de hoogste prioriteit heeft voor de gebruikers, is de betrouwbaarheid van de plaatsbepaling ook van cruciaal belang voor de gebruikersprestaties. De veelgebruikte praktijk in PPP-RTK om de correctionele onzekerheid te negeren, kan aanzienlijke effecten hebben, niet alleen op de prestaties van meerduidigheidsbepaling, maar, belangrijker nog, op de precisiebeschrijving die de gebruiker krijgt om zijn realtime prestaties te beoordelen. Om de optimale plaatsbepalingsprestaties te verkrijgen, moeten de gebruikers de kwaliteitsbeschrijving van de correcties opnemen in hun schattingsproces.

Het is duidelijk dat de convergentietijd en betrouwbaarheid van de PPP-RTK gebruikersplaatsbepaling nog steeds openstaande problemen zijn. Om de bovengenoemde beperkingen te overwinnen, worden in dit PhD proefschrift drie benaderingen onderzocht.

De eerste methode maakt gebruik van ionosferische informatie van regionale meerschalige netwerken om het gebruikersmodel te versterken door het vergroten van de redundantie, waardoor een snellere PPP-RTK meerduidigheidsbepaling mogelijk wordt. Een uitgebreide formele analyse toonde aan dat een dergelijke versnelling alleen mogelijk zou zijn als de nauwkeurigheid van de verstrekte ionosferische correcties gelijk is aan of beter is dan 5 cm. Er werd echter waargenomen dat dit kwaliteitsniveau mogelijk niet wordt bereikt met een functiegebaseerd tweedimensionaal ionosfeermodel dat rekening houdt met een enkellaagsmodel en een schuin-naar-verticale afbeeldingsfunctie. Om dit te ondervangen, werd een methodologie geïntroduceerd die de schuine vertragingen rechtstreeks gebruikt zoals geschat op basis van de PPP-RTK netwerkverwerking en voorspelt, door middel van het beste lineaire onbevooroordeelde predictieraamwerk, de schuine ionosferische correcties per satelliet en per epoche op de locatie van de gebruiker. Er werd getoond hoe het gebruikersmodel moet worden uitgebreid naar de ionosfeer-gewogen variant om deze correcties op te nemen, en hoe de bijbehorende kwaliteit betrouwbaar kan worden beoordeeld. De empirische analyse van een voldoende groot aantal monsters van plaatsbepalingsoplossingen toonde aan dat plaatsbepaling op centimeterniveau vrijwel onmiddellijk mogelijk is als de correcties worden geleverd door een kleinschalig netwerk. Nadere analyse van netwerken met variërende dichtheid onthulde, voor het eerst in termen van PPP-RTK, de impact die de netwerkdichtheid heeft op de bereikte convergentietijden en hun lineaire relatie met de gemiddelde afstand tussen stations.

Vervolgens werd de benadering van het integreren van multi-GNSS multi-frequentie gegevens geanalyseerd om de PPP-RTK convergentie te verbeteren, als alternatief voor de vergroting van de ionosferische correcties. Het voordeel van deze benadering in vergelijking met de vorige is dat het de strikte eis van het werken met een dichte netwerkinfrastructuur overbodig maakt en ook de noodzaak voor de gebruiker om zich binnen het werkbereik van het netwerk te bevinden om de geleverde ionosferische signalen te gebruiken. Een formele prestatieanalyse van wereldwijd gedistribueerde gebruikersstations toonde de impact van het toegenomen aantal satellieten en frequenties op de verwachte meerduidigheidsbepaling en plaatsbepalingsprestaties. Hoewel beide factoren aanzienlijke verbeteringen met zich meebrengen, werd onthuld dat de satellietredundantie een meer cruciale rol speelt bij het versnellen van de convergentietijd vanwege de verbeterde geometriesterkte. Analyse van verschillende gesimuleerde gegevens toonde aan dat de gevoeligheid van de prestaties van de gebruiker, als reactie op veranderingen in de meetprecisie, minder uitgesproken wordt voor multi-GNSS multi-frequentie modellen. Daarnaast

werd de impact van het aantal en de afstand tussen frequenties op de multi-frequentie PPP-RTK gebruikersprestaties voor het eerst in termen van PPP-RTK onderzocht. Het is zowel formeel als empirisch bewezen dat frequentie-afstand in grotere mate bijdraagt aan de gebruikers-meerduidigheidsbepaling en dus aan de convergentietijden dan het aantal frequenties. De rol van de geschatte satelliet code biases in multi-frequentie dataverwerking werd benadrukt en hun impact op de behaalde prestatie werd geëvalueerd. De plaatsbepalingsresultaten met behulp van multi-frequentie Galileo-plus-GPS gegevens toonden aan dat plaatsbepaling op centimeterniveau vrijwel onmiddellijk kan worden bereikt, zelfs bij afwezigheid van ionosferische informatie.

Ten slotte werd de PPP-RTK betrouwbaarheid van de gebruikersplaatsbepaling geanalyseerd in termen van de precisiebeschrijving die de gebruiker krijgt wanneer het stochastische gebruikersmodel verkeerd is gespecificeerd. Er werd een gegeneraliseerd Kalmanfilter geïntroduceerd dat in staat is om enerzijds dynamische systemen rigoureus te verwerken wanneer slechts een subset van de toestandsvectorelementen in de tijd is gekoppeld en anderzijds recursief de werkelijke precisie te verschaffen in het geval van een verkeerd gespecificeerd stochastisch model zoals het geval bij verwaarlozing van de onzekerheid van PPP-RTK correcties. Analyse van het gedrag van de filterprecisie gaf aan dat de werkelijke foutvariantie, als reactie op veranderingen in het veronderstelde stochastische model, moeilijk a priori te voorspellen is. De effecten van een dergelijke verkeerde specificatie op de mechanismen voor gegevenskwaliteitscontrole werden besproken en geanalyseerd met illustratieve voorbeelden. De impact van de verwaarloosde PPP-RTK correctionele onzekerheid op de gebruikersmeerduidigheidsbepalingen plaatsbepalingsprestaties werd empirisch geëvalueerd voor niet-nul correctielatenties. Het werd bewezen dat, afgezien van de verminderde succespercentages voor meerduidigheidsbepaling, het negeren van de kwaliteit van de correcties kan leiden tot een significante afwijking tussen de formele en empirische plaatsbepalingsfouten, waardoor de gebruikers worden misleid met onjuiste precisiebeschrijvingen. Er werden mitigatiemethoden ontwikkeld en hun prestaties werden numeriek gedemonstreerd voor variërende latentie en voor zowel single- als multi-constellatiemodellen.

1

Introduction

1.1 Background

Positioning based on Global Navigation Satellite Systems (GNSS) has been an integral part of a wide variety of scientific disciplines, including geodesy, navigation, surveying, geophysics and atmospheric sciences. The principle of GNSS-based positioning lies in measuring the time required for the GNSS signals (electromagnetic waves) to propagate from Earth-orbiting satellites, the position and clock information of which are made available through a broadcast navigation message, to a ground GNSS receiver on top of a point of interest [1]. When scaled by the speed of light, these measurements are referred to as *code* or *pseudorange* observables, which are of decimetre level precision and can be used to estimate the receiver's position in real-time with an accuracy on the order of a few meters. This is usually referred to as GNSS standard positioning.

The key to ultra-precise GNSS positioning solutions is to utilize the phase measurements of the carrier wave, namely the *carrier-phase* observables, that are of millimetre precision. Although they are approximately two orders of magnitude more precise than the code measurements, they are biased by an unknown integer number of cycles, namely the carrier-phase ambiguities. Once the unknown ambiguities are resolved as integers with a process called *integer ambiguity resolution*, the carrier-phase data will act as very precise pseudorange data, thus making fast and precise positioning possible [2]. This is, however, based on the assumption that one has exercised care regarding the handling of receiver- and satellite-specific hardware delays existing in the phase data, which spoil the integer property of ambiguities.

It was realized quite early during the implementation stage of GPS that this could be circumvented in a relative positioning setup so that precise positioning can be achieved [3]. In the relative positioning method, forming differences between the measurements of the user receiver and those of a nearby reference receiver (real-time kinematic; RTK) or of a network of receivers (network-RTK; NRTK) largely reduces or even eliminates most of the contributing errors, including spatially correlated atmospheric errors, orbital and clock biases, as well as receiver- and satellite-specific hardware delays. The basic requirement

of this method is the simultaneous acquisition of measurements from the user and reference receivers within a spatial operating range. These characteristics form the basis of the relative positioning method, with which the user localizes himself with respect to the position of the reference receiver(s) [4–6].

In 1997, a new modeling and processing method called precise point positioning (PPP) was developed that enabled single-receiver users to achieve high-accuracy positioning anywhere on the globe with undifferenced code and phase data using precise, instead of broadcast, satellite orbits and clocks [7]. It is, therefore, considered a logical extension of code-based standard positioning and owes its positioning performance to the use of the very-precise phase data and the precise information about satellite orbits and clocks computed by a global network of reference receivers. This implies that PPP dispenses with the restriction of requiring simultaneous measurements for the user and reference receivers, which makes the method more favorable and operationally flexible for areas without dense infrastructure.

Despite the aforementioned advantages of the PPP technique, it should be remarked that such high positioning accuracy can be achieved using data over long observational time spans, which can range from tens of minutes to several hours [8, 9]. This is mainly attributed to the user's carrier-phase ambiguities that are not integer-estimable, unlike in relative positioning setups, due to the existing receiver and satellite hardware delays in the code and phase data. As a result, a long observational time span with sufficient change in the satellite geometry is needed such that the very-precise phase data contribute to positioning and eventually govern the achieved precision. Another contributing factor to the long convergence time is the presence of ionospheric delays, which weaken the model due to the introduction of additional unknown parameters. Such delays are (almost) absent in not-too-sparse relative positioning setups as the ionospheric delays are highly correlated in space.

The idea of combining the PPP and RTK techniques, so that the advantages of both methods are harnessed, was first formed by Wubbena *et al.* [10] and resulted in a new positioning technique, namely PPP-RTK. In essence, PPP-RTK extends the PPP technique by means of providing single-receiver users, next to orbits and clocks, information about the satellite phase and code biases computed from either a single- or multi-station setup [11]. These biases, when properly provided and applied to the user's code and phase data as corrections, enable the recovery of the integerness of user ambiguities, thus enabling single-receiver integer ambiguity resolution [12–17]. Once the user integer-valued ambiguities are mapped to their integers, one can expect shorter convergence time compared to that of PPP and a substantial precision improvement in the model's parameters.

The main prerequisite for such an acceleration in convergence is that the data-driven ambiguities are mapped to their *correct* integers successfully. The reliability of this process strongly depends on the strength of the user's model setup, e.g. on the number of available satellites and frequencies, on the atmospheric errors' modeling, and on the stochastic model. For instance, it is known that the presence of ionospheric delays hampers fast and reliable ambiguity resolution using single-constellation dual-frequency data, due to the inherent model's weakness in the sense of its ambiguity resolution capabilities. It has been reported that the convergence time in such cases ranges from 30 to 60 min [18]. Such a long convergence time is not attractive for fast high-precision positioning and can-

not compete with relative positioning methods. Moreover, an incorrectly-specified user stochastic model, as usually happens when neglecting the correctional uncertainty, may lead to incorrect ambiguity fixing, as well as to a coordinate precision description that differs from the optimal one.

Therefore, there is strong motivation to come up with a framework and proper methodologies so that the limitations of long convergence times and unreliable quality descriptions get tackled. This dissertation focuses on two main enablers of fast convergence, those being the use of ionospheric corrections from regional PPP-RTK networks and the integration of multi-GNSS and multi-frequency data, as well as on methods to obtain reliable precision description in the positioning domain.

1.2 Literature review

PPP-RTK is the GNSS positioning mode that delivers ambiguity-resolved parameter solutions on the basis of single-receiver data. The realization of this method is based on the provision of network-derived information about the satellite orbits, satellite clocks and satellite phase and code biases. In the case such information is provided, a single-receiver user is able to correct his/her code and phase data and recover the integerness of user-ambiguities, thereby having the capability to reduce the convergence time through successful ambiguity resolution.

Thus, it is made clear that the satellite phase and code biases are key parameters in realizing PPP-RTK ambiguity resolution. Their determination usually relies on the data integration within a network setup, without forming differences between receivers as in relative positioning setups. Working with an undifferenced measurement setup implies that one has to deal with the existing rank deficiencies as not all parameters can be unbiasedly estimated, including the satellite phase biases. This is due to the fact that the information content of the network's undifferenced data is not sufficient enough to determine the absolute parameters, but only estimable functions of them. The underlying rank deficiencies of the network model can be solved for by constraining a minimum set of parameters (S-basis) according to the S-system theory [19, 20], thus leading to a full-rank model. Although the estimable satellite phase biases are not the original ones, but a biased variant of them, it has been shown that they can still do the job in ensuring that the user-ambiguities are of double-differenced nature, and thus integer-valued [21].

There have been several contributions in the past suggesting different methods for the estimation of satellite phase biases such that the integerness of user-ambiguities is recovered [12–17]. They usually utilize between-satellite measurement differences to eliminate receiver-specific parameters, and/or ionosphere-free linear combinations in order to eliminate the slant ionospheric delays. The differences among these implementations lie in the choice of S-basis, in the choice of parameterization, and in the estimation method. Although one may be inclined to conclude that these methods provide different corrections to the user, it has been proved through estimability analysis that their information content is the same and that they are related through one-to-one transformations [21].

Therefore, the satellite phase biases determined with any of the aforementioned methods can aid the single-receiver user in resolving his/her phase ambiguities, thereby achiev-

ing RTK-like positioning accuracy. As stated earlier, the time span needed to achieve successful ambiguity resolution and reduce the convergence time largely depends on the user's model strength. The latter can be considerably increased when, for instance, precise a priori information about the ionosphere is provided to the users. If such information would be available, however, it would be problematic to include in the traditional ionosphere-free model and would defy the purpose of such linear combinations. The incorporation of ionospheric information is straightforward with the uncombined formulation, the advantages of which have been recognized for a long time [22–26]. The uncombined GNSS formulation allows one to use the original and usually uncorrelated code and phase measurements and keeps all parameters in the observation equations, thus allowing a flexible and rigorous extension to multi-GNSS and multi-frequency models and the capability to constrain the temporal and spatial behavior of the ionosphere [18].

As such, even though the model that includes the ionospheric delays as unknown parameters, the so-called ionosphere-float model, is known to be relatively weak in the sense of its ambiguity resolution capabilities, its strength can be aided with precise ionospheric corrections so that successful ambiguity resolution is achieved in a much shorter time span. This is practically realized if the user treats the ionospheric corrections as stochastic parameters and takes into account their uncertainty by either empirical functions [27, 28] or by an active validation network that continuously monitors the quality of such corrections. In case they are treated as non-random corrections, the position solutions may be biased even with high ambiguity success rate [27]. This model is referred to as the ionosphere-weighted model, which was first introduced by Bock *et al.* [29].

In fact, this has been an active field of research since the advent of PPP-RTK, since a regional PPP-RTK network setup, making use of an ionosphere-float model, is able to also optionally provide information about the ionosphere. With ionospheric corrections obtained from two small-scale networks of 27 and 60 km station spacing in different locations, respectively, Teunissen *et al.* [16] showed that mm-level positioning accuracy can be achieved at an instant with single-epoch ionosphere-weighted PPP-RTK. Having employed a different parameterization, Zhang *et al.* [30] have showed comparable performance with corrections computed from two different networks of inter-station distances ranging from 60 to 100 km. Despite the excellent user performance, both studies based their analysis on an epoch-by-epoch data processing, which is not always optimal in terms of ambiguity resolution performance in case ionospheric residuals are present in sparser networks.

The contribution of Li *et al.* [31] has shown similar user performance in their analysis, but lacks the flexibility of continuously providing ionospheric corrections to users as their generation requires that the ambiguities of the network stations are successfully fixed. In addition, the stated contribution does not consider parameterizing the user's observation equations in terms of the receiver code bias, that becomes estimable due to the introduction of network-derived ionospheric corrections, but come up with the conclusion that this bias gets absorbed by the user receiver clock. This finding is also echoed in Li *et al.* [32]. The recent contribution of Psychas and Verhagen [33] has shown, however, that such a bias becomes estimable, due to the frequency-dependent multiplier factor used when applying the ionospheric corrections, and can be at the order of a few meters.

In the analysis of Banville *et al.* [9], sub-decimeter positioning accuracy was performed in 21 out of 24 hourly solutions in a day with quiet ionospheric conditions, with corrections computed from a 150 km spaced network with minimum distance to the user of 97 km. Wang *et al.* [34] have also shown, based on three 1-hour time intervals and ionospheric information computed from unevenly distributed networks in different locations with maximum inter-station spacings of 295 and 580 km, that 10 s are required for the horizontal positioning errors to go below 10 cm. Even though the aforementioned contributions have highlighted the role of the ionospheric information in accelerating the convergence in PPP-RTK solutions, the impact that the network's dimension has on the user performance has not been studied. This is considered an important open question as the operational flexibility that PPP-RTK provides, compared to RTK, is based on the premise that use is made of a few and sparse reference receivers. Moreover, a systematic analysis of the user performance with ionosphere-weighted PPP-RTK has not been presented in the literature, unlike for the ionosphere-float models [35–37], and requires further attention.

As the ionosphere-corrected variant of the PPP-RTK concept relies on the spatial coherence of the slant ionospheric delays experienced by the network and user receivers, it is understood that the user needs to be within the network's operating coverage to achieve fast PPP-RTK positioning. Having such dense networks, though, is cumbersome due to the high-cost and complex operation requirements involved, while their establishment might even be impossible in certain areas. In such cases, however, the rather weak ionosphere-float model can be strengthened by means of utilizing data from multiple GNSS systems and over multiple frequencies.

Fortunately, with the ongoing rapid development and modernization of navigation satellite systems, there is an increase in the number of visible satellites that can serve in improving both ambiguity resolution and positioning performance in ionosphere-float PPP-RTK. In general, a multi-system integration provides an improved satellite geometry that is favorable in terms of reduced convergence times and higher availability. This has been recently demonstrated for several system combinations, e.g., for GPS and BeiDou [38, 39], GPS and Galileo [40, 41], three-system GPS, Galileo and BeiDou [36, 42], four-system GPS, Galileo, BeiDou and GLONASS [43, 44], and five-system GPS, Galileo, BeiDou, GLONASS and QZSS [45]. Also, it has been shown that PPP-RTK ambiguity resolution has the potential of benefiting enormously from such multi-GNSS integrations in that the ambiguity success rates can experience significant increase, thereby leading to shorter time-to-fix-ambiguities (TTFA), as shown by Li *et al.* [43], Duong *et al.* [46], Li *et al.* [47]. However, the stated contributions tend to solely use the TTFA as an indicator of the ambiguity resolution capabilities, without investigating the potential gain in precision improvement, while a thorough analysis into the ambiguity resolution performance and the impact on the positioning precision on a global scale has not been conducted yet.

In addition, the performance of integer ambiguity resolution will improve by the plethora of frequencies that the current and modernized versions of GNSS systems provide. In particular, an integration of multi-frequency data leads to an increase of the model's redundancy and provides a stronger positioning model, which will bring an improvement to ambiguity resolution and, consequently, to the user-convergence. Several contributions have analyzed the role of a third frequency in reducing the TTFAs and convergence time using data from GPS [48], Galileo [49, 50], GPS and Galileo [41], Galileo and BeiDou [47], GPS, BeiDou, Galileo and QZSS combined [51]. An interesting case for investigating multi-frequency PPP-RTK capabilities is the European Galileo system, which provides data on five frequencies from all in-orbit satellites but has not been given a proper attention so far. Faster convergence times have been reported by Xin *et al.* [52] by using triple-frequency combinations including E6. They argued that this improvement was due to the fact that the selected triplet provided the lowest noise amplification factor of the wide-lane observables. In addition, Li *et al.* [53] and Geng and Guo [54] have reported faster convergence times in static mode and improved accuracy, respectively, with the use of five-frequency observations, without providing representative analyses and details on the underlying reasons of such improvements. As such, a thorough analysis into the PPP-RTK performance gain as a function of the number and spacing of frequencies and an understanding of the selection of frequencies that lead to optimal performance are still missing.

Finally, the user's ambiguity resolution and positioning performance may also be improved by a correct specification of the user stochastic model. The PPP-RTK corrections, although random, are often treated *as if* they are nonrandom quantities either for implementation reasons or due to the excessive amount of information that needs to be transmitted to the user [55]. Therefore, the user positioning solutions will be of minimum-variance only if the true stochastic model of the corrected data is involved so as to correctly incorporate their quality description into the estimation process. In case the uncertainty of only the uncorrected data is involved, the weight matrices underlying the user model will not represent the inverse of the actual variance matrices, thereby leading to parameter solutions that lose their minimum-variance property and become sub-optimal. This becomes more evident in real-time applications, where the corrections are subject to latency and, therefore, need to be predicted to bridge the gap between their generation time and the user positioning time, which in turn leads to an amplification of their uncertainty. Such predictions were shown to degrade the positioning accuracy, as shown for PPP [56, 57] and PPP-RTK [34, 36], and to reduce the ambiguity success rates [58]. The uncertainty involved in the time-predicted corrections is expected to have an impact also on the user's ambiguity-resolved positioning performance and its accompanied precision-description, for which an analysis is missing.

1.3 Thesis objectives

The main objective of this PhD thesis by publication is to establish a framework for analyzing and improving the single-receiver user positioning convergence time and reliability obtained with the integer ambiguity resolution-enabled precise point positioning technique, namely PPP-RTK. In order to deal with the aforementioned limitations, the following approaches are investigated:

- *Regional network-derived ionospheric corrections are utilized from multi-scale network configurations for rapid PPP-RTK convergence.*

  The provision of ionospheric corrections leads to an increase in the user model's redundancy, thus raising the potential for faster PPP-RTK ambiguity resolution thereby reducing the convergence time as compared to that in the presence of ionospheric delays. An extensive formal analysis is performed to investigate and analyze the quality of ionospheric corrections needed in yielding such improved performance. Through the development of a framework for the network-based prediction of ionospheric corrections at the user location by means of best linear unbiased prediction, the near-instantaneous centimeter-level single-receiver user positioning is investigated and the impact that the network density has on the user positioning convergence time is analyzed.

- *Integration of multi-GNSS and multi-frequency data is explored as an alternative to ionospheric information in order to improve the convergence performance.*

  Emphasis is then placed on the investigation of fast PPP-RTK convergence capabilities in the absence of ionospheric corrections, since their determination requires dense networks that are often not available. With the proliferation of navigation satellite systems, the increased number of available satellites and frequencies pave the way for further improving the user ambiguity resolution and positioning capabilities compared to those of a single-constellation dual-frequency model. Based on multi-system multi-frequency simulated data from globally distributed stations, it is investigated how the satellite and frequency redundancy improve the user's performance. Special attention is then paid to the role of the increasing number of frequencies as well as their spacing. Using both a formal and a real-data analysis to judge the ambiguity-resolved performance as a function of the number and spacing of frequencies, it is shown, for the first time in the PPP-RTK sense, how frequency separation drives the user ambiguity resolution capabilities.

- *The impact of an incorrectly-specified stochastic model on the user's performance is analyzed and mitigation methods are considered.*

  The user estimable parameters in positioning analyses are estimated through an adjustment and/or filtering of the user system of observation equations over time. Would one want to obtain minimum-variance positioning solutions, one needs to involve the true stochastic model of one's corrected data. It has been a common practice in PPP-RTK applications to assume that the network-derived corrections are of nonrandom nature. It is stressed that these are in fact stochastic parameters, as they are determined by GNSS data that are accompanied with uncertainty.

When the latter is ignored, the user's parameter solutions may lose their minimum-variance property, thereby lacking a proper quality description that goes along with them. To tackle this shortcoming, we first introduce a generalized Kalman-filter with variance matrices in recursive form in case the stochastic model is misspecified, and we analyze the behavior of the actual filter-precision in response to changes in the assumed stochastic model. Supported by real-data results, the impact of neglecting the PPP-RTK correctional uncertainty is analyzed and mitigation methods are presented.

1.4 Outline of the thesis

The structure of the thesis is organized by the following chapters including the main peer-reviewed journal publications (see List of publications) that cover the aforementioned objectives.

Chapter 2 presents an analysis of the formal precision of ionospheric corrections required to realize faster PPP-RTK user ambiguity resolution within a simulation environment. This is accompanied by the development of an ionosphere representation for the regional modelling of vertical ionosphere based on network-derived ambiguity-fixed slant ionospheric delays. This chapter is covered by the following publication:

- Psychas, D., Verhagen, S., Liu, X., Memarzadeh, Y. and Visser, H. (2019). Assessment of ionospheric corrections for PPP-RTK using regional ionosphere modelling. Measurement Science and Technology, 30(1), doi: 10.1088/1361-6501/aaefe5

In **Chapter 3**, the convergence capabilities of PPP-RTK positioning users are investigated when precise ionospheric corrections from networks of varying density are available. We present a strategy to predict the undifferenced ionospheric corrections at the user location using network-derived slant ionospheric delays by means of best linear unbiased prediction. It is shown how the provision of such information necessitates the parameterization of an estimable user receiver code bias, that tends to be ignored in literature. An empirical analysis based on GPS dual-frequency data is then conducted to demonstrate whether near-instantaneous centimeter-level positioning is feasible for not-too-sparse networks, and to analyze the user convergence performance in relation to the mean network density. This chapter is covered by the following publication:

- Psychas, D. and Verhagen, S. (2020). Real-Time PPP-RTK Performance Analysis Using Ionospheric Corrections from Multi-Scale Network Configurations. Sensors, 20(11):3012, doi: 10.3390/s20113012

Chapter 4 is devoted to an exhaustive formal analysis of the PPP-RTK user ambiguity resolution performance based on multi-GNSS multi-frequency data from globally distributed stations aiming to provide insight into the positioning performance that can be expected with an increased number of satellites and frequencies in the absence of ionospheric information. The performance of both full (FAR) and partial (PAR) ambiguity resolution are investigated in terms of the ambiguity success rate and the number of epochs (time-to-fix-ambiguities; TTFA) to achieve both an ambiguity success rate criterion and a formal horizontal positioning precision level. To encompass the potential applications of mass-market receivers, the sensitivity of TTFA to changes in the user measurements' precision is analyzed. This chapter is covered by the following publication:

- Psychas, D., Verhagen, S. and Teunissen, P.J.G. (2020). Precision analysis of partial ambiguity resolution-enabled PPP using multi-GNSS and multi-frequency signals. Advances in Space Research, 66(9):2075-2093, doi: 10.1016/j.asr.2020.08.010

In **Chapter 5**, the role of the number and spacing of frequencies in improving PPP-RTK ambiguity resolution, and therefore in speeding up PPP-RTK user convergence time, is studied with the ionosphere-float model. Special emphasis is given on the provision of satellite code biases from the third frequency onwards as standard corrections, which allow the multi-frequency user code data to properly contribute to the positioning solutions. A formal analysis is performed using the FAR success rate and the precision gain after successful PAR as tools for evaluating the ambiguity resolution performance as function of the frequency separation. Experimental results are also computed to demonstrate the user positioning convergence capabilities for Galileo as a standalone system and also in combination with GPS. This chapter is covered by the following publication:

- Psychas, D., Teunissen, P.J.G. and Verhagen, S. (2021). A Multi-Frequency Galileo PPP-RTK Convergence Analysis with an Emphasis on the Role of Frequency Spacing. Remote Sensing, 13(16):3077, doi: 10.3390/rs13163077

Chapter 6 introduces a generalized Kalman-filter with expressions for the error variance matrices when the employed stochastic model is misspecified. The recursive Kalman-filter is known to be 'best' in the minimum variance sense given that one correctly specifies the stochastic model. In case this is not satisfied, as happens with the positioning users that ignore the PPP-RTK corrections' uncertainty, the user parameter solutions may lose their minimum-variance property. This will affect the precision-description of the Kalman-filter in that the computed error variance matrices fail to represent the actual error variance. Expressions for the actual error variance matrices are provided, and a precision analysis is performed to analyze the actual filter-precision in response to changes in the assumed stochastic model. This chapter is covered by the following publication:

- Teunissen, P.J.G., Khodabandeh, A. and Psychas, D. (2021). A generalized Kalman-filter with its precision in recursive form when the stochastic model is misspecified. Journal of Geodesy, 95(9):108, doi: 10.1007/s00190-021-01562-0

Chapter 7 presents an analysis of the impact the neglected uncertainty of time-delayed corrections has on the PPP-RTK user ambiguity resolution and positioning performance. Emphasis is given, next to the estimation results, on their quality information and on the difference between the user-assumed and minimum-variance positioning precision in case of an incorrectly-specified user data variance matrix. To circumvent this limitation, two alternatives to the corrections' error variance matrix are developed, which can be entirely structured from the user with limited information from the provider. Real GPS and Galileo data are processed to demonstrate the user ambiguity resolution and positioning performance, along with its precision-description, when the variance matrix of the corrections is considered, ignored, and finally reconstructed with the aforementioned strategies. This chapter is covered by the following publication:

- Psychas, D., Khodabandeh, A. and Teunissen, P.J.G. (2021). Impact and mitigation of neglecting PPP-RTK correctional uncertainty. GPS Solutions, accepted for publication.

Finally, the thesis conclusions are given in **Chapter 8**.

References

[1] P. J. G. Teunissen and A. Kleusberg, *GPS for Geodesy*, 2nd ed. (Springer-Verlag, Berlin-Heidelberg-New York, 1998).

[2] P. J. G. Teunissen and O. Montenbruck, *Springer Handbook of Global Navigation Satellite Systems*, 1st ed. (Springer International Publishing, 2017).

[3] J. D. Bossler, C. C. Goad, and P. L. Bender, *Using the Global Positioning System (GPS) for geodetic positioning.* Bull. Geodesique **54** (1980), 10.1007/BF02530713.

[4] G. Blewitt, *Carrier Phase Ambiguity Resolution for the Global Positioning System Applied to Geodetic Baselines up to 2000 km.* Journal of Geophysical Research **94**, 10187 (1989).

[5] E. Frei and G. Beutler, *Rapid Static Positioning Based on the Fast Ambiguity Resolution Approach FARA: Theory and First Results.* Manuscripta Geodaetica **15** (1990).

[6] P. J. G. Teunissen, *Least squares estimation of the integer GPS ambiguities.* Invited lecture, Section IV Theory and Methodology, IAG General Meeting, Beijing (1993).

[7] J. F. Zumberge, M. B. Heflin, D. C. Jefferson, M. M. Watkins, and F. H. Webb, *Precise point positioning for the efficient and robust analysis of GPS data from large networks.* Journal of Geophysical Research **102**, 5005 (1997).

[8] R. Leandro, H. Landau, M. Nitschke, M. Glocker, S. Seeger, X. Chen, A. Deking, M. BenTahar, F. Zhang, K. Ferguson, R. Stolz, N. Talbot, G. Lu, T. Allison, M. Brandl, V. Gomez, W. Cao, and A. Kipka, *RTX positioning: The next generation of cm-accurate real-time GNSS positioning.* in *Proceedings of the 24th International Technical Meeting of the Satellite Division of The Institute of Navigation, ION GNSS 2011* (Portland, OR, 2011).

[9] S. Banville, P. Collins, W. Zhang, and R. B. Langley, *Global and regional ionospheric corrections for faster PPP convergence.* Navigation **61**, 115 (2014).

[10] G. Wubbena, M. Schmitz, and A. Bagge, *PPP-RTK: Precise Point Positioning Using State-Space Representation in RTK Networks.* in *Proceedings of the 18th International Technical Meeting of the Satellite Division of The Institute of Navigation, ION GNSS 2005* (Long Beach, CA, USA, 2005) pp. 2584–2594.

[11] A. Khodabandeh and P. J. G. Teunissen, *An analytical study of PPP-RTK corrections: precision, correlation and user-impact,* Journal of Geodesy **89**, 1109 (2015).

[12] M. Ge, G. Gendt, M. Rothacher, C. Shi, and J. Liu, *Resolution of GPS carrier-phase ambiguities in Precise Point Positioning (PPP) with daily observations.* Journal of Geodesy **82**, 389 (2005).

[13] P. Collins, *Isolating and Estimating Undifferenced GPS Integer Ambiguities.* in *Proceedings of the 2008 National Technical Meeting of The Institute of Navigation.* (San Diego, CA, 2008) pp. 720–732.

[14] L. Mervart, Z. Lukes, C. Rocken, and T. Iwabuchi, *Precise Point Positioning with Ambiguity Resolution in Real-Time.* in *Proceedings of the 21st International Technical Meeting of the Satellite Division of The Institute of Navigation, ION GNSS 2008* (Savannah, GA, 2008).

[15] D. Laurichesse, F. Mercier, J. P. Berthias, P. Broca, and L. Cerri, *Integer Ambiguity Resolution on Undifferenced GPS Phase Measurements and its Application to PPP and Satellite Precise Orbit Determination.* Journal of The Institute of Navigation **56**, 135 (2009).

[16] P. J. G. Teunissen, D. Odijk, and B. Zhang, *PPP-RTK: Results of CORS network-based PPP with integer ambiguity resolution,* Journal of Aeronautics, Astronautics and Aviation A, **42**, 223 (2010).

[17] J. Geng, C. Shi, M. Ge, A. H. Dodson, Y. Lou, Q. Zhao, and J. Liu, *Improving the estimation of fractional-cycle biases for ambiguity resolution in precise point positioning.* Journal of Geodesy **86**, 579 (2012).

[18] D. Odijk, B. Zhang, A. Khodabandeh, R. Odolinski, and P. J. G. Teunissen, *On the estimability of parameters in undifferenced, uncombined GNSS network and PPP-RTK user models by means of S-system theory,* Journal of Geodesy **90**, 15 (2016).

[19] W. Baarda, *S-transformations and criterion matrices.* in *Publications on Geodesy, 18*, Vol. 5 (Netherlands Geodetic Commission, Delft, The Netherlands, 1973).

[20] P. J. G. Teunissen, *Zero Order Design: Generalized Inverses, Adjustment, the Datum Problem and S-Transformations.* in *Optimization and Design of Geodetic Networks.*, edited by E. Grafarend and F. Sanso (Springer, Berlin, Heidelberg, 1985) pp. 11–55.

[21] P. J. G. Teunissen and A. Khodabandeh, *Review and principles of PPP-RTK methods,* Journal of Geodesy **89**, 217 (2015).

[22] C. C. Goad, *Precise relative position determination using global positioning system carrier phase measurements in a nondifference mode.* in *Proceedings of 1st international symposium on precise positioning with GPS.* (1985) pp. 347–356.

[23] P. J. G. Teunissen, *The least-squares ambiguity decorrelation adjustment: a method for fast GPS integer ambiguity estimation.* Journal of Geodesy **70**, 65 (1995).

[24] P. J. de Jonge, *A processing strategy for the application of the GPS in networks.*, Ph.D. thesis, Delft University of Technology (1998).

[25] E. Schönemann, M. Becker, and T. Springer, *A new approach for GNSS analysis in a multi-GNSS and multi-signal environment.* Journal of Geodetic Science **1**, 204 (2011).

[26] A. Lannes and J. L. Prieur, *Calibration of the clock-phase biases of GNSS networks: the closure-ambiguity approach.* Journal of Geodesy **87**, 709 (2013).

[27] D. Odijk, *Weighting ionospheric corrections to improve fast GPS positioning over medium distances.* in *Proceedings of the 13th International Technical Meeting of the Satellite Division of The Institute Of Navigation (ION GPS 2000)* (Salta Lake City, UT, 2000).

[28] G. Liu and G. Lachapelle, *Ionosphere weighted GPS cycle ambiguity resolution.* in *Proceedings of ION National Technical Meeting* (San Diego, CA, 2002).

[29] Y. Bock, S. A. Gourevitch, C. C. Counselman, R. W. King, and R. I. Abbot, *Interferometric analysis of GPS phase observations,* Manuscripta Geodaetica **11**, 282 (1986).

[30] B. Zhang, P. J. G. Teunissen, and D. Odijk, *A Novel Un-differenced PPP-RTK concept,* The Journal of Navigation **64**, S180 (2011).

[31] X. Li, X. Zhang, and M. Ge, *Regional reference network augmented precise point positioning for instantaneous ambiguity resolution.* Journal of Geodesy **85**, 151 (2011).

[32] X. Li, X. Zhang, and G. Guo, *Predicting atmospheric delays for rapid ambiguity resolution in precise point positioning.* Advances in Space Research **54**, 840 (2014).

[33] D. Psychas and S. Verhagen, *Real-Time PPP-RTK Performance Analysis Using Ionospheric Corrections from Multi-Scale Network Configurations.* Sensors **20**, 3012 (2020).

[34] K. Wang, A. Khodabandeh, and P. J. G. Teunissen, *A study on predicting network corrections in PPP-RTK processing,* Advances in Space Research **60**, 1463 (2017).

[35] D. Odijk, A. Khodabandeh, N. Nadarajah, M. Choudhury, B. Zhang, W. Li, and P. J. G. Teunissen, *PPP-RTK by means of S-system theory: Australian network and user demonstration,* Journal of Spatial Science **62**, 3 (2017).

[36] N. Nadarajah, A. Khodabandeh, K. Wang, M. Choudhury, and P. J. G. Teunissen, *Multi-GNSS PPP-RTK: From Large- to Small-Scale Networks,* Sensors **18**, 1078 (2018).

[37] B. Zhang, Y. Chen, and Y. Yuan, *PPP-RTK based on undifferenced and uncombined observations: theoretical and practical aspects.* Journal of Geodesy **93**, 1011 (2019).

[38] R. Odolinski, P. J. G. Teunissen, and D. Odijk, *Combined GPS+BDS for short to long baseline RTK positioning.* Measurement Science and Technology **26**, 045801 (2015).

[39] J. Geng, X. Li, Q. Zhao, and G. Li, *Inter-system PPP ambiguity resolution between GPS and BeiDou for rapid initialization.* Journal of Geodesy **93** (2019), 10.1007/s00190-018-1167-6.

[40] G. Katsigianni, S. Loyer, and F. Perosanz, *PPP and PPP-AR Kinematic Post-Processed Performance of GPS-Only, Galileo-Only and Multi-GNSS,* Remote Sensing **11** (2019), 10.3390/rs11212477.

[41] T. Liu, W. Jiang, D. Laurichesse, H. Chen, X. Liu, and J. Wang, *Assessing GPS/Galileo real-time precise point positioning with ambiguity resolution based on phase biases from CNES,* Advances in Space Research **66**, 810 (2020).

[42] P. Li, X. Jiang, X. Zhang, M. Ge, and H. Schuh, *GPS+Galileo+BeiDou precise point positioning with triple-frequency ambiguity resolution,* GPS Solutions **24** (2020), 10.1007/s10291-020-00992-1.

[43] X. Li, X. Li, Y. Yuan, K. Zhang, X. Zhang, and J. Wickert, *Multi-GNSS phase delay estimation and PPP ambiguity resolution: GPS, BDS, GLONASS, Galileo.* Journal of Geodesy **92**, 579 (2018).

[44] H. Ma, Q. Zhao, S. Verhagen, D. Psychas, and X. Liu, *Assessing the Performance of Multi-GNSS PPP-RTK in the Local Area,* Remote Sensing **12**, 3343 (2020).

[45] A. Brack, B. Männel, and H. Schuh, *GLONASS FDMA data for RTK positioning: a five-system analysis,* GPS Solutions **25** (2021), 10.1007/s10291-020-01043-5.

[46] V. Duong, K. Harima, S. Choy, D. Laurichesse, and C. Rizos, *Assessing the performance of multi-frequency GPS, Galileo and BeiDou PPP ambiguity resolution.* Journal of Spatial Science **0**, 1 (2019).

[47] X. Li, X. Li, G. Liu, G. Feng, Y. Yuan, K. Zhang, and X. Ren, *Triple-frequency PPP ambiguity resolution with multi-constellation GNSS: BDS and Galileo.* Journal of Geodesy **93**, 1105 (2019).

[48] J. Geng and Y. Bock, *Triple-frequency GPS precise point positioning with rapid ambiguity resolution.* Journal of Geodesy **87**, 449 (2013).

[49] G. Xiao, P. Li, Y. Gao, and B. Heck, *A Unified Model for Multi-Frequency PPP Ambiguity Resolution and Test Results with Galileo and BeiDou Triple-Frequency Observations.* Remote Sensing **11**, 116 (2019).

[50] G. Liu, X. Zhang, and P. Li, *Improving the Performance of Galileo Uncombined Precise Point Positioning Ambiguity Resolution Using Triple-Frequency Observations.* Remote Sensing **11**, 341 (2019).

[51] J. Geng, J. Guo, X. Meng, and G. Kao, *Speeding up PPP ambiguity resolution using triple-frequency GPS/BeiDou/Galileo/QZSS data.* GPS Solutions **94** (2020), 10.1007/s00190-019-01330-1.

[52] S. Xin, G. Geng, G. Guo, and X. Meng, *On the Choice of the Third-Frequency Galileo Signals in Accelerating PPP Ambiguity Resolution in Case of Receiver Antenna Phase Center Errors,* Remote Sensing **12**, 1315 (2020).

[53] X. Li, G. Liu, X. Li, F. Zhou, G. Feng, Y. Yuan, and K. Zhang, *Galileo PPP rapid ambiguity resolution with five-frequency observations.* GPS Solutions **24** (2020), 10.1007/s10291-019-0930-3.

[54] J. Geng and G. Guo, *Beyond three frequencies: an extendable model for single-epoch decimeter-level point positioning by exploiting Galileo and BeiDou-3 signals.* Journal of Geodesy **94** (2020), 10.1007/s00190-019-01341-y.

[55] D. Odijk, P. J. G. Teunissen, and A. Khodabandeh, *Single-Frequency PPP-RTK: Theory and Experimental Results.* in *Earth on the Edge: Science for a Sustainable Planet. International Association of Geodesy Symposia, Vol. 139*, edited by C. Rizos and P. Willis (Springer, Berlin, Heidelberg, 2014).

[56] A. Martin, T. Hadas, A. Dimas, A. B. Anquela, and J. L. Berne, *Influence of real-time products latency on kinematic PPP results.* in *Presented at the 5th International Colloquium Scientific and Fundamental Aspects of the Galileo Programme.* (Braunschweig, Germany, 2015).

[57] H. Yang, C. Xu, and Y. Gao, *Analysis of GPS satellite clock prediction performance with different update intervals and application to real-time PPP.* Survey Review **51**, 43 (2017).

[58] A. Khodabandeh, *Single-station PPP-RTK: correction latency and ambiguity resolution performance,* Journal of Geodesy **95** (2021), 10.1007/s00190-021-01490-z.

2

Assessment of ionospheric corrections for PPP-RTK

This study presents an analysis of the ionospheric corrections required to get a significant improvement in PPP-RTK performance. The main aim was to determine the improvement in the position precision and Time-To-First-Fix in the PPP-RTK user side using ionospheric corrections computed from a network. The study consists of two main steps. The first one includes an empirical investigation of the ionosphere model precision necessary to greatly improve the PPP-RTK performance in a simulated environment in terms of precision and convergence time. In the second one, an optimal ionosphere representation was developed to provide precise ionospheric corrections by parameterizing the ionospheric slant delays after the PPP-RTK network processing in terms of ionosphere model coefficients and differential code biases using real GNSS measurements. Experimental results demonstrate that the proposed methodology can be used for reliable regional ionosphere modeling and satellite code bias estimation, due to the consistency of the satellite code bias estimates with those provided from the International GNSS Service Analysis Centres, the high stability of the estimated receiver and satellite code biases and the low least-squares residuals of the network-based ionosphere modeling solution. Finally, it has been shown that the precision of ionospheric corrections at zenith needs to be better than 5 cm to enable faster PPP-RTK solutions.

This chapter has been published as: Psychas, D., Verhagen, S., Liu, X., Memarzadeh, Y. and Visser, H. (2019). Assessment of ionospheric corrections for PPP-RTK using regional ionosphere modelling. Measurement Science and Technology, 30(1), doi: 10.1088/1361-6501/aaefe5

2.1 Introduction

The integer ambiguity resolution (IAR) enabled precise point positioning (PPP) method, the so-called PPP-RTK [1], is a state-of-the-art Global Navigation Satellite Systems (GNSS) technique that allows to determine high-accuracy positions with short convergence time. The main idea behind PPP-RTK is to extend the PPP technique [2] by providing single-receiver users, apart from precise orbits and clocks, with additional corrections (satellite phase biases, ionospheric and tropospheric corrections) so as to enable IAR with fast or even instantaneous convergence to the centimeter level.

A single-receiver PPP user who uses ionosphere-free (IF) carrier-phase and code observations, along with precise satellite orbit and clock products provided by the International GNSS Service (IGS) [3], can achieve an accuracy on the order of a few centimeters and of a few decimeters within one hour using GPS-only data in static and kinematic modes, respectively [4, 5]. The long convergence time in the traditional PPP, in the absence of precise ionospheric corrections, is due to the fact that the carrier-phase ambiguities need time to converge. These ambiguities are not estimable as integers, because they are lumped with the receiver and satellite phase biases. In relative positioning techniques, such as with Real-Time-Kinematic (RTK), these biases are eliminated with double-differenced measurements and, as such, the double-differenced ambiguities can be fixed to their integers.

Several methods have been formulated in the past to recover the integerness of the user ambiguities [6–10], therefore enabling the PPP-IAR method realization. They usually employ either between-satellite single differencing or ionosphere-free linear combinations of the raw observations in order to eliminate receiver-related parameters or ionospheric slant delays, respectively. The differences among these implementations lie in the choice of parameterization, in the corrections applied and, on several cases, in the estimation method. Although at first glance one would say that different corrections are provided to the user due to the different S-basis choice, it has been shown that their information content is the same and can achieve the same goal, namely enabling the construction of a system of observation equations at the user component in mixed-integer form [11].

As a result, these methods are able to resolve the phase ambiguities in the single-receiver observations and lead to RTK-like (mm-cm level) positioning accuracy. The elimination of the ionospheric error, however, is unfavorable since such corrections are required for the transition to PPP-RTK mode which can achieve significant shortening in the convergence times of the PPP-IAR positioning results [12]. An undifferenced and uncombined PPP-RTK model formulation, as used in [13] and [14], shows an obvious advantage over differences and linear combinations, as it contains all GNSS estimable parameters and, therefore has the benefit of providing (biased) ionospheric slant delays of high-precision that can be used for measuring the Total Electron Content (TEC) of the Earth's ionosphere.

Over the years, there has been an extensive research on measuring the Earth's TEC using GNSS data [15–20]. The ionospheric observables, usually derived from the widely used geometry-free (GF) code or phase measurements and the Carrier-to-Code Levelling (CCL) method, do not represent the unbiased slant TEC, due to the presence of the unknown carrier phase ambiguities or code hardware delays. Although one should not base one's

precision analysis of TEC on that of the ionospheric observable [21], the CCL method has been proven inaccurate to levelling errors (code noise and multipath effects) which sometimes exceed a couple of TECU [22] (where 1 Total Electron Content Unit = $10^{16}\,e^{-}/m^{2}$ and corresponds to 16 cm at the L1 frequency).

In the last few years, the GNSS ionosphere research community started turning its attention to alternative approaches for retrieval of TEC measurements (TECM). A network-based geodetic processing was employed from the UPC (Technical University of Catalonia) to retrieve the ambiguity term [23], which is lumped in the GF phase measurements. Then, one is able to obtain the undifferenced ambiguity-fixed carrier-phase ionospheric observables, which are affected only by the code hardware delays.

Further, several recent studies have used the PPP approach with raw observations to retrieve ionospheric observables [24–28]. Although PPP relies on precise orbit/clock products and includes a more complicated data processing than that of the CCL method, the PPP-derived ionospheric slant delays are not affected by levelling errors (which might have undesired effects on ionosphere modeling) [18] and are more precise [25]. Due to its capability to resolve the integer ambiguities, PPP-IAR is expected to provide much more precise slant ionospheric observables, as shown in the current work, since IAR is the key to fast and high-precision GNSS parameter estimation [29].

As already stated, the variety of ionospheric observables is vast, the interpretability of which is important to take into account in TEC determination [21]. Regardless of the combination in use, it is easily understandable that there is lack of information content in the undifferenced GNSS data to obtain unbiased ionospheric delays. Therefore, in order to retrieve the unbiased TEC and the lumped biases, the rank-deficiency of the GNSS observations needs to be identified and removed using the *S*-system theory [30, 31]. A brief introduction to the singularity-system theory is given in this paper.

Then, in order to separate the TEC from the hardware delays, a mathematical representation function is necessary to describe the ionosphere in the spatial and temporal domain, assuming it as a single-layer model. It has already been shown that the spherical harmonic (SH) functions are suitable for VTEC (Vertical TEC) modeling on a global scale [32]. In the regional scale which we are interested for, low-order SH functions [33], adjusted SH functions [28], bi-quadratic basis functions [19] or the combination of SH functions with generalized trigonometric series functions [20] are usually used.

If one is aiming at improving the PPP-IAR user performance, in terms of precision and most importantly convergence time, one has to study how good the ionospheric corrections need to be to enable the realization of PPP-RTK. Therefore, in this work, we present the method to assess the precision of the ionospheric corrections required to improve the PPP-IAR performance at the user side by means of the necessary time to fix ambiguities to their integers. Our approach consists of a design computation scheme, where a user is simulated to process GPS-only dual-frequency undifferenced and uncombined code and carrier phase measurements using the PPP-RTK technique. By presenting this methodology, we propose an ionosphere modeling strategy to improve the TEC precision at a regional scale and obtained accurate satellite code biases that are useful for positioning, navigation and timing (PNT) applications. This is the main contribution of this work.

The structure of this work is as follows. Section 2.2 reviews in brief *S*-system theory for a general model formulation. In Section 2.3, the methodology of the design computation

is analyzed to obtain the required precision of ionospheric corrections for PPP-RTK. We close this section by describing in detail the real data and ionosphere representation used for retrieving the unbiased TEC and satellite code biases at a regional scale. Section 2.4 presents the results of the design computation and our ionosphere modeling approach based on PPP-IAR derived TECMs. We conclude in Section 2.5.

2.2 Brief review of S-system theory

Let us start with a linear model:

$$E(y) = A\,x, \quad D(y) = Q_{yy} \tag{2.1}$$

where the observation and parameter vectors of dimensions k and l are denoted by y and x, respectively. Here $E(\cdot)$ and $D(\cdot)$ denote the expectation and dispersion operators, respectively. The design matrix $A \in \mathbb{R}^{k\times l}$ is rank-deficient with $\text{rank}(A) = q \leq l$, while the measurement variance-covariance matrix (VCM) Q_{yy} is assumed positive definite. A rank-deficient design matrix implies that not all the unknown parameters can be unbiasedly determined, given the information content in y due to linear dependence of some of the columns of A. This rank deficiency is of size $\dim \mathcal{N}(A) = l - q$ with $\mathcal{N}(A) = \mathcal{R}(V)$, where $\mathcal{N}(\cdot)$ denotes the null space and $\mathcal{R}(\cdot)$ denotes the range space; these two spaces are complementary. V is an $l \times (l-q)$ basis matrix of $\mathcal{N}(A)$, such that $AV = 0$.

Due to this rank deficiency, the parameter vector can be decomposed into its estimable x_S and non-estimable part x_V, using the $l \times q$ and $l \times (l-q)$ basis matrices S and V, respectively:

$$\begin{aligned} x &= x_S + x_V \\ &= S\alpha + V\beta \end{aligned} \tag{2.2}$$

where α denotes the q-vector containing the estimable parameter functions, while β denotes the $(l-q)$-vector containing the non-estimable parameter functions. Although there is not a unique S, the choice of S determines which estimable parameters are solved for and what their interpretation is.

By inserting (2.2) into the rank-deficient linear observation model (2.1), one obtains the full-rank model:

$$E(y) = A\,x = A\,(x_S + x_V) = \underbrace{(A\,S)}_{\tilde{A}}\,\alpha \tag{2.3}$$

where $\tilde{A}$ denotes the $k \times q$ full-rank design matrix of rank q.

From (2.3), one can easily observe that the parameter changes leave the observations invariant. It should be highlighted here that the estimable parameters x_S and x'_S, based on the basis matrices S and S' respectively, cannot be directly compared due to the different choice of singularity-basis. If one wants to compare the two solutions, one out of the two needs to be transferred to the other's S-basis using an S-transformation matrix [30, 31].

2.3 Methodology

This section starts with the functional model of the PPP-RTK user and ends with the models and algorithms used in the regional VTEC modeling.

2.3.1 PPP-RTK user design computation

Faster convergence times are expected if the PPP-RTK user corrects a priori for the ionospheric delays, which are computed and modeled at the network side. The reason is that their presence significantly affects the resolution of integer ambiguities and, therefore, the solution's convergence time. Prior to the ionosphere modeling step, the first thing that one should do is to investigate how precise the ionospheric corrections need to be in order to enable faster integer ambiguity resolution, and therefore enable a significant reduction in the convergence time of the PPP-RTK solutions.

For this reason, a design computation is performed in this study, simulating a *GPS-only dual-frequency* PPP-RTK user environment in order to assess the effect of the ionospheric corrections precision on the Time-To-First-Fix (TTFF), instead of the convergence time since no real data are used in this case. TTFF here refers to the required amount of time needed to achieve successful integer ambiguity resolution based on a pre-defined success rate. The success rate is an important measure, since it indicates the probability that the ambiguities have been fixed to the correct integers. Once the ambiguities are resolved and TTFF is obtained, the estimable GNSS parameters will converge faster due to the stronger functional model.

The ionospheric corrections can be estimated and modeled within a PPP-RTK network component. The basis of the PPP-RTK network system in this study consists of the set of *undifferenced* and *uncombined* carrier phase and pseudorange observation equations. For a receiver-satellite combination $r-s$ at frequency j, they are defined as [34]:

$$\begin{aligned} E(\phi^s_{r,j}) &= \rho^s_r + (dt_r - dt^s) + m^s_r \tau_r - \mu_j \iota^s_r + \lambda_j(\delta_{r,j} - \delta^s_{,j} + a^s_{r,j}) \\ E(p^s_{r,j}) &= \rho^s_r + (dt_r - dt^s) + m^s_r \tau_r + \mu_j \iota^s_r + (d_{r,j} - d^s_{,j}) \end{aligned} \tag{2.4}$$

where $\phi^s_{r,j}$ and $p^s_{r,j}$ denote the phase and code measurements, ρ^s_r the receiver-satellite range, τ_r the tropospheric zenith delay, m^s_r the tropospheric mapping function, dt_r and dt^s the receiver and satellite clock offsets, ι^s_r the (first-order) slant ionospheric delays on the first frequency, μ_j the frequency-dependent ionospheric coefficient, $d_{r,j}$ and $d^s_{,j}$ the receiver and satellite code biases, $\delta_{r,j}$ and $\delta^s_{,j}$ the receiver and satellite phase biases, $a^s_{r,j}$ the integer phase ambiguity, and λ_j the wavelength at frequency j.

The above variables have a receiver index $r = 1,\ldots,n$, with n the number of receivers, a frequency index $j = 1,\ldots,f$, with f the number of frequencies ($f = 2$ in this paper), and a satellite index $s = 1,\ldots,m$, with m the number of satellites. All variables are time-dependent and are expressed in meters, except for the phase biases and ambiguities, which are expressed in cycles while the latter remain constant over time unless a cycle slip occurs. The ionospheric coefficient is defined as the squared ratio of frequencies: $\mu_j = (f_1/f_j)^2$. In a dual-frequency GPS-only case, $\mu_1 = 1$ and $\mu_2 = (77/60)^2$.

The above undifferenced observation equations cannot be used *directly* to estimate all the unknown parameters, since the design matrix is rank-deficient. To solve for the rank-deficient system of observation equations in the PPP-RTK network side, the *S*-system theory [31] is applied, according to which several parameters are mapped to others in order to allow for a full-rank system of observation equations. In this paper, a *Common Clocks (pivot) Receiver* (CC-R) *S*-basis [12] is used to overcome the rank deficiencies, and the estimable parameters (denoted using the $\tilde{(.)}$ symbol) at a single receiver r are presented in Table 2.1.

Assuming the receiver and satellite positions are known and precise enough, the observed-minus-computed observation equations become as follows:

$$E(\phi^s_{r,j}) = m^s_r \tau_r - \mu_j \tilde{\imath}^s_r + \begin{cases} \tilde{d}t_r \quad -\tilde{d}t^s \quad +\lambda_j \tilde{\delta}_{r,j} \quad -\lambda_j \tilde{\delta}^s_{,j} \quad +\lambda_j \tilde{a}^s_{r,j}, & \forall\, r \neq p,\ s \neq p \\ \tilde{d}t_r \quad -\tilde{d}t^s \quad +\lambda_j \tilde{\delta}_{r,j} \quad -\lambda_j \tilde{\delta}^s_{,j} \quad , & \forall\, r \neq p,\ s = p \\ \qquad\quad -\tilde{d}t^s \qquad\quad -\lambda_j \tilde{\delta}^s_{,j} \quad , & \forall\, r = p,\ s \neq p \\ \qquad\quad -\tilde{d}t^s \qquad\quad -\lambda_j \tilde{\delta}^s_{,j} \quad , & \forall\, r = p,\ s = p \end{cases} \tag{2.5}$$

$$E(p^s_{r,j}) = m^s_r \tau_r + \mu_j \tilde{\imath}^s_r + \begin{cases} \tilde{d}t_r \quad -\tilde{d}t^s \quad , & \forall\, r \neq p,\ s \neq p \\ \tilde{d}t_r \quad -\tilde{d}t^s \quad , & \forall\, r \neq p,\ s = p \\ \qquad -\tilde{d}t^s \quad , & \forall\, r = p,\ s \neq p \\ \qquad -\tilde{d}t^s \quad , & \forall\, r = p,\ s = p \end{cases} \tag{2.6}$$

The network-derived satellite clock offsets and satellite phase biases comprise the key for the single-receiver PPP-IAR users to enable integer ambiguity resolution. Although these estimable parameters are biased, they can still do the job for the PPP-IAR user if the latter employs the same functional model with the same parameter mapping that was used in the network component. In that case, the interpretation of the estimable user parameters is the same as this in the network component.

Linearizing the observation equations with respect to the unknown user position and applying the precise satellite orbits and network-derived corrections for the satellite clock offsets and phase biases, the user's dual-frequency code and carrier phase measurements (with user index u) are as follows:

$$\begin{aligned} E(\tilde{\phi}^s_{u,j}) &= \phi^s_{u,j} + g^{s^{\mathrm{T}}}_u x^s + \tilde{d}t^s + \lambda_j \tilde{\delta}^s_{,j} \\ &= g^{s^{\mathrm{T}}}_u \Delta x_u + \tilde{d}t_u + m^s_u \tau_u - \mu_j \tilde{\imath}^s_u + \lambda_j (\tilde{\delta}_{u,j} + \tilde{a}^s_{u,j}) \end{aligned} \tag{2.7}$$

$$\begin{aligned} E(\tilde{p}^s_{u,j}) &= p^s_{u,j} + g^{s^{\mathrm{T}}}_u x^s + \tilde{d}t^s \\ &= g^{s^{\mathrm{T}}}_u \Delta x_u + \tilde{d}t_u + m^s_u \tau_u + \mu_j \tilde{\imath}^s_u \end{aligned} \tag{2.8}$$

where $\tilde{\phi}^s_{u,j}$ and $\tilde{p}^s_{u,j}$ denote the observed-minus-computed phase and code measurements; $g^{s^{\mathrm{T}}}_u$ denotes the unit vectors pointing from the satellites to the receiver.

Table 2.1: Estimable dual-frequency network parameters, including their interpretation and conditions using the CC-R *S*-basis (the symbol p denotes the pivot satellite/receiver if it is used as superscript/subscript).

Estimable parameter	**Interpretation**	**Conditions**
Receiver clock	$\tilde{dt}_r = (dt_r + d_{r,\mathrm{IF}}) - (dt_p + d_{p,\mathrm{IF}})$	$\forall\, j,\, r \neq p$
Satellite clock	$\tilde{dt}^s = (dt^s + d^s_{,\mathrm{IF}}) - (dt_p + d_{p,\mathrm{IF}})$	$\forall\, j,\, s$
Ionospheric delay	$\tilde{\imath}^s_r = \imath^s_r + d_{r,\mathrm{GF}} - d^s_{,\mathrm{GF}}$	$\forall\, j,\, r,\, s$
Receiver phase bias	$\tilde{\delta}_{r,j} = \left(\delta_{r,j} - \frac{1}{\lambda_j}[d_{r,\mathrm{IF}} - \mu_j\, d_{r,\mathrm{GF}}] + a^p_{r,j}\right)$ $-\left(\delta_{p,j} - \frac{1}{\lambda_j}[d_{p,\mathrm{IF}} - \mu_j\, d_{p,\mathrm{GF}}] + a^p_{p,j}\right)$	$\forall\, j,\, r \neq p$
Satellite phase bias	$\tilde{\delta}^s_{,j} = \left(\delta^s_{,j} - \frac{1}{\lambda_j}[d^s_{,\mathrm{IF}} - \mu_j\, d^s_{,\mathrm{GF}}]\right)$ $-\left(\delta_{p,j} - \frac{1}{\lambda_j}[d_{p,\mathrm{IF}} - \mu_j\, d_{p,\mathrm{GF}}]\right) - a^s_{p,j}$	$\forall\, j,\, s$
Phase ambiguity	$\tilde{a}^s_{r,j} = (a^s_{r,j} - a^p_{r,j}) - (a^s_{p,j} - a^p_{p,j})$	$\forall\, j,\, r \neq p,\, s \neq p$
S-basis	$dt_p,\, d_{r,j},\, d^s_{,j},\, \delta_{p,j},\, a^p_{r,j},\, a^s_{p,j}$	$\forall\, j,\, r,\, s$

$(\cdot)_{,\mathrm{IF}} = \frac{1}{\mu_2 - \mu_1}[\mu_2\,(\cdot)_{,1} - \mu_1\,(\cdot)_{,2}]$; $(\cdot)_{,\mathrm{GF}} = -\frac{1}{\mu_2 - \mu_1}[(\cdot)_{,1} - (\cdot)_{,2}]$

It can be deduced that the user's receiver phase biases and integer carrier phase ambiguities are separable now, leading to a full-rank system of observation equations, due to the fact that the integer ambiguities vanish for the pivot satellite while the receiver phase biases do not, unlike (2.4) where the phase biases and ambiguities are lumped into one frequency-dependent ambiguity term. This separation is a direct consequence of the *S*-basis used in this study to overcome the rank deficiencies between the phase biases and ambiguities, as can be seen from Table 2.1. As a result, the user is able to perform IAR when the estimated ambiguities are precise enough and meet a pre-defined success rate threshold.

Ionosphere-float model

The PPP-IAR user model consisting of the observation equations (2.7) and (2.8), in which the (biased) ionospheric slant delays are estimated as unknown parameters, is the so-called *ionosphere-float* model [35].

The undifferenced and uncombined code and carrier phase measurements are described by the following stochastic model:

$$D\left(\begin{bmatrix} \tilde{\phi} \\ \tilde{p} \end{bmatrix}\right) = \begin{bmatrix} Q_{\tilde{\phi}\tilde{\phi}} & 0 \\ 0 & Q_{\tilde{p}\tilde{p}} \end{bmatrix} \tag{2.9}$$

where $Q_{\tilde{\phi}\tilde{\phi}}$ and $Q_{\tilde{p}\tilde{p}}$ denote the dual-frequency measurement VCMs for the observed-minus-computed phase and code measurements, respectively. It is usually assumed that no correlation exists between frequencies and between code and phase measurements. In

reality, however, there exists correlation **a)** between code and phase measurements since both of them have been corrected for the satellite orbits and the network-derived satellite clock offsets, and **b)** between frequencies for the phase measurements because of the applied satellite phase biases. Only the first type of correlation was taken into account in our study for simplicity.

The satellite phase biases and satellite clock offsets transmitted to the PPP user are the key for IAR-enabled precise point positioning. To achieve that, the integer ambiguities need to be fixed correctly. However, it is known that the ionosphere-float PPP-IAR model is rather weak in terms of integer ambiguity resolution, since the estimable parameters for the unknown ionospheric delays affect the solution's convergence time. Therefore, a great shortening in the convergence time is expected in case ionospheric corrections are available to PPP-IAR users [12].

Ionosphere-fixed model

In case ionospheric corrections are provided to PPP-IAR users, by either spatial interpolation or function-based modeling, faster integer ambiguity resolution than by using the ionosphere-float model is expected, since unknown parameters for the ionosphere do not need to be estimated.

This is the *ionosphere-fixed* model, in which such precise ionospheric corrections are provided to the PPP-IAR users that can be assumed to be deterministic. As a result, a combined parameter of the GF receiver and satellite code biases becomes estimable:

$$\tilde{d}^s_{u,\mathrm{GF}} = \mu_j (d_{u,\mathrm{GF}} - d^s_{,\mathrm{GF}}) \tag{2.10}$$

where $d_{u,\mathrm{GF}}$ and $d^s_{,\mathrm{GF}}$ are scaled versions of the satellite and receiver differential code biases (DCB). It is, therefore, intentional to estimate the satellite DCBs (SDCBs) at the network side, in order to provide them to and allow the user to solve for less parameters making the used observational model stronger. The receiver DCBs (RDCBs) and SDCBs can be separated by selecting a proper S-basis. Therefore, the provision of ionospheric corrections and SDCBs to the user allows the estimability of a scaled version of RDCB.

Ionosphere-weighted model

The aforementioned ionosphere-fixed model changes to an ionosphere-weighted model, firstly introduced by [36], in case the provided ionospheric corrections are assumed to be stochastic parameters, rather than deterministic. The functional model remains the same as in the ionosphere-fixed model, but with a different VCM. In particular, the uncertainty σ_ι of the provided ionospheric corrections is taken into account as follows:

$$D\left(\begin{bmatrix} \tilde{\phi} + \mu \otimes \iota \\ \tilde{p} - \mu \otimes \iota \end{bmatrix}\right) = \begin{bmatrix} Q_{\tilde{\phi}\tilde{\phi}} + \sigma^2_\iota \mu\mu^{\mathrm{T}} & -\sigma^2_\iota \mu\mu^{\mathrm{T}} \\ -\sigma^2_\iota \mu\mu^{\mathrm{T}} & Q_{\tilde{p}\tilde{p}} + \sigma^2_\iota \mu\mu^{\mathrm{T}} \end{bmatrix} \tag{2.11}$$

where $\otimes$ denotes the matrix Kronecker product [37], and $\mu = (\mu_1, \mu_2)^{\mathrm{T}}$ is the 2-vector containing the wavelength ratios.

Since the same ionospheric corrections are applied to both code and phase measurements, the VCM is no longer a block-diagonal matrix. Instead of applying the stochastic ionospheric corrections directly to the phase and code measurements, the user can use them as pseudo-observations and weight them based on their standard deviations.

Therefore, the ionosphere-weighted model is the general model, from which the aforementioned other two models can be produced. If unknown parameters for the ionospheric delays are estimated or prior ionospheric corrections do not contribute to the solution, the model is transformed into the ionosphere-float one ($\sigma_\iota = \infty$). If, on the other hand, the ionospheric corrections are precise enough to be assumed deterministic, the ionosphere-float model is transformed into the ionosphere-fixed one ($\sigma_\iota = 0$).

2.3.2 Ionosphere modeling

GNSS-based measurements have proven to be capable of remotely sensing the Earth's dynamic ionosphere. As already stated, there are several methods to extract slant ionospheric slant delays with varying interpretation and precision. Out of all of them, we selected the PPP-IAR technique in order to process *undifferenced* and *uncombined* code and phase measurements and obtain the estimable parameters as shown in Table 2.1.

The estimable ionospheric slant delays (expressed in meters) are biased by the receiver and satellite DCBs, using the chosen *S*-basis:

$$\begin{aligned} \tilde{\iota}_r^s &= \iota_r^s + d_{r,\mathrm{GF}} - d_{,\mathrm{GF}}^s \\ &= \iota_r^s - \frac{\mu_1}{\mu_2 - \mu_1}[(\underbrace{d_{r,1} - d_{r,2}}_{\mathrm{RDCB}}) - (\underbrace{d_{,1}^s - d_{,2}^s}_{\mathrm{SDCB}})] \end{aligned} \tag{2.12}$$

In order to estimate both the VTEC and the satellite and receiver DCBs simultaneously, one needs to make use of the thin-layer ionosphere model. According to the latter, the ionosphere is assumed to be a spherical shell at a height of 450 km above the Earth's surface. The slant total electron content ι_r^s (STEC) is mapped to its vertical counterpart v_r^s at the points where the satellite-to-receiver signal paths intersect the ionospheric shell, the so-called Ionospheric Pierce Points (IPPs), using the following mapping function $M_r^s(i)$ [19]:

$$M_r^s(i) = \left[1 - \left(\frac{R}{R+h} \cdot \sin(Z_r^s(i))\right)^2\right]^{-1/2} \tag{2.13}$$

where R is the mean Earth's radius, h is the height of the ionospheric shell (450 km in our case), and $Z_r^s(i)$ is the zenith angle of satellite s observed from receiver r at epoch i. Then, considering that $\iota_r^s(i) = M_r^s(i) \cdot v_r^s(i)$, the VTEC at an IPP can be mathematically modeled by a wide variety of representation functions in the time and space domain. In this study, the Generalized Trigonometric Series function [20] (sum of a polynomial function and a finite Fourier series) was used to model VTEC on a regional scale:

$$\begin{aligned} v_r^s(i) = &\sum_{a=0}^{A}\sum_{b=0}^{B}\left\{E_{ab}(\phi_{\mathrm{IPP}} - \phi_{\mathrm{REC}})^a \Lambda_{\mathrm{IPP}}^b\right\} \\ &+ \sum_{k=1}^{K}\{C_k \cos(k\,\Lambda_{\mathrm{IPP}}) + S_k \sin(k\,\Lambda_{\mathrm{IPP}})\} \end{aligned} \tag{2.14}$$

where ϕ_{IPP} and ϕ_{REC} denote the geomagnetic latitude of the IPPs and the receivers, respectively; Λ_{IPP} denote the solar longitude of the IPPs; A, B and K are the maximum orders of expansion; E_{ab}, C_k and S_k are the model coefficients to be estimated as functions of time.

Thus, if the model coefficients are stored in a vector w and their corresponding scaling factors at epoch i are stored in the design matrix A_r^s, the VTEC in units of meters is described as:

$$v_r^s(i) = A_r^s(i) \cdot w(i) \tag{2.15}$$

In addition to the VTEC, which is expressed as a function of ionosphere model coefficients, the biased ionospheric observables contain the RDCBs and the SDCBs, which also need to be estimated. The system of observation equations shows a rank-deficiency, though, since the receiver and satellite code biases cannot be unbiasedly estimated. For this reason, a proper S-basis was employed according to the S-system theory in order to form a full-rank system of observation equations.

From the observation equation (2.12) at a single receiver r, it can be deduced that the ionospheric observables determined by a single receiver r are not enough to determine both the ionosphere model coefficients and the receiver and satellite hardware delays. As such, the ionospheric observables from n receivers of a regional network shall be used. This also strengthens the observation model, since the satellites are tracked by multiple instead of only one receivers, which allows for reliable estimation of satellite DCBs.

Therefore, given the mapping function (2.13), the functional model reads:

$$\tilde{\imath}(i) = M(i)\, A(i)\, w(i) - \frac{\mu_1}{\mu_2 - \mu_1} \left[(I_n \otimes e_m)\, \tilde{d}_* - (e_n \otimes I_m)\, \tilde{d}^* \right] \tag{2.16}$$

with

$$\begin{aligned} \tilde{\imath} &= [\tilde{\imath}_1, \ldots, \tilde{\imath}_n]^{\mathrm{T}} \\ \tilde{\imath}_r &= [\tilde{\imath}_r^1, \ldots, \tilde{\imath}_r^m]^{\mathrm{T}} \\ \tilde{d}_* &= [\tilde{d}_1, \ldots, \tilde{d}_n]^{\mathrm{T}} \\ \tilde{d}^* &= [\tilde{d}^1, \ldots, \tilde{d}^m]^{\mathrm{T}} \end{aligned}$$

where $A(i)$ is the partial design matrix containing the scaling factors of the ionosphere model coefficients $w(i)$ for all receivers $r = 1, \ldots, n$, and $M(i)$ is a diagonal matrix of order $m \cdot n$ having the corresponding mapping functions at epoch i as its entries. The estimable receiver and satellite DCBs are denoted as $\tilde{d}_r$ and $\tilde{d}^s$, respectively. The n-vector having 1's as its entries is denoted as e_n, and the unit matrix of order n is denoted as I_n.

2.4 Results and analysis

We begin this section by describing the experimental setup both for the PPP-RTK user design computation and the ionosphere modeling using real GNSS data. These are then followed by numerical results, from which the major findings are described in detail.

2.4.1 Experimental setup

In the first part of our study, we simulated a dual-frequency GPS-only PPP-RTK user component in various receiver locations around the world, and employed the *Common Clocks*

(pivot) Receiver (CC-R) *S*-basis, shown in Section 2.3.1, to overcome the rank deficiencies. In this part, a formal analysis was performed and, therefore, no real data was used. The undifferenced code and carrier phase observations, sampled every 30 seconds during DOY 046/2014, were assigned with zenith-referenced a priori standard deviations (σ_p^0 and σ_ϕ^0) of 30 cm and 3 mm, respectively. An elevation-dependent scheme (el denotes the elevation angle) was used with the variances of the code and phase observations being calculated as [38]

$$\sigma_\diamond^2 = \frac{(\sigma_\diamond^0)^2}{\sin^2(el)}, \quad \diamond \in \{\phi, p\}. \tag{2.17}$$

An elevation mask of 10° was used in this study to avoid measurements acquired from satellites close to the horizon, while the precision of the precise orbit information was assumed to be equal to 2.5 cm, instead of considering it as a deterministic quantity. The ionosphere-float and ionosphere-fixed GNSS models were initially used to get the extreme cases for the obtained TTFFs, since **a)** in the first case, unknown parameters for the ionospheric delays are estimated by the user making the model weak in terms of IAR, while **b)** in the second case it is assumed that deterministic ionospheric corrections are provided to the user enabling fast IAR. The ionosphere-weighted model was then employed using a varying precision for the ionospheric corrections in order to find the optimal stochastic ionospheric corrections that can enable a shortening in the TTFF and, consequently, the convergence time.

The GNSS parameter estimation is performed in a Kalman filter. In this regard, the process noise of the parameters linked in time are listed in Table 2.2. The parameters not listed are estimated as unlinked parameters in time. The estimable parameters share the same process noise values as the unbiased ones.

The first step of the mixed-integer GNSS model solution results into the so-called *float* solution, if one ignores the integer property of the carrier phase ambiguities:

$$\begin{bmatrix} \hat{a} \\ \hat{b} \end{bmatrix} \sim \mathcal{N}\left(\begin{bmatrix} a \\ b \end{bmatrix}, \begin{bmatrix} Q_{\hat{a}\hat{a}} & Q_{\hat{a}\hat{b}} \\ Q_{\hat{b}\hat{a}} & Q_{\hat{b}\hat{b}} \end{bmatrix} \right) \tag{2.18}$$

where a is the $2(m-1)$ ambiguity vector, and b is the vector containing the rest of the estimated parameters (estimable receiver clock offset, tropospheric zenith delay, estimable ionospheric slant delays, estimable receiver code and phase bias).

The parameters of interest for the TTFF evaluation are the estimated float double-difference (DD) ambiguities, since their successful fixing depends on their precision, contained in $Q_{\hat{a}\hat{a}}$. This is the input of the second step of the mixed-integer GNSS model solution, which focuses on the integer constraint $a \in \mathbb{Z}^{2(m-1)}$, i.e. the mapping of the float ambiguities $\hat{a}$ into their corresponding integer ones $\check{a}$ with an integer mapping $\mathcal{I} : \mathbb{R}^{2(m-1)} \rightarrow \mathbb{Z}^{2(m-1)}$ such as $\check{a} = \mathcal{I}(\hat{a})$.

Table 2.2: Process noise standard deviation of the time-linked parameters in the Kalman filter for the ionosphere-weighted PPP-RTK user model. Parameters not listed in the table are estimated as unlinked parameters in time.

Parameter	Process noise
τ_r	$2\,\text{cm}/\sqrt{30\text{s}}$
$d_{r,j}$	$1\,\text{mm}/\sqrt{30\text{s}}$
$\delta_{r,j}$	$1\,\text{mm}/\sqrt{30\text{s}}$
$z^s_{r,j}$	0

In order to evaluate whether the integer ambiguities can be estimated successfully, the Integer Least Squares [39] lower bound was used, i.e. the bootsrapped success rate $P_{s,B}$. Since the bootstrapped estimator performs almost optimally after decorrelating the ambiguities using the Z-transformation of the LAMBDA method [40], the success rate $P_{s,B}$ is evaluated for the decorrelated ambiguities $\hat{z} = Z^{\mathrm{T}}\hat{a}$:

$$Q_{\hat{z}\hat{z}} = Z^{\mathrm{T}} Q_{\hat{a}\hat{a}} Z \tag{2.19}$$

Based on the decorrelated ambiguity VCM, the success rate can be evaluated [41]:

$$P_{s,B} = \prod_{i=1}^{n} \left(2\Phi\left(\frac{1}{2\sigma_{i|I}}\right) - 1 \right) \tag{2.20}$$

with Φ denoting the cumulative normal distribution, and $\sigma_{i|I}$ the standard deviation of the ith least-squares ambiguity obtained through a conditioning on the previous $I = 1, \ldots, i-1$ ambiguities. Given a user-defined minimum threshold for the ambiguity success rate, which we set to 99.5% in our study, successful integer ambiguity resolution occurs when the estimated bootstrapped success rate is larger than this threshold.

Apart from the simulations, we also used real GNSS data to validate the performance of the PPP-RTK technique with raw code and phase measurements for regional ionospheric VTEC modeling. For this reason, CORS geodetic-grade receivers in North Carolina (US) of the NGS (National Geodetic Survey) network were selected in order to form a regional network (see Figure 2.1), for the scope of this study. The dual-frequency GPS dataset (L1C, L2C, C1C, C2W) was sampled every 30 s by 45 geodetic-grade receivers of the same receiver type (TRIMBLE NETR5) over the DOY 046, 2014.

The data were processed in our PPP-RTK engine, according to the parameterization given in Table 2.1. The code and phase measurements were weighted according to their elevation, with an undifferenced zenith-referenced standard deviation of 30 cm and 3 mm, respectively. We also used a cut-off elevation angle of 5° to discard noisy measurements. A Kalman filter is used for the GNSS parameter estimation, using the precise orbit and clock products distributed by the European Space Operation Center (ESOC) of the European Space Agency (ESA). Unknown parameters for the ionospheric delays are estimated for every receiver-satellite link.

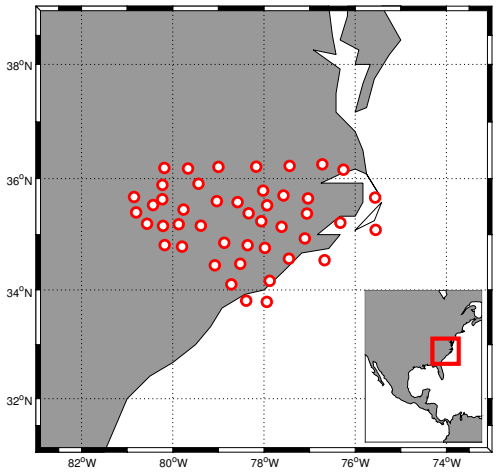


Figure 2.1: Geographic locations of the 45 CORS receivers (red-white dots) in North Carolina (US) that provide the GPS dataset used for ionosphere modeling. The average distance between the stations is about 50 km.

As stated earlier, the PPP-IAR-derived biased ionospheric slant delays serve as input for modeling the VTEC in the selected regional network. In order to allow for a rigorous and reliable determination of the ionospheric model coefficients and the RDCBs and SDCBs, a pre-processing of the TECM observables was applied. In particular, the data of the first and last 50 epochs (25 min) of each observable arc were excluded in order to avoid estimates computed during the convergence period and the satellite setting interval. The unknown parameters are the ionosphere model coefficients, receiver and satellite DCBs. At this stage, a Kalman filter was used to determine these parameters epoch by epoch, using a cut-off elevation angle of 12° to discard noisy measurements.

2.4.2 Results of the design computation

In this section, the impact of the zenith-referenced ionospheric corrections precision on ambiguities, and as such, on the achieved position precision and TTFF is investigated at the PPP-RTK user component. The TTFF is defined as the number of epochs required to obtain reliable integer ambiguity fixing, based on the pre-defined probability of correct integer ambiguity fixing which we set to 99.5%.

The achieved formal precision of the horizontal and vertical position components is illustrated in Figure 2.2 and Figure 2.3, using GPS dual-frequency measurements and making use of the ionosphere-float, -fixed and -weighted models. It can be easily seen that the TTFF is almost 30 min in case of the ionosphere-float model, while the ionosphere-fixed model achieves instantaneous IAR with the formal precision of the horizontal and vertical components reaching 2 and 5 cm, respectively. As expected, the achieved

formal precision in the vertical position component is worse than in the horizontal component for all examined cases.

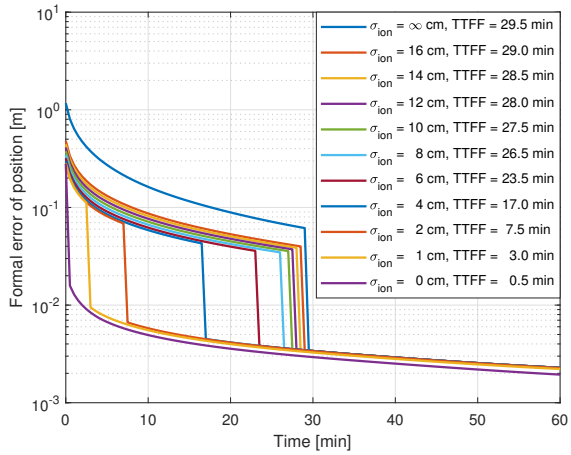


Figure 2.2: Formal precision (in meters) of the horizontal position achieved by the ionosphere-float, -fixed and -weighted PPP-IAR user models with the minimum required success rate set to 99.5%, employing various ionospheric corrections precisions.

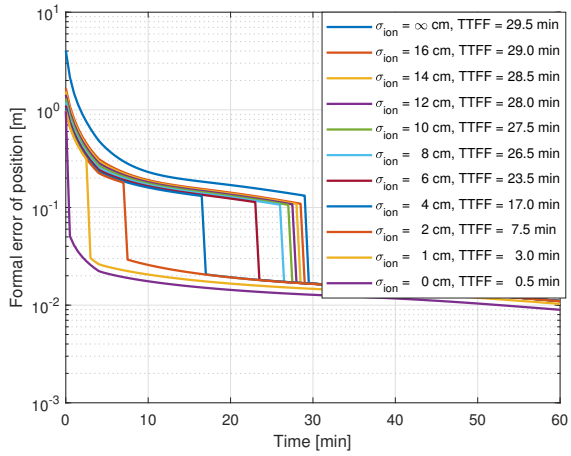


Figure 2.3: Formal precision (in meters) of the vertical position achieved by the ionosphere-float, -fixed and -weighted PPP-IAR user models with the minimum required success rate set to 99.5%, employing various ionospheric corrections precisions.

Moreover, one can observe the effect of the ionospheric corrections precision on the TTFF of the solutions. In particular, in case the precision of the corrections is 16 cm (almost 1 TECU), then the improvement in TTFF is negligible. It can be seen that although

an ionospheric precision ranging from 8 to 16 cm shortens the TTFF of the solutions, this improvement is in general small. Ionospheric corrections with precision of 4 cm lead to a TTFF equal to 17 min for the PPP-RTK model, almost half of the time required for the ionosphere-float PPP-IAR model to achieve successful integer ambiguity resolution.

After an extensive data analysis with various ionospheric error precisions and for 1440 initialization times during the day, i.e. for every minute of the day, in order to take into account the effect of satellite geometry, we present the final results in Figure 2.4. One can deduce that a significant improvement in the TTFF for the PPP-RTK user is observed in case the ionospheric corrections have a precision better than 5 cm.

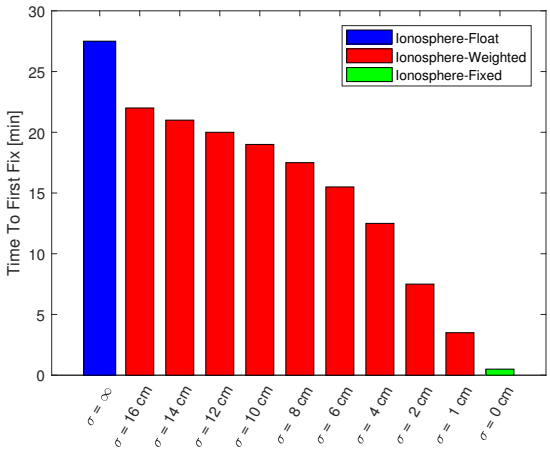


Figure 2.4: Time-To-First-Fix (in minutes) achieved from a simulated GPS dual-frequency PPP-IAR user using the ionosphere-float, -fixed and -weighted models, employing various ionospheric corrections precisions. The values have been computed for various receiver locations and for multiple initialization times during the day.

2.4.3 Results of the ionosphere VTEC modeling

First, we focus on Figure 2.5, illustrating the ambiguity-fixed estimable ionospheric slant delays from a single CORS receiver in North Carolina for all the observed satellites throughout a day. Ambiguity-fixed estimate is a parameter that has been estimated after successful integer ambiguity resolution. The magnitude of the ionospheric delays is relative since they are biased by the receiver and satellite DCBs. However, one can easily observe the typical signature of ionosphere due to the higher variation and larger magnitudes of the ionospheric observables at daytime than at night (North Carolina: UTC = LT - 4 hours).

In Figure 2.6, the formal precision of the ambiguity-float and ambiguity-fixed ionospheric delay estimates are depicted. The convergence process of the estimates at each arc beginning is obvious, in which formal precisions are within 10 TECU. Formal precisions converge to the 0.20 TECU level in 30 minutes at minimum and in 2 hours at maximum for the ambiguity-float case, depending on the observational session duration, while in 1

minute at minimum and in 10 minutes at maximum for the ambiguity-fixed case. After the convergence time, the ambiguity-float estimates have a formal precision still larger than 0.10 TECU, whereas the ambiguity-fixed ones can reach the 0.06 TECU precision level, clearly showing the dramatic improvement in precision after IAR. Moreover, it can be seen that formal precision becomes worse at the end of the arcs, which is due to the satellite setting towards the horizon.

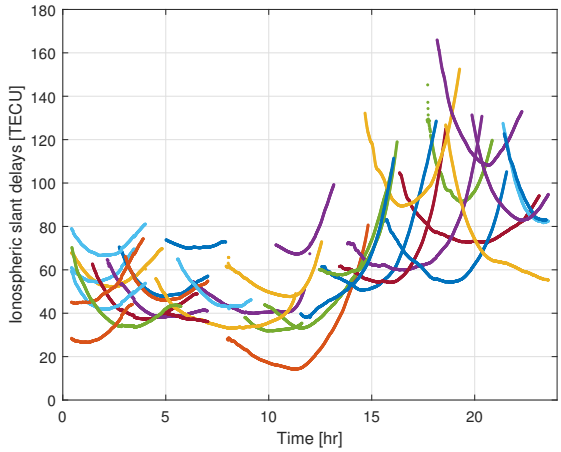
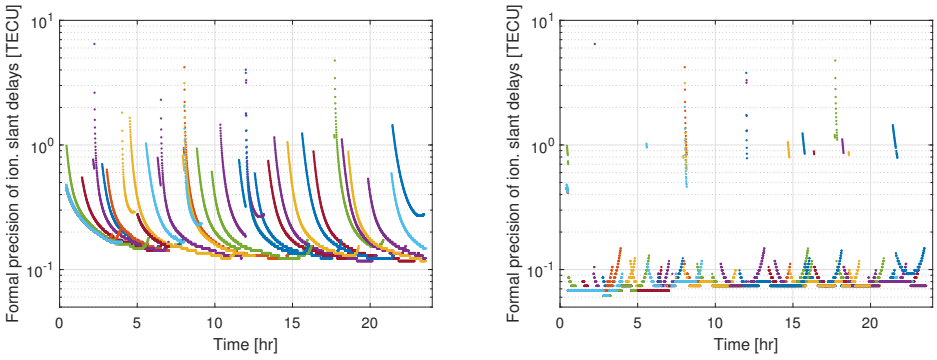


Figure 2.5: PPP-IAR ambiguity-fixed ionospheric slant delay estimates (in TECU) from a CORS receiver on DOY 046/2014 (UTC time). Each color represents a different satellite.



(a) Ambiguity-float (b) Ambiguity-fixed

Figure 2.6: Formal precision of PPP-IAR ambiguity-float (a) and ambiguity-fixed (b) ionospheric slant delay estimates (in TECU) from a CORS receiver on DOY 046/2014 (UTC time). Each color represents a different satellite.

Apart from the formal precisions, the precision of the ionospheric slant delay estimates can be validated with the between-receiver (BR) differences of short or zero base-

lines [18, 26]. The BR differences of STECs eliminate the lumped satellite DCBs and most of the ionospheric errors, with the BR RDCBs and the ionospheric delay residuals being the remaining parameters.

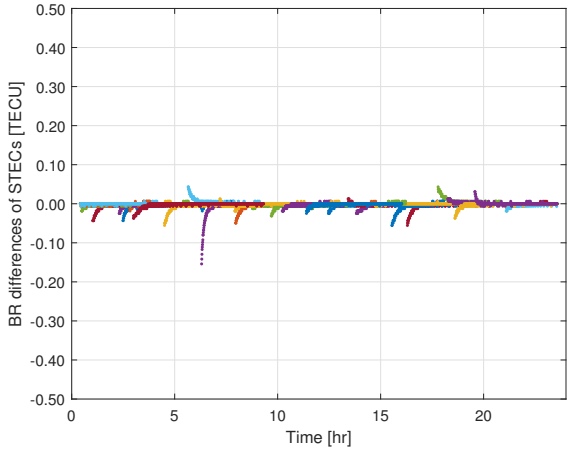


Figure 2.7: Between-receiver differences of PPP-IAR ambiguity-fixed ionospheric slant delay estimates (in TECU) for two CORS receivers with inter-station distance of 45 km on DOY 046/2014 (UTC time). Each color represents a different satellite.

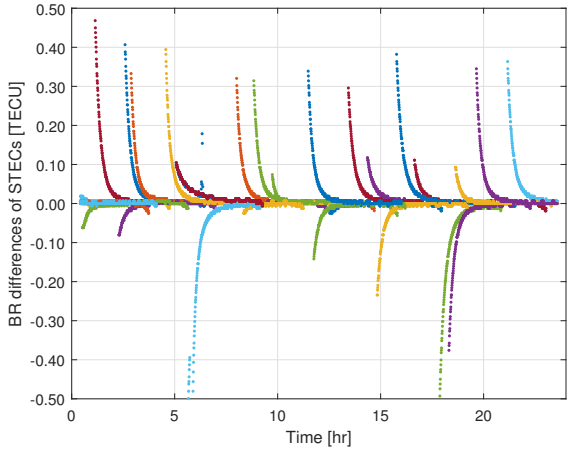


Figure 2.8: Between-receiver differences of PPP-IAR ambiguity-fixed ionospheric slant delay estimates (in TECU) for two CORS receivers with inter-station distance of 500 km on DOY 046/2014 (UTC time). Each color represents a different satellite.

The BR STEC differences of two CORS stations in North Carolina, with inter-station distances of 45 km and 500 km, are shown in Figure 2.7 and Figure 2.8, respectively, on

DOY 064, 2014. All four receivers share the same receiver type, meaning that the BR RDCBs are eliminated. In the 45 km baseline, it can be seen that the BR differences show a fast convergence, with most of the differences not exceeding the 0.01 TECU level.

Although the same level is achieved in the 500 km baseline, one can easily observe the much longer convergence time, probably due to small-scale changes in the ionosphere within this distance. Through this analysis, we conclude that PPP-IAR with raw observations can extract high-precision TEC measurements and avoid the levelling errors that are present in the CCL method.

The performance of the proposed regional ionosphere VTEC modeling algorithm was first evaluated based on the least-squares residuals of the ambiguity-fixed ionospheric observables over the selected day, as shown in Figure 2.9. It can be observed that most of the measurement residuals do not exceed the 1.00 TECU level, while 90% of them range within 0.50 TECU. However, a few measurement residuals exceeding the 2.00 TECU level can be observed. These residuals correspond to the measurements acquired by the newly tracked and lost satellites observed from the CORS network receivers and, therefore, their corresponding estimates need some time to converge. The Root Mean Square (RMS) of the residuals for all the receiver-satellite links throughout the selected day is equal to 0.48 TECU, which indicates that the selected representation function can fit well the ionosphere on the selected day.

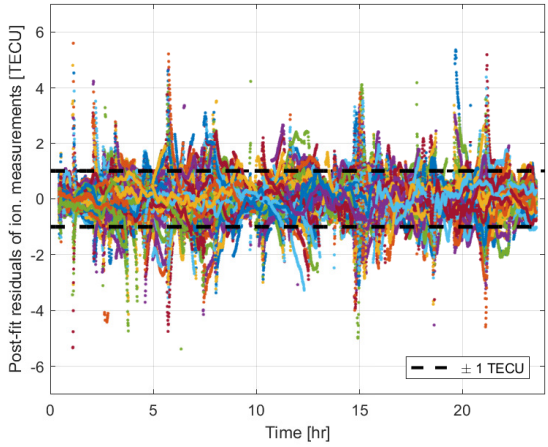


Figure 2.9: Least-squares residuals (in TECU) of PPP-IAR ambiguity-fixed ionospheric observables on DOY 046/2014. Each colour represents a different measurement.

Then, an assessment of the modeled ionospheric corrections followed. For this reason, the self-consistency test [42] was used, which analyzes the slant ionospheric delay variations along a continuous arc (satellite pass) over each station. The epoch in which the satellite is at its highest elevation was assigned as the reference epoch [43]. This is an internal consistency test, providing a quality measure for the STEC computed by the used ionosphere model. The self-consistency metric is defined by the daily root mean square of the STEC variation $\Delta\iota$:

$$\Delta\iota(i) = (\iota_0(i) - \iota_0(i_{el_{\max}})) - (\iota_m(i) - \iota_m(i_{el_{\max}})), \quad \forall\, i = 1,\ldots,n \tag{2.21}$$

where ι_0 is the PPP-IAR-derived ionospheric observable, ι_m is the ionospheric slant delay derived from the estimated model coefficients, $el_{\max}$ denotes the highest satellite elevation, i the epoch. The receiver and satellite code biases are assumed to be constant over time and are, therefore, cancelled in the differencing over a continuous arc.

Figure 2.10 illustrates the self-consistency RMS measure for all receiver-satellite pairs, where the receiver investigated for the self-consistency test was excluded from the modeling step to avoid over-optimistic results. One can easily observe that most of the RMS values do not exceed the 1.50 TECU level, while the overall RMS equals 1.10 TECU. However, it seems that there exist a few outliers, since RMS values greater than 2.00 TECU are observed for a few receiver-satellite pairs.

The estimated ionosphere model was externally validated using the IGS Global Ionosphere Map (GIM) over the selected region for the selected day of year. In particular, the global CODE (Center for Orbit Determination in Europe) GIM-derived gridded VTEC values were compared to the modeled VTEC in the regional area, resulting to a mean offset of 0.91 TECU and an RMS equal to 4.50 TECU. Therefore, one concludes to the fact that there is a bias between the modeled and IGS-derived TEC models, which is due to a variety of factors. First of all, the CODE-derived global TEC map was assumed to be our ground-truth, although it is known that its accuracy ranges from 2 to 8 TECU. Moreover, a further VTEC interpolation from the grid points to points of interest result in general to larger errors. In addition, the ionosphere representation function used in our study may not be able to model the medium-scale variations of the ionosphere in our regional network, causing the detected bias.

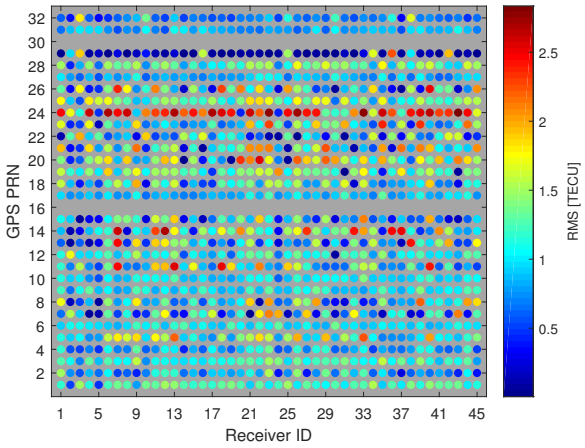


Figure 2.10: Self-consistency RMS measure (in TECU) for all receiver-satellite links.

Another performance indicator of our ionosphere modeling methodology is the behavior of the satellite and receiver DCBs. The estimates for the ambiguity-fixed GPS SDCBs on DOY 046 are shown in Figure 2.11. A stable behavior is easily observed for the code biases of almost all GPS satellites after the convergence process. The convergence time ranges from a few to several hours and, therefore, the SDCBs that are observed only for a short amount of time do not converge to a constant value. Actually, this is a disadvantage of the regional ionosphere modeling, whereas within a global network (for global VTEC modeling) the satellites are observed without gaps due to the global distribution of the stations. Moreover, it seems that the DCBs of several GPS satellites do not remain stable over the time interval during which the satellites are observed. This is attributed to the fact that those satellites are not tracked sufficiently well from all the CORS receivers of the regional network we used.

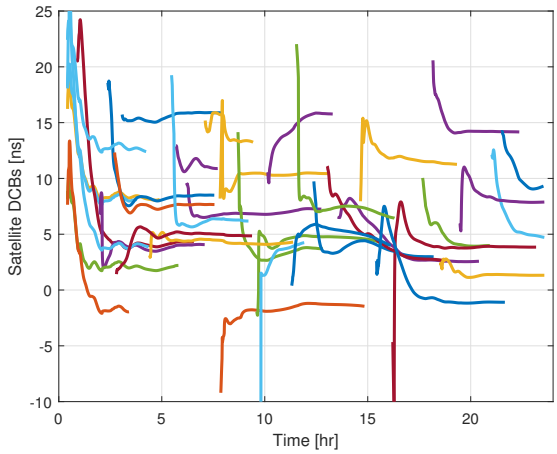


Figure 2.11: Satellite DCB estimates (in ns) on DOY 046/2014. Each colour represents a different satellite.

Figure 2.12 illustrates the formal precision of the GPS SDCBs. It is observed that most of the satellite code biases can reach a precision between 3 and 20 ps, or 1 and 6 mm respectively, depending on the observational session duration. It is deduced, therefore, that the longer a satellite is observed from the network, the more precise its DCB estimate becomes.

In order to further validate the performance of our proposed methodology for regional VTEC modeling and satellite DCB estimation, our estimable SDCBs were compared to those provided by the IGS. Within the Multi-GNSS Experiment (MGEX) [44], the German Aerospace Center (DLR) provides satellite DCB products for multi-GNSS signals, including the GPS C1C-C2W which we are interested in. Due to the fact that our estimable SDCBs are estimated based on a different S-basis than that of the IGS (zero-mean condition of satellites), their direct comparison is not possible. In order to allow for their comparison, they have to be transferred to a common S-basis. Given that, our estimable SDCBs were transferred to the S-basis of the IGS using an S-transformation [30].

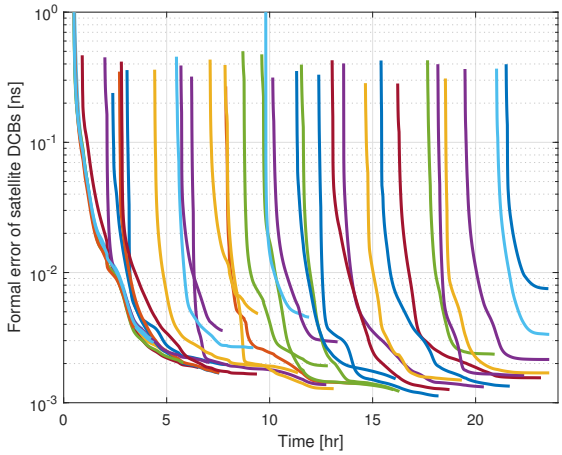


Figure 2.12: Formal precision of satellite DCB estimates (in ns) on DOY 046/2014. Each colour represents a different satellite.

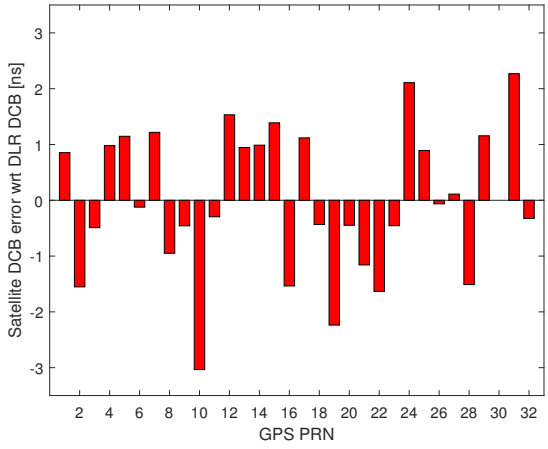


Figure 2.13: Errors (in ns) of GPS satellite DCB estimates (averaged after convergence) with respect to the DLR DCB products, on DOY 046/2014.

Figure 2.13 shows the errors of our estimable SDCBs (averaged after convergence), with respect to the DLR-derived SDCBs, based on a single-day dataset. In contrast to Figure 2.12 which shows the standard deviation of the satellite DCB estimates (derived from their variance-covariance matrix), the errors shown in Figure 2.13 serve as a measure of accuracy for the satellite DCB estimates. The satellite DCB errors show a zero mean, which was expected since both SDCBs are referred to the zero-mean condition. In addition, it can be deduced that the estimable DCBs of most of the GPS satellites do not deviate more than 2.0 ns from the published products, while 70% of them show errors lower than 1.5 ns.

Overall, the RMS of the errors is equal to 1.3 ns.

In addition to the SDCBs, the temporal behavior of the RDCBs is another performance indicator of the proposed algorithm. Figure 2.14 illustrates the estimates for the ambiguity-fixed GPS RDCBs of the CORS network receivers on DOY 046. A stable behavior can be observed for the code biases of all the used CORS receivers, which is more visible when their average is removed (Figure 2.15). Their standard deviation ranges from 0.02 to 0.17 ns within a day, and this observed receiver DCB stability is another indicator that DCB estimation is feasible in regional networks and can achieve high-precision results.

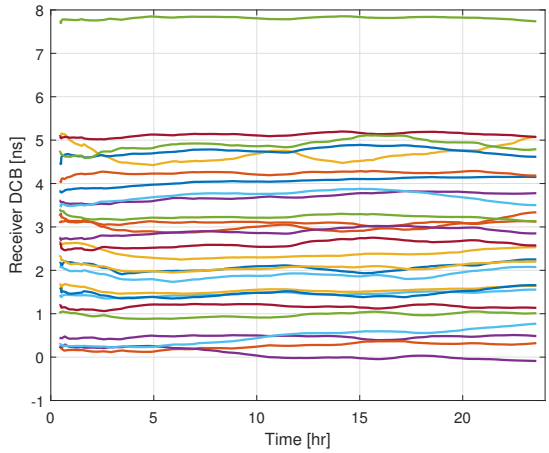


Figure 2.14: Receiver DCB estimates (in ns) on DOY 046/2014. Each colour represents a different receiver.

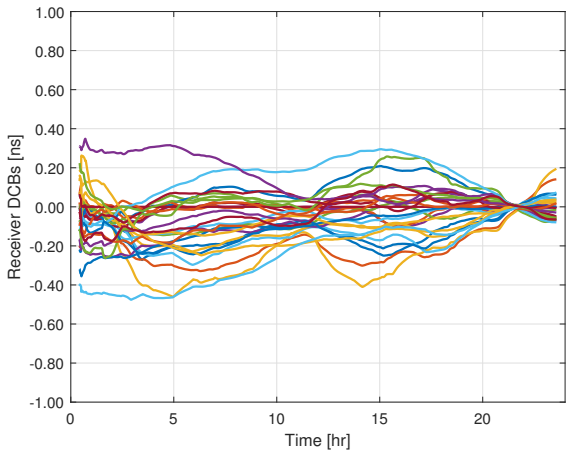


Figure 2.15: Receiver DCB estimates (in ns) on DOY 046/2014 with their average removed. Each colour represents a different receiver.

2.5 Conclusions

The main idea behind PPP-RTK is to extend the PPP technique by providing single-receiver users, apart from precise orbits and clocks, with external information (satellite phase biases, ionospheric and tropospheric corrections) so as to enable fast integer ambiguity resolution and, therefore, short convergence time. Although the undifferenced and uncombined GNSS observation model shows great flexibility for a potential multi-GNSS integration for strengthening the model with dynamic constraints on all the parameters, the unknown spatially correlated ionospheric errors still affect the GNSS observables and the convergence time, since the ionosphere-float PPP-IAR model is rather weak in terms of integer ambiguity resolution.

Faster convergence times are expected if ionospheric corrections are provided to the PPP-IAR users. Although the GNSS community has conducted a thorough research on measuring Earth's TEC, they extensively used the geometry-free code or phase measurements and the Carrier-to-Code Leveling method, which are prone to levelling errors. As a result, the alternative approach of undifferenced and uncombined PPP was recently introduced as a means of extracting more accurate TEC measurements, although still biased by hardware delays. Due to its capability to resolve the integer ambiguities, PPP-IAR is the key to obtain high-precision TEC observables which are still biased by hardware delays, but unaffected by code noise and multipath.

In this study, an analysis of the ionospheric corrections required to get a significant improvement in PPP-RTK performance was investigated. The main aim was to determine the improvement in the positioning precision and TTFF in the PPP-RTK user side using ionospheric corrections modeled from a network. The performed design computations clearly showed that faster PPP-RTK solutions are expected in case ionospheric corrections of 5 cm ($\sim$ 0.31 TECU) precision are available to the users, since the carrier-phase ambiguities can be fixed to their integer values faster.

Then, we proposed a methodology to model the PPP-IAR derived (biased) ionospheric delays on a regional scale, by parameterizing the ionospheric slant delays in terms of ionosphere model coefficients and DCBs using real GNSS measurements. PPP-IAR processing can provide high-precision ionospheric slant delays to be used for measuring the Earth's TEC. It was deduced that the proposed methodology can be used for reliable regional ionosphere modeling (RMS equal to 1.10 and 4.50 TECU for internal and external validation, respectively) and estimation of satellite DCBs (RMS of errors equal to 1.30 ns with respect to DLR products), which are required for the ionosphere-weighted PPP-RTK model. Although the zenith-referenced precision of our modeled VTEC reached the 5 cm level, a further investigation is needed to evaluate our modeled ionospheric corrections at the PPP-RTK user side in terms of convergence time reduction. Our method can be used for both real-time and post-processing, since in our study the measurements were processed epoch by epoch with a Kalman filter. The accuracy of the proposed methodology is expected to improve when a two-layer model is used for better modeling the ionospheric structure, and alternative ionosphere regional representation functions are employed.

References

[1] G. Wubbena, M. Schmitz, and A. Bagge, *PPP-RTK: Precise Point Positioning Using State-Space Representation in RTK Networks.* in *Proceedings of the 18th International Technical Meeting of the Satellite Division of The Institute of Navigation, ION GNSS 2005* (Long Beach, CA, USA, 2005) pp. 2584–2594.

[2] J. F. Zumberge, M. B. Heflin, D. C. Jefferson, M. M. Watkins, and F. H. Webb, *Precise point positioning for the efficient and robust analysis of GPS data from large networks.* Journal of Geophysical Research **102**, 5005 (1997).

[3] J. M. Dow, R. E. Neilan, and C. Rizos, *The International GNSS Service in a changing landscape of Global Navigation Satellite Systems.* Journal of Geodesy **83**, 191 (2009).

[4] S. Bisnath and Y. Gao, *Current State of Precise Point Positioning, Future Prospects and Limitations.* in *Observing Our Changing Earth. International Association of Geodesy Symposia.*, edited by M. Sideris (Springer, Berlin, Heidelberg, 2009).

[5] S. Banville, P. Collins, W. Zhang, and R. B. Langley, *Global and regional ionospheric corrections for faster PPP convergence.* Navigation **61**, 115 (2014).

[6] M. Ge, G. Gendt, M. Rothacher, C. Shi, and J. Liu, *Resolution of GPS carrier-phase ambiguities in Precise Point Positioning (PPP) with daily observations.* Journal of Geodesy **82**, 389 (2005).

[7] P. Collins, *Isolating and Estimating Undifferenced GPS Integer Ambiguities.* in *Proceedings of the 2008 National Technical Meeting of The Institute of Navigation.* (San Diego, CA, 2008) pp. 720–732.

[8] L. Mervart, Z. Lukes, C. Rocken, and T. Iwabuchi, *Precise Point Positioning with Ambiguity Resolution in Real-Time.* in *Proceedings of the 21st International Technical Meeting of the Satellite Division of The Institute of Navigation, ION GNSS 2008* (Savannah, GA, 2008).

[9] D. Laurichesse, F. Mercier, J. P. Berthias, P. Broca, and L. Cerri, *Integer Ambiguity Resolution on Undifferenced GPS Phase Measurements and its Application to PPP and Satellite Precise Orbit Determination.* Journal of The Institute of Navigation **56**, 135 (2009).

[10] J. Geng, C. Shi, M. Ge, A. H. Dodson, Y. Lou, Q. Zhao, and J. Liu, *Improving the estimation of fractional-cycle biases for ambiguity resolution in precise point positioning.* Journal of Geodesy **86**, 579 (2012).

[11] P. J. G. Teunissen and A. Khodabandeh, *Review and principles of PPP-RTK methods,* Journal of Geodesy **89**, 217 (2015).

[12] D. Odijk, A. Khodabandeh, N. Nadarajah, M. Choudhury, B. Zhang, W. Li, and P. J. G. Teunissen, *PPP-RTK by means of S-system theory: Australian network and user demonstration,* Journal of Spatial Science **62**, 3 (2017).

[13] D. Odijk, B. Zhang, A. Khodabandeh, R. Odolinski, and P. J. G. Teunissen, *On the estimability of parameters in undifferenced, uncombined GNSS network and PPP-RTK user models by means of S-system theory,* Journal of Geodesy **90**, 15 (2016).

[14] P. Henkel, D. Psychas, C. Gunther, and U. Hugentobler, *Estimation of satellite position, clock and phase bias corrections.* Journal of Geodesy **92**, 1199 (2018).

[15] S. Schaer, G. Beutler, L. Mervart, and M. Rothacher, *Global and regional ionosphere models using the GPS double difference phase observable.* 1995 IGS Workshop (1995).

[16] A. J. Manucci, B. D. Wilson, D. N. Yuan, C. H. Ho, U. J. Lindqwister, and T. F. Runge, *A global mapping technique for GPS-derived ionospheric total electron content measurements.* Radio Science **33**, 565 (1998).

[17] Y. Gao and Z. Z. Liu, *Precise Ionosphere Modeling Using Regional GPS Network Data.* Journal of Global Positioning Systems **1**, 18 (2002).

[18] L. Ciraolo, F. Azpilicueta, C. Brunini, A. Meza, and S. M. Radicella, *Calibration errors on experimental slant total electron content (TEC) determined with GPS.* Journal of Geodesy **81**, 111 (2007).

[19] C. Brunini and F. J. Azpilicueta, *Accuracy assessment of the GPS-based slant total electron content.* Journal of Geodesy **83**, 773 (2009).

[20] Z. Li, Y. Yuan, N. Wang, M. Hernandez-Pajares, and X. Huo, *SHPTS: towards a new method for generating precise global ionospheric TEC map based on spherical harmonic and generalized trigonometric series functions.* Journal of Geodesy **89**, 331 (2015).

[21] A. Khodabandeh and P. J. G. Teunissen, *S-system theory applied to array-based GNSS ionospheric sensing,* Stud. Geophys. Geod. **61**, 429 (2017).

[22] S. Banville, *Improved Convergence for GNSS Precise Point Positioning.*, Ph.D. thesis, University of New Brunswick (2014).

[23] A. Rovira-Garcia, J. M. Juan, J. Sanz, G. Gonzalez-Casado, and D. Ibanez, *Accuracy of ionospheric models used in GNSS and SBAS: methodology and analysis.* Journal of Geodesy **90**, 229 (2016).

[24] R. Tu, H. Zhang, M. Ge, and G. Huang, *A real-time ionospheric model based on GNSS Precise Point Positioning.* Advances in Space Research **52**, 1125 (2013).

[25] B. Zhang, *Three methods to retrieve slant total electron content measurements from ground-based GPS receivers and performance assessment.* Radio Science **51**, 972 (2016).

[26] T. Liu, Y. Yuan, B. Zhang, N. Wang, B. Tan, and Y. Chen, *Multi-GNSS precise point positioning (MGPPP) using raw observations.* Journal of Geodesy **91**, 253 (2017).

[27] B. Zhang, P. J. G. Teunissen, U. Yuan, H. Zhang, and M. Li, *Joint estimation of vertical total electron content (VTEC) and satellite differential code biases (SDCBs) using low-cost receivers.* Journal of Geodesy , 1 (2017).

[28] Z. Liu, Y. Li, F. Li, and G. Guo, *Near real-time PPP-based monitoring of the ionosphere using dual-frequency GPS/BDS/Galileo data.* Advances in Space Research **61**, 1435 (2018).

[29] P. J. G. Teunissen and O. Montenbruck, *Springer Handbook of Global Navigation Satellite Systems*, 1st ed. (Springer International Publishing, 2017).

[30] W. Baarda, *S-transformations and criterion matrices.* in *Publications on Geodesy, 18*, Vol. 5 (Netherlands Geodetic Commission, Delft, The Netherlands, 1973).

[31] P. J. G. Teunissen, *Zero Order Design: Generalized Inverses, Adjustment, the Datum Problem and S-Transformations.* in *Optimization and Design of Geodetic Networks.*, edited by E. Grafarend and F. Sanso (Springer, Berlin, Heidelberg, 1985) pp. 11–55.

[32] S. Schaer, *Mapping and Predicting the Earth's Ionosphere Using the Global Positioning System*, Ph.D. thesis, University of Bern (1999).

[33] R. Zhang, W. Song, Y. Yao, C. Shi, Y. Lou, and W. Yi, *Modeling regional ionospheric delay with ground-based BeiDou and GPS observations in China.* GPS Solutions **19**, 649 (2015).

[34] P. J. G. Teunissen and A. Kleusberg, *GPS for Geodesy*, 2nd ed. (Springer-Verlag, Berlin-Heidelberg-New York, 1998).

[35] P. J. G. Teunissen, *The geometry-free GPS ambiguity search space with a weighted ionosphere,* Journal of Geodesy **71**, 370 (1997).

[36] Y. Bock, S. A. Gourevitch, C. C. Counselman, R. W. King, and R. I. Abbot, *Interferometric analysis of GPS phase observations,* Manuscripta Geodaetica **11**, 282 (1986).

[37] H. V. Henderson, F. Pukelsheim, and S. R. Searle, *On the history of the kronecker product.* Linear and Multilinear Algebra **14**, 113 (1983).

[38] R. Dach, S. Lutz, P. Walser, and P. Fridez, *Bernese GNSS Software Version 5.2. User manual.* Astronomical Institute, University of Bern, Bern Open Publishing (2015), 10.7892/boris.72297.

[39] P. J. G. Teunissen, *Least squares estimation of the integer GPS ambiguities.* Invited lecture, Section IV Theory and Methodology, IAG General Meeting, Beijing (1993).

[40] P. J. G. Teunissen, *The least-squares ambiguity decorrelation adjustment: a method for fast GPS integer ambiguity estimation.* Journal of Geodesy **70**, 65 (1995).

[41] S. Verhagen, *The GNSS integer ambiguities: estimation and validation*, Ph.D. thesis, Delft University of Technology (2005).

[42] R. Orus, M. Hernandez-Pajares, J. M. Juan, and J. Sanz, *Improvement of global ionospheric VTEC maps by using kriging interpolation technique.* Journal of Atmospheric and Solar-Terrestrial Physics **67**, 1598 (2005).

[43] M. Hernandez-Pajares, D. Roma-Dollase, A. Krankowski, A. Garcia-Rigo, and R. Orus-Perez, *Methodology and consistency of slant and vertical assessment for ionospheric electron content models.* Journal of Geodesy **91**, 1405 (2017).

[44] O. Montenbruck, P. Steigenberger, L. Prange, Z. Deng, Q. Zhao, F. Perosanz, I. Romero, C. Noll, A. Sturze, G. Weber, R. Schmid, K. MacLeod, and S. Schaer, *The Multi-GNSS Experiment (MGEX) of the International GNSS Service (IGS) - Achievements, prospects and challenges.* Advances in Space Research **59**, 1671 (2017).

3

Ionosphere-weighted PPP-RTK user performances

The long convergence time required to achieve high-precision position solutions with integer ambiguity resolution-enabled precise point positioning (PPP-RTK) is driven by the presence of ionospheric delays. When precise real-time ionospheric information is available and properly applied, it can strengthen the underlying model and substantially reduce the time required to achieve centimeter-level accuracy. In this study, we present and analyze the real-time PPP-RTK user performance using ionospheric corrections from multi-scale regional networks during a day with medium ionospheric disturbance. It is the goal of this contribution to measure the impact the network dimension has on the ambiguity-resolved user position through the predicted ionospheric corrections. The user-specific undifferenced ionospheric corrections are computed at the network side, along with the satellite phase biases needed for single-receiver ambiguity resolution, using the best linear unbiased predictor. Such corrections necessitate the parameterization of an estimable user receiver code bias, on which emphasis is given in this study. To this end, we process GPS dual-frequency data from four four-station evenly distributed CORS networks in the United States with varying station spacings in order to evaluate if and to what extent the ionospheric corrections from multi-scale networks can improve the user convergence times. Based on a large number of samples, our experimental results showed that sub-10 cm horizontal accuracy can be achieved almost instantaneously in the ionosphere-weighted partially-ambiguity-fixed kinematic PPP-RTK solutions based on corrections from a network with 68 km spacing. Most of the solutions (90%) were shown to require less than 6.0 min, compared to the ionosphere-float PPP solutions that needed 68.5 min. In case of sparser networks with 115, 174 and 237 km spacing, 50% of the horizontal positioning errors are shown to become less than one decimeter after 1.5, 4.0 and 7.0 min, respectively, while 90% of them require 10.5, 16.5 and 20.0 min. We also numerically demonstrated that the user's convergence times bear a linear relationship with the network density and get shorter as the density increases, for both full and partial ambiguity resolution.

This chapter has been published as: Psychas, D. and Verhagen, S. (2020). Real-Time PPP-RTK Performance Analysis Using Ionospheric Corrections from Multi-Scale Network Configurations. Sensors, 20(11):3012, doi: 10.3390/s20113012

3.1 Introduction

PPP-RTK is the realization of integer ambiguity resolution-enabled precise point positioning (PPP), which was first conceptualized by Wübbena et al. [1]. The development of the PPP technique [2] enabled single-receiver users to achieve positioning accuracy on the order of a few centimeters and of a few decimeters in static and kinematic mode, respectively, using precise satellite orbits and clocks [3, 4].

In the frame of standard PPP, such accuracy can be obtained using data over long observational spans, ranging from tens of minutes to several hours [5, 6]. This has its roots in the incapability to resolve the phase ambiguities to integers since they cannot be separated from the receiver and satellite hardware biases existing in the code and phase data. To this end, PPP-RTK extends the PPP technique by means of providing single-receiver users, next to orbits and clocks, information about the satellite phase and code biases. This information, when properly provided, allows to recover the integerness of user-ambiguities and thus to enable single-receiver integer ambiguity resolution (IAR) [7–12].

It has to be remembered, though, that IAR is not the goal in itself. The purpose of resolving the carrier-phase ambiguities to their integers is to reduce the convergence time of PPP solutions, which is mainly governed by the presence of these unknown ambiguities. To do so, one has to map the data-driven ambiguities to their *correct* integers successfully. The reliability of this process heavily depends on the underlying model strength, which is inextricably linked to the number of available observations and unknown parameters, the stochastic model, the receiver-satellite geometry and the atmospheric errors' modeling. It has been shown that reliable ambiguity fixing in single-system PPP-RTK can be achieved when data over multiple epochs are accumulated, ranging from 30 to 60 min [13].

Such a long time span is not attractive, of course, for critical real-time applications that require fast high-precision positioning. One of the major bottlenecks of fast IAR is the presence of ionospheric delays, which need to be explicitly parameterized for in an uncombined GNSS formulation, where no a priori differencing or inter-frequency combinations take place. Such a model is weak in terms of its ambiguity resolution capabilities, due to the increased number of unknown parameters that need to be estimated.

However, an uncombined GNSS formulation has several advantages and flexibility that have already been identified [14–17]. Such an approach allows one to use the original code and phase data, usually uncorrelated, and keeps all parameters in the observation equations, thus allowing not only a flexible and rigorous extension to multi-GNSS and/or multi-frequency applications but also a possible further model strengthening. The latter can be achieved if one increases the number of observations by employing, for instance, a priori information for the ionosphere.

Successful ambiguity resolution, and thus convergence time, can be achieved much faster when precise a priori ionospheric information is provided to the users. In the present contribution, we make use of the uncombined GPS dual-frequency model to determine network-derived estimable satellite phase biases and predicted ionospheric corrections for single-receiver *fast* IAR. Although multi-frequency and multi-GNSS PPP-RTK have proven to bring an improvement in the convergence time [18, 19], the focus has been given mostly to the ionosphere-float models. In this study we focus solely on the ionosphere-weighted

model.

During recent years, there have been a few studies investigating the use of ionospheric information to reduce the PPP-RTK convergence times. Teunissen *et al.* [11] demonstrated that single-epoch ionosphere-weighted PPP-RTK can achieve mm-level horizontal accuracy using corrections from two small-scale networks with inter-station distances of around 27 and 60 km in different locations. Using a different parameter mapping and two networks with inter-station distances ranging from 60 to 100 km in different locations, Zhang *et al.* [20] showed a comparable single-epoch PPP-RTK performance. Although an excellent user performance was demonstrated in both studies, they were both based on a single-epoch model which is not always strong enough to achieve successful IAR and thus high accuracy, especially in sparser networks when ionospheric residuals are present. Li *et al.* [21] showed that instantaneous IAR at the user level is possible by using linearly interpolated atmospheric corrections from a regional network of 60 km spacing. Although cm-level accuracy was demonstrated based on a 2-h dataset, the generation of atmospheric corrections would be successful only when the ambiguities of the reference stations were fixed. A similar performance was found in Li *et al.* [22]. In both studies, though, the necessity to parameterize for the estimable user receiver code bias was not discussed, as it was assumed that the receiver clock offset can absorb it. Banville *et al.* [6] demonstrated that sub-decimeter positioning accuracy can be achieved instantaneously for 21 out of 24 h solutions in a day with quiet ionospheric conditions, by using regional corrections from a 150 km network with minimum distance to the user of 97 km. Based on three 1-h time intervals and ionospheric predictions from two unevenly distributed networks in different locations with the largest inter-station distances equal to 580 and 295 km, respectively, Wang *et al.* [23] found that 10 s are required to let most of the horizontal positioning errors to converge to less than 10 cm.

Therefore, although there has been given attention to the role the ionospheric corrections can play in reducing the PPP-RTK convergence time, the impact of the network dimension on the user's performance has not been explored in detail and needs further attention. Moreover, a rigorous assessment of the ionosphere-weighted PPP-RTK user performance has not yet been presented in the existing literature, which has been restricted to a small number of samples, unlike for this of the ionosphere-float model [13, 18, 24].

The goal of this contribution is to systematically analyze the performance of real-time ionosphere-weighted PPP-RTK by means of analyzing a large number of user ambiguity-resolved position solutions based on ionospheric corrections from regional networks of varying station spacing in the same area and in a day with existing ionospheric disturbance. Moreover, our aim is to provide numerical insight into what extent the ionospheric information can reduce the convergence times based on the network density and to show the capabilities of a sparse network in providing fast high-precision GNSS parameter estimation. To that end, we use the best linear unbiased predictor (BLUP) to interpolate undifferenced ionospheric corrections within the network processing. We also emphasize on the correct interpretation of the estimable ionospheric corrections, which is essential so as to estimate the corresponding biases at the user side.

This contribution is organized as follows. Section 3.2 presents the underlying model and estimable parameters of both PPP-RTK network and user components. Further, we review the predictor for generating user-specific ionospheric corrections based on network-

derived information. In Section 3.3, the data, setup and processing strategies are described, along with an analysis of the relevant estimated network corrections. Following this, we present and analyze the PPP-RTK user performance results based on a large number of solutions. We conclude in Section 3.4.

3.2 Methodology

In this section, we first present the PPP-RTK network and user observation models based on uncombined measurements, and then we review a strategy for the prediction of user-specific ionospheric corrections based on network-derived information.

3.2.1 GNSS observation equations

Let us commence with the set of uncombined carrier-phase and pseudorange observation equations. By uncombined observations, we mean that no inter-frequency linear combinations or differencing are applied in the observation domain, in order to apply dynamic constraints on all parameters. We dispense with the term undifferenced since an uncombined observation, per definition, is undifferenced. For a receiver-satellite combination $r-s$ at frequency j and at a single epoch, the uncombined phase ($\phi^s_{r,j}$) and code ($p^s_{r,j}$) measurements are defined as [25, 26]:

$$\begin{aligned} E(\phi^s_{r,j}) &= \rho^s_r + (dt_r - dt^s) + m^s_r \tau_r - \mu_j \iota^s_r + \lambda_j(\delta_{r,j} - \delta^s_{,j} + a^s_{r,j}) \\ E(p^s_{r,j}) &= \rho^s_r + (dt_r - dt^s) + m^s_r \tau_r + \mu_j \iota^s_r + (d_{r,j} - d^s_{,j}) \end{aligned} \tag{3.1}$$

where ρ^s_r denotes the receiver-satellite geometric range. The symbols dt_r and dt^s denote the receiver and satellite clock parameters, respectively. τ_r represents the wet component of the zenith tropospheric delay (ZTD), since the hydrostatic counterpart can be a priori corrected, and m^s_r is the tropospheric mapping function. The first-order slant ionospheric delays experienced on the first frequency (L1) are denoted by ι^s_r and are linked to the observations through the frequency-dependent ionospheric coefficient μ_j. The frequency-dependent receiver and satellite phase biases are denoted by $\delta_{r,j}$ and $\delta^s_{,j}$, respectively, while $d_{r,j}$ and $d^s_{,j}$ represent the receiver and satellite code biases. The integer phase ambiguity is denoted by $a^s_{r,j}$ and is linked to the phase data through the wavelength at frequency j, λ_j. $E(\cdot)$ denotes the expectation operator.

The above variables have a receiver index $r = 1,\ldots,n$ with n being the number of receivers, a frequency index $j = 1,\ldots,f$ with f being the number of frequencies ($f = 2$ in this study), and a satellite index $s = 1,\ldots,m$ with m being the number of tracked satellites. The code biases, phase biases and integer ambiguities are assumed to be time-invariant, unless a cycle slip occurs for the latter, while the other variables are time-dependent. All quantities are expressed in units of range, apart from the phase biases and ambiguities that are expressed in cycles. The ionospheric coefficient is defined as the squared ratio of frequencies: $\mu_j = (f_1/f_j)^2$.

The above observation equations apply for both PPP-RTK components: user and network. Moreover, the receiver positions are assumed to be a priori known in the network

component, allowing one to subtract ρ_r^s from the observations, given that precise orbits have been used. This is not the case for the user, as the observation equations need to be linearized with respect to the unknown user receiver position.

3.2.2 PPP-RTK network

The uncombined formulation of (3.1) cannot be used directly to estimate all the unknown parameters as is, i.e., in an unbiased form, since the system of observation equations is rank-deficient. According to *S*-system theory [27, 28], to solve for these rank deficiencies and obtain a full-rank network system, one has to find linearly independent estimable functions of these parameters based on a minimum constraint set or *S*-basis, the number of which equals to the rank deficiency. In this contribution, we opt for a *Common Clocks* *S*-system [29] resulting in a reformulation of (3.1) into:

$$\begin{aligned} E(\Delta\phi_{r,j}^s) &= d\tilde{t}_r - d\tilde{t}^s + m_r^s\tau_r - \mu_j\tilde{\imath}_r^s + \lambda_j(\tilde{\delta}_{r,j} - \tilde{\delta}_{,j}^s + \tilde{a}_{r,j}^s) \\ E(\Delta p_{r,j}^s) &= d\tilde{t}_r - d\tilde{t}^s + m_r^s\tau_r + \mu_j\tilde{\imath}_r^s \end{aligned} \tag{3.2}$$

where the interpretation of the estimable parameters (denoted using the tilde $\tilde{(\cdot)}$ symbol) and the *S*-basis parameters are listed in Table 3.1. The terms $\Delta\phi_{r,j}^s$ and $\Delta p_{r,j}^s$ denote the observed-minus-computed phase and code measurements, respectively, which include the receiver and satellite positions.

From Table 3.1, one can observe that all estimable parameters are functions of their original counterparts, biased by the *S*-basis parameters, except for the ZTD. This model is based on the ionosphere-float formulation, where the slant delays are estimated as unknown parameters for every receiver-satellite combination.

Table 3.1: Estimable dual-frequency PPP-RTK network parameters and their interpretation using the Common Clocks *S*-system (the symbol p denotes the pivot satellite/receiver if it is used as superscript/subscript).

Estimable Parameter	**Interpretation**
Receiver clock	$d\tilde{t}_{r\neq p} = dt_{pr} + d_{pr,\mathrm{IF}}$
Satellite clock	$d\tilde{t}^s = (dt^s + d^s_{,\mathrm{IF}}) - (dt_p + d_{p,\mathrm{IF}})$
Ionospheric slant delay	$\tilde{\imath}_r^s = \imath_r^s + d_{r,\mathrm{GF}} - d^s_{,\mathrm{GF}}$
Receiver phase bias	$\tilde{\delta}_{r\neq p,j} = \delta_{pr,j} - \frac{1}{\lambda_j}(d_{pr,\mathrm{IF}} - \mu_j d_{pr,\mathrm{GF}}) + a^p_{pr,j}$
Satellite phase bias	$\tilde{\delta}^s_{,j} = \delta^s_{,j} - \frac{1}{\lambda_j}\left([d^s_{,\mathrm{IF}} - d_{p,\mathrm{IF}}] - \mu_j[d^s_{,\mathrm{GF}} - d_{p,\mathrm{GF}}]\right) - \delta_{p,j} - a^s_{p,j}$
Phase ambiguity	$\tilde{a}^{s\neq p}_{r\neq p,j} = a^s_{pr,j} - a^p_{pr,j}$

Note: $(\cdot)_{,\mathrm{IF}} = \frac{1}{\mu_2-\mu_1}[\mu_2(\cdot)_{,1} - \mu_1(\cdot)_{,2}]$; $(\cdot)_{,\mathrm{GF}} = -\frac{1}{\mu_2-\mu_1}[(\cdot)_{,1} - (\cdot)_{,2}]$; $(\cdot)_{ij} = (\cdot)_j - (\cdot)_i$

3.2.3 Prediction of ionospheric corrections

Given the PPP-RTK network-derived estimates and the fact that the ionosphere decorrelates with increasing inter-station distance [30], the slant ionospheric delays of the network stations can serve as the basis for providing an educated guess of the user-specific delays. Therefore, in the present contribution, we treat the undifferenced (biased) slant ionospheric delay estimates of the reference network stations as observable random signals to spatially predict the unobservable random ionospheric signals at the user side, per satellite and per epoch, based on the spatial coherence of ionosphere. Several interpolation methods have been proposed for this matter, and it has been shown that their performance is comparable [31]. In this study, we apply the least-squares prediction theory [32] and use the trend-signal-noise model, which forms the basis of the least-squares collocation method [33].

Based on the satellite-by-satellite approach, we assume that the ionospheric delay experienced between the user and a certain satellite can be represented by the mean value of the delays experienced between the network receivers and the same satellite within the measurement cone, depicted in Figure 3.1, the base of which is formed by the network receiver positions and its vertex from the satellite position. We consider this assumption to be valid in the case of local and regional networks and in the absence of high ionospheric activity. Let us therefore consider the partitioned linear system of equations that relates the vector $\hat{\bar{\imath}}$ of observable slant delays of the reference stations, where $\hat{\bar{\imath}} = [\hat{\bar{\imath}}_1^{\mathrm{T}}, \ldots, \hat{\bar{\imath}}_n^{\mathrm{T}}]^{\mathrm{T}}$ and $\hat{\bar{\imath}}_r = [\hat{\bar{\imath}}_r^1, \ldots, \hat{\bar{\imath}}_r^m]^{\mathrm{T}}$, with the vector $\bar{\imath} = [\bar{\imath}^1, \ldots, \bar{\imath}^m]^{\mathrm{T}}$ of the spatial mean ionospheric delays per satellite and the unobservable vector $\tilde{\imath}_{net\to u} = [\tilde{\imath}_{net\to u}^1, \ldots, \tilde{\imath}_{net\to u}^m]^{\mathrm{T}}$ that contains the user-predicted ionospheric delays:

$$E\left(\begin{bmatrix} \hat{\bar{\imath}} \\ \tilde{\imath}_{net\to u} \end{bmatrix}\right) = \begin{bmatrix} e_n \otimes I_m & C_n \otimes e_m \\ I_m & 0_{m\times(n-1)} \end{bmatrix} \begin{bmatrix} \bar{\imath} \\ \tilde{d}_{p'r,\mathrm{GF}} \end{bmatrix} \tag{3.3}$$

where m and n denote the number of satellites and network stations, I_n denotes a unit matrix of order n, e_n is an n-vector having ones as its entries, C_n denotes a unit matrix of order n with its first column removed, and $\tilde{d}_{p'r,\mathrm{GF}} = [\tilde{d}_{p'2,\mathrm{GF}}, \ldots, \tilde{d}_{p'n,\mathrm{GF}}]^{\mathrm{T}}$. $\otimes$ denotes the Kronecker product.

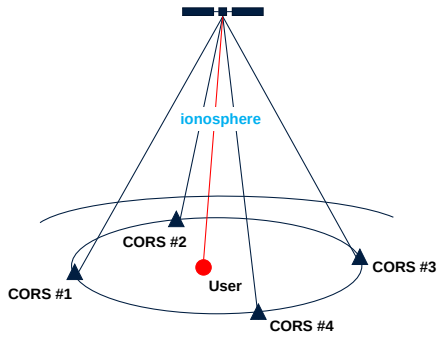


Figure 3.1: Schematic principle of the satellite-by-satellite approach used in predicting user-specific slant ionospheric corrections per satellite and per epoch.

In this model, we parameterized the trend in terms of the satellite-wise mean ionospheric delay and the network receiver differential code biases (DCBs). This was done for receiver code bias calibration reasons, considering as *S*-basis the receiver DCB of one of the network receivers contributing to the spatial prediction. It has to be mentioned at this point that the pivot receivers in the PPP-RTK network processing and the ionospheric delay prediction did not have to be necessarily the same. In the current section, we assume that the pivot receiver is the first one for notational convenience.

The variance-covariance (vc-) matrix of the observable ionospheric signals captures both the measurement and the signal noise. Since the network processing is assumed to continuously generate PPP-RTK corrections, the network-derived slant ionospheric delay estimates gain a high precision over time such that their corresponding vc-matrix can be neglected. In such a case, we are only left with the vc-matrix of the signals. To model the between-receiver spatial correlation of the ionosphere, we use a Gaussian function as it is a decreasing autocorrelation function that guarantees the positive definiteness of the ionospheric vc-matrix [34]:

$$h_{ij} = c_i^2 \exp\left(-\left(\frac{l_{ij}}{l_0}\right)^2\right) \tag{3.4}$$

where h_{ij} is the correlation function for receivers i and j, l_{ij} is the distance between them, and l_0 is a pre-defined applicable inter-station distance for ionospheric signal spatial correlation. The variance c_i^2 denotes the value of the covariance function when the inter-station distance is zero. $\exp(\cdot)$ denotes the natural exponential function. Based on all of the above, the ionospheric signal vc-matrix is defined as:

$$D\left(\begin{bmatrix} \hat{\bar{\imath}} \\ \tilde{\imath}_{net\to u} \end{bmatrix}\right) = \begin{bmatrix} H_{ij} & H_{iu} \\ H_{iu}^{\mathrm{T}} & H_{uu} \end{bmatrix} \otimes I_m, \; i,j = 1,\ldots,n$$

where $D(\cdot)$ denotes the dispersion operator and H denotes the correlation matrix, based on (3.4).

Therefore, based on BLUP [32, 35], the stochastic user-specific ionospheric corrections read as:

$$\hat{\tilde{\imath}}_{net\to u} = \hat{\bar{\imath}} + [(H_{iu}^{\mathrm{T}} H_{ij}^{-1}) \otimes I_m](\hat{\bar{\imath}} - [e_n \otimes I_m]\,\hat{\bar{\imath}} - [C_n \otimes e_m]\,\hat{\tilde{d}}_{p'r,\mathrm{GF}}) \tag{3.5}$$

with the best linear unbiased estimators of $\bar{\imath}$ and $\tilde{d}_{p'r,\mathrm{GF}}$ being obtained from the normal equation:

$$\begin{bmatrix} (e_n^{\mathrm{T}} H_{ij}^{-1} e_n) \otimes I_m & (e_n^{\mathrm{T}} H_{ij}^{-1} C_n) \otimes e_m \\ (C_n^{\mathrm{T}} H_{ij}^{-1} e_n) \otimes e_m^{\mathrm{T}} & (C_n^{\mathrm{T}} H_{ij}^{-1} C_n) \cdot m \end{bmatrix} \begin{bmatrix} \hat{\bar{\imath}} \\ \hat{\tilde{d}}_{p'r,\mathrm{GF}} \end{bmatrix} = \begin{bmatrix} (e_n^{\mathrm{T}} H_{ij}^{-1}) \otimes I_m \\ (C_n^{\mathrm{T}} H_{ij}^{-1}) \otimes e_m^{\mathrm{T}} \end{bmatrix} \hat{\bar{\imath}} \tag{3.6}$$

For the expectation of the user-predicted ionospheric corrections, we have:

$$E(\hat{\tilde{\imath}}^s_{net\to u}) = \tilde{\imath}^s_{net\to u} = \iota^s_u - \tilde{d}^s_{,\mathrm{GF}}, \quad \text{with} \quad \tilde{d}^s_{,\mathrm{GF}} = d^s_{,\mathrm{GF}} - d_{p',\mathrm{GF}} \tag{3.7}$$

Therefore, the predicted ionospheric delays are biased, apart from the satellite DCBs, by the network pivot receiver DCB. This needs to be carefully considered when applied at the user model and will be discussed in the next section. The predictor variance is computed with the variance propagation law.

3.2.4 PPP-RTK user

This section presents the ionosphere-float and ionosphere-weighted variants of the user's model.

Ionosphere-float model

The network-derived corrections that enable the PPP-RTK realization are the estimable satellite clocks and satellite phase biases. If we linearize the observation equations, shown in (3.1), with respect to the unknown user position (index r changes to u) and apply both satellite orbits and network-derived corrections, the user's single-system dual-frequency uncombined phase and code observation equations turn into:

$$\begin{aligned} E(\Delta\phi^s_{u,j} + \hat{\tilde{d}}t^s + \lambda_j\hat{\tilde{\delta}}^s_{,j}) = E(\Delta\tilde{\phi}^s_{u,j}) &= g_u^{s^{\mathrm{T}}}\Delta x_u + d\tilde{t}_u + m^s_u\tau_u - \mu_j\tilde{\imath}^s_u + \lambda_j(\tilde{\delta}_{u,j} + \tilde{a}^s_{u,j}) \\ E(\Delta p^s_{u,j} + \hat{\tilde{d}}t^s) = E(\Delta\tilde{p}^s_{u,j}) &= g_u^{s^{\mathrm{T}}}\Delta x_u + d\tilde{t}_u + m^s_u\tau_u + \mu_j\tilde{\imath}^s_u \end{aligned} \tag{3.8}$$

where Δx_u denotes the user position increment vector and g^s_u denotes the 3-vector containing the line-of-sight unit vectors. The precise satellite orbits are assumed to be included in the observed-minus-computed terms. In the case that both network and user models employ the same S-system, the parameter estimability and interpretation between them remains invariant.

From Table 3.1, one is able to recognize that the user's receiver phase biases and integer ambiguities are not linearly dependent anymore since the integer ambiguities of the pivot satellite are taken as S-basis in this contribution, making the two parameters separable. The user's ambiguities are now of double-differenced form and, therefore, integer-estimable.

The stochastic model, which is captured by the vc-matrix of the uncombined phase and code measurements, of the single-epoch single-system ionosphere-float model is given as:

$$Q_{yy} = \mathrm{blkdiag}(Q_{\Delta\tilde{\phi}_u\Delta\tilde{\phi}_u}, Q_{\Delta\tilde{p}_u\Delta\tilde{p}_u}), \text{ with } Q_{\diamond\diamond} = C_{\diamond\diamond} \otimes W_u^{-1}, \text{ and } \diamond \in \{\Delta\tilde{\phi}_u, \Delta\tilde{p}_u\} \tag{3.9}$$

where $y = [\Delta\tilde{\phi}_u^{\mathrm{T}}, \Delta\tilde{p}_u^{\mathrm{T}}]^{\mathrm{T}}$ denotes the complete $4m$ measurement vector with $\Delta\tilde{\phi}_u = [\Delta\tilde{\phi}^1_{u,1}, \ldots, \Delta\tilde{\phi}^m_{u,1}, \Delta\tilde{\phi}^1_{u,2}, \ldots, \Delta\tilde{\phi}^m_{u,2}]^{\mathrm{T}}$ and $\Delta\tilde{p}_u = [\Delta\tilde{p}^1_{u,1}, \ldots, \Delta\tilde{p}^m_{u,1}, \Delta\tilde{p}^1_{u,2}, \ldots, \Delta\tilde{p}^m_{u,2}]^{\mathrm{T}}$, and the frequency-specific zenith-referenced standard deviations of the phase and code data are captured in the sub-matrices $C_{\Delta\tilde{\phi}_u\Delta\tilde{\phi}_u} = \mathrm{diag}(\sigma^2_{\phi_{u,1}}, \sigma^2_{\phi_{u,2}})$ and $C_{\Delta\tilde{p}_u\Delta\tilde{p}_u} = \mathrm{diag}(\sigma^2_{p_{u,1}}, \sigma^2_{p_{u,2}})$, respectively. The matrix $W_u = \mathrm{diag}(w^1_u, \ldots, w^m_u)$ contains the satellite elevation-dependent weights $w^s_u = \sin^2(\beta^s_u)$ of the GNSS measurements, with β^s_u denoting the elevation of satellite s from receiver u. The notations diag and blkdiag denote a diagonal and a block diagonal matrix, respectively.

The user model consisting of (3.8) and (3.9) is the so-called ionosphere-float model, in which the biased slant ionospheric delays are estimated as unknown parameters. As a result, data over a long observational time span need to be accumulated for the position solution to gain high precision.

Ionosphere-weighted model

If precise ionospheric information is available, the user's model will be strengthened, which will improve the ambiguity resolution performance and, therefore, shorten the convergence time. The ionospheric corrections should be treated as stochastic parameters, implying that the user's model needs to be extended and include unknown parameters for the ionospheric residuals, which one can weigh according to the distance of the user from the network receivers. In any other case, the position solutions will be biased even when the ambiguity success rate is high [36]. This model will be referred to hereafter as the ionosphere-weighted model, which was first introduced by [37].

Let us now assume that the network is able to provide, next to satellite clocks and satellite phase biases, regionally network-derived user-specific ionospheric corrections, the interpretation of which is based on (3.7). In such a case, the uncombined terms of code and phase data will result in the following adapted formulation:

$$\begin{aligned} E(\Delta\phi^s_{u,j} + \hat{\tilde{d}}t^s + \lambda_j\hat{\tilde{\delta}}^s_{,j} + \mu_j\hat{\tilde{\iota}}^s_{net\to u}) &= g_u^{s^{\mathrm{T}}}\Delta x_u + d\tilde{t}_u + m^s_u\tau_u - \mu_j(\iota^s_u - \iota^s_{u,net\to u}) + \lambda_j(\tilde{\delta}_{u,j} + \tilde{a}^s_{u,j}) \\ E(\Delta p^s_{u,j} + \hat{\tilde{d}}t^s - \mu_j\hat{\tilde{\iota}}^s_{net\to u}) &= g_u^{s^{\mathrm{T}}}\Delta x_u + d\tilde{t}_u + m^s_u\tau_u + \mu_j(\iota^s_u - \iota^s_{u,net\to u}) + \mu_j\tilde{d}_{u,\mathrm{GF}} \end{aligned} \tag{3.10}$$

The interpretation of the estimable parameters in the ionosphere-weighted model is identical to the ionosphere-float counterpart, except for user's phase biases that are biased by the network, instead of the user's DCB as shown in Table 3.2. The main difference between the two models is that the receiver code bias becomes estimable due to the introduction of the external ionospheric corrections. In our contribution we will show that the user DCB estimate lies at the meter level, which can degrade the positioning performance if ignored, as it has been observed in existing analysis [21].

Table 3.2: Changes in parameter estimability and interpretation in the PPP-RTK user model due to the introduction of external ionospheric corrections

Estimable Parameter	**Interpretation**
Receiver phase bias	$\tilde{\delta}_{u,j} = \delta_{pu,j} - \frac{1}{\lambda_j}(d_{pu,\mathrm{IF}} - \mu_j d_{pp',\mathrm{GF}}) + a^p_{pu,j}$
Receiver code bias	$\tilde{d}_{u,\mathrm{GF}} = d_{u,\mathrm{GF}} - d_{p',\mathrm{GF}}$

The prevailing advantage of the ionosphere-weighted model becomes clear: one is able to a priori weigh the ionospheric residuals, $\iota^s_u - \iota^s_{net\to u}$, according to the ionospheric prediction error that depends on the network density, i.e., the user's proximity to the network receivers, and improve the performance by this model strengthening. Introducing a priori stochastic pseudo-observables, as shown in (3.11), extends our functional model of (3.10), which gets a redundancy gain of $m-1$ at a single epoch compared to the ionosphere-float model.

$$E(\Delta\iota) = \iota^s_u - \iota^s_{net\to u} \tag{3.11}$$

The provided ionospheric corrections will now be correlated both between themselves and in time, since they come from a previous adjustment. In this study, we neglect such

correlation due to the excessive information that needs to be transmitted to the user and we weigh the ionospheric residuals based on the accuracy of the user-interpolated ionospheric corrections. This is empirically assessed by comparing the per-network-derived user-specific predicted corrections with the slant ionospheric delays at the user stations which have been estimated with ionosphere-float PPP-RTK and considered as truth.

In this case, the stochastic model is extended, as shown in (3.12), assuming that all ionospheric pseudo-observations are assigned with the same a priori standard deviation $\sigma_{\Delta\iota}$ (that can be transmitted in real-time along with the corrections), neglecting any dependency on other factors (e.g., elevation angle):

$$Q_{yy} = \text{blkdiag}(Q_{\Delta\tilde{\phi}_u\Delta\tilde{\phi}_u}, Q_{\Delta\tilde{p}_u\Delta\tilde{p}_u}, Q_{\Delta\iota\Delta\iota}), \quad \text{with} \quad Q_{\Delta\iota\Delta\iota} = \sigma^2_{\Delta\iota} I_m \tag{3.12}$$

3.3 Results and analysis

In this section, we first introduce the data and processing strategy followed at both network and user components. We then present and analyze the network-corrections, focusing on the user-specific ionospheric corrections. In the following, we numerically demonstrate and analyze the performance of the single-system ionosphere-weighted PPP-RTK user using ionospheric corrections from multi-scale regional network configurations.

3.3.1 Data and processing strategy

To carry out our case study, we used 24-h GPS dual-frequency code and phase data sampled every 30 s on 16 February 2014 (47th day of year), close to the solar maximum, from mid-latitude CORS receivers of the National Geodetic Survey (NGS) network in North Carolina, United States. Their geographic distribution is shown in Figure 3.2. To measure the impact of a network's dimension on the achieved performance, we selected and split the network receivers into four evenly distributed networks; each consisted of four receivers, with average inter-station distances (user-to-reference receiver distances) of 68, 115, 174 and 237 km. The users are denoted by blue dots and are within the coverage of all four networks. During the selected day, there was a medium ionospheric disturbance since the final Kp-index ranged from 2o to 5o with a mean equal to 3+, as determined by GeoForschungsZentrum [38]. The final Kp-index is expressed in a scale of thirds and ranges between 0o, 0+, 1−, 1o, 1+ ... all the way up to 9o (28 values in total).

At the network side, the GPS observations were processed independently for each network. In this study, we employed the geometry-plus-satellite-clock-fixed variant of the uncombined PPP-RTK network model [24] using IGS precise orbits and clocks, while the station coordinates were a priori precisely known. For the parameter estimation, the Kalman filter was utilized assuming that the receiver clock offsets and the slant ionospheric delays are unlinked in time. The carrier-phase ambiguities were treated as time-invariant parameters unless a cycle slip occurs, and the receiver and satellite phase biases were assumed to be time-constant as well. A random-walk stochastic process was assumed for the wet zenith tropospheric delay using a process noise of 0.1 mm/$\sqrt{30\text{s}}$.

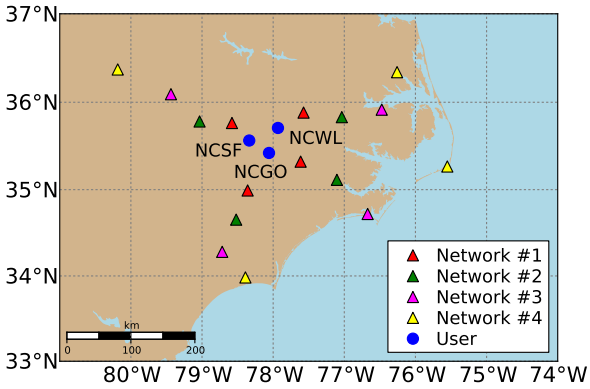


Figure 3.2: Geographic distribution of the selected CORS receivers in North Carolina used for the PPP-RTK network and user processing. The network receivers are classified in groups of four to form networks of varying inter-station distance and are denoted by red, green, magenta and yellow triangles in ascending order by distance. The remaining three receivers, denoted by blue dots, represent the user stations.

At the user component, the GPS observations were processed on a receiver-by-receiver basis for all user stations after being corrected by the IGS precise orbits and clocks and the network-derived satellite phase biases. The time correlation that was inherent in the latter products, as they come from the previous network adjustment, was neglected. Moreover, we started the user processing 1 h after the network processing had been initialized in order to allow the corrections to gain high precision, since in real conditions the network processing is assumed to generate corrections continuously. It is also important to note that the newly tracked satellites were excluded during their first few minutes at the user processing as the associated network corrections were not precise enough. The dynamic model settings for the Kalman-filtered PPP-RTK user processing were set identical to the network counterparts, with the only difference that the newly introduced parameters for the unknown receiver positions were assumed to be unlinked in time as we considered only kinematic positioning in this study. In case of the ionosphere-weighted user model, the receiver DCB was treated as a time-constant parameter. Although not shown in this contribution, we did not find any difference in the ambiguity resolution and positioning performance by treating the receiver DCB unlinked in time. It has been reported by Zhang and Teunissen [40] and Zha *et al.* [41] that receiver hardware temperature variations cause the receiver DCB to vary over time, which should be taken into account in such cases.

At both the network and user levels, the uncombined code and phase measurements were empirically assigned with a zenith-referenced standard deviation of 30 cm and 3 mm, respectively, which is a reasonable choice for most applications [42], and were further weighted according to the sine of their elevation. A cut-off elevation angle of 10° was used to discard noisy measurements at low elevations. We assumed that no correlation existed between frequencies, as well as between code and phase measurements. In case of any tracked C1 observables from the receivers, they were aligned to the P1 observables using the monthly P1-C1 satellite DCB products provided by the Centre for Orbit Determination in Europe (CODE) in order to be consistent with the satellite clocks provided by IGS. Both PPP-RTK network and user data were corrected for a priori corrections, including

tidal effects, phase windup and tropospheric delays. For the detection and identification of outliers, we made use of the recursive detection, identification and adaptation (DIA) procedure [39]. It is worth mentioning that the data in both components were processed in emulated real-time mode, since only forward filter processing was used.

We performed full (FAR) and partial (PAR) integer ambiguity resolution [43] with the LAMBDA (Least-squares AMBiguity Decorrelation Adjustment) method [15, 44] using as input the float ambiguity solution, which was obtained from our Kalman filter in real-time based on our mixed-integer GNSS user model. It is important to notice that, unlike many studies, we did not a priori form any linear combinations of the ambiguities, such as the widelane combination, aiming to accelerate the search process. This is because the Z-transformation, embedded in the LAMBDA method, is known to maximally decorrelate the ambiguities by determining the optimal ambiguity combinations that transform the ellipsoidal ambiguity search space into more spheroid-like [45].

Further, we used the Fixed Failure-rate Ratio Test (FFRT) to decide whether or not the resolved ambiguities can be accepted as the *correct* ones [46], as an incorrect integer solution will hamper the positioning solutions. In this regard, a model-driven critical value was used with a fixed failure rate of 0.1% in order to have high confidence in the correctness of the integer outcomes. After the integer ambiguities had been accepted, we performed a single-epoch standard least-squares adjustment to obtain the ambiguity-resolved solution of the other parameters. The process of IAR+FFRT was executed on an epoch-by-epoch basis.

3.3.2 PPP-RTK network corrections

In this section, we present the network-derived results. Figure 3.3 depicts the total number of commonly tracked satellites from at least two receivers in network #1 above the elevation cut-off angle of 10° during 16 February 2014. It can be seen that the number of commonly tracked GPS satellites varied from 6 to 13.

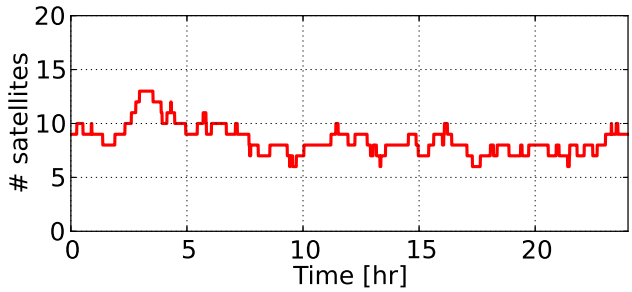


Figure 3.3: Number of GPS satellites tracked in network #1 during 16 February 2014.

Regarding the PPP-RTK network-derived estimates, we restricted our attention to the satellite phase biases and user-predicted ionospheric corrections. Figure 3.4 shows the satellite phase bias estimates on L1, $\tilde{\delta}^s_{,1}$, the interpretation of which can be seen from Table 3.1, along with their formal standard deviations (STDs) as determined from their vc-matrix. We chose to present the estimates of all GPS satellites in order to get a general insight into their behavior. It can be seen that the L1 satellite phase biases of the majority of GPS satellites showed remarkable stability over time. Most of these estimates achieved a formal precision of 0.20 cycles after 1–2 h, while the 0.10 cycles level was reached after 3–4 h. The longer a satellite was observed from the network, the better the precision of its associated phase biases became over time.

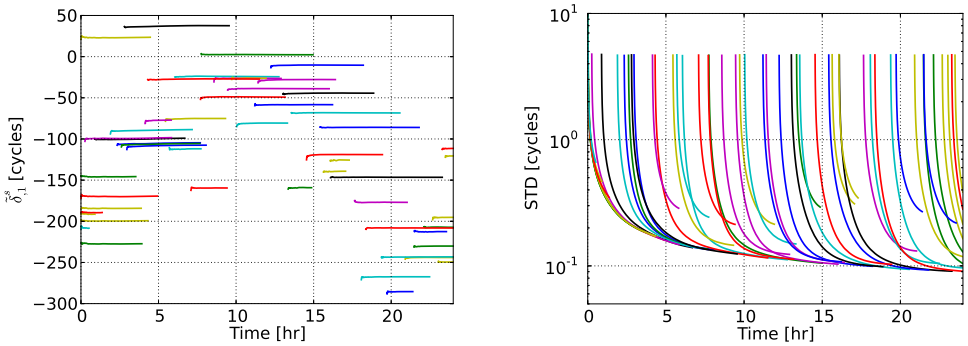


Figure 3.4: (**a**) Satellite phase bias estimates on L1 (in cycles) and (**b**) their formal standard deviations for all GPS satellites during the selected day. Each color represents a different GPS satellite.

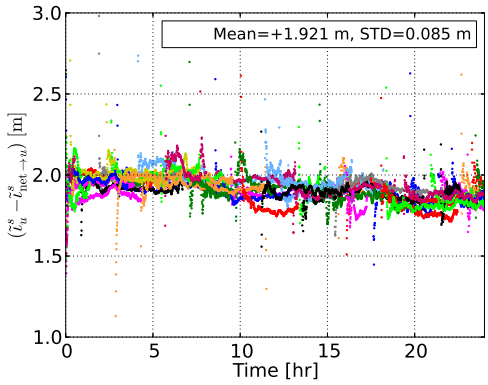
The second set of PPP-RTK corrections we discuss here is the one of the user-predicted ionospheric corrections. After using the Kalman-filter-based slant ionospheric delay estimates of the network receivers, the undifferenced ionospheric corrections at the users were predicted on an epoch-by-epoch basis with the BLUP model, as discussed in Section 3.2.3. To make use of the ionosphere-weighted model at the PPP-RTK user processing, as shown in (3.10)–(3.12), one has to make assumptions on the standard deviation of these corrections. To this end, the accuracy of the user-interpolated ionospheric corrections was assessed by comparing them to the estimated slant delays from an ionosphere-float PPP-RTK user processing. In such a comparison, one would get:

$$\tilde{\imath}^s_u - \tilde{\imath}^s_{net\to u} = (\imath^s_u - \imath^s_{net\to u}) + (d_{u,\mathrm{GF}} - d_{p',\mathrm{GF}}) \tag{3.13}$$

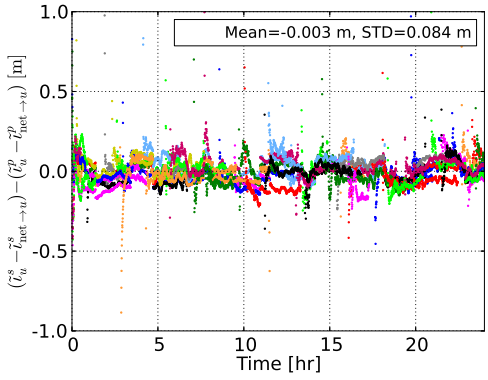
Therefore, although one would expect their difference to be unbiased in the absence of ionospheric residuals, we recall that the user-predicted and user-estimated slant ionospheric delays differ by an unknown offset, that is the difference of the user and network-receiver DCBs. As already discussed, this network-user DCB needs to be estimated by the user.

Figure 3.5 shows the differences between the user-estimated and user-predicted slant ionospheric delays, based on network #2, of all GPS satellites at the user station NCWL as

well as their between-satellite single-differenced counterparts. It can be seen from the top panel that the time-series of differences between the estimated and predicted delays were biased by an offset of about 1.9 m. This is due to the remaining network-user DCB and it will be shown later that this is the value that the network-user DCB estimate fluctuates around. This bias was eliminated after applying a between-satellite single-differencing operator, with the resulting zero-mean time-series of differences being shown in the bottom panel of the same figure.



(a)



(b)

Figure 3.5: (**a**) Differences (in meters) of the undifferenced regionally network-derived user-predicted slant ionospheric delays and their counterparts estimated by the user NCWL, and (**b**) their between-satellite single-differenced results. Each color represents a different GPS satellite. This ionospheric correction prediction is referred to network #2 (mean station spacing of 115 km). The empirical mean and STDs were calculated for the complete 24-h time-series.

Using the ambiguity-fixed slant delays from the network receivers, the same procedure was followed for all l user stations to assess the accuracy of the ionospheric corrections per

network:

$$\sigma_{\Delta\iota} = \sqrt{\frac{\sum_{u=1}^{l}\sum_{i=1}^{k}\sum_{s=1}^{m}\left(\Delta\iota_{u,i}^{s} - \Delta\bar{\iota}_{u}\right)^{2}}{l\cdot k\cdot m - 1}} \tag{3.14}$$

where $\Delta\iota_{u,i}^{s}$ denotes the ionospheric residual of the user u and satellite s at epoch i, $\Delta\bar{\iota}_{u}$ the average of the user-specific residuals (translated into the user DCB) over all satellites m and all epochs k.

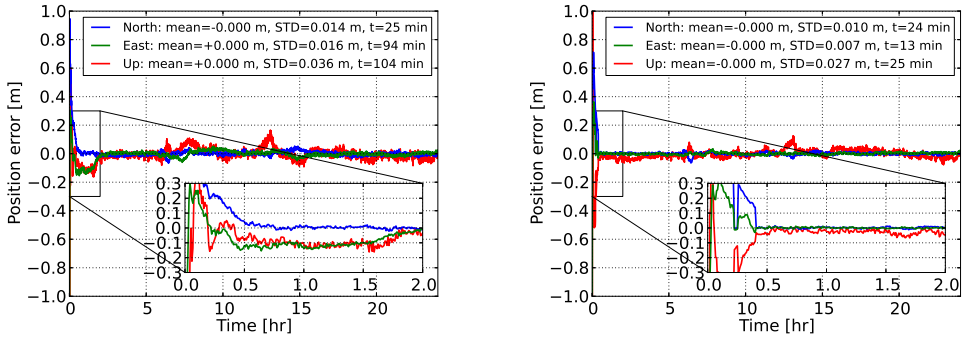
3.3.3 Real-time PPP-RTK performance

The GPS dual-frequency data of the user stations were processed in kinematic mode, i.e., treating the receiver position components as time-unlinked parameters, after being corrected for the network-derived estimates for satellite phase biases and predicted ionospheric corrections. The processing was performed with and without IAR, leading to ambiguity-float (PPP) and ambiguity-fixed (PPP-RTK) results, considering both the ionosphere-float and ionosphere-weighted models.

To get an initial numerical insight into the achieved positioning performance, we commence our discussion with Figure 3.6, which illustrates the ambiguity-float and ambiguity-resolved kinematic user position solutions with respect to the ground truth for the arbitrarily chosen station NCWL. The convergence time was defined here as the minimum accumulated observational time span required to achieve accuracy (position error with respect to ground truth) better than 10 cm for the remaining time window. One can observe that the ionosphere-float PPP solution achieved cm-level accuracy during the 24-h period. It was seen, though, that a long convergence time was needed to reach the 10 cm level, namely 25, 94 and 104 min for the north, east and up components, respectively. It can be seen that at about 13 h the error along the up component deviated instantly from the 10 cm level, which is probably due to errors contaminated in the measurements that were not filtered out in our user processing.

The performance gain via single-receiver PPP-RTK ambiguity resolution is shown in Figure 3.6 (b). The benefit in terms of precision is evident at the beginning of the time-series, while this is not the case after a few hours. This is due to the fact that the float ambiguities get more precise over time and as a result the positioning solution's precision is dictated by the carrier-phase measurements. In the ambiguity-fixed case, the convergence time was reduced to 24, 13 and 25 min along the north, east and up components, respectively, while the accuracy reached the level of 1.0, 0.7 and 2.7 cm, respectively.

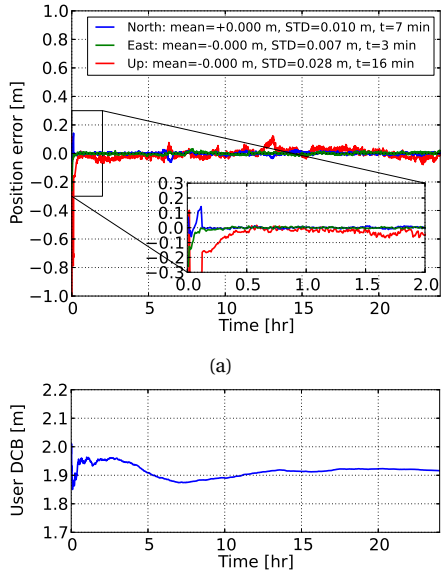
It is interesting to note that the north error got better than 10 cm at the 13th min (same as the east error) but deteriorated in the subsequent epochs. A consistent accuracy better than 10 cm along the north component was achieved from the 24th min onwards. This was due to the inclusion of a new satellite above the elevation cut-off angle in the solution. In the above ambiguity-resolved solutions, the process of FAR and FFRT was repeated at every epoch with the fixed ambiguity (and updated position) solution being accepted only when the FFRT was passed. This is as expected, since the float solution needed time to converge, implying that each time new satellites were tracked it would take a few epochs before the ambiguities could be reliably fixed.



(a) Ambiguity-float solution

(b) Ambiguity-fixed solution

Figure 3.6: Time-series of the GPS dual-frequency ionosphere-float (**a**) PPP and (**b**) Full integer ambiguity resolution (FAR)-based PPP-RTK kinematic user position for station NCWL with respect to its ground-truth. The empirical means and STDs are calculated for the estimated positions after 2 h. A zoom-in window during the first 2 h is provided.



(a)

(b)

Figure 3.7: Time-series of (**a**) the GPS dual-frequency ionosphere-weighted FAR-based PPP-RTK kinematic user position for station NCWL with respect to its ground-truth, and (**b**) its associated network-user scaled DCB estimate. The ionospheric corrections were determined from network #2. The empirical means and STDs are calculated for the estimated positions after 2 h. A zoom-in window during the first 2 h is provided.

Then, as our initial goal was to evaluate the gain in PPP-RTK user positioning performance by using precise ionospheric corrections, we used the network-derived predictions to strengthen the ionosphere-float user model, turning it into an ionosphere-weighted one. Figure 3.7 shows the time-series of the ionosphere-corrected PPP-RTK user kinematic position errors using corrections from network #2. It is evident that the a priori ionospheric information played a substantial role in reducing the convergence time, since it took only 7 and 3 min for the north and east ambiguity-fixed position errors to converge below 10 cm. This was more than 3 times faster compared to the ionosphere-float model. The estimable user code bias is shown in the same figure. It can be seen that the user DCB estimate showed a stable temporal behavior and, more importantly, it fluctuated around the mean value of the differences between the user-predicted and user-estimated ionospheric delays, as shown in Figure 3.5.

Convergence time

Although the provision of ionospheric corrections seems to bring a substantial improvement in convergence time, a single solution cannot be assumed to be representative of the general case. Due to the random nature of the GNSS data, a large number of samples are required to infer the empirical distribution of the achieved convergence times and to come up with realistic deductions. To that end, we processed the data of all user stations using both FAR and PAR on 16 February 2014, with a 3-h processing window being re-initialized every 1 min, in order to capture the different receiver-satellite geometry changes and obtain a representative sample of solutions (3780). The computed absolute horizontal (radial) position errors with respect to the ground-truth were collected and sorted for each epoch according to their magnitude. Further, we identified the 50th and 90th percentiles of the 2D horizontal errors, and obtained the so-called percentile curves as a measure to represent the convergence times.

The convergence behavior of the user positioning results with and without IAR, as well as by utilizing predicted ionospheric corrections from multi-scale networks are discussed in the following. Figure 3.8 shows the 50th and 90th percentiles of the absolute horizontal errors for the first 3 processing hours. The ambiguity-float results show that 28.5 and 68.5 min are needed to let 50% and 90% of the horizontal position errors to converge, respectively. The gain due to single-receiver IAR is evident in both FAR- and PAR-based results, as for 90% of the samples the convergence times reduced to 51.0 (26% improvement) and 41.0 (40% improvement) min, respectively. This shows that single-receiver PPP-RTK ambiguity resolution could reduce the convergence time substantially, since the convergence curves had a sharper decrease, especially with PAR. Similar results were reported by Odijk *et al.* [13] and Zhang *et al.* [24], in the context of ionosphere-float ambiguity-fixed kinematic positioning results, with an about 50 and 45 min convergence time, respectively.

In this study, we present to our knowledge for the first time percentile convergence curves when precise ionospheric corrections are employed from multi-scale regional networks. From Figure 3.8, it can be seen that the time required for the FAR-based horizontal position errors to get below the decimeter level reduced to 18-41 min (90% of samples) for network spacings between 68 and 237 km thanks to the use of the ionospheric corrections. As expected, the smallest-scale network #1 with a mean station spacing of 68 km provided the best performance, while the largest-scale network #4 with a mean station

spacing of 237 km gives the worst. However, the latter still provided better performance compared to the ionosphere-float PPP-RTK case where the slant ionospheric delays were entirely unknown. It is also interesting to notice that these convergence times showed a linear relationship with the average inter-station spacing, as shown in Figure 3.9, which demonstrates the clear impact that the dimension of a network had on the achieved user's performance.

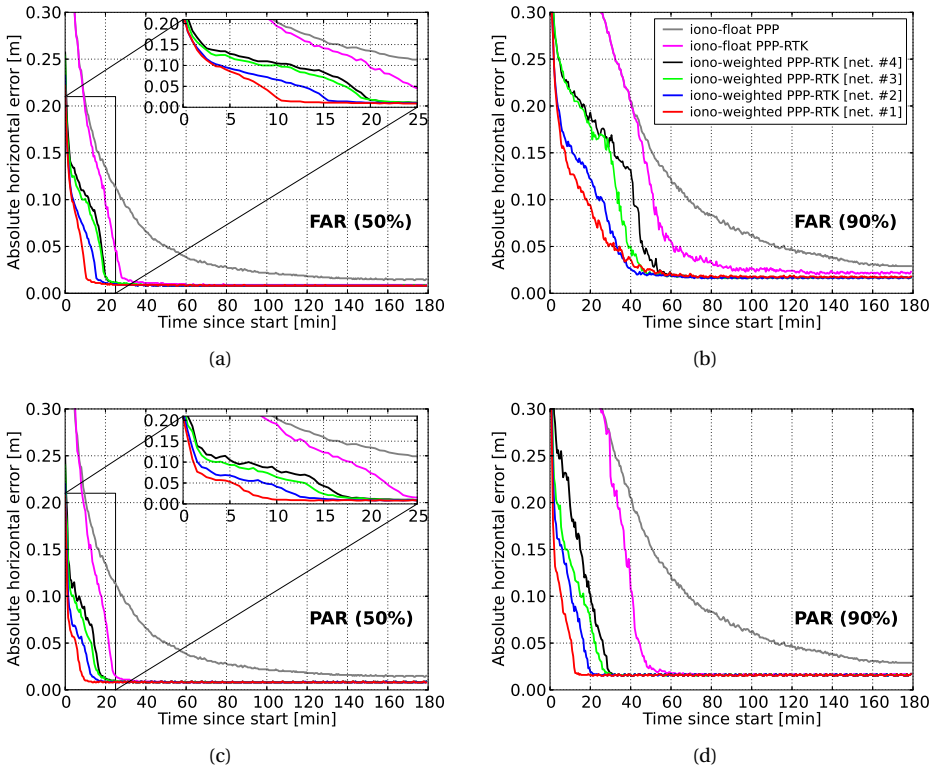


Figure 3.8: Convergence behavior of the horizontal radial positioning errors for (**a**) 50% of the FAR-based solutions, (**b**) 90% of the FAR-based solutions, (**c**) 50% of the PAR-based solutions, and (**d**) 90% of the PAR-based solutions of all user stations as a function of time since the processing start. The processing window has been re-initialized every 1 min within the selected day for all available solutions and networks.

Further reduction in the convergence times can be seen from the PAR-based results. In particular, the 90% percentile curves show that the time needed to surpass the decimeter level ranged from 5.5 to 20.0 min for network spacings between 68 and 237 km, showing the superior performance of PAR over FAR. This is due to the fact that regional ionospheric corrections were able to strengthen the underlying model in such a way that a large enough subset of ambiguities could be identified and fixed in a shorter time span to allow for centimeter-level position results. It is also remarkable that for 50% of the cases the regional corrections were able to reduce the convergence times to 1.0, 1.5, 4.0 and 7.0 min for the 68, 115, 174 and 237 km spaced networks, respectively. The linear relationship

between the convergence times and the average inter-station spacing is also obvious in PAR for both 50% and 90%, as shown in Figure 3.9. Therefore, we conclude that the GPS-only ionosphere-weighted PAR-based PPP-RTK user convergence times to 10 cm can be less than 6 min when regional ionospheric corrections from a 68 km spaced network are used in 90% of the cases. For 50% of the cases this even reduces to 1 min. These results are valid for a medium ionosphere-disturbed day. In the case that corrections from an about 237 km spaced network are used, the convergence times are expected to be shorter than 20 min in a single-system dual-frequency solution.

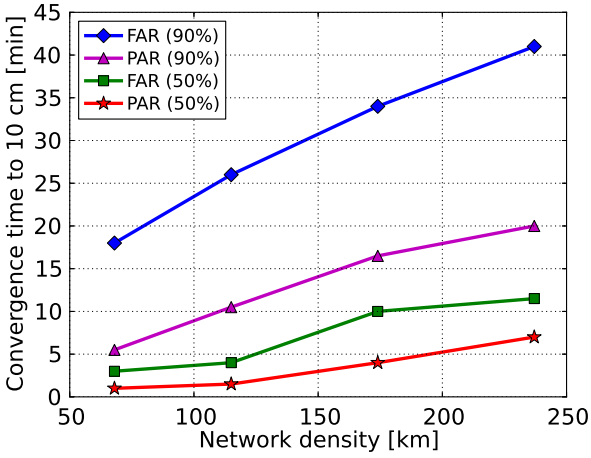


Figure 3.9: Convergence time of the horizontal radial position errors to 10 cm as a function of the network density for both FAR and PAR, based on 50% and 90% of the sample solutions.

Positioning accuracy

It is also of interest to get an insight into the achieved partially-ambiguity-fixed PPP-RTK user positioning accuracy using external ionospheric corrections. Figure 3.10 shows the 2D horizontal positioning errors at the first epoch and several minutes since start based on 90% of the sample runs. It can be observed that centimeter-level accuracy could be achieved when a long time span was accumulated in the filter. Although the errors were at the meter-level at the first minute, the regional ionospheric constraints could improve the accuracy by more than 60%, with the accuracy reaching the 25 cm level when corrections from network #1 were used. The differences in the achieved accuracy using ionospheric information from multi-scale networks were evident, which were absent when the time span was longer than 30 min as the underlying model was strong enough to allow for PAR-based cm-level accuracy. It is important to notice here that 20 cm accuracy could be achieved within the first 5 min of processing using a four-receiver network of maximum 174 km spacing, while at the same time the accuracy could be even 11 cm if a 68 km spaced network was used. Using data over a time span of 20 min showed that all networks used in this study were able to provide ionospheric corrections that lead to sub-10 cm horizontal accuracy, while the smallest-scale network can bring the accuracy down to 1.5 cm. If the time span was longer, then it can be seen that the performance

was equivalent for all networks. One concludes, therefore, that there is a significant improvement at the first processing epochs by using regional ionospheric corrections, with the performance being linearly scaled based on the network density.

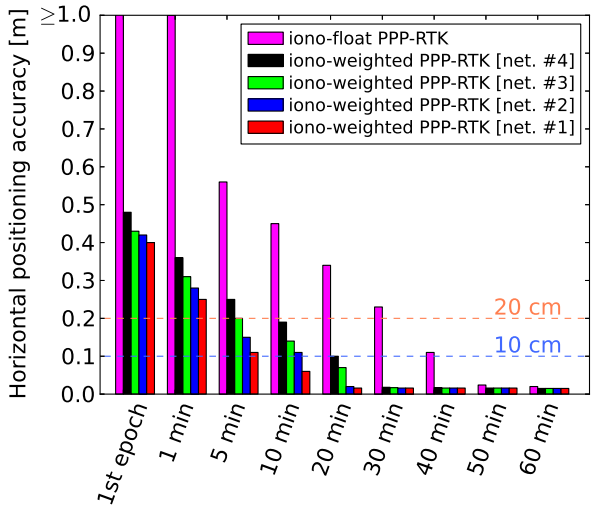


Figure 3.10: Horizontal positioning accuracy (90th percentile) at the first epoch and 1, 5, 10, 20, 30, 40, 50, 60 min since start for the PAR-based PPP-RTK user solutions.

Similar performance should be expected from users when they perform PPP-RTK positioning in similar conditions as those of the current study. The convergence times may vary depending on the user's geographical location, atmospheric activity, receiver type and possible multipath contamination due to the nearby environment. It has to be noted, though, that such results should not be expected in equatorial areas and during ionospheric storms.

3.4 Conclusions

In this contribution, we rigorously analyzed the key role of ionospheric corrections in achieving fast high-precision positioning. To this end, we measured the impact that the network density has on the achieved performance, for the first time in terms of PPP-RTK. Given that the data-driven integer-estimable ambiguities have been successfully mapped to their correct integers, the observational time span required to reach high positioning accuracy can be greatly reduced compared to PPP. In case there is no a priori information about the ionosphere, the PPP-RTK user model is weak in terms of its ambiguity resolution capabilities because the unknown parameters for the ionosphere need to be estimated.

We first gave a detailed presentation of the uncombined PPP-RTK network and user models, along with their parameter estimability and interpretation. The transition from the ionosphere-float to the ionosphere-weighted variant of the PPP-RTK user model is achieved through incorporating prior information about the ionosphere. It was shown

that such user-specific ionospheric corrections can be predicted with BLUP based on the network-derived slant delays and then used at the user to achieve fast PPP-RTK ambiguity resolution and, therefore, fast convergence.

We also numerically demonstrated for the first time the capabilities, in terms of positioning convergence curves and achieved accuracy, of the GPS-only dual-frequency ionosphere-weighted PPP-RTK user model using ionospheric corrections from multi-scale regional networks. To evaluate the effect that the network stations' spacing has on the user performance through the ionospheric corrections, we processed GPS dual-frequency data from four regional networks with varying station spacings, ranging from 68 to 237 km. We determined and presented the PPP-RTK network results, including the stable satellite phase biases over time and the predicted user-specific slant ionospheric delays, as well as their quality.

Given the network corrections, ground-truth coordinates and datasets from several single-receiver users, we computed a large number of kinematic 2D horizontal positioning error samples to get representative convergence curves. As numerically shown, for 90% of the samples the convergence times of the ambiguity-float solutions to reach 10 cm were reduced from 68.5 to 51.0 min after full ambiguity resolution and to 41.0 min after partial ambiguity resolution. It was then demonstrated that when ionospheric corrections are available from the smallest-scale network of 68 km spacing, sub-10 cm horizontal accuracy can be achieved almost instantaneously in the ionosphere-weighted partially-ambiguity-fixed solutions, with 90% of them requiring less than 6 min. Moreover, it was empirically found that the convergence time bears a linear relationship with the mean inter-station distance of the considered networks, with the smallest one providing the best performance, as expected. Based on the 50th (90th) percentile of 2D horizontal positioning errors, sub-decimeter level accuracy can be reached within 1.5 (10.5), 4.0 (16.5) and 7.0 (20.0) min when ionospheric corrections from networks of 115, 174 and 237 km spacing are used, respectively, showing that sparser networks can provide sufficiently precise ionospheric information to achieve faster PPP-RTK solutions.

Based on the above performance studies, further improvement in the kinematic PPP-RTK convergence time can be expected when multi-frequency and/or multi-GNSS data are integrated, as it has been shown for the ionosphere-float model (see e.g., [18, 47]). We, therefore, believe that the synergetic use of multiple systems and frequencies will further improve the ionosphere-weighted single-system PPP-RTK user performance, which we will investigate in the future.

References

[1] G. Wubbena, M. Schmitz, and A. Bagge, *PPP-RTK: Precise Point Positioning Using State-Space Representation in RTK Networks.* in *Proceedings of the 18th International Technical Meeting of the Satellite Division of The Institute of Navigation, ION GNSS 2005* (Long Beach, CA, USA, 2005) pp. 2584–2594.

[2] J. F. Zumberge, M. B. Heflin, D. C. Jefferson, M. M. Watkins, and F. H. Webb, *Precise point positioning for the efficient and robust analysis of GPS data from large networks.* Journal of Geophysical Research **102**, 5005 (1997).

[3] J. Kouba and P. Heroux, *Precise Point Positioning Using IGS Orbit and Clock Products.* GPS Solutions **5**, 12 (2001).

[4] S. Bisnath and Y. Gao, *Current State of Precise Point Positioning, Future Prospects and Limitations.* in *Observing Our Changing Earth. International Association of Geodesy Symposia.*, edited by M. Sideris (Springer, Berlin, Heidelberg, 2009).

[5] R. Leandro, H. Landau, M. Nitschke, M. Glocker, S. Seeger, X. Chen, A. Deking, M. BenTahar, F. Zhang, K. Ferguson, R. Stolz, N. Talbot, G. Lu, T. Allison, M. Brandl, V. Gomez, W. Cao, and A. Kipka, *RTX positioning: The next generation of cm-accurate real-time GNSS positioning.* in *Proceedings of the 24th International Technical Meeting of the Satellite Division of The Institute of Navigation, ION GNSS 2011* (Portland, OR, 2011).

[6] S. Banville, P. Collins, W. Zhang, and R. B. Langley, *Global and regional ionospheric corrections for faster PPP convergence.* Navigation **61**, 115 (2014).

[7] M. Ge, G. Gendt, M. Rothacher, C. Shi, and J. Liu, *Resolution of GPS carrier-phase ambiguities in Precise Point Positioning (PPP) with daily observations.* Journal of Geodesy **82**, 389 (2005).

[8] P. Collins, *Isolating and Estimating Undifferenced GPS Integer Ambiguities.* in *Proceedings of the 2008 National Technical Meeting of The Institute of Navigation.* (San Diego, CA, 2008) pp. 720–732.

[9] L. Mervart, Z. Lukes, C. Rocken, and T. Iwabuchi, *Precise Point Positioning with Ambiguity Resolution in Real-Time.* in *Proceedings of the 21st International Technical Meeting of the Satellite Division of The Institute of Navigation, ION GNSS 2008* (Savannah, GA, 2008).

[10] D. Laurichesse, F. Mercier, J. P. Berthias, P. Broca, and L. Cerri, *Integer Ambiguity Resolution on Undifferenced GPS Phase Measurements and its Application to PPP and Satellite Precise Orbit Determination.* Journal of The Institute of Navigation **56**, 135 (2009).

[11] P. J. G. Teunissen, D. Odijk, and B. Zhang, *PPP-RTK: Results of CORS network-based PPP with integer ambiguity resolution,* Journal of Aeronautics, Astronautics and Aviation A, **42**, 223 (2010).

[12] J. Geng, C. Shi, M. Ge, A. H. Dodson, Y. Lou, Q. Zhao, and J. Liu, *Improving the estimation of fractional-cycle biases for ambiguity resolution in precise point positioning.* Journal of Geodesy **86**, 579 (2012).

[13] D. Odijk, A. Khodabandeh, N. Nadarajah, M. Choudhury, B. Zhang, W. Li, and P. J. G. Teunissen, *PPP-RTK by means of S-system theory: Australian network and user demonstration,* Journal of Spatial Science **62**, 3 (2017).

[14] C. C. Goad, *Precise relative position determination using global positioning system carrier phase measurements in a nondifference mode.* in *Proceedings of 1st international symposium on precise positioning with GPS.* (1985) pp. 347–356.

[15] P. J. G. Teunissen, *The least-squares ambiguity decorrelation adjustment: a method for fast GPS integer ambiguity estimation.* Journal of Geodesy **70**, 65 (1995).

[16] P. J. de Jonge, *A processing strategy for the application of the GPS in networks.*, Ph.D. thesis, Delft University of Technology (1998).

[17] E. Schönemann, M. Becker, and T. Springer, *A new approach for GNSS analysis in a multi-GNSS and multi-signal environment.* Journal of Geodetic Science **1**, 204 (2011).

[18] N. Nadarajah, A. Khodabandeh, K. Wang, M. Choudhury, and P. J. G. Teunissen, *Multi-GNSS PPP-RTK: From Large- to Small-Scale Networks,* Sensors **18**, 1078 (2018).

[19] X. Li, G. Liu, X. Li, F. Zhou, G. Feng, Y. Yuan, and K. Zhang, *Galileo PPP rapid ambiguity resolution with five-frequency observations.* GPS Solutions **24** (2020), 10.1007/s10291-019-0930-3.

[20] B. Zhang, P. J. G. Teunissen, and D. Odijk, *A Novel Un-differenced PPP-RTK concept,* The Journal of Navigation **64**, S180 (2011).

[21] X. Li, X. Zhang, and M. Ge, *Regional reference network augmented precise point positioning for instantaneous ambiguity resolution.* Journal of Geodesy **85**, 151 (2011).

[22] X. Li, X. Zhang, and G. Guo, *Predicting atmospheric delays for rapid ambiguity resolution in precise point positioning.* Advances in Space Research **54**, 840 (2014).

[23] K. Wang, A. Khodabandeh, and P. J. G. Teunissen, *A study on predicting network corrections in PPP-RTK processing,* Advances in Space Research **60**, 1463 (2017).

[24] B. Zhang, Y. Chen, and Y. Yuan, *PPP-RTK based on undifferenced and uncombined observations: theoretical and practical aspects.* Journal of Geodesy **93**, 1011 (2019).

[25] P. J. G. Teunissen and A. Kleusberg, *GPS for Geodesy*, 2nd ed. (Springer-Verlag, Berlin-Heidelberg-New York, 1998).

[26] P. J. G. Teunissen and O. Montenbruck, *Springer Handbook of Global Navigation Satellite Systems*, 1st ed. (Springer International Publishing, 2017).

[27] W. Baarda, *S-transformations and criterion matrices.* in *Publications on Geodesy, 18*, Vol. 5 (Netherlands Geodetic Commission, Delft, The Netherlands, 1973).

[28] P. J. G. Teunissen, *Zero Order Design: Generalized Inverses, Adjustment, the Datum Problem and S-Transformations.* in *Optimization and Design of Geodetic Networks.*, edited by E. Grafarend and F. Sanso (Springer, Berlin, Heidelberg, 1985) pp. 11–55.

[29] D. Odijk, B. Zhang, A. Khodabandeh, R. Odolinski, and P. J. G. Teunissen, *On the estimability of parameters in undifferenced, uncombined GNSS network and PPP-RTK user models by means of S-system theory,* Journal of Geodesy **90**, 15 (2016).

[30] B. Schaffrin and Y. Bock, *A unified scheme for processing GPS dual-band observations.* Bulleting Geodesique **62**, 142 (1988).

[31] L. Dai, S. Han, J. Wang, and C. Rizos, *Comparison of interpolation algorithms in network-based GPS techniques.* Navigation **50**, 277 (2003).

[32] P. J. G. Teunissen, *Least-squares prediction in linear models with integer unknowns.* Journal of Geodesy **81**, 565 (2007).

[33] H. Moritz, *Least-squares collocation.* Reviews of Geophysics and Space Physics **16**, 421 (1978).

[34] H. Moritz, *Covariance functions in least-squares collocation.* Reports of the Department of Geodetic Science, Report No. 240 (1976).

[35] A. S. Goldberger, *Best linear unbiased prediction in the generalized linear regression model.* Journal of the American Statistical Association **57**, 369 (1962).

[36] D. Odijk, *Weighting ionospheric corrections to improve fast GPS positioning over medium distances.* in *Proceedings of the 13th International Technical Meeting of the Satellite Division of The Institute Of Navigation (ION GPS 2000)* (Salta Lake City, UT, 2000).

[37] Y. Bock, S. A. Gourevitch, C. C. Counselman, R. W. King, and R. I. Abbot, *Interferometric analysis of GPS phase observations,* Manuscripta Geodaetica **11**, 282 (1986).

[38] GeoForschungsZentrum, *Geomagnetic Kp Index,* (2019).

[39] P. J. G. Teunissen, *An integrity and quality control procedure for use in multi sensor integration.* in *Proceedings of ION GPS 1990* (Colorado Springs, CO, 1990) pp. 513–522, also published in: Volume VII of *GPS Red Book*: Integrated systems, ION Navigation, 2012.

[40] B. Zhang and P. J. G. Teunissen, *Characterization of multi-GNSS between-receiver differential code biases using zero and short baselines.* Science Bulletin **60**, 1840 (2015).

[41] J. Zha, B. Zhang, Y. Yuan, X. Zhang, and M. Li, *Use of modified carrier-to-code leveling to analyze temperature dependence of multi-GNSS receiver DCB and to retrieve ionospheric TEC.* GPS Solutions **23** (2019), 10.1007/s10291-019-0895-2.

[42] B. Li, Y. Shen, and P. Xu, *Assessment of stochastic models for GPS measurements with different types of receivers.* Chinese Science Bulletin **53**, 3219 (2008).

[43] P. J. G. Teunissen, P. Joosten, and C. C. J. M. Tiberius, *Geometry-free ambiguity success rates in case of partial fixing.* in *Proceedings of ION NTM 1999.* (San Diego, CA, 1999) pp. 201–207.

[44] P. J. G. Teunissen, *Least squares estimation of the integer GPS ambiguities.* Invited lecture, Section IV Theory and Methodology, IAG General Meeting, Beijing (1993).

[45] P. J. G. Teunissen, *On the GPS widelane and its decorrelating property.* Journal of Geodesy **71**, 577 (1997).

[46] P. J. G. Teunissen and S. Verhagen, *The GNSS ambiguity ratio-test revisited: A better way of using it.* Survey Review **41**, 138 (2009).

[47] K. Wang, A. Khodabandeh, and P. J. G. Teunissen, *Five-frequency Galileo long-baseline ambiguity resolution with multipath mitigation,* GPS Solutions **22** (2018), 10.1007/s10291-018-0738-6.

4

Multi-GNSS multi-frequency PPP-RTK user performances: Part I

A single-receiver integer ambiguity resolution-enabled precise point positioning (PPP-RTK) user experiences a long convergence time when the rather weak single-constellation dual-frequency ionosphere-float model is used. Nowadays, the rapid development of Global Navigation Satellite Systems (GNSS) provides a multitude of available satellites and frequencies that can serve in improving the user's model strength and, therefore, its ambiguity resolution and positioning capabilities. In this study, we provide insight into and analyze the global impact of a multi-GNSS (GPS, Galileo, BeiDou-3) multi-frequency integration on the expected ambiguity resolution and positioning performance of the ionosphere-float uncombined PPP-RTK user model, and demonstrate whether it is the increased number of satellites or frequencies, or a combination thereof, that speeds up ambiguity-resolved positioning. Moreover, we explore the capabilities of both full (FAR) and partial (PAR) ambiguity resolution, considering the full ambiguity information content with the LAMBDA method, and investigate whether PAR is an efficient solution to the multi-dimensional ambiguity case. The performance of our solutions is assessed in terms of the ambiguity success rate (ASR), the number of epochs (TTFA) to achieve both an ASR criterion and a horizontal positioning precision better than 10 cm, as well as the gain in precision improvement. Based on multi-system multi-frequency simulated data from nine globally distributed stations and a large number of kinematic solutions over a day, we found that the increase in number of frequencies enhances the ambiguity resolution performance, with PAR achieving a TTFA reduction of 70% when five instead of two Galileo frequencies are used, while the ambiguity-float solution is only slightly improved. Further, our numerical results demonstrated that the increase in number of satellites leads to an improvement in both the positioning and ambiguity resolution performance, due to the improved geometry strength. It is shown that the GPS+Galileo+BeiDou solutions can achieve a TTFA of 6.5 and 4.5 min (at 90%) on a global scale when two and three frequencies are used, respectively, without any a priori information on the ionospheric delays. Finally, we analyzed the sensitivity of the PPP-RTK user's performance to changes in the precision of the measurements.

This chapter has been published as: Psychas, D., Verhagen, S. and Teunissen, P.J.G. (2020). Precision analysis of partial ambiguity resolution-enabled PPP using multi-GNSS and multi-frequency signals. Advances in Space Research, 66(9):2075-2093, doi: 10.1016/j.asr.2020.08.010

4.1 Introduction

Integer ambiguity resolution (IAR) is the key to fast and precise Global Navigation Satellite System (GNSS) parameter estimation [1, 2]. The purpose of resolving the carrier-phase ambiguities as integers is to gain a significant improvement upon the precision of the remaining model parameters, with the position components being usually the main parameters of interest. This improvement takes place because one can take full advantage of the carrier-phase data that act as ultra-precise pseudoranges, once the integer ambiguities are resolved successfully.

The reliability of ambiguity resolution, usually expressed by the probability of correct integer estimation or the so-called *ambiguity success rate* (ASR), depends on the applied integer estimator and on the strength of the underlying observation model. Assuming that the selected method for integer estimation is the one that maximizes the success rate, it is then the model strength that purely drives the ASR. Given that there are no mis-specifications in the applied functional and stochastic models, one can use the model-driven ASR as a diagnostic measure for the *expected* IAR performance. This measure is solely based on the precision of the least-squares estimated float ambiguities, which is captured by the variance-covariance (vc-) matrix of the ambiguities. Therefore, the stronger the model, the more precise the ambiguities and the higher the ASR will be.

However, it is well known that the single-constellation dual-frequency ionosphere-float model is weak in the sense of its IAR capabilities due to the presence of ionospheric delays. It is expected that additional observations, e.g. due to inclusion of data over multiple frequencies and from multiple GNSS systems or a priori atmospheric information, will strengthen the model and lead to higher ASRs. In this contribution, we analyze the performance of IAR in the context of multi-system multi-frequency integration in the IAR-enabled precise point positioning (PPP; [3]) method, namely PPP-RTK [4], and in particular the gain in position precision improvement one should expect.

The rapid development and modernization of multiple satellite systems along with a plethora of new signals and frequencies provide an improved satellite geometry, thus stronger positioning model, and higher redundancy than the until recently traditional GPS dual-frequency model. It is, thus, expected that both positioning and ambiguity resolution capabilities will be improved in light of these developments. On the other hand, such an integration also leads to an increased dimension of the vector of to-be-resolved ambiguities, implying a probable decrease of the ASR, mainly because of rising satellites, and an IAR slowdown. In case of a strong model, either by accumulating data over many epochs or by integrating multi-system and/or multi-frequency data, it might not be necessary to resolve the complete vector of integer ambiguities, but instead a sufficiently large subset such that the gain in position precision is significant. We will, therefore, explore the capabilities of both full (FAR) and partial (PAR) ambiguity resolution, and investigate whether PAR is an efficient solution for such a high-dimensional problem.

Diverse studies have shown the benefit of using multi-constellation and multi-frequency data to obtain more precise and reliable solutions, claiming, also faster convergence in the absence of precise ionospheric corrections. Using simulated GPS and Galileo dual-frequency data, Tiberius *et al.* [5] have shown that the combined-system model can achieve instantaneous IAR for short and medium baselines, unlike long baselines, with formal

ASRs above 99.9% and 95.0%, respectively. They also found that the inclusion of a third frequency brings only a slight improvement in the performance, which was later observed by Verhagen *et al.* [6], Odijk *et al.* [7] and Xiao *et al.* [8].

According to Zhang *et al.* [9], the mean time-to-fix-ambiguities (TTFA) is about 70 and 35 s for 50 km baselines in GPS-only and Galileo-only triple-frequency solutions, respectively, using simulated 1 Hz data. Moreover, Ji *et al.* [10] showed that it takes over 39 s to resolve the ambiguities for long baselines using simulated Galileo 1 Hz data on four frequencies with cascade ambiguity resolution. After analyzing triple-frequency GPS and Galileo 30 s data from a single baseline, Odijk *et al.* [7] showed that the mean TTFA is about 32 and 25 min for FAR and PAR, respectively, in a GPS-only dual-frequency mode, while a slight improvement was observed when using a third frequency. In the dual-system solution, the mean TTFA was about 7 min for FAR and 2 min for PAR. Based on real five-frequency Galileo data in Australia, Wang *et al.* [11] concluded that a high number of frequencies is helpful to achieve high ASRs within a short time at the network side, which can be higher than 99.9% within the first 5 epochs of processing using all five frequencies.

Li *et al.* [12] analyzed the IAR performance of static PPP using dual-frequency GPS, BeiDou, GLONASS and Galileo data from a global network of stations. Based on solely wide-lane combinations, it was found that the four-system solution enables a TTFA of 10 min compared to the GPS-only solution which required 18 min on average to achieve successful IAR. Using real triple-frequency GPS, Galileo and BeiDou 1 s measurements from 17 stations around the world and wide-lane ambiguity combinations, Duong *et al.* [13] found that the average ASR using the multi-system multi-frequency kinematic PPP model was about 15% higher than the triple-frequency GPS-only counterpart, with the former showing a TTFA of 199 s and the latter of 553 s. In addition, according to the experimental results for receivers mainly located in the Asia-Pacific area, Li *et al.* [14] concluded that the average TTFA of a combined BeiDou and Galileo dual-frequency static PPP solution can be reduced by using the third frequency from 34 to 29 min.

Despite different combinations of systems and frequencies, underlying models, sampling rates and receiver locations, the above reported results are indicative of the great importance of a multi-system multi-frequency integration for IAR, in terms of higher ASRs, reduced TTFAs and shorter positioning convergence times. However, it has been a common practice to use the traditional TTFA as a sole indicator of the PAR capabilities, see, e.g., [12–14], without considering whether there is a gain in precision improvement or a criterion on the position precision has been met, as done for instance by Odijk *et al.* [7] and Brack [15]. In addition to this, the effect of a high-dimensional ambiguity vector on the ASR has not been studied satisfactorily yet, and is addressed in our study by providing numerical insight into the PAR capabilities as a solution to the dimensional curse. Moreover, we believe that a thorough insight into the expected multi-dimensional ambiguity resolution performance has not been yet provided, since most of the recent studies are restricted to static positioning applications and/or to the characterization of the performance in local or regional areas, see [7, 8, 12, 14, 16–18]. An analysis of the IAR performance on a global scale and under kinematic mode would provide potential multi-system multi-frequency users with a *baseline indicator* regarding the performance level they should expect.

In this contribution, we study and assess the expected performance of multi-GNSS (GPS, Galileo, BeiDou-3) multi-frequency ambiguity resolution on the basis of the ionosphere-float uncombined PPP-RTK user functional and stochastic models, thus without the need to process or simulate real data. Based on realistic functional and stochastic assumptions, a formal analysis allows us to gain clear insight into the factors contributing to ambiguity resolution and conclude on whether the improved satellite geometry or the high number of frequencies, or a combination thereof, is mainly driving the ambiguity resolution and positioning performance. Compared to other studies, the kinematic PPP-RTK user performance is predicted based on globally distributed stations and on a large number of samples. Instead of forming *a priori* linear combinations of multi-frequency system-specific ambiguities, as commonly used in recent studies, we use the Least-Squares AMBiguity Decorrelation Adjustment (LAMBDA) method [1] to determine the best-resolvable ambiguity (subset) combinations without any loss of information. We close our analysis by a systematic comparison of the performance of different models in terms of the TTFA, the achieved position precision and the expected gain in position precision after IAR.

This contribution is organized as follows. In Section 4.2, we briefly review the theory of integer ambiguity resolution, the success rate and the partial ambiguity estimator chosen in this study. Then, Section 4.3 introduces the basis of our uncombined ionosphere-float PPP-RTK underlying model, its estimable parameters, the experimental setup and processing settings. This is then followed, in Section 4.4, by an analysis of the numerical results for various multi-system multi-frequency models using both FAR and PAR. Finally, the work is concluded in Section 4.5.

4.2 Integer ambiguity resolution

In this section, a brief review of the principles of integer ambiguity resolution is given, along with a discussion on the selected PAR estimator.

4.2.1 Mixed-integer GNSS model

Any carrier-phase based GNSS model can be cast into the following general linear(ized) system of observation equations:

$$E(y) = Aa + Bb; \quad D(y) = Q_{yy} \tag{4.1}$$

where $E(\cdot)$ and $D(\cdot)$ denote the expectation and dispersion operators, respectively; y the vector of uncombined observed-minus-computed (O-C) carrier-phase and code observations, $a \in \mathbb{Z}^n$ the vector of integer double-differenced carrier-phase ambiguities, $b \in \mathbb{R}^q$ the vector of real-valued parameters such as position components, clocks, atmospheric delays and hardware delays, A and B their respective partial design matrices, and Q_{yy} the vc-matrix of the observations.

This mixed-integer GNSS model is solved mainly in three steps. In the *first* step, the best linear unbiased estimation takes place, ignoring the integer property of the carrier-phase ambiguities, resulting in the so-called *float* solution of all parameters (with $\hat{\cdot}$- sym-

bol):

$$\begin{bmatrix} \hat{a} \\ \hat{b} \end{bmatrix} = \left(\begin{bmatrix} A^{\mathrm{T}} \\ B^{\mathrm{T}} \end{bmatrix} Q_{yy}^{-1} \begin{bmatrix} A & B \end{bmatrix} \right)^{-1} \begin{bmatrix} A^{\mathrm{T}} \\ B^{\mathrm{T}} \end{bmatrix} Q_{yy}^{-1} y \tag{4.2}$$

$$\begin{bmatrix} Q_{\hat{a}\hat{a}} & Q_{\hat{a}\hat{b}} \\ Q_{\hat{b}\hat{a}} & Q_{\hat{b}\hat{b}} \end{bmatrix} = \left(\begin{bmatrix} A^{\mathrm{T}} \\ B^{\mathrm{T}} \end{bmatrix} Q_{yy}^{-1} \begin{bmatrix} A & B \end{bmatrix} \right)^{-1} \tag{4.3}$$

where $\hat{a}$ and $\hat{b}$ are the float estimators of the ambiguity and the real-valued parameters, respectively. $Q_{\hat{a}\hat{a}}$, $Q_{\hat{b}\hat{b}}$ and $Q_{\hat{a}\hat{b}} = Q_{\hat{b}\hat{a}}^{\mathrm{T}}$ are the corresponding (co-)variance matrices.

The *second* step focuses on the integer constraint $a \in \mathbb{Z}^n$. Its objective is to map the float ambiguity solution $\hat{a}$ into the integer solution $\breve{a} = \mathscr{I}(\hat{a})$ using an integer mapping $\mathscr{I} : \mathbb{R}^n \mapsto \mathbb{Z}^n$ from the n-dimensional space of reals to the n-dimensional space of integers. Various integer estimators can be selected for this step, with the most popular ones being the following: integer rounding (IR), integer bootstrapping (IB) and integer least-squares (ILS). ILS is the optimal method for integer estimation in the sense that it maximizes the probability of correct integer estimation, i.e. the success rate [19]. The ILS estimator, $\breve{a}_{\mathrm{ILS}} = \arg\min_{a \in \mathbb{Z}^n} \|\hat{a} - a\|^2_{Q_{\hat{a}\hat{a}}}$, is efficiently mechanized in the LAMBDA method, in which the real-valued ambiguities are transformed and decorrelated with the Z-matrix, such that the ambiguity search space turns from an elongated hyper-ellipsoid into spheroid-like, enabling a fast integer search in the transformed search space:

$$\hat{z} = Z^{\mathrm{T}} \hat{a}; \quad Q_{\hat{z}\hat{z}} = Z^{\mathrm{T}} Q_{\hat{a}\hat{a}} Z \tag{4.4}$$

where $\hat{z}$ and $Q_{\hat{z}\hat{z}}$ denote the transformed float ambiguities and their vc-matrix, respectively.

Once the integer outcomes $\breve{a} = Z^{-\mathrm{T}} \breve{z}$ are accepted, the ambiguity-float solution of the real-valued parameters, $\hat{b}$, is corrected by virtue of their correlation with the ambiguities, obtaining the so-called ambiguity-fixed solution (with $\breve{.}$- symbol):

$$\begin{aligned} \breve{b} &= \hat{b} - Q_{\hat{b}\hat{a}} Q_{\hat{a}\hat{a}}^{-1} (\hat{a} - \breve{a}) \\ Q_{\breve{b}\breve{b}} &= Q_{\hat{b}\hat{b}} - Q_{\hat{b}\hat{a}} Q_{\hat{a}\hat{a}}^{-1} Q_{\hat{a}\hat{b}} + Q_{\hat{b}\hat{a}} Q_{\hat{a}\hat{a}}^{-1} Q_{\breve{a}\breve{a}} Q_{\hat{a}\hat{a}}^{-1} Q_{\hat{a}\hat{b}} \end{aligned} \tag{4.5}$$

4.2.2 Ambiguity success rate

The ambiguity-fixed solution will enjoy a precision that is in accordance with the high precision of carrier-phase data, due to the imposed integer ambiguity constraints. However, this is based on the assumption that the ILS integer solution corresponds to the *correct* solution. In any other case, a wrong integer solution can cause significant biases in the position solution that may exceed the error of the ambiguity-float solution.

The probability of correct integer estimation is driven by the chosen integer estimator and the precision of the float ambiguity solution, $Q_{\hat{a}\hat{a}}$, which depends on the strength of the underlying model at hand. Therefore, to infer whether the integer outcomes can be reliably used, one requires a diagnostic measure in order to decide on their acceptance or rejection. In this study, we use the formal bootstrapping success rate as a measure for successful ambiguity resolution, which lower bounds the success rate of the optimal ILS

estimator [19], since an exact easy-to-compute expression is available:

$$P(\check{a}_{\mathrm{ILS}} = a) = P(\check{z}_{\mathrm{ILS}} = z) \geq P(\check{z}_{\mathrm{IB}} = z) = \prod_{i=1}^{n} \left(2\Phi \left(\frac{1}{2\sigma_{\hat{z}_{i|I}}} \right) - 1 \right) \tag{4.6}$$

with $\Phi(x)$ denoting the cumulative normal distribution function:

$$\Phi(x) = \int_{-\infty}^{x} \frac{1}{\sqrt{2\pi}} \exp\left(-\frac{u^2}{2} \right) du \tag{4.7}$$

where $P(\check{z}_{\mathrm{ILS}} = z)$ and $P(\check{z}_{\mathrm{IB}} = z)$ denote the ILS and IB ASRs of the decorrelated ambiguities z, respectively, n the number of the decorrelated ambiguities, and $\exp(\cdot)$ is the natural exponential function. $\sigma_{\hat{z}_{i|I}}$ represents the standard deviations of the i^{th} decorrelated ambiguities conditioned on the previous $I = i+1, \ldots, n$ ambiguities, and are provided by the square roots of the entries of the diagonal matrix D after an $L^{\mathrm{T}}DL$-decomposition of the decorrelated ambiguity vc-matrix $Q_{\hat{z}\hat{z}}$. The reason why we evaluate the ASR based on the decorrelated ambiguities is that the IB estimator depends on the ambiguity parametrization and, by applying the Z-transformation of LAMBDA, the IB ASR becomes a sharp lower bound to the ILS ASR [20]. If the ASR is high and close to 1, the integer ambiguities can be assumed to be deterministic and, then, the vc-matrix of the ambiguity-fixed parameters from (4.5) turns into:

$$Q_{\check{b}\check{b}} = Q_{\hat{b}\hat{b}} - Q_{\hat{b}\hat{a}} Q_{\hat{a}\hat{a}}^{-1} Q_{\hat{a}\hat{b}} \tag{4.8}$$

4.2.3 Partial ambiguity resolution

The capability to resolve the full set of ambiguities with a high ASR is not always feasible, as the observation model might not be strong enough. It is well known that the presence of ionospheric delay parameters in the ionosphere-float model makes the latter weak in terms of instantaneous (single-epoch) FAR. In such a case, one would need to accumulate data over several epochs to ensure that a high ASR is achieved. In addition, the rising of new satellites would require even more epochs to be accumulated, due to the introduction of estimated float ambiguities of low precision that bring down the ASR because of the multiplicative definition of the IB ASR.

The same situation occurs in a multi-system multi-frequency integration, where the number of to-be-resolved ambiguities can be very large. This can lead to a dimensional curse, because the event that each of the ambiguities is correct should have a probability close to 1 [21]. As the dimension of the ambiguity vector increases, this probability tends to get smaller due to the multiplication of probabilities, which by definition are smaller than or equal to 1.

Despite the incapability to rapidly resolve the complete ambiguity vector in these cases, it may still be possible to resolve a subset of ambiguities, referred to hereafter as PAR. Several PAR methods have been proposed in literature, including e.g. the fixing of (extra) wide-lane ambiguities in multi-frequency models [22, 23], the fixing of ambiguities that are identical in the LAMBDA-based best and second-best solution [24, 25], or the fixing of only the ambiguities that have been individually accepted based on fixed-failure-rate critical values after FAR [26].

In this contribution, we describe and use the model-driven approach of Teunissen *et al.* [27], which is easy to implement and defines the ambiguity subset to be resolved based on a minimum required success rate. The method commences with the decorrelation of ambiguities using the LAMBDA Z-transformation and then selects the largest possible subset, starting from the last decorrelated ambiguity, such that the user-defined success rate requirement is met:

$$P(\check{z}_{n-k+1,\mathrm{IB}} = z_{n-k+1}) = \prod_{i=k}^{n} \left(2\Phi\left(\frac{1}{2\sigma_{\hat{z}_{i|I}}} \right) - 1 \right) \geq P_0, \;\; k \geq 1 \tag{4.9}$$

where P_0 is the minimum required success rate and z_{n-k+1} is the subset containing the last $n-k+1$ decorrelated ambiguities. The reason why one starts from the n-th decorrelated ambiguity and continues until selecting the last $n-k+1$ entries is that the LAMBDA algorithm orders the entries of the decorrelated ambiguity vector in ascending order in terms of precision. This means that only the last $n-k+1$ decorrelated ambiguities, $\hat{z}_{n-k+1}$, will be fixed to their integers using an integer estimator, while the remaining subset, $\hat{z}_{k-1}$, will be kept as float. In case $k = 1$, then the selected subset is identical to the full set and, thus, PAR would coincide with FAR. Once the $n-k+1$ ambiguities are fixed to their integers in the transformed ambiguity domain, the partially ambiguity-fixed solution of the real-valued parameters follows as:

$$\begin{aligned} \check{b} &= \hat{b} - Q_{\hat{b}\hat{z}_{n-k+1}} Q^{-1}_{\hat{z}_{n-k+1}\hat{z}_{n-k+1}} (\hat{z}_{n-k+1} - \check{z}_{n-k+1}) \\ Q_{\check{b}\check{b}} &= Q_{\hat{b}\hat{b}} - Q_{\hat{b}\hat{z}_{n-k+1}} Q^{-1}_{\hat{z}_{n-k+1}\hat{z}_{n-k+1}} Q_{\hat{z}_{n-k+1}\hat{b}} \end{aligned} \tag{4.10}$$

It can be seen from (4.10) that the improvement of the real-valued parameters after successful PAR is based on the decorrelated integer ambiguity subset. Unless $k = 1$, the back-transformation of the full set of decorrelated ambiguities $\check{z}_{\mathrm{PAR}} = [\hat{z}^{\mathrm{T}}_{k-1|K=k,\ldots,n}, \check{z}^{\mathrm{T}}_{n-k+1}]^{\mathrm{T}}$ into the original set $\check{a}_{\mathrm{PAR}}$ will not contain integer entries anymore, since these entries will be linear functions of all decorrelated ambiguities that contain both the integer-valued and the conditional real-valued ambiguities.

In general, the PAR-based solution will be less precise than the FAR-based counterpart, at least until the identified subset corresponds to the full set, but still more precise than the ambiguity-float solution. This does not necessarily imply that the PAR solution will be significantly more precise than the float one, since this is inextricably linked to the number of fixed ambiguities. Therefore, the availability of a PAR solution should not be confused with the availability of a high-precision position solution.

4.3 PPP-RTK processing strategy

This section provides a detailed description of the observational model and parameter estimability for the PPP-RTK concept, defines the performance measures and gives an overview of the data and experimental setup considered in our study.

4.3.1 Full-rank observation model

The observation equations for the single-system single-epoch uncombined carrier-phase ($\phi^{s_\star}_{r,j}$) and code ($p^{s_\star}_{r,j}$) measurements between the receiver r and the satellite $s_\star$ of system $\star$ on frequency j can be formulated as [2]:

$$\begin{aligned} E(\phi^{s_\star}_{r,j}) &= \rho^{s_\star}_r + (dt_r - dt^{s_\star}) + m^{s_\star}_r \tau_r - \mu_j \iota^{s_\star}_r + \lambda_j(\delta^\star_{r,j} - \delta^{s_\star}_{,j} + a^{s_\star}_{r,j}) \\ E(p^{s_\star}_{r,j}) &= \rho^{s_\star}_r + (dt_r - dt^{s_\star}) + m^{s_\star}_r \tau_r + \mu_j \iota^{s_\star}_r + (d^\star_{r,j} - d^{s_\star}_{,j}) \end{aligned} \tag{4.11}$$

where $j = 1,\ldots,f$ is the frequency index with f being the number of frequencies, and $s_\star = 1_\star,\ldots,m_\star$ is the system-specific satellite index with $m_\star$ being the number of satellites per $\star$-system, with $\star \in \{\mathrm{G},\mathrm{E},\mathrm{C}\}$. The letters G, E and C denote the GPS, Galileo and BeiDou systems, respectively. In the following, we make systematic use of the satellite index $s_\star$ to discriminate between the satellites of different GNSSs and keep a generalized form of the equations. The term $\rho^{s_\star}_r$ denotes the geometric receiver-satellite range. The receiver clock and system-specific satellite clock parameters are represented by dt_r and $dt^{s_\star}$, respectively. τ_r and $m^{s_\star}_r$ represent the zenith tropospheric delay parameter and the troposphere mapping function, respectively. The slant ionospheric delay for a receiver r and a system-specific satellite $s_\star$ is denoted by $\iota^{s_\star}_r$ and is linked to the observations through the ionospheric coefficient μ_j for frequency j. The system-specific receiver and satellite phase biases are denoted with $\delta^\star_{r,j}$ and $\delta^{s_\star}_{,j}$, respectively, while $d^\star_{r,j}$ and $d^{s_\star}_{,j}$ denote those for code observations, respectively. The integer phase ambiguity is represented by $a^{s_\star}_{r,j}$ and is linked to the phase data through the wavelength λ_j at frequency j. The phase biases and ambiguities are expressed in cycles, while the other parameters in units of range.

In this contribution, by means of *uncombined* measurements we refer to measurements that have not undergone any differencing and/or linear combinations. Using such a formulation provides the flexibility of having all parameters available for a possible further model strengthening and of easily extending the model to any number of frequencies [28].

In our PPP-RTK network processing, the carrier-phase and code measurements from (4.11) are corrected for the receiver and satellite positions (lumped in the geometric range), assuming that they are both precisely known. This network system of equations is rank-defect as the information content is not sufficient to determine the *absolute* parameters, but only *estimable* functions of them. The rank-deficiencies of the network model can be identified and removed by defining a minimum set of S-basis parameters according to the S-system theory [29, 30]. After reformulation, the O-C terms of the uncombined phase ($\Delta\phi^{s_\star}_{r,j}$) and code ($\Delta p^{s_\star}_{r,j}$) measurements for a full-rank single-system multi-frequency model read as:

$$\begin{aligned} E(\Delta\phi^{s_\star}_{r,j}) &= d\tilde{t}^\star_{r\neq p} - d\tilde{t}^{s_\star} + m^{s_\star}_r \tau_r - \mu_j \tilde{\iota}^{s_\star}_r + \lambda_j(\tilde{\delta}^\star_{r\neq p,j} - \tilde{\delta}^{s_\star}_{,j} + \tilde{a}^{s_\star \neq p_\star}_{r\neq p,j}) \\ E(\Delta p^{s_\star}_{r,j}) &= d\tilde{t}^\star_{r\neq p} - d\tilde{t}^{s_\star} + m^{s_\star}_r \tau_r + \mu_j \tilde{\iota}^{s_\star}_r + \tilde{d}^\star_{r\neq p,j>2} - \tilde{d}^{s_\star}_{,j>2} \end{aligned} \tag{4.12}$$

where $r = 1,\ldots,n$ with n being the number of network receivers, and p denote the pivot receiver/satellite depending on whether it is used as subscript/superscript. The interpretation of the estimable parameters, denoted with the $\tilde{}$-symbol, and the chosen

S-basis are given in Table 4.1. The notations $(\cdot)_{,\mathrm{IF}}$ and $(\cdot)_{,\mathrm{GF}}$ denote the ionosphere-free and geometry-free linear combinations of parameters $(\cdot)$ in the first two frequencies used per GNSS, respectively.

The network parameters that are of essence to the PPP-RTK users are the estimable variants of the satellite clocks $d\tilde{t}^{s\star}$, satellite phase biases $\tilde{\delta}^{s\star}_{,j}$ and satellite code biases $\tilde{d}^{s\star}_{,j}$ ($f > 2$). After bringing together and applying these corrections along with the orbital corrections at the observational level, the user-corrected single-system linearized observation equations (replacing the index r by the user index u) for the O-C phase ($\Delta\phi^{s\star}_{u,j}$) and code ($\Delta p^{s\star}_{u,j}$) data follow as:

$$\begin{aligned} E(\Delta\phi^{s\star}_{u,j} + d\tilde{t}^{s\star} + \lambda_j\tilde{\delta}^{s\star}_{,j}) &= g^{s\mathrm{T}}_{u\star}\Delta x_u + d\tilde{t}^{\star}_u + m^{s\star}_u\tau_u - \mu_j\tilde{\imath}^{s\star}_u + \lambda_j(\tilde{\delta}^{\star}_{u,j} + \tilde{a}^{s\star\neq p\star}_{u,j}) \\ E(\Delta p^{s\star}_{u,j} + d\tilde{t}^{s\star} + \tilde{d}^{s\star}_{,j>2}) &= g^{s\mathrm{T}}_{u\star}\Delta x_u + d\tilde{t}^{\star}_u + m^{s\star}_u\tau_u + \mu_j\tilde{\imath}^{s\star}_u + \tilde{d}^{\star}_{u,j>2} \end{aligned} \tag{4.13}$$

where $g^{s\star}_u$ is the receiver-satellite direction vector and Δx_u is the position increment vector. The interpretation of the estimable parameters follows from the user version of those in Table 4.1, with r replaced by u. Note that the user estimable ambiguities, $\tilde{a}^{s\star}_{u,j} = a^{s\star}_{pu,j} - a^{p\star}_{pu,j}$, are now in double-differenced form and thus integer.

Assuming that the network corrections are sufficiently precise, the stochastic model of the single-epoch single-system ionospheric-float user model is given as:

$$D\left(\begin{bmatrix}\Delta\phi_u\\ \Delta p_u\end{bmatrix}\right) = \begin{bmatrix}\mathrm{diag}(\sigma^2_{\Delta\phi_{u,1}},\ldots,\sigma^2_{\Delta\phi_{u,f}}) & 0\\ 0 & \mathrm{diag}(\sigma^2_{\Delta p_{u,1}},\ldots,\sigma^2_{\Delta p_{u,f}})\end{bmatrix} \otimes W_u^{-1} \tag{4.14}$$

where $\Delta\phi_u = [\Delta\phi^{1\star}_{u,1},\ldots,\Delta\phi^{m\star}_{u,1},\ldots,\Delta\phi^{1\star}_{u,f},\ldots,\Delta\phi^{m\star}_{u,f}]^{\mathrm{T}}$ and $\Delta p_u = [\Delta p^{1\star}_{u,1},\ldots,\Delta p^{m\star}_{u,1},\ldots,\Delta p^{1\star}_{u,f},\ldots,\Delta p^{m\star}_{u,f}]^{\mathrm{T}}$ denote the phase and code measurement vectors, respectively, per GNSS system. The terms $\sigma_{\Delta\phi_{u,j}}$ and $\sigma_{\Delta p_{u,j}}$ denote the zenith-referenced formal precision of the phase and code data, respectively, while the $m\times m$ matrix $W_u = \mathrm{diag}(w^1_u,\ldots,w^m_u)$ contains the weights for every satellite. The symbol $\otimes$ denotes the Kronecker product.

The above model formulation can be easily extended when multiple GNSS systems are employed, as the rank-deficiency removal concept is applicable in the same manner for every $\star$-system. In a multi-system integration, one has to be aware that the receiver code and phase biases are not experienced in the *same* way from system to system in *common* frequencies [31–33], i.e. $\tilde{\delta}^{\mathrm{G}}_{r,1} \neq \tilde{\delta}^{\mathrm{E}}_{r,1}$ and $\tilde{d}^{\mathrm{G}}_{r,1} \neq \tilde{d}^{\mathrm{E}}_{r,1}$. This is the reason why the full-rank system model (4.12) results in system-specific estimable receiver code/phase biases and receiver clock offsets. One could take advantage of the overlapping frequencies among systems and parameterize the network model in terms of the inter-system biases (ISB) that can be estimated and then used for strengthening the multi-system PPP-RTK user model as shown in Khodabandeh and Teunissen [34]. In this contribution, we chose to parameterize the system of equations in system-specific parameters treating each $\star$-system independently, with only the coordinate and troposphere parameters being common for all GNSSs. A consequence of this approach is that one pivot satellite should be taken per system, and not a common one across systems. The variance-covariance (vc) matrix of the single-GNSS measurements is extended by appending the measurement vc-matrices of the additional systems in a block-diagonal manner.

Table 4.1: Estimable parameters and chosen S-basis of the system-specific multi-frequency network model (the symbol p denotes the pivot satellite/receiver if it is used as superscript/subscript).

Parameter	**Interpretation**
Receiver clocks	$d\tilde{t}^{\star}_{r\neq p} = dt_{pr} + d^{\star}_{pr,\mathrm{IF}}$
Satellite clocks	$d\tilde{t}^{s\star} = (dt^{s\star} + d^{s\star}_{,\mathrm{IF}}) - (dt_p + d^{\star}_{p,\mathrm{IF}})$
Ionospheric delays	$\tilde{\imath}^{s\star}_{r} = \imath^{s\star}_{r} + d^{\star}_{r,\mathrm{GF}} - d^{s\star}_{,\mathrm{GF}}$
Phase ambiguities	$\tilde{a}^{s\star\neq p\star}_{r\neq p,j} = a^{s\star}_{pr,j} - a^{p\star}_{pr,j}$
Receiver phase biases	$\tilde{\delta}^{\star}_{r\neq p,j} = \delta^{\star}_{pr,j} + \frac{1}{\lambda_j}(\mu_j d^{\star}_{pr,\mathrm{GF}} - d^{\star}_{pr,\mathrm{IF}}) + a^{p\star}_{pr,j}$
Satellite phase biases	$\tilde{\delta}^{s\star}_{,j} = \delta^{s\star}_{,j} + \frac{1}{\lambda_j}(\mu_j[d^{s\star}_{,\mathrm{GF}} - d^{\star}_{p,\mathrm{GF}}] - [d^{s\star}_{,\mathrm{IF}} - d^{\star}_{p,\mathrm{IF}}]) - \delta^{\star}_{p,j} - a^{s\star}_{p,j}$
Receiver code biases	$\tilde{d}^{\star}_{r\neq p,j>2} = d^{\star}_{pr,j} - (d^{\star}_{pr,\mathrm{IF}} + \mu_j d^{\star}_{pr,\mathrm{GF}})$
Satellite code biases	$\tilde{d}^{s\star}_{,j>2} = [d^{s\star}_{,j} - (d^{s\star}_{,\mathrm{IF}} + \mu_j d^{s\star}_{,\mathrm{GF}})] - [d^{\star}_{p,j} - (d^{\star}_{p,\mathrm{IF}} + \mu_j d^{\star}_{p,\mathrm{GF}})]$
S-basis	$dt^{\star}_{p}$, $d^{\star}_{p,j}$, $\delta^{\star}_{p,j}$, $a^{p\star}_{r,j}$, $a^{s\star}_{p,j}$, $d^{\star}_{r\neq p,j=1,2}$, $d^{s\star}_{,j=1,2}$

$(\cdot)_{,\mathrm{IF}} = \frac{1}{\mu_2-\mu_1}[\mu_2(\cdot)_{,1} - \mu_1(\cdot)_{,2}]$; $(\cdot)_{,\mathrm{GF}} = -\frac{1}{\mu_2-\mu_1}[(\cdot)_{,1} - (\cdot)_{,2}]$; $(\cdot)_{ij} = (\cdot)_j - (\cdot)_i$.

4.3.2 Performance measures

In our study, we use several indicators to analyze the expected positioning capabilities of multi-system multi-frequency user models and show the impact of ambiguity resolution. Using the recursively estimated parameter solutions as a basis for our measures, we evaluate the formal ASR, the TTFA, the formal position precision and the precision gain after successful IAR. It is worth mentioning at this point that there is no need of simulating the code and phase data themselves or the integer ambiguities that are derived thereof, because our computations are based on a formal analysis making use of the model's design matrix and the measurement vc-matrix.

The formal ASR is based on (4.6) and is used to infer whether the ambiguities can be reliably fixed to their correct integers. Its estimation is solely based on the vc-matrix of the estimated float ambiguities, $Q_{\hat{a}\hat{a}}$, which is available at every epoch of our Kalman-filter-based processing. When FAR is attempted, the TTFA demonstrates the required time span to exceed a minimum ASR criterion, which was set equal to 99.5% in our computations. However, TTFA in PAR would be the required time to meet the ASR criterion but at the same time to achieve a horizontal positioning precision of better than 10 cm. For our ambiguity resolution computations, we used the LAMBDA software that has been recently released in Python [35].

The positioning precision along the north, east and up components was derived from the corresponding entries of $Q_{\hat{b}\hat{b}}$ which were available at every epoch, with the ambiguity-fixed counterparts from $Q_{\check{b}\check{b}}$ being available only after successful IAR. The contribution of

IAR into the positioning domain was measured by means of the gain numbers [36]:

$$\gamma_k = \frac{f_k^{\mathrm{T}} Q_{\hat{b}\hat{b}} f_k}{f_k^{\mathrm{T}} Q_{\check{b}\check{b}} f_k} \tag{4.15}$$

where $f_{k=1,2,3}$ are the gain vectors along the three directions. In our study, we analyze the precision gain only in the horizontal (radial) position.

4.3.3 Experimental setup

To analyze the ambiguity resolution and positioning performance of the ionosphere-float PPP-RTK user model based on multiple combinations of systems and frequencies, we selected 9 globally distributed International GNSS Service (IGS; [37]) stations for our simulation, the locations of which are shown in Figure 4.1. Due to differences in the satellite visibility from site to site, the selection of user stations across the globe allows us to get a clear insight into the expected performance, that is globally applicable and not location-restricted. The receiver-satellite geometries for GPS, Galileo and BeiDou-3 were reconstructed based on the precisely known station coordinates and the satellite positions, derived from the IGS merged broadcast ephemeris files[1] [38], on a randomly chosen day of 2019. To conduct a global-scale numerical analysis, we used only the BeiDou-3 Medium Earth Orbit (MEO) satellites, as they are the ones that provide global service and can transmit triple-frequency signals.

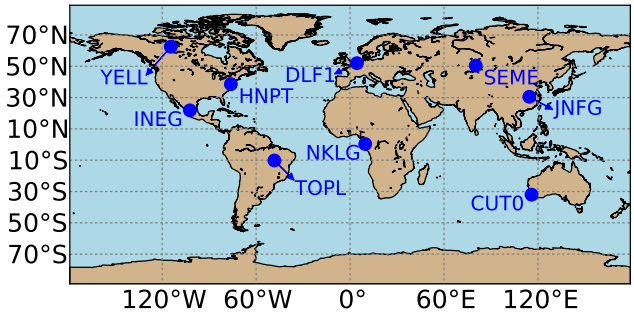


Figure 4.1: Distribution of the IGS multi-system multi-frequency user stations used in the simulation.

The real-time parameter estimation in the multi-GNSS multi-frequency PPP-RTK user models was performed with the recursive minimum-mean-squared-error Kalman filter using a dynamic model. Moreover, in our analysis the user positioning is performed in kinematic mode, therefore treating the user's position components as unlinked parameters in time. Details concerning the user's data, filter and processing settings are given in Table 4.2. It is worth mentioning that we chose the same code and phase zenith-referenced

[1] Found in: https://cddis.nasa.gov/archive/gnss/data/daily/

standard deviation for all GNSS systems and frequencies. We also assumed that the network corrections, provided to the user for realizing single-receiver IAR, are deterministic quantities, while no correlation between frequencies or in time was assumed. Moreover, the ASR criterion we used to decide on whether or not the ambiguities have been reliably fixed to their correct integers was set to 99.5% for both FAR and PAR.

Finally, we emphasize that our numerical results are linked to the selected sampling rate of 30 s. An increase in the sampling rate will have a positive effect on the achieved performance. Although a low sampling rate is beneficial for ambiguity resolution due to the greater change in the receiver-satellite geometry from epoch to epoch, a higher sampling rate leads to a higher model strength within the same time span.

Table 4.2: Information on the user's data and dynamic model settings as used in the experimental analysis.

Date and time	October 1, 2019 (274^{th} day), 24-hour dataset
Data (GNSS, frequencies)	GPS (L1/L2/L5), Galileo (E1/E5a/E5b/E5/E6), BeiDou-3 MEOs (B1/B2/B3)
Data sampling rate	30 sec
Zenith-referenced STDs	code: 30 cm, phase: 3 mm
Satellite-dependent weighting	$w_u^s = \sin^2(\beta_u^{s_\star})$, $\beta_u^{s_\star}$: elevation of satellite $s_\star$ tracked by receiver u
Tropospheric zenith delay	modeled by a random-walk process with system noise standard deviation of $0.1\text{mm}/\sqrt{30\text{s}}$
Receiver code/phase biases	time-invariant
Phase ambiguities	time-invariant
Other parameters	time-unlinked

4.4 Results and analysis

In the following section, we will present the performance results achieved with the ionosphere-float Kalman-filtered PPP-RTK user model using multiple GNSSs and multiple frequencies on a multitude of user stations.

4.4.1 Single-station analysis

This subsection provides an initial analysis of the expected ambiguity resolution and positioning performance in a single user station, namely DLF1 (in the Netherlands), in order to get a first insight into the factors that contribute mostly to IAR and positioning. Figure 4.2 shows the number of observed GPS, Galileo and BeiDou-3 satellites as tracked by DLF1 on the selected day. It can be observed that the number of satellites for a combined GPS+Galileo+BeiDou system almost triples compared to a single GNSS separately. The single- and multi-GNSS results are shown in the following subsections.

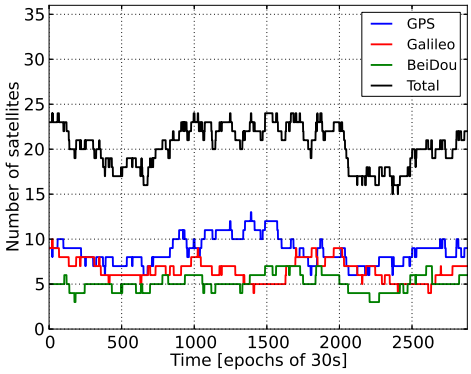


Figure 4.2: Number of GPS, Galileo and BeiDou-3 satellites tracked by station DLF1 as function of time during the 274th day of 2019 using an elevation cut-off angle of 10°: GPS (blue), Galileo (red), BeiDou (green), combined (black).

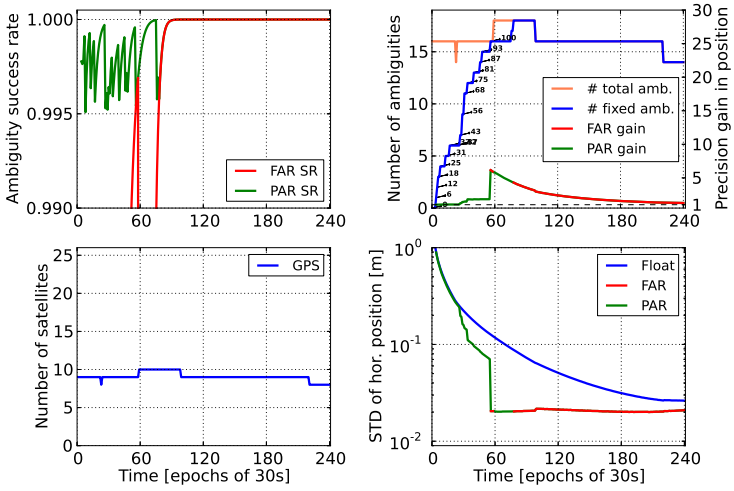


Figure 4.3: **GPS dual-frequency** (L1/L2) FAR/PAR and kinematic positioning performance at station DLF1 during the first 2 hours on DOY 274 of 2019. *Top left* ASR for FAR and PAR using a minimum criterion of 99.5%, with the number of tracked satellites shown at the *bottom left* figure. At *top right* the number of total and fixed ambiguities over time (with the percentage of fixed ambiguities being shown next to the blue curve) along with the horizontal position precision gain after IAR. The formal precision of the ambiguity-float and ambiguity-fixed horizontal position is shown at *bottom right*, with FAR being on top of PAR.

Single-GNSS performance

Figure 4.3 presents the GPS-only ambiguity resolution and positioning performance results, using both FAR and PAR, during the first 2 hours (240 epochs) on DOY 274 of 2019. The results indicate that 56 epochs since the start are needed to exceed the ASR criterion of 99.5% in order to resolve the full set of ambiguities and achieve centimeter-level positioning. Despite the gain that the user experiences in the position precision compared to the ambiguity-float solution, the ASR shows a sharp decrease at the very next epoch that restricts the availability of a FAR-based solution. This is due to a newly tracked GPS satellite at the 57^{th} epoch. We recall here that the formal bootstrapped ASR is defined as a multiplication of probabilities of correct integer estimation, with the one of the newly tracked satellite being poorly determined. This, practically, means that with every introduction of a new satellite into our filter solution and with the attempt to resolve the full set of ambiguities, the ASR will show large fluctuations and will not meet the ASR criterion consistently.

This is where the prominent advantage of PAR lies in, since the PAR technique attempts to fix a subset of ambiguities, instead of the full vector, that meets the ASR criterion. In this way, the user has an automatic method of discarding ambiguities of poor precision that are usually linked to newly tracked satellites, thereby solving the effect of rapid fluctuations due to rising satellites. The ASR criterion for PAR is met in 4 epochs in this case. However, this does not necessarily mean that the partially-ambiguity-fixed solution achieves centimeter level position precision, as it can be observed from the figure, since a large enough subset is needed for that. The results show that the PAR solution achieves a 10 cm horizontal position precision after 39 epochs (19.5 min) where 75% of the decorrelated ambiguities have been reliably fixed. The maximum precision gain of about 6 is observed a few epochs later, when the full set of ambiguities has been reliably fixed, as expected. At this epoch, the FAR-based and PAR-based results are identical, with an achieved accuracy of 2 cm. Based on this result, we conclude that a GPS-only dual-frequency user will not experience the ultimate cm-level precision in an instant with PAR, but a gradual improvement compared to the ambiguity-float solution, as has also been shown by Odijk *et al.* [7]. Despite the continuous availability of IAR in the next epochs, it can be seen that the precision gain decreases exponentially towards the value 1, which marks the point where the ambiguity-float solution shares the same quality with the ambiguity-fixed counterpart. This is expected because our ambiguity-float PPP solution is based on an implicit accumulation of data over epochs due to the employed Kalman filter, which allows the ambiguity-float solution to become more precise over time.

Further, our intention is to investigate whether it is the increased number of frequencies or satellites, or a combination thereof, that contributes mostly to the ambiguity resolution and positioning performance. We start our analysis with the introduction of the third GPS frequency, namely L5. Figure 4.4 depicts the GPS-only triple-frequency results of DLF1 during the same time interval. Two main conclusions can be drawn in this case. First, it can be observed that there is only a slight improvement in the ambiguity-float position solution by incorporating the L5 measurements. The reason that the triple-frequency model provides almost the same ambiguity-float positioning performance with the dual-frequency model lies in the fact that the receiver-satellite geometry remains invariant when data in more frequencies are used, since the number of observed satellites remained

constant.

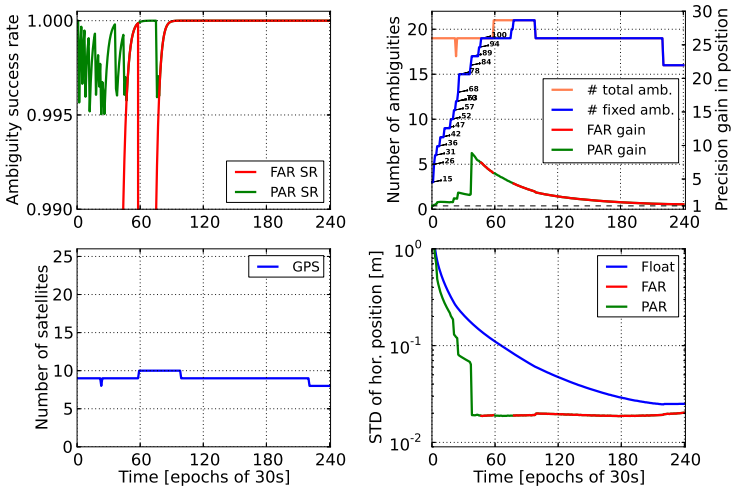


Figure 4.4: **GPS triple-frequency** (L1/L2/L5) FAR/PAR and kinematic positioning performance at station DLF1 during the first 2 hours on DOY 274 of 2019. *Top left* ASR for FAR and PAR using a minimum criterion of 99.5%, with the number of tracked satellites shown at the *bottom left* figure. At *top right* the number of total and fixed ambiguities over time (with the percentage of fixed ambiguities being shown next to the blue curve) along with the horizontal position precision gain after IAR. The formal precision of the ambiguity-float and ambiguity-fixed horizontal position is shown at *bottom right*, with FAR being on top of PAR.

The impact of the multi-frequency integration is visible, though, in the ambiguity-fixed solution. It can be seen that the TTFA for FAR is shortened compared to the dual-frequency case and is equal to 47 epochs (23 min), while PAR can instantaneously meet the ASR criterion. Despite the PAR availability, it can be seen that only a small subset of ambiguities was reliably fixed at the first epochs, with the maximum gain of 8.9 being acquired at the 38th epoch where 89% of the full decorrelated ambiguity vector has been fixed. Thus, after a time span of 38 epochs (18.5 min) the user enjoys a 2 cm position precision using PAR, which in case of FAR it would be delayed by 10 epochs (5 min). It can be concluded, therefore, that although the receiver-satellite geometry is not improved by using data in more frequencies, IAR is successfully achieved in a shorter time span that leads to high-precision positioning solutions.

Multi-GNSS performance

The combined GPS+Galileo dual-frequency ambiguity resolution and positioning performance results of station DLF1 are illustrated in Figure 4.5. In this case, the initial TTFA for FAR is 77 epochs (38 min) and, as expected, longer than the GPS-only dual-frequency TTFA. This is mainly due to multiplicative nature of the bootstrapped ASR, because in a multi-system integration the dimension of the ambiguity vector increases and, therefore, the probability of correct integer estimation has the tendency to get smaller.

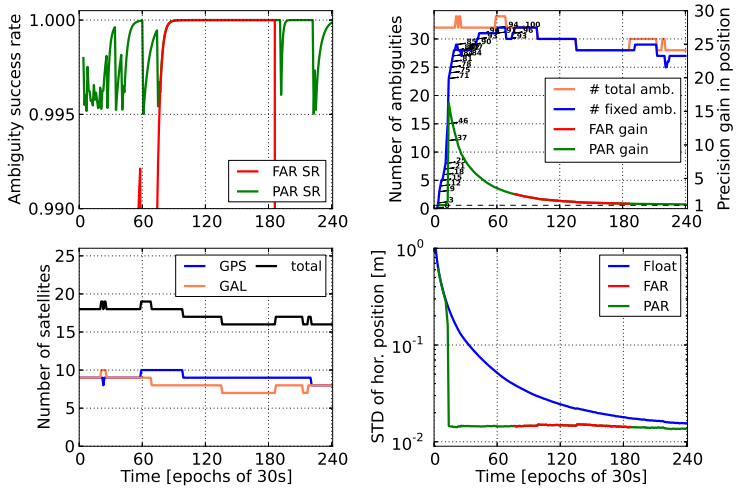
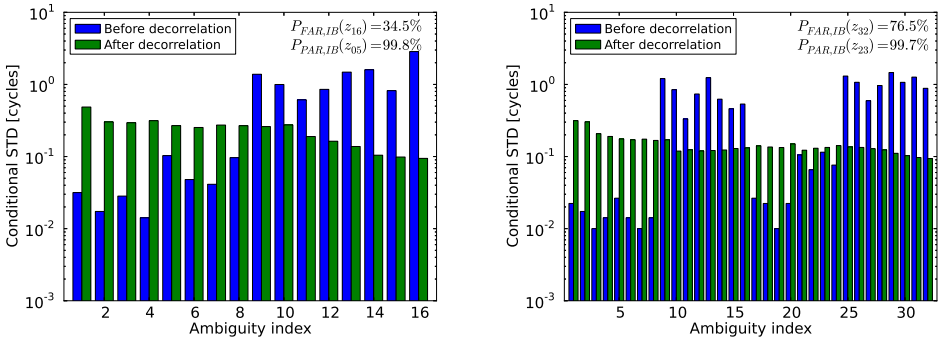


Figure 4.5: **GPS+Galileo dual-frequency** (L1/L2+E1/E5a) FAR/PAR and kinematic positioning performance at station DLF1 during the first 2 hours on DOY 274 of 2019. *Top left* ASR for FAR and PAR using a minimum criterion of 99.5%, with the number of tracked satellites shown at the *bottom left* figure. At *top right* the number of total and fixed ambiguities over time (with the percentage of fixed ambiguities being shown next to the blue curve) along with the horizontal position precision gain after IAR. The formal precision of the ambiguity-float and ambiguity-fixed horizontal position is shown at *bottom right*, with FAR being on top of PAR.

However, an improved positioning performance can be seen compared to the GPS-only dual- and triple-frequency solutions, due to mainly two reasons. First, the user enjoys an ambiguity-float position solution of higher precision that reaches the 10 cm level in 34 epochs (16.5 min), which is due to the improved satellite geometry after using both GPS and Galileo satellites in our processing. The second reason lies in the improved PAR performance. Despite the higher dimension of the ambiguity vector, it is observed that within only 14 epochs (6.5 min) the PAR strategy was able to identify 71% of all the decorrelated ambiguities that meet the pre-defined ASR criterion. At this time instance, the positioning precision experiences a significant gain of about 16, with the precision improving from about 24 to 1.5 cm. If one attempts FAR, a time span of 77 epochs (38 min) is needed.

To understand the underlying reason of the better PAR performance in the GPS+GAL solution compared to the GPS-only solution, we did an inspection of the conditional standard deviations (STDs) of the ambiguities at the 14^{th} epoch before and after decorrelation, which are shown in Figure 4.6. Looking at the conditional STDs before decorrelation, one can see that there are several discontinuities in the GPS+GAL ambiguity spectrum, with the number of conditional ambiguities of a few centi-cycles STD being larger than this of the GPS-only spectrum. Therefore, the presence of satellite redundancy and of many more small conditional STDs in the GPS+GAL solution allowed, after the Z-transformation, to pull down more large STDs than in the GPS-only case. And as it can be seen, a subset of 23 decorrelated ambiguities was identified in the combined solution that meets the ASR criterion and achieved a 1.5 cm precision, while the subset of only 5 ambiguities in the

GPS-only solution did not improve the ambiguity-float solution.



(a) GPS dual-frequency model (b) GPS+GAL dual-frequency model

Figure 4.6: LAMBDA-based conditional STDs for the GPS (left) and GPS+GAL (right) dual-frequency ambiguities at the 14th epoch of DOY 274 in 2019 for station DLF1, where 9 GPS and 9 GAL satellites are tracked. STD stands for standard deviation.

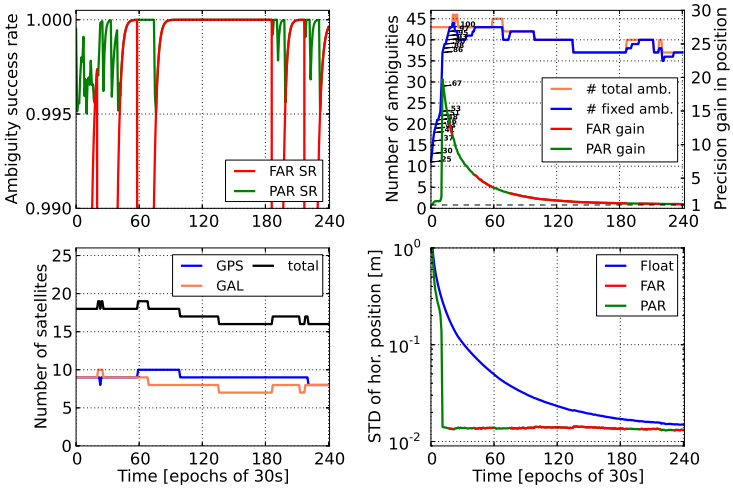


Figure 4.7: **GPS+Galileo triple-frequency** (L1/L2/L5+E1/E5a/E5b) FAR/PAR and kinematic positioning performance at station DLF1 during the first 2 hours on DOY 274 of 2019. *Top left* ASR for FAR and PAR using a minimum criterion of 99.5%, with the number of tracked satellites shown at the *bottom left* figure. At *top right* the number of total and fixed ambiguities over time (with the percentage of fixed ambiguities being shown next to the blue curve) along with the horizontal position precision gain after IAR. The formal precision of the ambiguity-float and ambiguity-fixed horizontal position is shown at *bottom right*, with FAR being on top of PAR.

The GPS+Galileo triple-frequency results are shown in Figure 4.7. It is shown that the incorporation of the third frequency brings only a marginal improvement in the ambiguity-float position precision, due to the invariant satellite geometry, that reaches 10 cm in 32 epochs (15.5 min) compared to 34 epochs (16.5 min) in the dual-frequency case. On the other hand, a significant shortening of the TTFA for FAR is observed, which reduces from 77 epochs (38 min) to 18 epochs (8.5 min) using the additional L5/E5a measurements. In analyzing the PAR-based results, it was found that 86% of decorrelated ambiguities are identified as the best-resolvable ambiguity subset within 11 epochs to meet the ASR criterion, compared to 14 epochs in dual-frequency case. By resolving this subset, the user's position precision increases from 28 to 1.5 cm, with a gain of about 19. Therefore, it is again demonstrated that the increase in number of frequencies slightly improves the ambiguity-float performance, but improves the IAR performance, which in turn improves the ambiguity-fixed positioning precision.

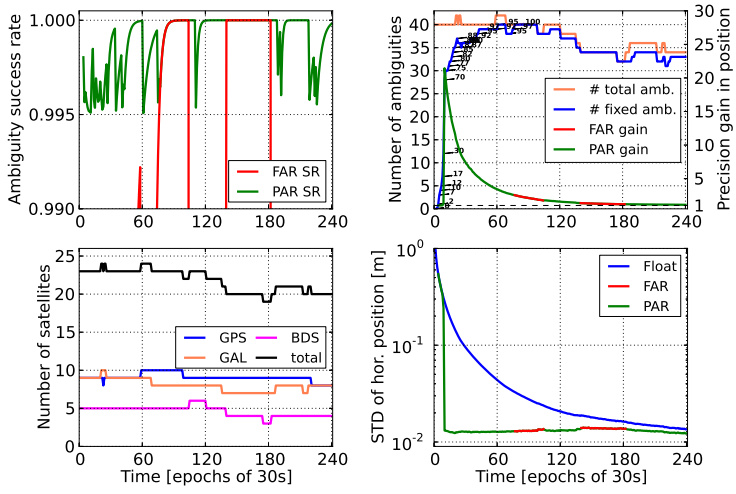


Figure 4.8: **GPS+Galileo+BeiDou dual-frequency** (L1/L2+E1/E5a+B1/B2) FAR/PAR and kinematic positioning performance at station DLF1 during the first 2 hours on DOY 274 of 2019. *Top left* ASR for FAR and PAR using a minimum criterion of 99.5%, with the number of tracked satellites shown at the *bottom left* figure. At *top right* the number of total and fixed ambiguities over time (with the percentage of fixed ambiguities being shown next to the blue curve) along with the horizontal position precision gain after IAR. The formal precision of the ambiguity-float and ambiguity-fixed horizontal position is shown at *bottom right*, with FAR being on top of PAR.

To further investigate the integration of more than 2 systems, we evaluated the ambiguity resolution and positioning performance of the GPS+GAL+BDS dual-frequency PPP-RTK user model at station DLF1, with the results being illustrated in Figure 4.8. It can be observed that the ambiguity-float position precision reaches the 10 cm level in 29 epochs (14 min) which is an improvement of 15% compared to the GPS+GAL dual-frequency solution. The improvement is smaller compared to the addition of GAL satellites in the GPS-only solution, as the GPS+GAL model was already strong enough. The TTFA for FAR is 76 epochs (37.5 min) and is therefore almost equal to the one of the GPS+GAL dual-

frequency model, while the PAR solution achieves a 1.3 cm horizontal position precision within the first 10 epochs (4.5 min) having 70% of the decorrelated ambiguities fixed and a gain of 21.5. Therefore, using the BDS measurements reduces the convergence time to 10 cm by 2 min.

The triple-GNSS triple-frequency solution is shown in Figure 4.9. As it was previously concluded, it can be seen that the addition of the third frequency of BDS does not contribute in improving considerably the ambiguity-float position precision. Then, although the TTFA shows a decrease compared to the triple-GNSS dual-frequency solution, it does not improve compared to the dual-GNSS triple-frequency solution. It is seen, therefore, that the addition of an additional frequency has a great impact in reducing the FAR TTFA when the receiver-satellite geometry remains invariant. The partially-ambiguity-fixed solution surpasses the 10 cm level and reaches a position precision of 1.5 cm within the first 7 epochs (3 min), when 83% of ambiguities have been fixed and the corresponding gain is 23. Compared to all the previous solutions, the triple-GNSS triple-frequency solution was able to achieve centimeter-level positioning in the shortest time span, equal to 3 min.

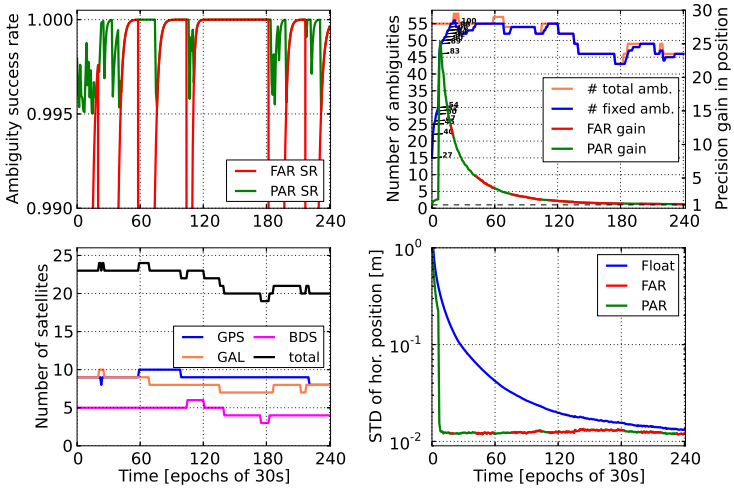
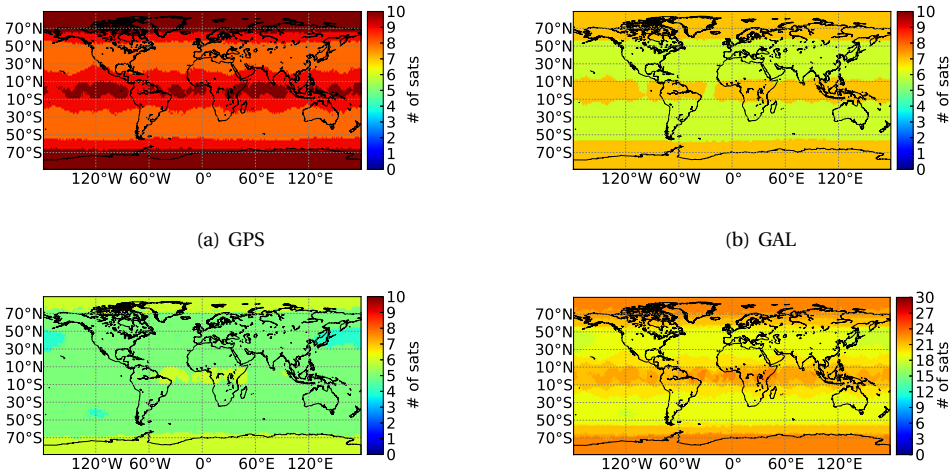


Figure 4.9: **GPS+Galileo+BeiDou triple-frequency** (L1/L2/L5+E1/E5a/E5b+B1/B2/B3) FAR/PAR and kinematic positioning performance at station DLF1 during the first 2 hours on DOY 274 of 2019. *Top left* ASR for FAR and PAR using a minimum criterion of 99.5%, with the number of tracked satellites shown at the *bottom left* figure. At *top right* the number of total and fixed ambiguities over time (with the percentage of fixed ambiguities being shown next to the blue curve) along with the horizontal position precision gain after IAR. The formal precision of the ambiguity-float and ambiguity-fixed horizontal position is shown at *bottom right*, with FAR being on top of PAR.

4.4.2 Global analysis

In this section, we present and analyze the multi-system multi-frequency user performance on a global scale. To conduct a rigorous analysis of the global IAR performance, one needs a sufficient number of sample solutions in order to infer realistic conclusions about the expected performance. To this end, we performed our formal analysis, based on kinematic PPP-RTK user positioning, for the 9 selected globally distributed IGS stations with a 2-hour processing window being re-initialized every 1 minute, in order to capture all possible receiver-satellite geometry changes, having in total 1320 sample solutions per model per station. The measures we used in this case to characterize the performance are the achieved positioning precision and expected gain after IAR. Thus, we sorted the horizontal position precision of all solutions for every epoch and identified the maximum precision that does not exceed 90% of all the sorted solutions, while the same procedure was followed for the gain numbers as well. Since it was shown that PAR performs better than FAR and can provide centimeter-level positioning results in a significantly shorter time span, we considered only PAR in this analysis.

The average number of observed satellites for GPS, Galileo and BeiDou-3 in the selected day is depicted in Figure 4.10. The average number of tracked satellites in a single-system scenario is 9 for GPS, followed by 7 for Galileo and 5 for BeiDou. When satellites from multiple systems are combined, the number of visible satellites ranges from 18 to 23 on a global scale, leading to improved geometry for the users.



(a) GPS

(b) GAL

(c) BDS

(d) GPS+GAL+BDS

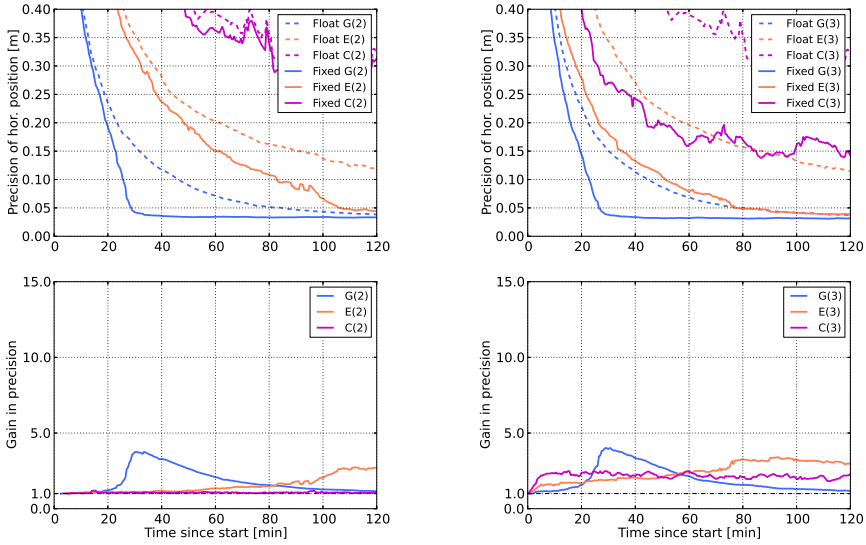
Figure 4.10: Average number of visible GPS, Galileo and BeiDou-3 satellites on DOY 274 of 2019. The elevation cut-off angle is 10°. Note that the scale is different in the bottom right figure.

The convergence behavior and TTFA of the multi-system multi-frequency user positioning results, along with the precision gain after IAR, are illustrated in Figure 4.11. The reported results are, therefore, indicative of the performance one should expect at 90% of the cases on a global scale.

From the single-GNSS results, it is clear that the GPS solutions can achieve better performance compared to the Galileo and BeiDou counterparts, using either two or three frequencies, which is due to the complete GPS constellation with 9 observed satellites on average, unlike Galileo and BeiDou with 7 and 5 observed satellites on average, respectively. Moreover, the GPS-only solution shows a TTFA of 25.5 min using PAR. Due to their incomplete constellations, the Galileo-only solution shows a TTFA of 83 min, while the BDS-only solution requires more than 2 hours to resolve a sufficiently large enough subset to achieve high precision. Further, it can be seen that the addition of a third frequency in the single-constellation models does not improve the ambiguity-float position precision, as expected, which is due to the invariant satellite geometry. However, the ambiguity-fixed positioning precision enjoys a great increase due to the improved ambiguity resolution performance, which is more profound in the weaker Galileo-only and BeiDou-only solutions. In particular, the triple-frequency GPS-only and Galileo-only solutions show a TTFA of 23 and 51.5 min, respectively, while the BeiDou-only solution shows a considerable improvement compared to the dual-frequency case but still requires more than 120 min. This can be also seen in the bottom figures of panels **(a)** and **(b)**, where the gain numbers of Galileo and BeiDou seem to increase earlier than in the dual-frequency case.

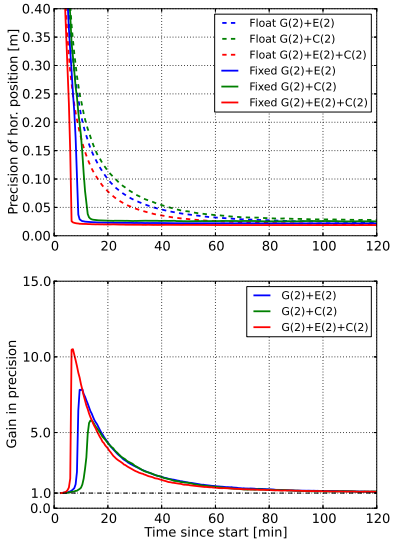
When at least two GNSS systems are combined, a tremendous improvement in the TTFA and positioning performance can be observed in both ambiguity-float and ambiguity-fixed solutions. Due to the increase of number of satellites in the solution, the ambiguity-float positioning precision shows a dramatic increase, with the best performance being reported from the combined GPS+Galileo+BeiDou solution. The worst performance, compared to the rest multi-GNSS solutions, is the one of the GPS+BDS solution due to the incomplete BeiDou-3 MEO constellation. In particular, the 10 cm precision level can be achieved within 20, 23 and 16.5 min (TTFA) for the GPS+Galileo, GPS+BeiDou and GPS+Galileo+BeiDou dual-frequency ambiguity-float solutions, while the addition of an extra frequency for all GNSSs does not improve the precision, as expected.

The PAR-based positioning solutions converge faster and are of higher precision for both dual and triple-frequency solutions. The TTFA for the dual-frequency GPS+Galileo, GPS+BeiDou and GPS+ Galileo+BeiDou solutions are equal to 8.5, 11 and 6.5 min, respectively, with the triple-GNSS solution showing a horizontal precision gain above 10, while the two dual-GNSS solutions have a gain between 5 and 8. As expected, the incorporation of the third frequency per GNSS improves IAR and, therefore, the partially-ambiguity-fixed positioning. The TTFA for the triple-frequency GPS+Galileo, GPS+BeiDou and GPS+Galileo+BeiDou solutions are equal to 7.5, 9.5 and 4.5 min, respectively, with the improvement being on the order of about 13%, 16% and 44% compared to the dual-frequency counterparts. The TTFAs of the user's PAR-based positioning results are summarized in Figure 4.12.

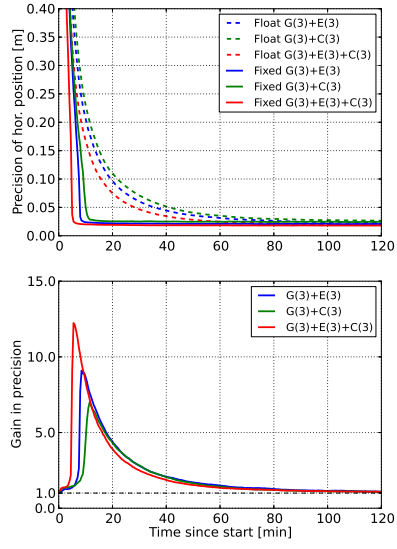


(a) **Single-GNSS dual-frequency**

(b) **Single-GNSS triple-frequency**



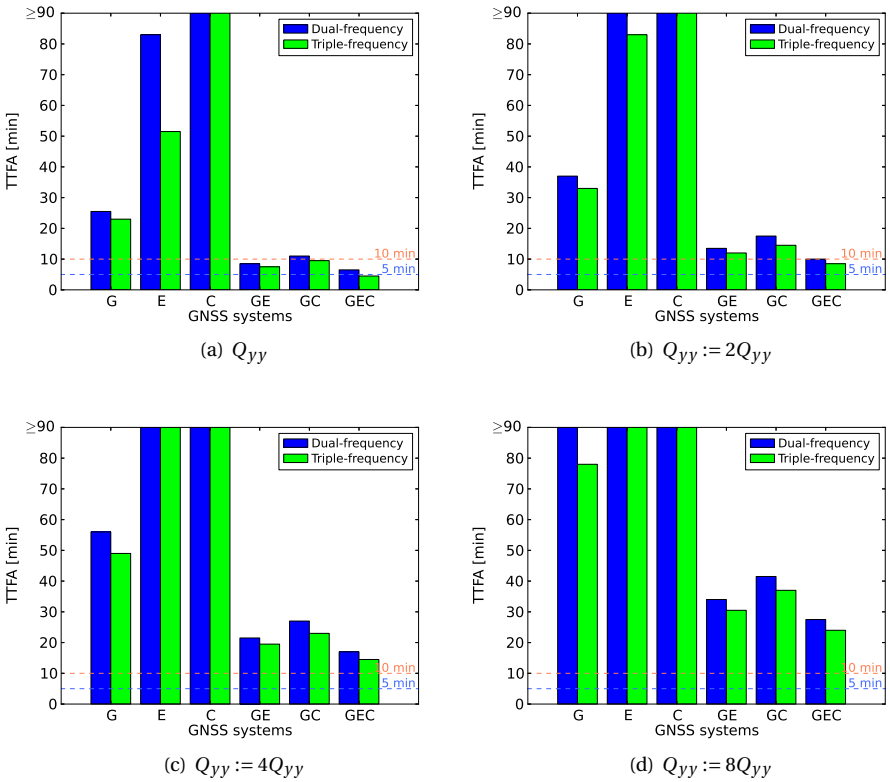
(c) **Multi-GNSS dual-frequency**



(d) **Multi-GNSS triple-frequency**

Figure 4.11: PPP-RTK user horizontal positioning precision and gain (90^{th} percentile) as function of time since the processing start, using PAR and the initially defined measurement vc-matrix Q_{yy}. The processing window is re-initialized every 1 minute within the selected day for all stations and system/frequency combinations. G, E, C stand for GPS, Galileo and BeiDou-3, while the numbers within the parentheses denote the number of frequencies. The number of observed GPS, Galileo and BeiDou-3 satellites is 9, 7 and 5 on average.

At this point, it is important to emphasize that these results are sensitive to our measurement uncertainty assumptions, since the stochastic model affects both the ambiguity resolution and the positioning performance. In particular, the code and phase measurement STDs used were equal to 30 cm and 3 mm, respectively, with these choices being inappropriate in case a low-cost receiver is used. In addition, our stochatic model was also based on the simplifying assumption, as is commonly done in literature, that the PPP-RTK user-provided network corrections are sufficiently precise such that they can be treated as deterministic. This assumption might be valid when a network continuously generates such corrections that allows them to gain high precision over time, but this might not hold in sparse networks where data over short time spans are used and IAR is not successfully realized.



(a) Q_{yy} (b) $Q_{yy} := 2Q_{yy}$

(c) $Q_{yy} := 4Q_{yy}$ (d) $Q_{yy} := 8Q_{yy}$

Figure 4.12: TTFA (90$^{\text{th}}$ percentile) for PAR-based kinematic PPP-RTK user solutions for varying measurement precision. The results are based on the sample solutions computed at the selected 9 globally distributed IGS stations with a 2-hour processing window being re-initialized every 1 minute for several system/frequency combinations.

To investigate the impact of the stochastic model on the user's performance, we computed the user's positioning solutions based on varying measurement precision, with the PAR-based TTFAs being shown in Figure 4.12. In general, one can observe that an increase of the observation STDs in the stochastic model deteriorates the user's performance in terms of TTFA, gain in position precision and achieved positioning precision over time, as expected. The reason for the increased TTFAs lies in the fact that it takes longer to achieve successful PAR with a positioning precision of better than 10 cm due to the increased measurement noise that directly affects the parameter estimation. In this way, one will experience less wrongly fixed solutions, as an overoptimistic stochastic model will lead to faster PAR realizations and, therefore, a larger number of wrongly fixed solutions. When the initial measurement vc-matrix is scaled by a factor of 4 or 8, implying the use of low-cost receiver data with a code observation STD of 60 or about 85 cm at zenith, respectively, the best-performing-single-GNSS GPS dual-frequency model achieves a TTFA of 56 or 93 min, respectively. Adding the third frequency signals reduces the TTFAs by 12% and 16%, respectively. As it can be seen, it is the integration of multi-GNSS signals that contributes the most to the reduction of TTFAs. The GPS+Galileo+BeiDou solutions achieve successful PAR with a positioning precision better than 10 cm within 17 and 27.5 min when two frequencies are used, respectively, with a 13-15% improvement by adding the third frequency signals. This sensitivity for varying observation STD seems to be less pronounced in the multi-GNSS multi-frequency models, especially for the triple-frequency GPS+Galileo+BeiDou model. Thus, as the user's model strength increases, by using multi-satellite and/or multi-frequency data, the TTFA sensitivity for varying code and phase precision becomes less.

4.4.3 Five-frequency Galileo PPP-RTK

The European satellite navigation system Galileo undergoes a rapid development in the last years, with the declaration of its initial services in December 2016 [39]. The capability of Galileo to transmit signals on five frequencies allows for faster ambiguity resolution compared to the rather weak dual-frequency model. It is, therefore, of great interest to evaluate the IAR and positioning performance of a multi-frequency Galileo user. To this end, we computed the PPP-RTK user's positioning solutions for the 9 globally distributed stations with every-1-minute initializations of a 2-hour processing window, having in total about 12000 sample solutions. We emphasize here that in our computations the Galileo observables of different frequencies were assumed to be uncorrelated, based on the fact that no significant correlation has been empirically found, even for the Galileo E5a/E5/E5b observables that are derived from the same wideband signal [40]. The extracted 90^{th} percentiles of the ambiguity-float and ambiguity-fixed positioning precision over time, as well as of the gain in horizontal position precision, are shown in Figure 4.13.

One can observe that the dual-frequency ambiguity-float position solution requires more than 2 hours to reach the 10 cm level, while the increase in number of frequencies brings only a slight improvement in the performance, as it was observed in the previous sections. However, the increasing number of frequencies seems to bring a significant improvement in the PAR-based solutions. In particular, the dual-frequency ambiguity-fixed solution (90%) achieves a TTFA of more than 1 hour, while the triple- and four-frequency

solutions bring the TTFA to 51 and 48 min, respectively. Although no significant improvement is observed when adding the fourth frequency, the five-frequency user's model is shown to be greatly strengthened in terms of its PAR capabilities, having a TTFA of 25 min that is a reduction of almost 60 min compared to the dual-frequency counterpart. Therefore, it is concluded that a high number of frequencies is critical in achieving high ASRs, ambiguity-resolved positioning of high precision and large precision gains in a short time span.

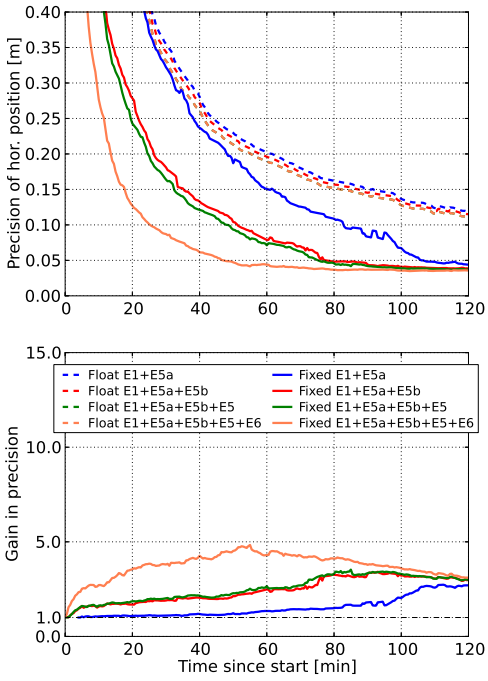


Figure 4.13: Galileo multi-frequency PPP-RTK user horizontal positioning precision and gain (90^{th} percentile) as function of time since the processing start, with the processing window being re-initialized every 1 minute within the selected day for all stations. The ambiguity-fixed results are obtained using PAR.

In summary, and based on all of the above numerical results, it can be concluded that multiple GNSSs and multiple frequencies can bring a significant benefit to IAR, with the first being the main driving factor. Even though no *a priori* information was assumed for the slant ionospheric delays, the incorporation of multiple signals strengthens the model in such a way that IAR can be achieved in a short time span. This, of course, comes to a cost. The high-dimensional vc-matrix of the estimated float ambiguities seems to be a computational bottleneck. From our experiments, it was observed that the higher the dimension of the ambiguity vector, the higher the computational burden is in the decorrelation process and the construction of the Z-transformation matrix of LAMBDA. To speed up the decorrelation, one can make use of the Z-matrix from previous epochs to decorrelate $Q_{\hat{a}\hat{a}}$ in successive epochs assuming that no significant change exists in the satellite geometry, as proposed by Nardo *et al.* [41].

4.5 Conclusions

In this contribution, we provided insight into and analyzed the expected ambiguity resolution and kinematic positioning performance of the ionosphere-float PPP-RTK user's model based on several multi-GNSS multi-frequency models without any a priori ionospheric information. The user's performance was formally evaluated at several globally distributed stations and measured in terms of the formal ambiguity success rate, the required time to fix ambiguities, the achieved horizontal position precision and the expected gain after successful ambiguity resolution. Our first finding is that the increase in number of frequencies brings only a small improvement in the ambiguity-float position precision, due to the invariant satellite geometry, but improves the ambiguity resolution performance by providing a shorter TTFA for both FAR and PAR and, therefore, centimeter-level positioning can be achieved in a shorter time span. This was also demonstrated by analyzing the five-frequency Galileo user's performance, which shows a significant improvement of 70% compared to the dual-frequency model and a TTFA of 25 min. We also numerically demonstrated that PAR outperforms FAR for all solutions, in the sense that a sufficiently large subset of ambiguities can meet the ASR criterion and provide a position precision of better than 10 cm in a shorter time span and in a consistent manner. Although no considerable improvement in the position precision was found for single-constellation solutions using PAR, it was shown that significant gains can be expected when at least two GNSS systems are combined. Further, we showed that the increase in number of satellites used in the model improves both positioning and ambiguity resolution capabilities due to the strengthened geometry. Therefore, it is concluded that the satellite and frequency redundancy work in tandem to improve the user's performance, with the former being the main driving force for speeding up ambiguity-resolved positioning in the absence of ionospheric information. Despite the increase in the dimension of the ambiguity vector and the potential decrease of the FAR ASR, PAR was shown to be an efficient solution to the upcoming dimensional curse such that a large enough subset can be identified to both meet the ASR criterion and surpass the 10 cm precision level. Based on an extensive sample of solutions computed on a global scale, it was found that the dual- and triple-frequency GPS+Galileo+BeiDou PPP-RTK user solutions can reliably achieve a TTFA of 6.5 and 4.5 min (90^{th} percentile), respectively, within which the user's position precision enjoys an improvement by more than one order of magnitude and gets better than 10 cm, based on the current status of constellations. Both triple-GNSS solutions provide significant gains and much shorter TTFAs compared to the single-GNSS solutions, which would be 23 min in case of the best-performing triple-frequency GPS solution. Finally, we provided numerical evidence on the sensitivity of the user's performance for varying code and phase precision, characterizing both high-grade geodetic and low-cost receivers, as well as considering the network corrections' precision. It was found that a longer time span is required to achieve PAR with significant gains due to the increased measurement noise, with the sensitivity being less pronounced for multi-GNSS multi-frequency models.

References

[1] P. J. G. Teunissen, *The least-squares ambiguity decorrelation adjustment: a method for fast GPS integer ambiguity estimation.* Journal of Geodesy **70**, 65 (1995).

[2] P. J. G. Teunissen and O. Montenbruck, *Springer Handbook of Global Navigation Satellite Systems*, 1st ed. (Springer International Publishing, 2017).

[3] J. F. Zumberge, M. B. Heflin, D. C. Jefferson, M. M. Watkins, and F. H. Webb, *Precise point positioning for the efficient and robust analysis of GPS data from large networks.* Journal of Geophysical Research **102**, 5005 (1997).

[4] G. Wubbena, M. Schmitz, and A. Bagge, *PPP-RTK: Precise Point Positioning Using State-Space Representation in RTK Networks.* in *Proceedings of the 18th International Technical Meeting of the Satellite Division of The Institute of Navigation, ION GNSS 2005* (Long Beach, CA, USA, 2005) pp. 2584–2594.

[5] C. Tiberius, T. Pany, B. Eissfeller, K. de Jong, P. Joosten, and S. Verhagen, *Integral GPS-Galileo ambiguity resolution.* in *Proceedings of the European Navigation Conference GNSS 2002* (Copenhagen, Denmark, 2002).

[6] S. Verhagen, P. J. G. Teunissen, and D. Odijk, *Carrier-phase Ambiguity Success Rates for Integrated GPS-Galileo Satellite Navigation.* in *Proceedings Space, Aeronautical and Navigational Electronics Symposium SANE2007, The Institute of Electronics, Information and Communication Engineers (IEICE).*, Vol. 107 (Japan, 2007) pp. 139–144.

[7] D. Odijk, B. S. Arora, and P. J. G. Teunissen, *Predicting the success rate of long-baseline GPS + Galileo (partial) ambiguity resolution.* Journal of Navigation **67**, 385 (2014).

[8] G. Xiao, P. Li, Y. Gao, and B. Heck, *A Unified Model for Multi-Frequency PPP Ambiguity Resolution and Test Results with Galileo and BeiDou Triple-Frequency Observations.* Remote Sensing **11**, 116 (2019).

[9] W. Zhang, M. E. Cannon, O. Julien, and P. Alves, *Investigation of combined GPS/GALILEO cascading ambiguity resolution schemes.* in *Proceedings of the 16th International Technical Meeting of The Satellite Division of the Institute of Navigation (ION GPS/GNSS 2003).* (Portland, OR, 2003) pp. 2599–2610.

[10] S. Y. Ji, W. Chen, X. L. Ding, Y. Q. Chen, C. M. Zhao, and C. W. Hu, *An improved cascading ambiguity resolution (CAR) method with Galileo multiple frequencies.* Survey Review **45**, 51 (2013).

[11] K. Wang, A. Khodabandeh, and P. J. G. Teunissen, *Five-frequency Galileo long-baseline ambiguity resolution with multipath mitigation,* GPS Solutions **22** (2018), 10.1007/s10291-018-0738-6.

[12] X. Li, X. Li, Y. Yuan, K. Zhang, X. Zhang, and J. Wickert, *Multi-GNSS phase delay estimation and PPP ambiguity resolution: GPS, BDS, GLONASS, Galileo.* Journal of Geodesy **92**, 579 (2018).

[13] V. Duong, K. Harima, S. Choy, D. Laurichesse, and C. Rizos, *Assessing the performance of multi-frequency GPS, Galileo and BeiDou PPP ambiguity resolution.* Journal of Spatial Science **0**, 1 (2019).

[14] X. Li, X. Li, G. Liu, G. Feng, Y. Yuan, K. Zhang, and X. Ren, *Triple-frequency PPP ambiguity resolution with multi-constellation GNSS: BDS and Galileo.* Journal of Geodesy **93**, 1105 (2019).

[15] A. Brack, *Long Baseline GPS+BDS RTK Positioning with Partial Ambiguity Resolution,* in *Proceedings of the 2017 International Technical Meeting of The Institute of Navigation* (Monterey, California, 2017) pp. 754–762.

[16] B. Li, *Review of triple-frequency GNSS: ambiguity resolution, benefits and challenges.* Journal of Global Positioning Systems **216** (2018), 10.1186/s41445-018-0010-y.

[17] M. Deo and A. El-Mowafy, *A method for precise point positioning with integer ambiguity resolution using triple-frequency GNSS data.* Measurement Science and Technology **30**, 065009 (2019).

[18] X. Liu, H. Chen, W. Jiang, R. Xi, W. Zhao, C. Song, and X. Zhou, *Modeling and Assessment of GPS/Galileo/BDS Precise Point Positioning with Ambiguity Resolution.* Remote Sensing **11**, 2693 (2019).

[19] P. J. G. Teunissen, *An Optimality Property of the Integer Least-Squares Estimator,* Journal of Geodesy **73**, 587 (1999).

[20] S. Verhagen, B. Li, and P. J. G. Teunissen, *Ps-LAMBDA: Ambiguity success rate evaluation software for interferometric applications.* Computers and Geosciences **54**, 361 (2013).

[21] S. Verhagen, C. Tiberius, B. Li, and P. J. G. Teunissen, *Challenges in ambiguity resolution: biases, weak models, and dimensional curse.* in *2012 6th ESA Workshop on Satellite Navigation Technologies (Navitec 2012) European Workshop on GNSS Signals and Signal Processing* (2012) pp. 1–8.

[22] W. Cao, K. O'Keefe, and M. Cannon, *Partial ambiguity fixing within multiple frequencies and systems.* in *Proceedings of the 20th International Technical Meeting of The Satellite Division of the Institute of Navigation (ION GNSS 2007).* (Fort Worth, TX, 2007) pp. 312–323.

[23] B. Li, Y. Feng, and Y. Shen, *Three carrier ambiguity resolution: distance-independent performance demonstrated using semi-generated triple frequency GPS signals.* GPS Solutions **14**, 177 (2010).

[24] L. Dai, D. Eslinger, and T. Sharpe, *Innovative algorithms to improve long range RTK reliability and availability.* in *Proceedings of the 2007 National Technical Meeting of The Institute of Navigation.* (San Diego, CA, 2007) pp. 860–872.

[25] D. Lawrence, *A New Method for Partial Ambiguity Resolution.* in *Proceedings of the 2009 International Technical Meeting of The Institute of Navigation.* (Anaheim, CA, 2009) pp. 652–663.

[26] A. Brack and C. Günther, *Generalized integer aperture estimation for partial GNSS ambiguity fixing.* Journal of Geodesy **88**, 479 (2014).

[27] P. J. G. Teunissen, P. Joosten, and C. C. J. M. Tiberius, *Geometry-free ambiguity success rates in case of partial fixing.* in *Proceedings of ION NTM 1999.* (San Diego, CA, 1999) pp. 201–207.

[28] D. Odijk, B. Zhang, A. Khodabandeh, R. Odolinski, and P. J. G. Teunissen, *On the estimability of parameters in undifferenced, uncombined GNSS network and PPP-RTK user models by means of S-system theory,* Journal of Geodesy **90**, 15 (2016).

[29] W. Baarda, *S-transformations and criterion matrices.* in *Publications on Geodesy, 18*, Vol. 5 (Netherlands Geodetic Commission, Delft, The Netherlands, 1973).

[30] P. J. G. Teunissen, *Zero Order Design: Generalized Inverses, Adjustment, the Datum Problem and S-Transformations.* in *Optimization and Design of Geodetic Networks.*, edited by E. Grafarend and F. Sanso (Springer, Berlin, Heidelberg, 1985) pp. 11–55.

[31] C. Hegarty, E. Powers, and B. Fonville, *Accounting for timing biases between GPS, modernized GPS, and Galileo signals.* in *Proceedings of 36th annual precise time and time interval (PTTI) meeting.* (Washington, DC, 2004) pp. 307–317.

[32] O. Montenbruck, A. Hauschild, and U. Hessels, *Characterization of GPS/GIOVE sensor stations in the CONGO network.* GPS Solutions **15**, 193 (2011).

[33] D. Odijk and P. J. G. Teunissen, *Characterization of between-receiver GPS-Galileo inter-system biases and their effect on mixed ambiguity resolution.* GPS Solutions **17**, 521 (2013).

[34] A. Khodabandeh and P. J. G. Teunissen, *PPP-RTK and inter-system biases: the ISB look-up table as a means to support multi-system PPP-RTK.* Journal of Geodesy **90**, 837 (2016).

[35] D. Psychas, S. Verhagen, and P. J. G. Teunissen, *LAMBDA - Python implementation, Version 1.0* (Delft University of Technology, 2019).

[36] P. J. G. Teunissen, *The Ionosphere-weighted GPS baseline precision in canonical form,* Journal of Geodesy **72**, 107 (1998).

[37] J. M. Dow, R. E. Neilan, and C. Rizos, *The International GNSS Service in a changing landscape of Global Navigation Satellite Systems.* Journal of Geodesy **83**, 191 (2009).

[38] O. Montenbruck, P. Steigenberger, L. Prange, Z. Deng, Q. Zhao, F. Perosanz, I. Romero, C. Noll, A. Sturze, G. Weber, R. Schmid, K. MacLeod, and S. Schaer, *The Multi-GNSS Experiment (MGEX) of the International GNSS Service (IGS) - Achievements, prospects and challenges.* Advances in Space Research **59**, 1671 (2017).

[39] GSA, *Galileo Initial Services,* (2018).

[40] D. Odijk, P. Teunissen, and A. Khodabandeh, *Galileo IOV RTK positioning: standalone and combined with GPS,* Survey Review **46**, 267 (2014).

[41] A. Nardo, B. Li, and P. J. G. Teunissen, *Partial Ambiguity Resolution for Ground and Space-Based Applications in a GPS+Galileo scenario: A simulation study.* Advances in Space Research **57**, 30 (2016).

5

Multi-GNSS multi-frequency PPP-RTK user performances: Part II

The single-receiver integer ambiguity resolution-enabled variant of precise point positioning (PPP), namely PPP-RTK, has proven to be crucial in reducing the long convergence time of PPP solutions through the recovery of the integerness of the user-ambiguities. The proliferation of global navigation satellite systems (GNSS) supports various improvements in this regard through the availability of more satellites and frequencies. The increased availability of the Galileo E6 signal from GNSS receivers paves the way for speeding up integer ambiguity resolution, as more frequencies provide for a stronger model. In this contribution, the Galileo-based PPP-RTK ambiguity resolution and positioning convergence capabilities are studied and numerically demonstrated as a function of the number and spacing of frequencies, aiming to shed light on which frequencies should be used to obtain optimal performance. Through a formal analysis, we provide insight into the pivotal role of frequency separation in ambiguity resolution. Using real Galileo data on up to five frequencies and our estimated PPP-RTK corrections, representative kinematic user convergence results with partial ambiguity resolution are presented and discussed. Compared to the achieved performance of dual-frequency fixed solutions, it is found that the contribution of multi-frequency observations is significant and largely driven by frequency separation. When using all five available frequencies, it is shown that the kinematic user can achieve a sub-decimeter level convergence in 15.0 min (90% percentile). In our analysis, we also show to what extent the provision of the estimable satellite code biases as standard PPP-RTK corrections accelerates convergence. Finally, we numerically demonstrate that, when integrated with GPS, the kinematic user solution achieves convergence in 3.0 and 5.0 min on average and at 90%, respectively, in the presence of ionospheric delays, thereby indicating the single-receiver user's fast-convergence capabilities.

This chapter has been published as: Psychas, D., Teunissen, P.J.G. and Verhagen, S. (2021). A Multi-Frequency Galileo PPP-RTK Convergence Analysis with an Emphasis on the Role of Frequency Spacing. Remote Sensing, 13(16):3077, doi: 10.3390/rs13163077

5.1 Introduction

Integer ambiguity resolution-enabled precise point positioning (PPP-RTK) is the global navigation satellite systems (GNSS) positioning mode that offers ambiguity-resolved parameter solutions on the basis of a single receiver. The purpose of integer ambiguity resolution (IAR) is to gain a substantial precision improvement in the user's model parameters in a shorter timespan, thereby reducing the relatively long convergence time of precise point positioning (PPP) solutions, which usually last for up to a few hours [1–3].

In the presence of ionospheric delays, however, fast and reliable ambiguity resolution with a single-GNSS dual-frequency model is known to be hindered, due to its inherent weakness in the sense of its IAR capabilities, and thus requires measurements over multiple epochs. This can be overcome, to a certain extent, with model strengthening by means of either using data from multiple systems and frequencies, or incorporating regional ionospheric corrections, or a combination thereof. In such cases, the uncombined GNSS formulation, i.e., when no differencing or combinations of measurements are used, seems to be the most suitable choice as it allows for a rigorous and straightforward extension to multi-GNSS and multi-frequency models, but also provides the possibility of constraining the temporal and spatial behaviour of the ionosphere [3].

Since the advent of PPP-RTK, efforts have been made to achieve fast (i.e., instantaneous or near-instantaneous) centimeter-level accuracy. Applying precise ionospheric corrections from regional networks with a station spacing of a few hundreds of kilometers has been shown to provide almost-instantaneous positioning solutions based on GPS dual-frequency data [2, 4–6]. The establishment of such dense networks, however, is not highly attractive because of the cost and complex operation requirements involved, and is also difficult or even impossible in certain areas.

With the current proliferation of GNSS systems, the availability of more satellites paves the way for further improvements to PPP-RTK ambiguity resolution and positioning based on the ionosphere-float model, i.e., the model which parameterizes the ionospheric delays as completely unknown parameters. In general, combining systems brings an improved satellite geometry that translates into reduced convergence times, as was demonstrated for GPS and BeiDou [7], GPS and Galileo [8, 9], three-system GPS, Galileo and BeiDou [10, 11], four-system GPS, Galileo, BeiDou and GLONASS [12, 13], and five-system GPS, Galileo, BeiDou, GLONASS and QZSS [14].

It is also expected that the ambiguity resolution capabilities will improve due to the plethora of frequencies that the GNSS systems provide. In particular, the integration of multi-frequency data increases the model's redundancy and provides a stronger positioning model, which will improve ambiguity resolution and, therefore, the user convergence. Experimental studies have demonstrated that the addition of a third frequency (GPS L5, Galileo E5b, BeiDou B3) reduces the time-to-fix-ambiguities and convergence times using data from GPS [15], Galileo [16, 17], GPS and Galileo [9], Galileo and BeiDou [18], GPS, BeiDou, Galileo and QZSS combined [19].

Further, the use of data in more frequencies allows, in contrast with the dual-frequency case, for estimating functions of receiver and satellite code biases without making use of an ionospheric model, as is the usual GNSS practice [20]. Thus, to fully exploit the multi-frequency data and ensure that the users benefit the most in terms of speeding up conver-

gence, satellite code bias corrections need to be provided to the users. One may also opt to treat them as unknown time-stable parameters without experiencing the advantages of correcting for the code biases. The reason for this lies in the fact that the code user equations in the third and following frequencies will mimic the carrier-phase equations in the sense that only when a sufficient change in relative receiver-satellite geometry takes place, will the contribution of the extra measurements be sensed.

Europe's Galileo satellite navigation system provides data on five frequencies from all in-orbit satellites for all users [21, 22]. Despite the public release of information needed to facilitate the development of E6-capable receivers [23], little attention has been given to the multi-frequency standalone Galileo ambiguity-resolved PPP performance using E6 to date. As demonstrated from Xin *et al.* [24], faster convergence was achieved with E6-aided triple-frequency ambiguity-fixed solutions, compared to the E1+E5a+E5b solutions. In supporting their numerical evidence, they argued that this was due to the fact that the first triplet provides for the lowest noise amplification factor of the wide-lane observables. In addition, preliminary efforts have been made to investigate the integration of all available Galileo frequencies. Based on (extra) widelane measurement combinations, Li *et al.* [25] showed that using five frequencies reduces the *static* positioning convergence times to 15 min, on average. In an epoch-by-epoch data processing of Galileo-only uncombined measurements with ambiguity resolution, Geng and Guo [26] showed that an instant position accuracy of about 20 cm can be achieved in the horizontal components with 5–6 observed satellites. Using prior ionospheric information and the BIE estimator [27], Laurichesse and Banville [28] showed an improved PPP-RTK user ambiguity resolution performance by combining multiple Galileo frequencies.

Despite the promising results of the aforementioned studies, we believe that a thorough insight into the performance gain as a function of the number and spacing of frequencies has not been provided yet. It is observed that when selecting additional frequencies to improve PPP-RTK ambiguity resolution, it is usually the precision or the wavelength of the wide-lane observables that are taken into account, see, e.g., [16, 18, 24, 29], instead of the overall success rate, which is an objective measure of the ambiguity resolution quality. Moreover, a sub-optimal strategy commonly used in the literature regarding the satellite code biases is either to neglect them or to estimate the combined receiver and satellite code biases as unknown time-constant parameters, see, e.g., [24–26, 30], thereby lacking the convergence acceleration capability in the presence of such available corrections. Therefore, these intricacies of multi-frequency PPP-RTK have not been explored in detail and need further attention. Moreover, an exhaustive assessment of the user's Galileo ambiguity-resolved *kinematic* performance with up to five frequencies has not been analyzed yet in terms of its convergence times, for both standalone and combined-system forms.

In this contribution, we focus on Galileo multi-frequency, ionosphere-float, kinematic PPP-RTK using uncombined observations on up to five frequencies and satellite code bias corrections to strengthen the user's model. We present a formal analysis of the user ambiguity resolution capabilities for an increasing number of frequencies up to five, and shed light on the role of the number and spacing of frequencies in ambiguity resolution. Further, we provide numerical insight into what extent multiple frequencies can reduce the user's convergence times using real Galileo data in Australia and a large number of

ambiguity-resolved positioning solutions. Finally, we numerically explore the PPP-RTK user capabilities of the combined Galileo+GPS model in achieving rapid centimeter-level positioning in the absence of prior ionospheric information.

This contribution is organized as follows. Section 5.2 introduces our underlying observation model, estimable parameters and experimental setup. In Section 5.3, we present and analyze the formal and real Galileo data results regarding the ambiguity resolution and positioning capabilities, with a focus on the number and spacing of frequencies, and then we show whether instantaneous convergence is feasible with the combined Galileo+GPS model. We conclude in Section 5.4.

5.2 Processing strategy

5.2.1 Observation model

Let us commence our discussion with the multi-frequency network model to understand the PPP-RTK estimability. For the observed-minus-computed (O-C) phase ($\Delta\phi^s_{r,j}$) and code ($\Delta p^s_{r,j}$) observations of a receiver r tracking satellite s on frequency j, the single-system, uncombined, multi-frequency, linearized observation equations are formulated as [31]:

$$\begin{aligned} E(\Delta\phi^s_{r,j}) &= g_r^{s\mathrm{T}}\Delta x_r + dt_r - dt^s + m^s_r\tau_r - \mu_j\iota^s_r + \lambda_j(\delta_{r,j} - \delta^s_{,j} + a^s_{r,j}) \\ E(\Delta p^s_{r,j}) &= g_r^{s\mathrm{T}}\Delta x_r + dt_r - dt^s + m^s_r\tau_r + \mu_j\iota^s_r + (d_{r,j} - d^s_{,j}) \end{aligned} \tag{5.1}$$

where $r = 1,\ldots,n$ is the receiver index with n being the number of network receivers, $j = 1,\ldots,f$ is the frequency index, with f being the number of frequencies, and $s = 1,\ldots,m$ is the satellite index, with m being the number of satellites. Here and in the following, the O-C observations are assumed to include the precise orbital corrections. The position increment Δx_r is linked to the observations through the receiver–satellite direction vector g^s_r. The common receiver and satellite clock parameters are denoted with dt_r and dt^s, respectively. The zenith tropospheric delay (ZTD) for receiver r, after removing the a priori value, and its mapping function for receiver r and satellite s, are represented by τ_r and m^s_r, respectively. The first-order slant ionospheric delay experienced between the receiver r and satellite s on the first frequency is denoted by ι^s_r, and its linkage to the observations is done through the coefficient $\mu_j = \lambda_j^2/\lambda_1^2$ that depends on the wavelength λ_j. $\delta_{r,j}$ and $\delta^s_{,j}$ stand for the receiver and satellite phase biases, respectively, while $d_{r,j}$ and $d^s_{,j}$ denote those for the code observations, respectively. The integer phase ambiguity is represented by $a^s_{r,j}$. Apart from $\delta_{r,j}$, $\delta^s_{,j}$ and $a^s_{r,j}$, which are expressed in units of cycles, the rest of the parameters are all expressed in units of range. $E(\cdot)$ denotes the expectation operator.

This network system of GNSS observation equations is rank-deficient as the information content is not sufficient to determine the absolute parameters, but only estimable functions of them. The underlying rank deficiencies of the network model can be solved through the application of the S-system theory [32, 33]. Given that the common clocks pivot receiver S-basis is selected [3], and assuming that the network receivers' positions

are precisely known, the full-rank network model reads:

$$E(\Delta\phi^s_{r,j} - g_r^{s\mathrm{T}}\Delta x_r) = d\tilde{t}_r - d\tilde{t}^s + m^s_r\tau_r - \mu_j\tilde{\imath}^s_r + \lambda_j(\tilde{\delta}_{r,j} - \tilde{\delta}^s_{,j} + \tilde{a}^s_{r,j}) \tag{5.2}$$
$$E(\Delta p^s_{r,j} - g_r^{s\mathrm{T}}\Delta x_r) = d\tilde{t}_r - d\tilde{t}^s + m^s_r\tau_r + \mu_j\tilde{\imath}^s_r + (\tilde{d}_{r,j} - \tilde{d}^s_{,j})$$

where the interpretation of the estimable parameters, denoted using the *tilde* ($\tilde{\cdot}$) symbol, the conditions for their existence, and the *S*-basis parameters are listed in Table 5.1. The table shows how the estimable parameters are formed as linear combinations of the original parameters with the parameters of the reference receiver $r = 1$, those of the reference satellite $s = 1$ and the satellite code biases on the first two frequencies. $(\cdot)_{,\mathrm{IF}}$ and $(\cdot)_{,\mathrm{GF}}$ stand for the 'ionosphere-free' and 'geometry-free' combinations of the parameters $(\cdot)$, respectively, in the first two defined frequencies (i.e., $j = 1,2$). Note that in the *S*-basis choice given here, the estimable code biases of the receivers ($\tilde{d}_{r,j}$) and satellites ($\tilde{d}^s_{,j}$) only exist on the third frequency and beyond ($j > 2$). As such, no estimable code biases exist for a dual-frequency setup given the presented full-rank model. In particular, it can be shown that this estimable satellite code bias is a function of the satellite *modernized* differential code bias (DCB) $d^s_{,1} - d^s_{,j}$ and the *legacy* DCB $d^s_{,1} - d^s_{,2}$:

$$\tilde{d}^s_{,j} = -\left[(d^s_{,1} - d^s_{,j}) - \frac{\mu_j - \mu_1}{\mu_2 - \mu_1}(d^s_{,1} - d^s_{,2})\right] + \left[(d_{1,1} - d_{1,j}) - \frac{\mu_j - \mu_1}{\mu_2 - \mu_1}(d_{1,1} - d_{1,2})\right] \tag{5.3}$$

Table 5.1: Estimable parameters and *S*-basis parameters of the single-system multi-frequency network model.

Parameter	**Interpretation**
Receiver clocks	$d\tilde{t}_r = dt_{1r} + d_{1r,\mathrm{IF}}; \quad r \neq 1$
Satellite clocks	$d\tilde{t}^s = (dt^s + d^s_{,\mathrm{IF}}) - (dt_1 + d_{1,\mathrm{IF}})$
Ionospheric delays	$\tilde{\imath}^s_r = \imath^s_r + d_{r,\mathrm{GF}} - d^s_{,\mathrm{GF}}$
Receiver phase biases	$\tilde{\delta}_{r,j} = \delta_{1r,j} + \frac{1}{\lambda_j}(\mu_j d_{1r,\mathrm{GF}} - d_{1r,\mathrm{IF}}) + a^1_{1r,j}; \quad r \neq 1$
Satellite phase biases	$\tilde{\delta}^s_{,j} = \delta^s_{,j} + \frac{1}{\lambda_j}\left(\mu_j[d^s_{,\mathrm{GF}} - d_{1,\mathrm{GF}}] - [d^s_{,\mathrm{IF}} - d_{1,\mathrm{IF}}]\right) - \delta_{1,j} - a^s_{1,j}$
Phase ambiguities	$\tilde{a}^s_{r,j} = a^s_{1r,j} - a^1_{1r,j}; \quad r \neq 1,\ s \neq 1$
Receiver code biases	$\tilde{d}_{r,j} = d_{1r,j} - (d_{1r,\mathrm{IF}} + \mu_j d_{1r,\mathrm{GF}}); \quad r \neq 1,\ j > 2$
Satellite code biases	$\tilde{d}^s_{,j} = [d^s_{,j} - (d^s_{,\mathrm{IF}} + \mu_j d^s_{,\mathrm{GF}})] - [d_{1,j} - (d_{1,\mathrm{IF}} + \mu_j d_{1,\mathrm{GF}})]; \quad j > 2$
S-basis parameters	$dt_1,\ d_{1,j},\ \delta_{1,j},\ a^s_{1,j},\ a^1_{r,j},\ d_{r\neq1,j=1,2},\ d^s_{,j=1,2}$

$(\cdot)_{,\mathrm{IF}} = \frac{1}{\mu_2-\mu_1}[\mu_2(\cdot)_{,1} - \mu_1(\cdot)_{,2}];\ (\cdot)_{,\mathrm{GF}} = -\frac{1}{\mu_2-\mu_1}[(\cdot)_{,1} - (\cdot)_{,2}];\ (\cdot)_{ij} = (\cdot)_j - (\cdot)_i.$

In practice, this means that when GNSS observations in more than two frequencies are available, one is able to directly estimate combinations of the modernized satellite and legacy DCBs needed for multi-frequency user processing, without the explicit need for a prior ionosphere model as is the usual GNSS practice.

From the estimated network parameters, the ones that are essential for realizing PPP-RTK are the estimable variants of the satellite clocks, satellite phase biases and satellite code biases ($f > 2$). In their combined form, these corrections for the phase ($\hat{c}^s_{\phi,j}$) and code ($\hat{c}^s_{p,j}$) observations read:

$$\hat{c}^s_{\phi,j} = d\hat{\tilde{t}}^s + \lambda_j \hat{\tilde{\delta}}^s_{,j} \tag{5.4}$$
$$\hat{c}^s_{p,j} = \begin{cases} d\hat{\tilde{t}}^s & j = 1,2 \\ d\hat{\tilde{t}}^s + \hat{\tilde{d}}^s_{,j} & j > 2 \end{cases}$$

Given the correction-component (5.4), the full-rank user's model follows from the network counterpart (5.2), and the estimability and interpretation of the user's parameters is automatically obtained from the user version of those in Table 5.1 (with index $r = u$):

$$E(\Delta\phi^s_{u,j} + \hat{c}^s_{\phi,j}) = g_u^{s\mathrm{T}}\Delta x_u + d\tilde{t}_u + m^s_u \tau_u - \mu_j \tilde{\imath}^s_u + \lambda_j(\tilde{\delta}_{u,j} + \tilde{a}^s_{u,j}) \tag{5.5}$$
$$E(\Delta p^s_{u,j} + \hat{c}^s_{p,j}) = g_u^{s\mathrm{T}}\Delta x_u + d\tilde{t}_u + m^s_u \tau_u + \mu_j \tilde{\imath}^s_u + \tilde{d}_{u,j}$$

The main difference is that, in the user component, the position increment is estimated as an unknown parameter. We remark here that, in both network and user components, the ionosphere-float model is used, which treats the slant ionospheric delays as completely unknown parameters both spatially and temporally. It is also important to state here that user ambiguity-resolved positioning can be performed even without using the satellite code biases as standard network corrections. The drawback of this approach is that one should estimate, instead of $f-2$ receiver code biases in the presence of such corrections, $(f-2)m$ receiver-plus-satellite code biases (hereafter referred to as satellite code biases), thereby reducing the redundancy of one's model by $(f-2)(m-1)$. In such a case, the estimability and interpretation of the satellite code biases (compare with Table 5.1) read as follows:

$$\tilde{d}^s_{u,j} = [d_{u,j} - (d_{u,\mathrm{IF}} + \mu_j d_{u,\mathrm{GF}})] - [d^s_{,j} - (d^s_{,\mathrm{IF}} + \mu_j d^s_{,\mathrm{GF}})];\ j > 2 \tag{5.6}$$

In this contribution, we make use of the estimated satellite code biases allowing the multi-frequency user code data to properly contribute to the user solution, thereby improving the ambiguity resolution and positioning performance.

The stochastic model, as encapsulated in the variance–covariance (vc-) matrix of the measurements, is given as:

$$D\left(\begin{bmatrix}\Delta\phi_r \\ \Delta p_r\end{bmatrix}\right) = \mathrm{blkdiag}(C_{\phi\phi}, C_{pp}) \otimes W^{-1} \tag{5.7}$$

where $\Delta\phi_r = [\Delta\phi^1_{1,1},\ldots,\Delta\phi^m_{1,1},\ldots,\Delta\phi^1_{n,1},\ldots,\Delta\phi^m_{n,1},\ldots,\Delta\phi^1_{1,f},\ldots,\Delta\phi^m_{1,f},\ldots,\Delta\phi^1_{n,f},\ldots,\Delta\phi^m_{n,f}]^{\mathrm{T}}$ is the phase measurement vector. Similarly, Δp_r stands for the code measurement vector. The $f \times f$ matrices $C_{\phi\phi}$ and C_{pp} are, respectively, (co)variance matrices of the phase and code observable types in zenith. The $mn \times mn$ matrix $W = \mathrm{diag}(w^1_1,\ldots,w^m_1,\ldots,w^1_n,\ldots,w^m_n)$ contains the weights for every network receiver–satellite link. For simplicity, the interpretation of the network parameters in Table 5.1 and the definition of the weight matrix

W are based on the all-in-view case, i.e., when all n receivers of the network track all the m satellites. This stringent assumption does not apply in our implemented algorithm, which considers the minimum spanning tree concept [34] for processing the data of widely distributed receivers. Moreover, we have assumed that the network receivers provide measurements of the same quality (cf. 5.7), but this, of course, does not affect the generality of our analysis. $D(\cdot)$ denotes the dispersion operator and $\otimes$ the Kronecker product. The notations diag and blkdiag represent a 'diagonal' and a 'block-diagonal' matrix, respectively. The user's stochastic model follows automatically from the user version of (5.7), assuming that the network corrections are sufficiently precise that they can be assumed to be deterministic.

5.2.2 Experimental setup

In this study, the processing is performed using 30-s Galileo code and phase observations on E1, E5a, E5b, E5 and E6, collected by continuously operating reference stations (CORS) belonging to the Australian Regional GNSS Network (ARGN) on three days starting from DOY 166 of 2020, which is an arbitrary choice. The geographic distribution of the 17 network stations for the estimation of network corrections and of the seven user stations for PPP-RTK positioning is shown in Figure 5.1. All stations are equipped with Septentrio PolaRx5 receivers, which are able to track all five frequency signals of Galileo. The cut-off elevation mask for all the data analysis in this work is set as 10°.

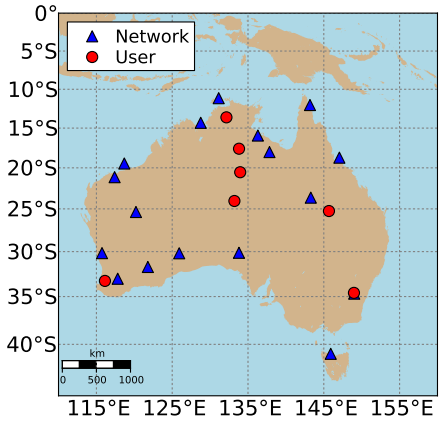


Figure 5.1: Geographic distribution of the network (blue triangles) and user (red circles) stations used for the Galileo PPP-RTK data processing.

In our analysis, the precise Galileo satellite orbits calculated by the Centre for Orbit Determination in Europe (CODE), as part of the Multi-GNSS Experiment (MGEX) [35], were used as the known parameters for both network and user components. The ground-truth coordinates of the stations were retrieved from Geoscience Australia [36] and were used as

known parameters in the network processing, while in the user processing they served as a means of evaluating the positioning errors. Concerning the receiver and satellite phase center offsets (PCOs) and variations (PCVs) for our network and user processing, we used the official antenna calibration file (igsR3_2107.atx: provided by Dr. Arturo Villiger from the Astronomical Institute of the University of Bern) used in the 3rd International GNSS Service (IGS, [37]) data reprocessing campaign. The selection of network and user stations was based on the availability of multi-frequency calibration information for the antennas that the stations are equipped with. In addition, a priori ZTD corrections are computed based on Saastamoinen's model [38] with the Ifadis tropospheric mapping function [39]. The observation weights of the satellite s were calculated using the natural exponential function $\exp(\cdot)$ based on the elevation angle β_r^s (in degrees) [40]:

$$w_r^s = \left(1 + 10\exp\left(-\frac{\beta_r^s}{10}\right)\right)^{-2} \tag{5.8}$$

In both network and user data processing, the estimable parameters listed in Table 5.1 are estimated in a Kalman filter, the initialization of which is performed with a standard least-squares estimation based on the data of the first epoch. The phase ambiguities, receiver/satellite phase and code biases are assumed to be time-constant, while the temporal behaviour of the ZTDs is modeled by a random-walk process with system noise of $0.1\ \text{mm}/\sqrt{30\,\text{s}}$. The position components, receiver/satellite clocks and slant ionospheric delays are assumed to be completely unlinked in time. Therefore, our user processing is restricted to kinematic-only processing, while no prior spatial or temporal ionospheric information is used. The uncombined code and phase data were empirically assigned with a zenith-referenced standard deviation (STD) of 30 cm and 3 mm, respectively, which is a reasonable choice for most applications [41]. For the detection and identification of outliers, such as phase slips, we made use of the recursive Detection, Identification and Adaptation (DIA) procedure [42]. We remark here that the data in both network and user components are processed in emulated real-time mode, since only forward filter processing is performed.

After computing the ambiguity-float solutions in the Kalman filter, the user's double-differenced ambiguities are decorrelated and fixed to their integers with the integer least-squares (ILS) estimator, which is efficiently mechanized in the Least-squares AMBiguity Decorrelation Adjustment (LAMBDA) method [43]. As a measure for successful ambiguity resolution, we use the formal integer bootstrapping (IB) success rate, which lower bounds the success rate of the optimal ILS estimator [44]:

$$P(\check{a}_{\text{ILS}} = a) = P(\check{z}_{\text{ILS}} = z) \geq P(\check{z}_{\text{IB}} = z) = \prod_{i=1}^{f(m-1)} \left(2\Phi\left(\frac{1}{2\sigma_{\hat{z}_{i|I}}}\right) - 1\right) \tag{5.9}$$

with $\Phi(x)$ denoting the cumulative normal distribution function:

$$\Phi(x) = \int_{-\infty}^{x} \frac{1}{\sqrt{2\pi}} \exp\left(-\frac{u^2}{2}\right) du \tag{5.10}$$

where $P(\cdot)$ denotes the formal ambiguity success rate; a and z denote the vectors of true but unknown original and transformed ambiguities, respectively, while the use of $\check{}$-symbol

indicates the determined integers; $\sigma_{\hat{z}_{i|I}}$ with $I = i+1,\ldots,f(m-1)$ stands for the conditional standard deviations of the decorrelated ambiguities, which are calculated as the square roots of the entries of the diagonal matrix D after an $L^{\mathrm{T}}DL$-decomposition of the decorrelated ambiguity vc-matrix. In our analysis, we consider the ILS-based partial ambiguity resolution (PAR) strategy that defines the to-be-resolved ambiguity subset based on a minimum success rate [45] that is defined as equal to 99.9%.

5.3 Experimental results and analysis

5.3.1 Formal analysis

To obtain an understanding of the impact of the number and spacing of frequencies in standalone Galileo ambiguity resolution and an insight into the real data results presented in the next section, we formally analyze the user's ambiguity resolution performance.

Frequency spacing

Successful ambiguity resolution is key to the realization of PPP-RTK user positioning [4, 46]. As a measure to analyze the full-ambiguity resolution (FAR) capabilities of the Galileo multi-frequency model, we use the formal success rate in (5.9). The FAR success rate acts as an objective measure of the ambiguity resolution quality, and allows us to obtain a clear insight into the added value of the more-than-two frequencies and the importance of frequency separation in ambiguity resolution.

We remark here that in the multi-frequency analysis presented here and in the following, we use E1 and E5a as 'starting' frequencies. We reasonably consider this a natural choice for a multitude of reasons. First, the combination E1+E5a is the most commonly used dual-frequency combination in Galileo related studies, see, e.g., [8, 10, 12, 19], while these frequencies allow for the interoperability of GPS and Galileo in mixed-system positioning due to the overlapping frequencies L1/E1 and L5/E5a [47]. Moreover, most of the MGEX analysis centres provide E1/E5a-based ionosphere-free clock products for the Galileo satellites [48]. Last but not least, E1 and E5a serve as the *edge* frequencies of Galileo, since they are the ones that are most apart in the frequency domain, which allows us to observe several patterns, formed by the addition of extra frequencies in terms of frequency separation.

We start our analysis by selecting a single epoch on DOY 166 of 2020, where six Galileo satellites are visible from station MTCV (denoted as a user station in Figure 5.1). Figure 5.2 (left) shows the single-epoch, ionosphere-float, triple-frequency formal ambiguity success rates as a function of a varying third frequency. The first two frequencies are held constant to E1 and E5a, and we assumed a frequency-independent zenith-referenced code and phase formal precision of 30 cm and 3 mm, respectively. We show the location of the E6 signal in the figure for convenience in our discussion, while the locations of E5b and E5 are not shown for clarity, as they are very close to E5a. When compared to the almost zero success rate of the dual-frequency model at the same epoch, the figure shows that the addition of a third frequency can improve the success rate. However, it is clear that it is at such low levels that successful ambiguity resolution at a single epoch is not possible, indi-

cating the incapability of an ionosphere-float model to perform instantaneous ambiguity resolution with this setup.

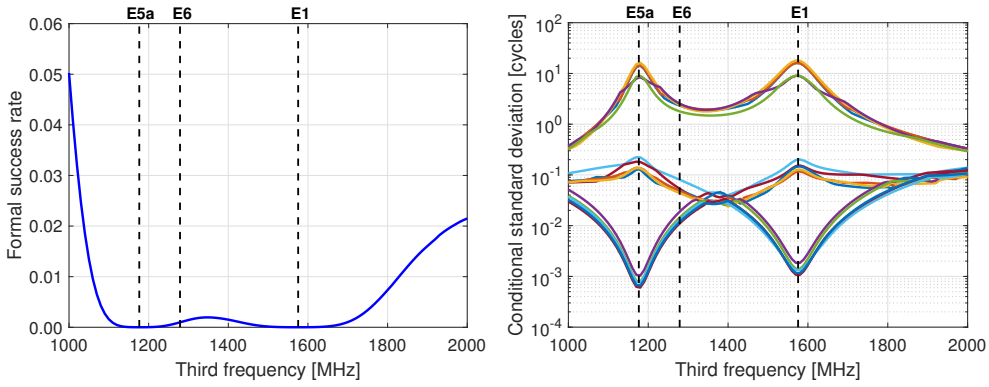


Figure 5.2: Single-epoch, ionosphere-float, triple-frequency FAR formal success rate (**left**) and conditional STDs of LAMBDA-transformed ambiguities (**right**) as function of a varying third frequency for six observed Galileo satellites on DOY 166 of 2020. Each color in the right panel denotes a different transformed ambiguity. The undifferenced code and phase STDs are fixed at 30 cm and 3 mm, respectively, at zenith. The results are obtained at the ARGN station MTCV. The first two frequencies are held fixed at the Galileo E1 and E5a values. The dashed vertical lines indicate the E1, E5a and E6 frequencies. The locations of E5b and E5 are not shown for clarity, as they are close to E5a.

To explain the signature of the success rate curve, we consider the conditional STDs of the LAMBDA-transformed ambiguities, which are provided by the square roots of the entries of the diagonal matrix D after an $L^{\mathrm{T}}DL$-decomposition of the decorrelated-ambiguity vc-matrix. We stress here that an analysis of the formal ambiguity STDs is far from sufficient to judge the ambiguity resolution performance. This would be possible only if the ambiguities were uncorrelated. Therefore, the precision of the transformed ambiguities, due to the decorrelation involved, can serve to explain the success rate curve to a good approximation. Figure 5.2 (right) shows the precision curves of the transformed ambiguities as a function of a varying third frequency. One can observe that some of the transformed ambiguities are of high precision, while others are of poor precision. As a result, the signature of the precision curves of the poorly determined ambiguities will dominate the typical shape of the success rate curve.

Further, Figure 5.2 shows that the success rate curve reaches its minimum values when the third frequency is selected to be at one of the two 'starting' frequencies, with these two minima being of the same order as the dual-frequency success rate. Although not distinguishable from the figure, we confirm that these two minima are not equal to zero, as would be the case for the rank-deficient dual-frequency model with two identical frequencies. The reason for this is that not all three frequencies are identical, which prevents us from a rank deficiency issue. The minima and maxima of the precision curves shown in the figure are explained as follows. When the third frequency is selected to be equal to the first one, i.e., $f_3 = f_1$, one is able to estimate the difference between the first- and third-frequency ambiguities using only the phase data, therefore with very high precision. The

case when $f_3 = f_2$ is similar. This explains the two minima in the higher-precision curves at the bottom of the graph. In these cases, however, there are also ambiguities that cannot be determined in a phase-only solution and require the presence of code data. It is, therefore, the poor precision of the code data that leads to high standard deviations and, therefore, to the two maxima shown in the lower-precision curves.

In addition, it is evident that the success rate gets larger with larger frequency separation and that an improved ambiguity resolution performance is expected if the third selected frequency is as far as possible from E1 and E5a. Identical conclusions have been drawn for GPS long-baseline ambiguity resolution [49]. Given that the overall success rate is an objective measure of the quality of FAR, one can conclude that the selection of E6 as the third frequency in E6-capable receivers, and of E5b in E6-non-capable receivers, would be more beneficial than others in achieving higher success rates.

From the results of Figure 5.2, it is clear that an increase in the number of frequencies from two to three, even with large frequency separation, does not really 'push' the single-epoch success rates closer to the ideal value of one. Therefore, we consider an increasing number of epochs and assess whether the impact of number and spacing of frequencies is more pronounced. In our multi-epoch model, we consider the receiver phase biases, receiver code biases and phase ambiguities as time-constant parameters, while the other parameters are treated as being unlinked in time. The multi-epoch triple-frequency success rate curves as a function of a varying third frequency and a varying number of considered epochs are shown in Figure 5.3 (left). Note that these results are linked to the selected 30 s sampling rate, while the use of a higher data rate would improve the user performance. Although ambiguity resolution benefits from a low sampling rate due to the greater change in receiver-satellite geometry as times goes on, a higher sampling rate leads to a model of higher strength within the same timespan.

First, the results in Figure 5.3 (left) show that higher FAR success rates can be achieved by increasing the number of epochs and depict how the former is driven by the selection of the third frequency. The dual-frequency success rates are also shown in the figure with horizontal dashed lines. Compared to the dual-frequency performance, one can observe that, with an additional frequency, one ends up with higher FAR success rates, with the improvement being more prominent with an increased number of epochs. Regarding frequency separation, one clearly observes its distinct effect in the multi-epoch setup, with the addition of a third frequency far away from E1 and E5a being able to considerably increase the user success rate. As an example, the success rate would be equal to about 50% by selecting E5b as the third frequency after 20 epochs, while this would increase to 80% by selecting E6. After 30 epochs, the success rates would be 82% and 95%, respectively. Thus, we observe that the impact of increased number of frequencies is heavily pronounced in the first epochs, while it is rather modest after a considerable amount of accumulated epochs, since the model is already strong.

The above results underline the importance of an increased number of frequencies, which can boost the user ambiguity resolution capabilities. In achieving the highest possible FAR success rates, the user should opt for signals with frequencies that are as far as possible from the two 'starting' ones. Since a considerable amount of time is needed to achieve reliable FAR with a success rate higher than 99.9%, we opt to fix only a subset of the ambiguities with the same criterion in order to obtain a considerable precision gain in

shorter time. In the top-right panel of Figure 5.3, we present the positioning precision gain after successful PAR as the ratio of the float and fixed horizontal positioning precision, as a function of a varying third frequency and an increasing number of epochs. We reasonably opt to show the precision gain after PAR, rather than the formal success rate, as done in FAR, because the PAR success rate, by definition, is larger than 99.9%, and therefore not sufficient to show the contribution to the user performance.

The results in the top-right panel of Figure 5.3 confirm that frequency separation plays a dominant role also in PAR-based user performance, as the further the third frequency is from the 'starting' frequencies, the larger the gain. With an increased number of epochs involved, we see an increase in the position precision gain as well, due to the fact that more ambiguities become precise enough to be included in the fixable PAR-subset. We make clear, however, that no direct comparison of the precision-gain curves can be made, since the gains depend on the ambiguity-float horizontal position precision that also improves with more epochs. This becomes clear if one observes the 30- and 60-epoch precision gain curves that are shown with the blue and purple color, respectively. Although one would intuitively think that a larger gain should be expected when 60 epochs are used, the achievable gain with 60 epochs is smaller than the one with 30 epochs because of the higher precision of the 60-epoch-based ambiguity-float position solution. We recall here that, over a sufficiently large time interval, the ambiguity-float solution will share the same quality as the ambiguity-fixed counterpart, leading to a gain value of 1, because the former becomes more precise over time.

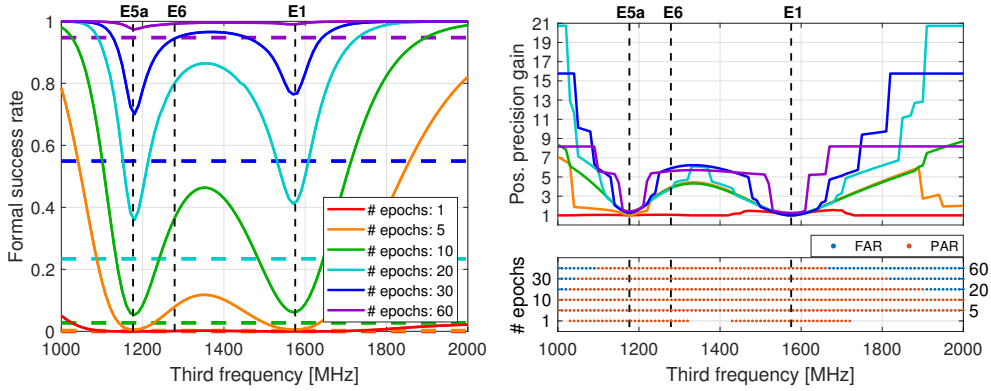


Figure 5.3: Multi-epoch, ionosphere-float, triple-frequency user ambiguity resolution performance as function of a varying third frequency and a varying number of used epochs for six observed Galileo satellites on DOY 166 of 2020: (**Left**) formal FAR success rate for triple- (solid lines) and dual-frequency (horizontal dashed lines) models; (**Right-top**) horizontal positioning precision gain after successful PAR; (**Right-bottom**) availability of successful FAR and PAR (when the success rate threshold is exceeded). The success rate criterion to indicate successful FAR/PAR is 99.9%. The undifferenced code and phase STDs are fixed at 30 cm and 3 mm, respectively, at zenith. The results are obtained at the ARGN station MTCV. The first two frequencies are held fixed at the Galileo E1 and E5a values. The dashed vertical lines indicate the E1, E5a and E6 frequencies

Note that a precision gain value of 1 indicates that either ambiguity resolution cannot be reliably executed, leaving the user only with a float solution, or that the ambiguity-resolved performance is equivalent to the ambiguity-float counterpart. The bottom-right panel of Figure 5.3 shows the availability of successful FAR and PAR for a varying third frequency, that is, when the success rate criterion of 99.9% is exceeded. It is very interesting to note that PAR is shown to be feasible in an instant for frequencies between E1 and E5a, including those of E5b, E5 and E6. However, the corresponding precision gains are shown to be equal to approximately 1. To understand the underlying reasons for this behaviour, we conducted an inspection of the conditional standard deviations of the transformed ambiguities and the LAMBDA Z-transformation matrix. For all the frequencies between E1 and E5a, we found out that the fixable ambiguities are widelane-like ones, while when the third frequency is closer to E1 or E5a (e.g., E5 and E5b), only the extra-wide-lane ambiguities are fixable. It is shown, therefore, that fixing these widelanes hardly improves the partially-fixed positioning precision, thereby the value of 1.

It is worth mentioning here that although we focused on Galileo and its existing frequencies in our formal analysis, the concept and results discussed above are generally applicable to any GNSS system and can easily serve to show the achievable gain after ambiguity resolution when more than two frequencies are employed, e.g., with BeiDou-3 multi-frequency data.

More frequencies, shorter convergence time ?

The question that comes now naturally to the fore is how much time is representatively needed to achieve reliable partially-fixed solutions based on the number and spacing of frequencies. To do so, we compute multiple hourly Galileo-only Kalman-filtered kinematic user positioning solutions with PAR in a formal analysis setup. Based on the conclusions of the previous section, it would make sense to consider E6 as the third frequency when operating with an E6-capable receiver, while E5b should be considered with other receivers. For compactness in our study, and due to the fact that only a minority of receivers currently support E6, we naturally consider E5b as the third frequency, E5 as the fourth, and E6 as the fifth. In such a setup, we are able to present results that are representative of an E6-non-capable receiver, as well as results for the current and future E6-capable ones with the further addition of E6. As the combination E1+E5a+E6 was shown to be the natural triple-frequency choice in an E6-capable receiver in the ambiguity resolution sense, we decide to also show results for this combination for completeness.

The timespans needed for the formal horizontal positioning precision values (90% percentiles) to be better than 10 cm are listed in Table 5.2. One can observe that the convergence time of the formal solutions is improved with an increased number of frequencies. It is further seen that the dual-frequency user enjoys a considerable improvement by adding E5b, but a much smaller increase after adding E5 as the fourth frequency, due to the small frequency spacing between E5 and the involved signals.

Table 5.2: Time span (in minutes) needed for the standalone Galileo, multi-frequency, ionosphere-float, PAR-based, kinematic PPP-RTK user models to obtain formal positioning precision better than 10 cm in 90% of the cases, with and without the provision of satellite code bias corrections.

	Provision of Satellite Code Biases	**Estimating Satellite Code Biases**
E1+E5a+E5b	17.5	18.0
E1+E5a+E5b+E5	16.0	18.0
E1+E5a+E6	13.0	13.0
E1+E5a+E5b+E5+E6	12.0	12.5

The corresponding time span for the standalone Galileo dual-frequency solution is 31.0 min. Satellite code biases are treated, when estimated, as time-constant parameters.

With the further integration of E6, which was previously shown to significantly boost the user ambiguity resolution capabilities due to its large spacing with the other frequencies, one easily notes a substantial decrease in the time needed to reach the 10 cm level. It is important to mention here that the E1+E5a+E6 triple-frequency integration outperforms the E1+E5a+E5b+E5 combination in the sense of fast successful ambiguity resolution, due to the fact that E6, compared to E5b and E5, has a larger frequency spacing from E1 and E5a. This underlines the pivotal role of frequency separation, since the user can achieve better performance with fewer frequencies, given that they are widely spaced. Therefore, when evaluating the user ambiguity-resolved performance, one should not only consider the number of frequencies involved but, even more importantly, the spacing between the already used and additional frequencies. In cases where all available Galileo signals are integrated, we observe that the convergence time is the shortest among all cases.

Impact of satellite code bias corrections

It is also of interest to gain insight into the role of the satellite code bias corrections in speeding up user convergence through the increased model redundancy. To do so, we compute the formal positioning solutions with the same settings as used previously, with the only difference being that the satellite code biases are estimated as time-constant parameters, instead of being corrected for. The results in Table 5.2 reveal that the provision of the satellite code biases brings a reduction of up to 2.0 min in the formal user-convergence (90% percentile). When the code precision improves, their contribution is expected to be larger, especially during the initial convergence that relies on the code data (cf. Section 5.3.1). It is interesting to see that the E1+E5a+E6 model requires the same timespan to reach 10 cm in both the presence and absence of satellite code biases, which is due to the frequency-dependent correlation of the latter with the user-ambiguities.

Figure 5.4 presents the correlation coefficient between the user-estimated satellite code biases and float ambiguities of a representative individual satellite as a function of a varying third frequency. The stated correlation is shown to range up to 0.65 (in magnitude). Moreover, it is observed that the correlation for E6 is smaller than that for E5b and E5. Therefore, one expects that the provision of the satellite code bias corrections will have a stronger impact on user ambiguity resolution and convergence performance when E5 or E5b is selected as the third frequency than when E6 is used.

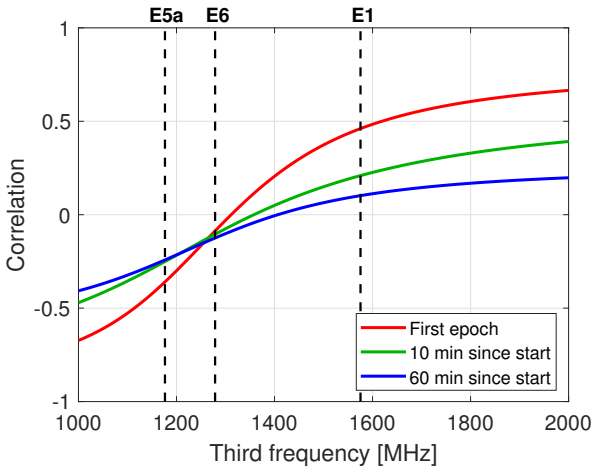


Figure 5.4: Correlation coefficient between the user-estimated satellite code biases and phase ambiguities as function of a varying third frequency and varying time instances since the processing start. The results correspond to Galileo satellite E07 and are obtained at the ARGN station MTCV. The first two frequencies are fixed at the Galileo E1 and E5a values. The dashed vertical lines indicate the E1, E5a and E6 frequencies.

5.3.2 Empirical analysis

In this section, we use real data to verify the formal analysis findings and assess the empirical user convergence times of multi-frequency Galileo-only and Galileo+GPS PPP-RTK positioning.

Network corrections

We first estimate with a Kalman filter the network corrections needed to realize single-receiver, multi-frequency PPP-RTK positioning in real-time. These corrections consist of the satellite clocks, satellite phase (SPBs) and code biases (SCBs). We chose to determine the estimable code biases, rather than obtaining DCBs from an external source as in Li *et al.* [50], in order to have a consistent estimation of the highly correlated PPP-RTK corrections. Based on our observation model and chosen S-basis (cf. Section 5.2.1), as well as a rigorous integration of the network's redundant data, we estimated SPBs on all five frequency signals and SCBs on the higher-than-two frequencies, which are E5b, E5 and E6 in our case. That is, we selected E1 and E5a as the 'starting' frequencies so that our estimable satellite clocks were similar to those of most MGEX analysis centres. The estimable SCBs are observable-specific signal biases and can be directly applied to the uncombined code data from the third frequency onwards to strengthen the user's model. For brevity, we hereafter present only the SCB estimates.

Figure 5.5 presents the multi-frequency code bias estimates of the Galileo satellites on DOY 166 of 2020. It can be seen that the code biases of all satellites show, after their initial convergence period, remarkable time-stability. Moreover, one can observe another interesting feature of the E5b and E5 SCBs. For most of the Galileo satellites the E5b and E5 code biases fluctuate within a narrow range of about 50 and 25 cm, respectively. Given

that these estimable satellite code biases are functions of the modern and legacy DCBs (cf. 5.3), and due to the magnitude of the coefficient $(\mu_j - \mu_1)/(\mu_2 - \mu_1)$ of one of them that is close to the value one for these frequencies, one may reasonably conclude that the *absolute* satellite code biases on E5a, E5b and E5 are almost identical. As a result, the satellite DCBs between E5b and E5 signals are almost zero, as also shown in Li *et al.* [50]. The only exception to this case is satellite E24, for which a code bias of larger magnitude is seen, while high differential biases have also been reported earlier in Ammar *et al.* [51]. In the case of E6, we observe that the satellite code biases do not fluctuate within a narrow range, unlike E5b and E5, indicating that the satellite DCBs between E6 and the other signals are not equal to zero. For the same reason as before, the E6 code bias of satellite E24 shows a large offset compared to those of the other satellites.

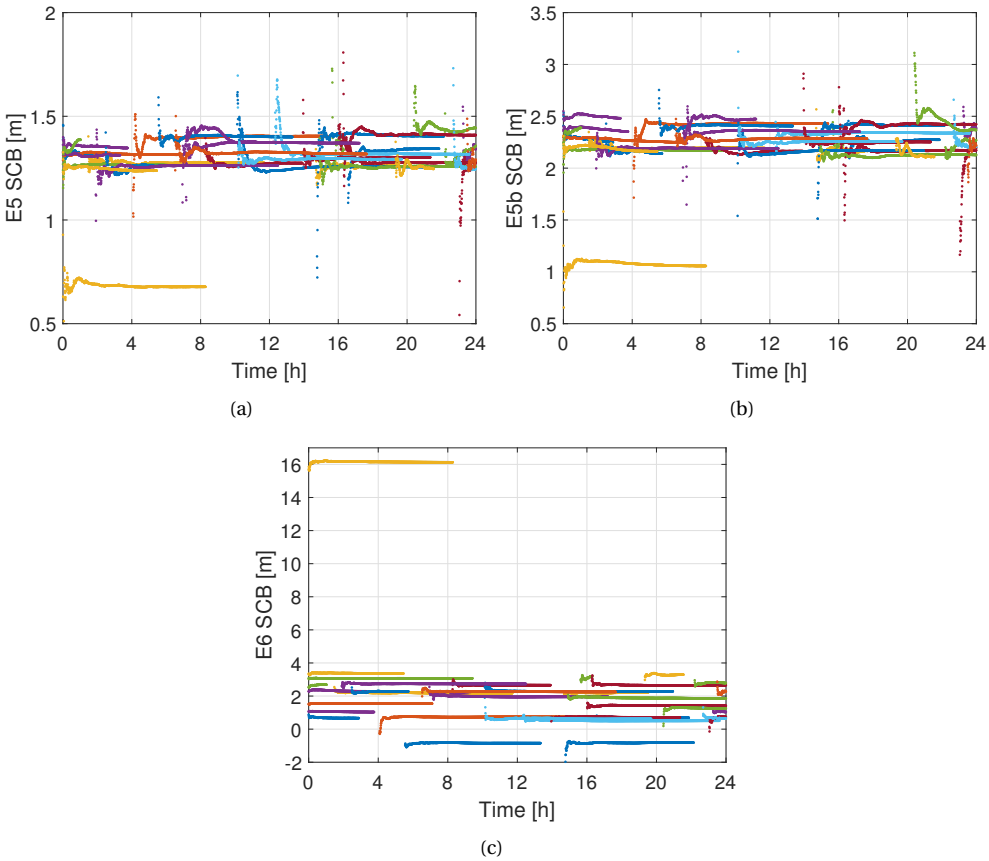


Figure 5.5: Multi-frequency Galileo satellite code bias estimates on E5 (**a**), on E5b (**b**) and on E6 (**c**) for all observed satellites above 10° on DOY 166 of 2020. Each color represents a different satellite.

Galileo-only PPP-RTK positioning

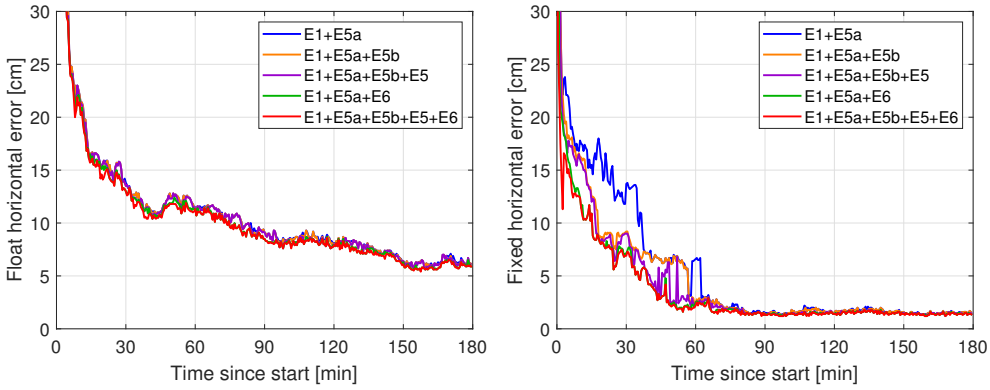
With the network-derived multi-frequency satellite corrections applied in the code and phase data (cf. 5.5), the user positioning performance, in terms of the achieved convergence times, is analyzed using real data from the seven user stations shown in Figure 5.1. The user-processing strategy was discussed in Section 5.2.2. To infer the empirical distribution of the achieved convergence times and realistically judge the standalone Galileo multi-frequency performance, we aimed to obtain a representative sample of solutions. We did this by processing the Galileo data of all user stations with a 3-h processing window being re-initialized every minute over the selected three days so as to capture all possible receiver-satellite geometries. The user's positioning errors were computed using precise benchmark coordinates and sorted for each epoch according to their absolute magnitude. From this set, we then identified the mean, 50% and 90% percentile values of the horizontal and vertical errors, resulting into convergence curves that are used in the following to characterize the user's achieved performance. We remark here that convergence time, in this study, is defined as the time interval needed for the horizontal and vertical positioning errors to go below and stay below 10 cm (or 5 cm). Note also that the 'starting' frequencies used are E1 and E5a, while the multi-frequency models are based on integrating first E5b and then E5 to obtain results for E6-non-capable receivers, and later E6 to cover the E6-capable receivers. For the sake of completeness, we also show results for the E1+E5a+E6 solution, as in Section 5.3.1.

Figure 5.6 shows the convergence behaviour of the standalone Galileo multi-frequency ambiguity float (left panel) and PAR-fixed (right panel) kinematic horizontal radial positioning errors, whereas those for the vertical errors are not shown for brevity, but their achieved convergence times in both ambiguity float and fixed setups are listed in Table 5.3. The ambiguity-float solutions, with time-constant ambiguities, gain a high accuracy over time, because the float ambiguities become more precise over time and, as a result, the positioning accuracy is dictated by the very precise phase data. Adding more frequencies to the system seems to bring only slight improvements, with similar results being shown in Guo *et al.* [29], due to the invariance of satellite geometry [52]. It is clear that the float solutions do not converge to 5 cm within the first 3 h, and the results in Table 5.3 reveal that more than 1 h is needed for the horizontal errors to go below and stay below 10 cm for all multi-frequency solutions.

Moving from the float solutions in the left panel to the fixed solutions in the right panel of Figure 5.6, a performance gain via ambiguity resolution is evident. In particular, considering the model-driven PAR strategy for resolving the integer ambiguities, we observe a rapid decrease in the horizontal positioning errors, with the dual-frequency solution going below and staying below 10 cm after 37 min, which is an about 56% improvement compared to the float solution. When the model is of sufficient strength and all ambiguities are successfully fixed, a positioning accuracy of 1.5 cm is achieved on a continuous basis.

The integration of E5b as the third frequency seems to considerably improve the user's performance, as is also demonstrated in our formal analysis, with the reduction in convergence time being about 50% compared to the dual-frequency fixed solution, while the further addition of E5 leads only to a marginal improvement. This is due to the fact that, in the absence of E6, it is E5b that offers larger frequency separation than E5 in the triple-frequency setup. The additional inclusion of E5 does not boost the performance, as its

frequency is between and very close to the ones of E5a and E5b.



(a) Ambiguity-float solution

(b) Ambiguity-fixed solution

Figure 5.6: Convergence behaviour of the 90% percentiles of the horizontal radial positioning errors for standalone Galileo ambiguity-float (**a**) and PAR-based (**b**) kinematic PPP-RTK user positioning with an increasing number of frequencies of up to five. The results have been calculated on the basis of all user stations in 3-h time windows, re-initialized every 1 min within the selected days. The positioning errors were computed by comparing the estimated positions to precise benchmark coordinates. The PAR success rate criterion was set to 99.9%.

The transition to the penta-frequency solution considers the use of the E6 signal. We observe in Figure 5.6 that the PPP-RTK user benefits from the integration of all Galileo frequencies, as predicted by the formal analysis, since the time needed for the horizontal errors to go below and stay below 10 cm is 15 min, the shortest one among all multi-frequency models and 12% shorter than the four-frequency one. The main reason for this performance lies in the improved model strength with regard to ambiguity resolution, as a result of the frequency separation that E6 offers (cf. Section 5.3.1). An even greater improvement is seen for the convergence time to 5 cm, of about 26%, with the integration of E6. Shortened convergence times are also observed for the vertical component. Compared to the dual-frequency fixed vertical solution, the inclusion of the third, fourth and fifth frequency brings a convergence time reduction of 17%, 23% and 41%, respectively.

Figure 5.6 and Table 5.3 also show the achieved convergence time of the E1+E5a+E6 solution. Our formal analysis revealed that this is the triple-frequency combination that brings the largest benefit in terms of ambiguity resolution in E6-capable receivers, as shown here. Interestingly enough, we observe that the convergence curves of the E1+E5a+E6 and penta-frequency solutions almost overlap, with their 90% percentiles being equal, as was well predicted in our formal analysis (cf. Table 5.2). The penta-frequency solution seems to perform only slightly better when assessing the mean and 50% values. Thus, from a convergence point of view, the addition of E5b and E5 does not boost the E1+E5a+E6 solution, because of the vicinity of E5b and E5 to E5a and because the largest possible frequency spacing was already harnessed after integrating E6 with E1+E5a. This result confirms our formal analysis finding that the user ambiguity resolution capabilities are mainly driven by the frequency spacing and, to a smaller extent, by the number of additional frequencies.

Table 5.3: Convergence time (in minutes) of standalone Galileo, multi-frequency, ionosphere-float, kinematic PPP-RTK user positioning solutions to achieve horizontal and vertical accuracy better than 10 cm (and 5 cm in square brackets). The mean, 50% and 90% percentiles are provided.

	Horizontal			**Vertical**		
	Mean	**50%**	**90%**	**Mean**	**50%**	**90%**
Float						
E1+E5a	13.0 [67.0]	9.5 [34.5]	84.5 [-]	45.5 [132.0]	26.0 [74.5]	130.0 [-]
E1+E5a+E5b	13.0 [67.0]	9.5 [34.5]	84.5 [-]	45.5 [132.0]	26.0 [74.5]	127.5 [-]
E1+E5a+E5b+E5	12.5 [67.0]	8.5 [34.5]	84.5 [-]	45.0 [132.0]	25.5 [74.0]	127.5 [-]
E1+E5a+E6	12.5 [67.0]	8.5 [30.0]	75.0 [-]	45.0 [132.0]	25.5 [69.0]	127.5 [-]
E1+E5a+E5b+E5+E6	12.5 [67.0]	8.5 [30.0]	75.0 [-]	43.5 [105.0]	24.5 [69.0]	127.5 [-]
Fixed						
E1+E5a	12.5 [33.0]	8.0 [24.5]	37.0 [62.5]	35.0 [62.5]	22.0 [28.0]	64.0 [144.0]
E1+E5a+E5b	5.5 [18.0]	3.5 [15.5]	18.0 [57.0]	27.0 [52.5]	14.0 [22.5]	53.0 [144.0]
E1+E5a+E5b+E5	5.0 [17.5]	3.5 [14.0]	17.0 [52.5]	24.5 [48.5]	14.0 [21.5]	49.0 [120.5]
E1+E5a+E6	4.5 [15.5]	3.5 [10.0]	15.0 [39.0]	23.5 [38.5]	13.5 [19.5]	38.0 [83.0]
E1+E5a+E5b+E5+E6	3.5 [15.0]	2.0 [9.5]	15.0 [39.0]	20.5 [38.5]	13.0 [18.0]	38.0 [83.0]

The convergence time is defined as the timespan needed for the positioning errors to go below and stay below 10 cm (or 5 cm). The convergence times indicated with a dash denote that no convergence was achieved within the 3-h time windows. Note also that the mean, 50% and 90% percentiles were calculated on the basis of all user stations in 3-h time windows being re-initialized every 1 min within the selected days. The PAR success rate criterion was set to 99.9%.

As in our formal analysis, we consider it essential to provide numerical insight into the empirical user-convergence in the absence of satellite code bias corrections. As such, we process the multi-frequency Galileo data of all user stations with the same settings as used previously, but treating the satellite code biases as time-constant parameters. Table 5.4 lists the empirical convergence times (90% percentiles) of the multi-frequency models to achieve a horizontal error that is consistently below 10 cm. From the numerical results shown, one can observe that the multi-frequency PPP-RTK user-convergence benefits by applying externally provided satellite code bias corrections, as was well predicted by our simulations. Unlike the formal analysis results, we observe here that the E1+E5a+E6 solution benefits from external satellite code biases, despite the small correlation of user-estimated ambiguities and satellite code biases for E6. The small differences from the formal results (cf. Table 5.2) are due to the fact that the latter makes use of only the design and vc-matrices, not real data. We remark here that one can still perform ambiguity-resolved positioning in the absence of such corrections, but with a penalty in the achieved convergence times in the order of a few minutes. Note also that the stronger the user model is in terms of its ambiguity resolution capabilities, the less the convergence sensitivity becomes. From the results shown, one can conclude that the provision of the satellite code biases as standard corrections to multi-frequency PPP-RTK users is essential to fully exploit the user code data from the third and following frequencies, thereby accelerating convergence.

Table 5.4: Convergence time (in minutes) of standalone Galileo, multi-frequency, ionosphere-float, kinematic PPP-RTK user fixed horizontal positioning solutions (90% percentiles) with and without the provision of satellite code bias corrections.

	Provision of Satellite Code Biases	**Estimating Satellite Code Biases**
E1+E5a+E5b	18.0	22.0
E1+E5a+E5b+E5	17.0	21.0
E1+E5a+E6	15.0	16.0
E1+E5a+E5b+E5+E6	15.0	15.5

The convergence time is defined as the timespan needed for the positioning errors to go below and stay below 10 cm.

Galileo+GPS PPP-RTK positioning

Standalone Galileo was shown to be weak to support fast centimeter-level positioning with reliable integer ambiguity resolution in the presence of ionospheric delays. Our real data analysis demonstrated that its five-frequency signal integration is able to significantly speed up the user's convergence, with 90% of the computed horizontal positioning solutions requiring 15 min to reach an accuracy equal to or better than 10 cm. In this section, we investigate the feasibility of achieving rapid convergence with the integration of GPS data in an ionosphere-float setup, i.e., without any prior spatial or temporal information about the ionosphere. We focus here on the use of GPS dual-frequency data, since L5 is transmitted only by GPS Block IIF satellites.

The GPS network-derived positioning corrections were computed based on the same network that was used for the generation of the Galileo corrections, on the basis of the processing strategy in Section 5.2.2. In the next step, the GPS and Galileo network-derived positioning corrections were applied to correct the code and phase data of all user stations, and positioning solutions were obtained in 3-h time windows that were shifted and re-initialized every minute to obtain a representative sample of solutions. In this process, the user settings were identical to those of the standalone Galileo processing. Note also that, in the combined system analysis, the systems were treated separately, with only the receiver position increments and ZTD being common for the systems. That is, one reference satellite was taken per system, and not a common one across systems to exploit the overlapping frequencies. Given the computed solutions and the precise benchmark coordinates, the horizontal radial and vertical positioning errors were computed per epoch, from which the convergence curves are determined.

In the following, the positioning results of the combined model are visualized and further discussed. Figure 5.7 shows the mean, 50% and 90% percentiles of the partially-ambiguity-fixed positioning errors as a function of time for Galileo+GPS kinematic positioning. The benefit of integrating multi-GNSS multi-frequency data is evident. With the combined system, one can observe that fast and reliable ambiguity resolution can be achieved much faster than when using only Galileo data (cf. Figure 5.6), which is obvious from the significantly steeper convergence curves.

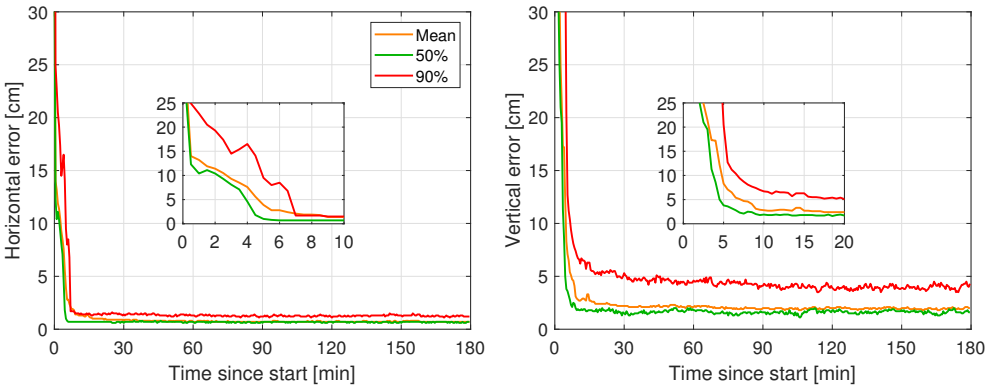


Figure 5.7: Convergence behaviour of the 90% percentiles of the horizontal radial (**left**) and vertical (**right**) positioning errors for combined Galileo E1/E5a/E5b/E5/E6 + GPS L1/L2 PAR-based kinematic PPP-RTK user positioning. The mean, 50% and 90% percentiles of positioning errors are shown with orange, green and red colors, respectively. The results have been calculated on the basis of all user stations in 3-h time windows that are re-initialized every 1 min within the selected days. The positioning errors were computed by comparing the estimated positions to precise benchmark coordinates. The zoom-in windows are used to depict the positioning errors for the horizontal and vertical components during the first 10 and 20 min, respectively. The PAR success rate criterion was set to 99.9%.

Making use of the provided zoom-in windows, we can observe that the mean and 90% percentiles of the ambiguity-fixed horizontal positioning errors become smaller than 10 cm after 3.0 and 5.0 min, respectively. This result shows the advantage of integrating GPS with Galileo data, as the average number of satellites increased from almost 7 in the Galileo-only setup to 16 in the combined-system setup. Therefore, we provide supporting evidence that rapid centimeter-level PPP-RTK positioning can actually be obtained with this combined model in the absence of any prior information for the ionosphere. This is of great importance for single-receiver users, as they can quite rapidly reach centimeter-level accuracy, even when they do not operate within a dense network of receivers, so that they benefit from regional ionospheric corrections (cf. [5, 6, 53]).

Such a gain in performance is also observed in the vertical positioning results. We observe that the vertical positioning errors are better than 10 cm after 7.0 min in 90% of cases, or after 5.0 min on average. The achieved vertical positioning accuracy, after convergence, is 4.3 cm. With these results in mind, we show that applications requiring fast high-accuracy results also in the vertical component can benefit from the combined system.

5.4 Conclusions

In this contribution, we studied and presented the key role of multiple frequencies in PPP-RTK ambiguity resolution and numerically demonstrated the multi-frequency, ionosphere-float, standalone Galileo kinematic PPP-RTK positioning performance for an increasing number of frequencies up to five. As more frequencies provide a stronger model

and, therefore, improved integer ambiguity resolution, we analyzed the role of the increasing number of frequencies, as well as their spacing, in speeding up the convergence times of kinematic users.

We started off with a detailed review of the PPP-RTK network and user observation models using uncombined, and therefore undifferenced, GNSS measurements. It was shown that, in the given *S*-basis choice, the receiver and satellite code biases become estimable for the third and following frequencies without the explicit use of a prior ionospheric model, as is the usual practice. We emphasized that the provision of the satellite code biases as standard PPP-RTK corrections, through the increased user's model redundancy, allows the multi-frequency user code data to properly contibute to the user solutions.

We then formally studied the user ambiguity resolution capabilities of the standalone Galileo multi-frequency model as a function of the number and spacing of frequencies. Using the full-ambiguity success rate as a tool to evaluate the ambiguity resolution performance, we showed that a single-epoch, ionosphere-float, triple-frequency PPP-RTK user model is too weak to support instantaneous ambiguity resolution. Although not very obvious in the single-epoch case, we demonstrated in the multi-epoch setup that frequency separation plays a dominant role in ambiguity resolution, as the further the third frequency is from the 'starting' two frequencies, the higher the success rate. Similarly, frequency separation was shown to have strong impact on the PAR-based positioning precision gain. It was, therefore, concluded that E5b would serve as the optimal third frequency choice in E6-non-capable receivers, while E6 would serve in E6-capable ones. Further, we computed multiple Kalman-filtered user solutions throughout a day to evaluate the formal user-convergence. It was found that increasing the number of frequencies can indeed accelerate convergence. More interestingly, we showed that frequency separation has a larger *weight* than the number of frequencies used in ambiguity resolution performance, which was evidenced by the fact that the E1+E5a+E6 solutions performed better than the E1+E5a+E5b+E5 counterparts, while the former had an almost identical performance with the E1+E5a+E5b+E5+E6 solutions.

In addition, the empirical ionosphere-float PPP-RTK user performance was assessed with real Galileo data from Australian stations on all five frequencies. In the prior step, that being the corrections' generation, we found that the satellite code biases have a remarkable time-stability, and we showed that the absolute code biases of E5a, E5b and E5 are almost identical. Given the satellite PPP-RTK corrections, we computed a representative sample of standalone Galileo positioning solutions for an increasing number of frequencies up to five to realistically judge the user's performance in terms of the achieved convergence times. We showed that the long convergence time of the dual-frequency ambiguity-float horizontal positioning errors to go below and stay below 10 cm was reduced from >1 h to 37.0 min (90% percentile) with PAR. The addition of E5b significantly reduced the convergence time to 18.0 min (90% percentile), while the further integration of E5 only marginally improved the performance due to the small frequency spacing. The penta-frequency solution, with the addition of E6 to the system, was shown to have, as a result of the large frequency separation, the shortest convergence time of 15.0 min in the horizontal component among all multi-frequency solutions. As was well predicted by our formal analysis, the E1+E5a+E6 solution had almost the same performance, indicating that it suf-

fices to use these three signals to achieve the optimal Galileo-based performance. Then, we showed how and to what extent the satellite code bias corrections, provided as standard PPP-RTK corrections, contribute to the user-convergence. Through our numerical analysis, we demonstrated that, by correcting for the estimable code biases, the multi-frequency user code data properly contribute to speeding up the convergence time, with the improvement ranging up to 4.0 min.

Finally, we investigated the capabilities of the combined Galileo+GPS multi-frequency model to achieve rapid centimeter-level positioning. Using Galileo and GPS data and corrections from the same network in Australia, we numerically demonstrated that the kinematic PPP-RTK horizontal positioning errors required 3.0 min on average, and 5.0 min at 90% of cases, to go below and stay below 10 cm in the presence of ionospheric delays. This fast convergence to the centimeter level is of great importance, as it implies that a single-receiver user can achieve such rapid positioning results without the use of a precise ionosphere model and, more importantly, without the need for a dense reference network to provide regional atmospheric corrections. With the above real data results, we believe that more studies can be considered for achieving near-instantaneous PPP-RTK positioning by incorporating GLONASS, BeiDou and QZSS data, similar to the five-system analysis of Brack *et al.* [14].

References

[1] R. Leandro, H. Landau, M. Nitschke, M. Glocker, S. Seeger, X. Chen, A. Deking, M. BenTahar, F. Zhang, K. Ferguson, R. Stolz, N. Talbot, G. Lu, T. Allison, M. Brandl, V. Gomez, W. Cao, and A. Kipka, *RTX positioning: The next generation of cm-accurate real-time GNSS positioning.* in *Proceedings of the 24th International Technical Meeting of the Satellite Division of The Institute of Navigation, ION GNSS 2011* (Portland, OR, 2011).

[2] S. Banville, P. Collins, W. Zhang, and R. B. Langley, *Global and regional ionospheric corrections for faster PPP convergence.* Navigation **61**, 115 (2014).

[3] D. Odijk, B. Zhang, A. Khodabandeh, R. Odolinski, and P. J. G. Teunissen, *On the estimability of parameters in undifferenced, uncombined GNSS network and PPP-RTK user models by means of S-system theory,* Journal of Geodesy **90**, 15 (2016).

[4] P. J. G. Teunissen, D. Odijk, and B. Zhang, *PPP-RTK: Results of CORS network-based PPP with integer ambiguity resolution,* Journal of Aeronautics, Astronautics and Aviation A, **42**, 223 (2010).

[5] X. Li, X. Zhang, and G. Guo, *Predicting atmospheric delays for rapid ambiguity resolution in precise point positioning.* Advances in Space Research **54**, 840 (2014).

[6] D. Psychas and S. Verhagen, *Real-Time PPP-RTK Performance Analysis Using Ionospheric Corrections from Multi-Scale Network Configurations.* Sensors **20**, 3012 (2020).

[7] J. Geng, X. Li, Q. Zhao, and G. Li, *Inter-system PPP ambiguity resolution between GPS and BeiDou for rapid initialization.* Journal of Geodesy **93** (2019), 10.1007/s00190-018-1167-6.

[8] G. Katsigianni, S. Loyer, and F. Perosanz, *PPP and PPP-AR Kinematic Post-Processed Performance of GPS-Only, Galileo-Only and Multi-GNSS,* Remote Sensing **11** (2019), 10.3390/rs11212477.

[9] T. Liu, W. Jiang, D. Laurichesse, H. Chen, X. Liu, and J. Wang, *Assessing GPS/Galileo real-time precise point positioning with ambiguity resolution based on phase biases from CNES,* Advances in Space Research **66**, 810 (2020).

[10] N. Nadarajah, A. Khodabandeh, K. Wang, M. Choudhury, and P. J. G. Teunissen, *Multi-GNSS PPP-RTK: From Large- to Small-Scale Networks,* Sensors **18**, 1078 (2018).

[11] P. Li, X. Jiang, X. Zhang, M. Ge, and H. Schuh, *GPS+Galileo+BeiDou precise point positioning with triple-frequency ambiguity resolution,* GPS Solutions **24** (2020), 10.1007/s10291-020-00992-1.

[12] X. Li, X. Li, Y. Yuan, K. Zhang, X. Zhang, and J. Wickert, *Multi-GNSS phase delay estimation and PPP ambiguity resolution: GPS, BDS, GLONASS, Galileo.* Journal of Geodesy **92**, 579 (2018).

[13] H. Ma, Q. Zhao, S. Verhagen, D. Psychas, and X. Liu, *Assessing the Performance of Multi-GNSS PPP-RTK in the Local Area,* Remote Sensing **12**, 3343 (2020).

[14] A. Brack, B. Männel, and H. Schuh, *GLONASS FDMA data for RTK positioning: a five-system analysis,* GPS Solutions **25** (2021), 10.1007/s10291-020-01043-5.

[15] J. Geng and Y. Bock, *Triple-frequency GPS precise point positioning with rapid ambiguity resolution.* Journal of Geodesy **87**, 449 (2013).

[16] G. Xiao, P. Li, Y. Gao, and B. Heck, *A Unified Model for Multi-Frequency PPP Ambiguity Resolution and Test Results with Galileo and BeiDou Triple-Frequency Observations.* Remote Sensing **11**, 116 (2019).

[17] G. Liu, X. Zhang, and P. Li, *Improving the Performance of Galileo Uncombined Precise Point Positioning Ambiguity Resolution Using Triple-Frequency Observations.* Remote Sensing **11**, 341 (2019).

[18] X. Li, X. Li, G. Liu, G. Feng, Y. Yuan, K. Zhang, and X. Ren, *Triple-frequency PPP ambiguity resolution with multi-constellation GNSS: BDS and Galileo.* Journal of Geodesy **93**, 1105 (2019).

[19] J. Geng, J. Guo, X. Meng, and G. Kao, *Speeding up PPP ambiguity resolution using triple-frequency GPS/BeiDou/Galileo/QZSS data.* GPS Solutions **94** (2020), 10.1007/s00190-019-01330-1.

[20] P. J. G. Teunissen, *Positioning, Navigation and Timing Technologies in the 21st Century: Integrated Satellite Navigation, Sensor Systems, and Civil Applications,* (Wiley, 2019) Chap. GNSS Precise Point Positioning.

[21] GNSS Science Support Centre, *Galileo Signal Plan,* (2020).

[22] GNSS Science Support Centre, *Galileo High Accuracy Service (HAS),* (2021).

[23] European GNSS Agency, *GNSS User Technology Report. Issue 3,* (2020), 10.2878/565013.

[24] S. Xin, G. Geng, G. Guo, and X. Meng, *On the Choice of the Third-Frequency Galileo Signals in Accelerating PPP Ambiguity Resolution in Case of Receiver Antenna Phase Center Errors,* Remote Sensing **12**, 1315 (2020).

[25] X. Li, G. Liu, X. Li, F. Zhou, G. Feng, Y. Yuan, and K. Zhang, *Galileo PPP rapid ambiguity resolution with five-frequency observations.* GPS Solutions **24** (2020), 10.1007/s10291-019-0930-3.

[26] J. Geng and G. Guo, *Beyond three frequencies: an extendable model for single-epoch decimeter-level point positioning by exploiting Galileo and BeiDou-3 signals.* Journal of Geodesy **94** (2020), 10.1007/s00190-019-01341-y.

[27] P. J. G. Teunissen, *Theory of integer equivariant estimation with application to GNSS,* Journal of Geodesy **77**, 402 (2003).

[28] D. Laurichesse and S. Banville, *Instantaneous centimeter-level multi-frequency precise point positioning,* (2018), gPS World.

[29] J. Guo, J. Geng, and C. Wang, *Impact of the third frequency GNSS pseudorange and carrier phase observations on rapid PPP convergences,* GPS Solutions **25** (2021), 10.1007/s10291-020-01079-7.

[30] G. Guo and S. Xin, *Toward single-epoch 10-centimeter precise point positioning using Galileo E1/E5a and E6 signals.* in *Proceedings of the 32nd International Technical Meeting of the ION Satellite Division, ION GNSS+ 2019* (Miami, Florida, 2019).

[31] B. Hofmann-Wellenhof, H. Lichtenegger, and E. Wasle, *GNSS - global navigation satellite systems: GPS, GLONASS, Galileo, and more* (Springer, Wien, 2008).

[32] W. Baarda, *S-transformations and criterion matrices.* in *Publications on Geodesy, 18,* Vol. 5 (Netherlands Geodetic Commission, Delft, The Netherlands, 1973).

[33] P. J. G. Teunissen, *Zero Order Design: Generalized Inverses, Adjustment, the Datum Problem and S-Transformations.* in *Optimization and Design of Geodetic Networks.*, edited by E. Grafarend and F. Sanso (Springer, Berlin, Heidelberg, 1985) pp. 11–55.

[34] P. J. de Jonge, *A processing strategy for the application of the GPS in networks.*, Ph.D. thesis, Delft University of Technology (1998).

[35] O. Montenbruck, P. Steigenberger, L. Prange, Z. Deng, Q. Zhao, F. Perosanz, I. Romero, C. Noll, A. Sturze, G. Weber, R. Schmid, K. MacLeod, and S. Schaer, *The Multi-GNSS Experiment (MGEX) of the International GNSS Service (IGS) - Achievements, prospects and challenges.* Advances in Space Research **59**, 1671 (2017).

[36] Geoscience Australia, *Weekly Station Coordinates from ARGN, SPRGN, AuScope and APREF,* (2020).

[37] G. Johnston, A. Riddell, and G. Hausler, *Springer Handbook of Global Navigation Satellite Systems (1st ed.),* (Cham, Switzerland: Springer International Publishing, 2017) Chap. The International GNSS Service.

[38] J. Saastamoinen, *Contributions to the theory of atmospheric refraction.* Bulletin Geodesique **105**, 279 (1972).

[39] I. I. Ifadis, *The atmospheric delay of radio waves: modelling the elevation dependence on a global scale. Technical report no 38L,* Tech. Rep. (Chalmers University of Technology, Gothenburg, 1986).

[40] H. J. Euler and C. C. Goad, *On optimal filtering for GPS dual-frequency observations without using orbit information,* Bulletin Geodesique **65**, 130 (1991).

[41] B. Li, Y. Shen, and P. Xu, *Assessment of stochastic models for GPS measurements with different types of receivers.* Chinese Science Bulletin **53**, 3219 (2008).

[42] P. J. G. Teunissen, *An integrity and quality control procedure for use in multi sensor integration.* in *Proceedings of ION GPS 1990* (Colorado Springs, CO, 1990) pp. 513–522, also published in: Volume VII of *GPS Red Book*: Integrated systems, ION Navigation, 2012.

[43] P. J. G. Teunissen, *The least-squares ambiguity decorrelation adjustment: a method for fast GPS integer ambiguity estimation.* Journal of Geodesy **70**, 65 (1995).

[44] P. J. G. Teunissen, *An Optimality Property of the Integer Least-Squares Estimator,* Journal of Geodesy **73**, 587 (1999).

[45] P. J. G. Teunissen, P. Joosten, and C. C. J. M. Tiberius, *Geometry-free ambiguity success rates in case of partial fixing.* in *Proceedings of ION NTM 1999.* (San Diego, CA, 1999) pp. 201–207.

[46] G. Wubbena, M. Schmitz, and A. Bagge, *PPP-RTK: Precise Point Positioning Using State-Space Representation in RTK Networks.* in *Proceedings of the 18th International Technical Meeting of the Satellite Division of The Institute of Navigation, ION GNSS 2005* (Long Beach, CA, USA, 2005) pp. 2584–2594.

[47] D. Odijk and P. J. G. Teunissen, *Characterization of between-receiver GPS-Galileo inter-system biases and their effect on mixed ambiguity resolution.* GPS Solutions **17**, 521 (2013).

[48] F. Guo, X. Li, X. Zhang, and J. Wang, *Assessment of precise orbit and clock products for Galileo, BeiDou, and QZSS from IGS Multi-GNSS Experiment (MGEX).* GPS Solutions **21**, 279 (2017).

[49] P. J. G. Teunissen, P. Joosten, and N. F. Jonkman, *Evaluation of long range GNSS ambiguity resolution.* in *Proceedings of the 8th European CGSIC IISC Meeting.* (Prague, Czech Republic, 1999) pp. 171–177.

[50] X. Li, X. Li, G. Liu, W. Xie, F. Guo, Y. Yuan, K. Zhang, and G. Feng, *The phase and code biases of Galileo and BDS-3 BOC signals: effect on ambiguity resolution and precise positioning*. Journal of Geodesy **94** (2020), 10.1007/s00190-019-01336-9.

[51] M. Ammar, M. Aquino, and S. Vadakke Veettil, *Estimation and analysis of multi-GNSS differential code biases using a hardware signal simulator*. GPS Solutions **22**, 1 (2018).

[52] D. Psychas, S. Verhagen, and P. J. G. Teunissen, *Precision analysis of partial ambiguity resolution-enabled PPP using multi-GNSS and multi-frequency signals,* Advances in Space Research **66**, 2075 (2020).

[53] B. Zhang, P. J. G. Teunissen, and D. Odijk, *A Novel Un-differenced PPP-RTK concept,* The Journal of Navigation **64**, S180 (2011).

6

A generalized Kalman filter in case of a misspecified stochastic model

In this contribution we introduce a generalized Kalman filter with precision in recursive form when the stochastic model is misspecified. The filter allows for a relaxed dynamic model in which not all state vector elements are connected in time. The filter is equipped with a recursion of the actual error-variance matrices so as to provide an easy-to-use tool for the efficient and rigorous precision analysis of the filter in case the underlying stochastic model is misspecified. Different mechanizations of the filter are presented, including a generalization of the concept of predicted residuals as needed for the recursive quality control of the filter.

This chapter has been published as: Teunissen, P.J.G., Khodabandeh, A. and Psychas, D. (2021). A generalized Kalman filter with its precision in recursive form when the stochastic model is misspecified. Journal of Geodesy, 95(9):108, doi: 10.1007/s00190-021-01562-0

6.1 Introduction

The recursive Kalman filter [1–5] is known to be a 'best' filter in the minimum variance sense in case the underlying model is correctly specified. In practical applications, however, it may be challenging to correctly specify the stochastic model. Due to a lack of information, for instance, one may be unsure about the variance-matrices that need to be specified and, thus, be forced to make use of approximations, or alternatively, because of computational constraints, one may have to oversimplify the model, thereby neglecting particular stochastic contributions. An example of the first case occurs in the context of precise point positioning (PPP), where often the uncertainty in the PPP-corrections is either neglected or approximated in the mechanization of the Kalman filter [6–9]. Examples of the latter can be found in the context of navigation, where the characteristics of the assumed system noise may be too simplistic to catch the actual uncertainty in the dynamic behaviour of the system [10].

With an incorrectly specified stochastic model, the recursive Kalman filter loses its property of being 'best'. Although this is a pitfall, a far more serious problem than not being 'best' is the lack of a proper quality description that goes along with it. With an incorrectly specified stochastic model, also all the error-variance matrices that are recursively produced by the Kalman filter become incorrect and thus fail to provide a means for describing the actual quality of the filter. As an illustrative example, consider a GNSS short-baseline setup in which code measurements of two receivers are processed to deliver, next to other parameter solutions, also filtered solutions of the relative code biases of the two receivers. Their single-epoch time series are presented in the left panel of Figure 6.1. The temporal behaviour of the code biases is assumed to follow a random-walk process, while the corresponding relative clock offsets are assumed unlinked in time [11, 12]. Let us now assume that the code biases' system noise is *incorrectly* specified to 0.2 nsec/$\sqrt{\text{sec}}$ (instead of 0.5 nsec/$\sqrt{\text{sec}}$). As shown in the right panel of Figure 6.1, the Kalman filter would then report a 'misspecified' quality description of the filtered solutions (thick red lines) rather than the 'actual' ones (dashed green lines). The results also indicate that such misspecified choice does affect not only the quality description of the code bias solutions, but also that of other parameters like the receiver clock offsets.

In this contribution, we show how in case of a misspecified stochastic model the actual error-variance matrices of the filter can be computed recursively and thus provide an efficient online way to describe and study the actual quality of the filter. This will be done for a generalized version of the Kalman filter, namely one in which the dynamic model is relaxed such that not all state-vector components are required to be linked in time. We believe this generalization to be necessary as the measurement model in many practical applications contains state-vector elements that are not connected in time. As such cannot be treated with the standard Kalman filter, the 'engineering' solution is often to set the corresponding part of the variance matrix of the system noise to very large values, thereby mimicking numerically an infinite system noise. As this is unsatisfactorily and clearly not rigorous, we show how a rigorous Kalman filter based solution to this problem can be formulated. Our solution is different from the information filter, which would use instead of the state-vector estimation, the information vector and information matrix [13]. We thereby also show the need to generalize the concept of predicted residuals or

'innovations' [14], as the relaxed dynamic model now only allows certain functions of the observables to be predicted.

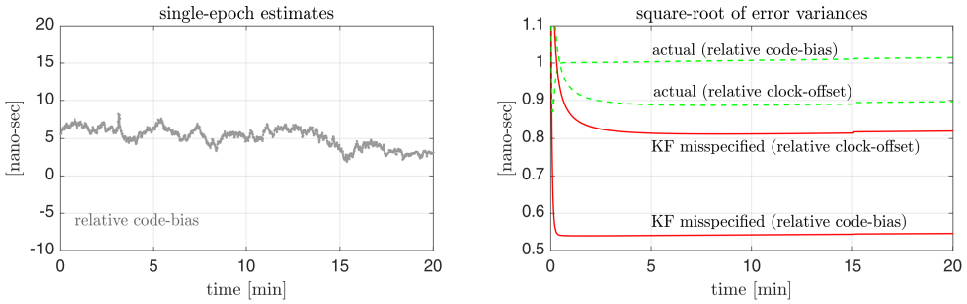


Figure 6.1: Estimation of relative code biases/clock offsets between two u-blox [ZED-F9P] receivers: (left) code bias time series; (right) square root of the Kalman filter (KF) error variances. Assuming the code biases' system noise is *incorrectly* specified to 0.2 nsec/$\sqrt{\text{sec}}$ (instead of 0.5 nsec/$\sqrt{\text{sec}}$), the Kalman filter reports the 'misspecified' error variances (thick red lines) rather than the 'actual' ones (dashed green lines).

This contribution is organized as follows. In Section 6.2, we give a brief review of the standard Kalman filter with a special attention to its assumed stochastic model. In Section 6.3, we generalize the Kalman filter by allowing that not all state-vector components are linked in time. Its dynamic model is assumed valid for only some functions of the state vector, and these functions are permitted to vary in time. Different mechanizations of the corresponding recursive filters are presented. In Section 6.4, we study the error-variance matrices of the different state vectors in case the generalized filter is executed with an incorrect stochastic model. We show how they can be computed in recursive form and thus evaluated online parallel to the actual running of the filter. In Section 6.5, we pay special attention to the predicted residuals, the concept of which needs to be generalized since our relaxed dynamic model now only allows certain functions of the observables to be predicted. We show how they can be used in the recursive testing for the detection of model biases and how the incorrectly specified stochastic model affects the precision of predicted residuals and corresponding test statistics. We also show how the recursive form of the affected precision of the predicted residuals can be used to study how well biases can still be detected even under the usage of a misspecified stochastic model.

We make use of the following notation: We use the underscore to denote a random vector. Thus, $\underline{x}$ is random, while x is not. $\mathsf{E}(.)$ and $\mathsf{D}(.)$ denote the expectation and dispersion operator, while $\mathsf{C}(.,.)$ denotes the covariance operator. Thus, $\mathsf{D}(\underline{x}) = \mathsf{C}(\underline{x},\underline{x})$ represents the variance matrix of $\underline{x}$. Error-variance matrices are denoted with the capital letter P. For two positive-definite matrices, M_1 and M_2, the matrix inequality $M_1 \geq M_2$ means that $M_1 - M_2$ is positive semi-definite.

6.2 Kalman filter and its assumptions

In this section, we briefly review the Kalman filter with a special attention to its underlying stochastic assumptions.

6.2.1 Model assumptions

First, we state the measurement and dynamic model assumptions.

The measurement model: The link between the random vector of observables $\underline{y}_i$ and the random state vector $\underline{x}_i$ is assumed given as

$$\underline{y}_i = A_i \underline{x}_i + \underline{n}_i,\ i = 0,1,\ldots,t, \tag{6.1}$$

together with

$$\mathsf{E}(\underline{x}_0) = x_0 \text{ (unknown)}, \quad \mathsf{E}(\underline{n}_i) = 0, \tag{6.2}$$

and

$$\mathsf{C}(\underline{x}_0, \underline{n}_i) = 0, \quad \mathsf{C}(\underline{n}_i, \underline{n}_j) = R_i \delta_{ij},\ i = 0,1,\ldots,t \tag{6.3}$$

with δ_{ij} being the Kronecker delta. The time-index and number of epochs after initialization are indicated by i and t, respectively. Thus, the zero-mean measurement noise $\underline{n}_i$ is assumed to be uncorrelated in time and to be uncorrelated with the initial state vector $\underline{x}_0$. The design matrices $A_i \in \mathbb{R}^{m_i \times n}$ and variance matrices $R_i \in \mathbb{R}^{m_i \times m_i}$ are assumed given, with A_0 of full rank, $\operatorname{rank}(A_0) = n$, and all R_i positive definite. The design matrices A_i ($i \geq 1$) need not be of full rank. Note that we assume the mean x_0 of the initial state vector to be unknown.

The dynamic model: The linear dynamic model, describing the time evolution of the random state vector $\underline{x}_i$, is given as

$$\underline{x}_i = \Phi_{i,i-1} \underline{x}_{i-1} + \underline{d}_i,\ i = 1,2,\ldots,t \tag{6.4}$$

with

$$\mathsf{E}(\underline{d}_i) = 0,\ \mathsf{C}(\underline{x}_0, \underline{d}_i) = 0, \tag{6.5}$$

and

$$\mathsf{C}(\underline{d}_i, \underline{n}_j) = 0,\ \mathsf{C}(\underline{d}_i, \underline{d}_j) = S_i \delta_{ij},\ i,j = 1,2,\ldots,t \tag{6.6}$$

where $\Phi_{i,i-1}$ denotes the transition matrix and the random vector $\underline{d}_i$ is the system noise. The system noise $\underline{d}_i$ is thus also assumed to have a zero mean, to be uncorrelated in time and to be uncorrelated with the initial state-vector and the measurement noise.

6.2.2 The Kalman filter

The Kalman filter is a recursive Best Linear Predictor (BLP) in case the means of $\underline{x}_i$, $i = 0,\ldots,t$, are known and a recursive BLUP (Best Linear Unbiased Predictor) in case these means are unknown [15]. In our case, it is a recursive BLUP, since we assume x_0 unknown.

As x_0 is unknown, the *initialization* of the filter requires the BLUP of $\underline{x}_0$, which is given as

$$\underline{\hat{x}}_{0|0} = (A_0^T R_0^{-1} A_0)^{-1} A_0^T R_0^{-1} \underline{y}_0. \tag{6.7}$$

Note that the variance (vc)-matrix of $\underline{\hat{x}}_0 - x_0$ is given as $Q_{0|0} = (A^T R_0^{-1} A_0)^{-1} + Q_{x_0 x_0}$, in which $Q_{x_0 x_0}$ is the unknown vc-matrix of $\underline{x}_0$. In our case, however, we do not need the vc-matrix of the estimation error $\underline{\hat{x}}_0 - x_0$, but rather the vc-matrix of the BLUP error $\underline{\hat{x}}_0 - \underline{x}$, which is given as

$$P_{0|0} = (A_0^T R_0^{-1} A_0)^{-1} \tag{6.8}$$

Following the initialization and any other measurement update, we have the *time update* (TU) in which the linear dynamic model is used to predict the state-vector one epoch ahead. The TU and its error-variance matrix are given as

$$\begin{array}{rcl} \underline{\hat{x}}_{t|t-1} & = & \Phi_{t,t-1} \underline{\hat{x}}_{t-1|t-1}, \\ P_{t|t-1} & = & \Phi_{t,t-1} P_{t-1|t-1} \Phi_{t,t-1}^T + S_t. \end{array} \tag{6.9}$$

With any measurement epoch, we have a *measurement update* (MU) to improve upon the state-vector TU. The MU and its error-variance can be given in two different forms, the *information* form or the *variance* form. The MU information form is given as

$$\begin{array}{rcl} \underline{\hat{x}}_{t|t} & = & \underline{\hat{x}}_{t|t-1} + K_t(\underline{y}_t - A_t \underline{\hat{x}}_{t|t-1}), \\ P_{t|t} & = & [P_{t|t-1}^{-1} + A_t^T R_i^{-1} A_i]^{-1} \end{array} \tag{6.10}$$

with gain matrix $K_t = P_{t|t} A_t^T R_t^{-1}$. The MU variance form is given as

$$\begin{array}{rcl} \underline{\hat{x}}_{t|t} & = & \underline{\hat{x}}_{t|t-1} + K_t(\underline{y}_t - A_t \underline{\hat{x}}_{t|t-1}), \\ P_{t|t} & = & [I - K_t A_t] P_{t|t-1} \end{array} \tag{6.11}$$

with the gain matrix expressed as $K_t = P_{t|t-1} A_t^T (R_t + A_t P_{t|t-1} A_t^T)^{-1}$.

Although we will focus ourselves in the following on the first two moments of the Kalman filter, the random vectors $\underline{x}_0$, $\underline{n}_i$ and $\underline{d}_i$ will be assumed normally distributed when required.

6.3 Generalized Kalman filter

In the standard Kalman filter, it is assumed that a dynamic model is available for the complete state vector $\underline{x}_t$ (cf. 6.4). In many practical applications, however, this is not the case. It often happens that a dynamic model is only valid for a part of $\underline{x}_t$. As the other part will then have to be modelled as unlinked in time, the 'engineering' solution is often to set the corresponding part of the vc-matrix S_t to very large values, thereby mimicking numerically an infinite system noise. This is rather unsatisfactorily and clearly not rigorous. Below we show how a rigorous solution to this problem can be formulated.

6.3.1 A relaxed dynamic model

Instead of the dynamic model (6.4), we assume that only of certain functions of the state vector,

$$\underline{z}_i = F_i^T \underline{x}_i\,,\ \ i = 0, 1, \ldots, t \tag{6.12}$$

a dynamic model is available,

$$\underline{z}_i = \Phi^z_{i,i-1}\underline{z}_{i-1} + \underline{d}_i^z\,,\ \ i = 1, \ldots, t. \tag{6.13}$$

Thus, $\underline{z}_i$ denotes the 'linked-in-time' state vectors. As we assume the functions to be linearly independent, the matrices $F_i \in \mathbb{R}^{n\times p_i}$ are all of full column rank. The simplest case of such functions occurs when a dynamic model is available for only one part of $\underline{x}_i$, say for the first p components. Then, the functions take the simple form $F_i^T = [I_p, 0]$. In the above formulation, we allow, however, general functions which may also be time dependent. They are therefore permitted to change over time.

As with (6.5) and (6.6), the system noise $\underline{d}_i^z$ of (6.13) is assumed to obey

$$\mathsf{E}(\underline{d}_i^z) = 0,\ \mathsf{C}(\underline{x}_0, \underline{d}_i^z) = 0, \tag{6.14}$$

and

$$\mathsf{C}(\underline{d}_i^z, \underline{n}_j) = 0,\ \mathsf{C}(\underline{d}_i^z, \underline{d}_j^z) = S_i^z \delta_{ij},\ i, j = 1, 2, \ldots, t. \tag{6.15}$$

6

6.3.2 A reparametrized measurement model

For the purpose and ease of deriving the generalized Kalman filter, we reparametrize the observation equation $\underline{y}_i = A_i \underline{x}_i + \underline{n}_i$ (cf. 6.1) so that it becomes parametrized in $\underline{z}_i$ and in a part that is annihilated by F_i^T.

Recall that for the standard Kalman filter it was sufficient to assume A_0 to be of full column rank. All the other design matrices A_i, $i \neq 0$, were allowed to be rank defect. For the present case, this is still allowed, provided that all the matrices $[F_i, A_i^T]^T$, $i \neq 0$, are of full column rank. Note that this condition is automatically fulfilled if $F_i = I_n$. The reparametrization that we choose is given as

$$\underline{x}_i = M_i F_i^+ \underline{z}_i + G_i \underline{u}_i \tag{6.16}$$

with G_i being a basis matrix of the null space of F_i^T. Thus, $F_i^T G_i = 0$ and matrix $[F_i, G_i]$ is square and nonsingular. Moreover,

$$\begin{aligned} M_i &= I_n - G_i (G_i^T A_i^T R_i^{-1} A_i G_i)^{-1} G_i^T A_i^T R_i^{-1} A_i \\ F_i^+ &= F_i (F_i^T F_i)^{-1}. \end{aligned} \tag{6.17}$$

Thus, $\underline{u}_i$ denotes the 'unlinked-in-time' state vectors. Note, since $F_i^T G_i = 0$ and $F_i^T F_i^+ = I_{p_i}$, that (6.16) indeed satisfies $F_i^T \underline{x}_i = \underline{z}_i$. Also note that $A_i G_i$ is of full column rank, since $[F_i, A_i^T]^T$ is of full column rank and G_i is a basis matrix of the null space of F_i^T. As $A_i G_i$ is of full column rank, the inverse in the expression of M_i exists. Also note that M_i is idempotent, $M_i M_i = M_i$. It is an oblique projector that projects along the range space of G_i and onto the null space of $G_i^T A_i^T R_i^{-1} A_i$.

It is not difficult to verify that the square matrix $[M_i F_i^+, G_i]$ is invertible and thus that (6.16) is a genuine reparametrization. If we substitute the reparametrization into the observation equations $\underline{y}_i = A_i \underline{x}_i + \underline{n}_i$, we obtain the reparametrized observation equations as

$$\underline{y}_i = A_i^z \underline{z}_i + A_i^u \underline{u}_i + \underline{n}_i \tag{6.18}$$

with

$$A_i^z = P_{A_i^u}^{\perp} A_i F_i^+ \text{ and } A_i^u = A_i G_i \tag{6.19}$$

in which $P_{A_i^u}^{\perp} A_i = A_i M_i$, $P_{A_i^u}^{\perp} = I_{m_i} - P_{A_i^u}$ and $P_{A_i^u} = A_i^u (A_i^{uT} R_i^{-1} A_i^u)^{-1} A_i^{uT} R_i^{-1}$ is the orthogonal projector (idempotent matrix) that projects onto the range space (column space) of $A_i^u = A_i G_i$. Orthogonality is here with respect to the metric of R_i^{-1}, i.e. $P_{A_i^u}^T R_i^{-1} P_{A_i^u}^{\perp} = 0$. An important property of the reparametrized observation equation (6.18) is that the range spaces of its design matrices, A_i^z and A_i^u, are mutually orthogonal in the metric of R_i^{-1}. Hence,

$$A_i^{zT} R_i^{-1} A_i^u = 0. \tag{6.20}$$

This implies that the measurement updates for $\underline{z}_i$ and $\underline{u}_i$ can be determined independently from each other, thereby easing the derivation of the generalized Kalman filter. Hence, the solution $\hat{\underline{u}}_{t|t}$ will then be solely driven by the observable $\underline{y}_t$ and is thus given as

$$\hat{\underline{u}}_{t|t} = (A_t^{uT} R_t^{-1} A_t^u)^{-1} A_t^{uT} R_t^{-1} \underline{y}_t. \tag{6.21}$$

We will now first determine the filter for $\underline{z}_t$ and then for $\underline{x}_t$.

6.3.3 The filter for $\underline{z}_t$

In some applications, one may be interested solely in the recursive estimation of the state-vector components for which a dynamic model is available and, thus, in the recursive estimation of $\underline{z}_t = F_t^T \underline{x}_t$, rather than in that of the complete state vector $\underline{x}_t$. We present this recursive filter in information form and variance form.

The initialization of the z-filter takes (6.7) and (6.8) as input, to give

$$\hat{\underline{z}}_{0|0} = F_0^T \hat{\underline{x}}_{0|0} \text{ with } P_{0|0}^z = F_0^T P_{0|0} F_0. \tag{6.22}$$

Following the initialization, we have the time update (TU) in which the linear dynamic model (6.13) is used to predict the state-vector components one epoch ahead. Similar to (6.9), the TU and its error-variance matrix are given as

$$\begin{array}{rcl} \hat{\underline{z}}_{t|t-1} & = & \Phi_{t,t-1}^z \hat{\underline{z}}_{t-1|t-1}, \\ P_{t|t-1}^z & = & \Phi_{t,t-1}^z P_{t-1|t-1}^z \Phi_{t,t-1}^{zT} + S_t^z. \end{array} \tag{6.23}$$

To determine the measurement update (MU), we first formulate it in information form, whereby now good use can be made of the orthogonality property (6.20) of the reparametrized observation equations (6.18). Due to this orthogonality, it follows that

$\underline{\hat{z}}_{t|t} = [(P^z_{t|t-1})^{-1} + A_t^{zT} R_t^{-1} A_t^z]^{-1}[(P^z_{t|t-1})^{-1}\underline{\hat{z}}_{t|t-1} + A_t^{zT} R_t^{-1}\underline{y}_t]$, which can be written in the more familiar MU information form as

$$\begin{aligned} \underline{\hat{z}}_{t|t} &= \underline{\hat{z}}_{t|t-1} + K_t^z(\underline{y}_t - A_t^z\underline{\hat{z}}_{t|t-1}) \\ P^z_{t|t} &= \left[(P^z_{t|t-1})^{-1} + A_t^{zT} R_t^{-1} A_t^z\right]^{-1} \end{aligned} \tag{6.24}$$

with $K_t^z = P^z_{t|t} A_t^{zT} R_t^{-1}$. Similar to the variance form (6.11), the MU variance form of the z-filter is given as

$$\begin{aligned} \underline{\hat{z}}_{t|t} &= \underline{\hat{z}}_{t|t-1} + K_t^z(\underline{y}_t - A_t^z\underline{\hat{z}}_{t|t-1}) \\ P^z_{t|t} &= [I_{p_t} - K_t^z A_t^z]P^z_{t|t-1} \end{aligned} \tag{6.25}$$

with $K_t^z = P^z_{t|t-1} A_t^{zT}[R_t + A_t^z P^z_{t|t-1} A_t^{zT}]^{-1}$. Note, since $A_t^{zT} R_t^{-1} A_t^z = A_t^{zT} R_t^{-1} A_t F_t^+$, that $K_t^z A_t^z = K_t^z A_t F_t^+$ and that therefore the residual $\underline{y}_t - A_t^z\underline{\hat{x}}_{t|t-1}$ in (6.24) and (6.25) can be replaced by $\underline{y}_t - A_t F_t^+\underline{\hat{x}}_{t|t-1}$.

The above shows that the whole cycling sequence of TUs and MUs can be done solely in terms of estimations of $\underline{z}_t$, without the need to resort to an estimation of the complete state vector $\underline{x}_t$. Note, however, although both (6.24) and (6.25) have the same structure as the MUs of the standard Kalman filter (cf. 6.10 and 6.11), that $A_t^z\underline{\hat{z}}_{t|t-1}$ (or $A_t F_t^+\underline{\hat{z}}_{t|t-1}$) is *not* a predictor of $\underline{y}_t$. The residual $\underline{y}_t - A_t^z\underline{\hat{z}}_{t|t-1}$ (or $\underline{y}_t - A_t F_t^+\underline{\hat{z}}_{t|t-1}$) in (6.24) and (6.25) is therefore not a predicted residual, this in contrast to $\underline{v}_t = \underline{y}_t - A_t\underline{\hat{x}}_{t|t-1}$, which is the predicted residual of the standard Kalman filter. We will come back to this in Section 6.5.

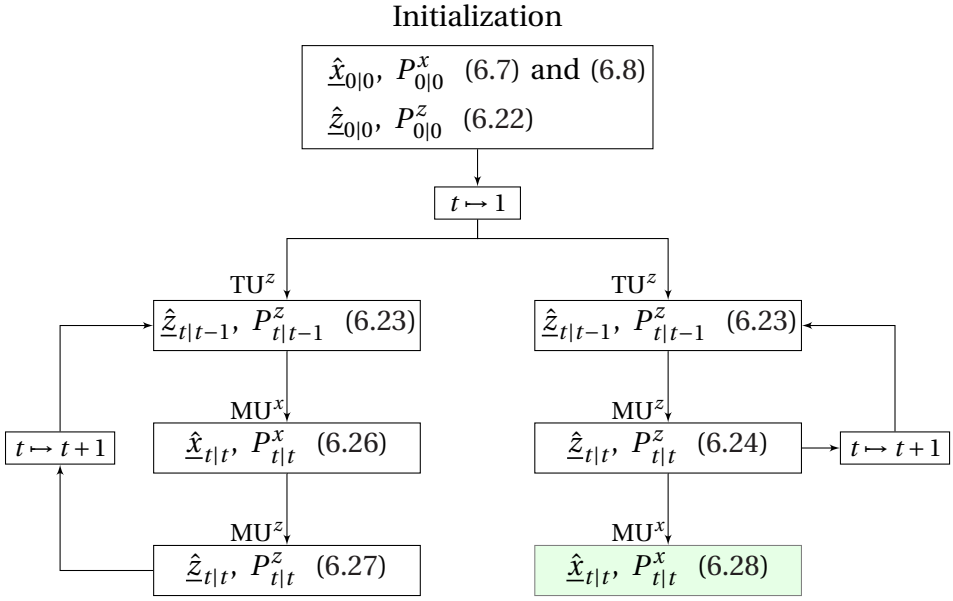


Figure 6.2: Flowchart of the generalized Kalman filter: x-filter (left) versus z-filter (right). The step inside the green box is optional.

6.3.4 The filter for $\underline{x}_t$

As there is no dynamic model for the complete state vector $\underline{x}_t$, time updates of it like (6.9) do not exist. However, for every epoch a solution $\underline{\hat{x}}_{t|t}$ can be determined, either from $\underline{\hat{z}}_{t|t-1}$ and $\underline{y}_t$, or from $\underline{\hat{z}}_{t|t}$ and $\underline{y}_t$.

First, we present the information form of $\underline{\hat{x}}_{t|t}$ based on $\underline{\hat{z}}_{t|t-1}$ and $\underline{y}_t$. As $[F_t, A_t^T]^T$ is of full column rank, we have $\underline{\hat{x}}_{t|t} = P^x_{t|t}[F_t(P^z_{t|t-1})^{-1}\underline{\hat{z}}_{t|t-1} + A_t^T R_t^{-1}\underline{y}_t]$, with $P^x_{t|t} = [F_t(P^z_{t|t-1})^{-1}F_t^T + A_t^T R_t^{-1}A_t]^{-1}$. This can be written in the more familiar update form as

$$\begin{array}{rcl} \underline{\hat{x}}_{t|t} & = & F_t^+\underline{\hat{z}}_{t|t-1} + K_t^x(\underline{y}_t - A_t F_t^+\underline{\hat{z}}_{t|t-1}) \\ P^x_{t|t} & = & [F_t(P^z_{t|t-1})^{-1}F_t^T + A_t^T R_t^{-1}A_t]^{-1} \end{array} \tag{6.26}$$

with $K_t^x = P^x_{t|t}A_t^T R_t^{-1}$. When one insists on using (6.26), for instance because it automatically provides $\underline{\hat{x}}_{t|t}$ for every epoch, one still will have to compute $\underline{\hat{z}}_{t|t}$ in order to proceed with the next time update. Hence, when using (6.26), the MUs of the z-filter, (6.24) or (6.25), get replaced by (6.26) and

$$\underline{\hat{z}}_{t|t} = F_t^T\underline{\hat{x}}_{t|t} \text{ with } P^z_{t|t} = F_t^T P^x_{t|t}F_t. \tag{6.27}$$

Note, when (6.26) is substituted into (6.27), that one indeed gets (6.24) again. This follows, since $F_t^T F_t^+ = I_n$, $F_t^T K_t^x = K_t^z$ and $K_t^z A_t^z = K^z A_t F^+$.

With (6.26) and (6.27), the computation of $\underline{\hat{x}}_{t|t}$ is an integral part of the generalized Kalman filter. Its computation is needed to be able to proceed with the next time update. This can be avoided if one computes $\underline{\hat{x}}_{t|t}$ from $\underline{\hat{z}}_{t|t}$ and $\underline{y}_t$, instead of from $\underline{\hat{z}}_{t|t-1}$ and $\underline{y}_t$. From the reparametrization (6.16) follows $\underline{\hat{x}}_{t|t} = \Pi_t F_t^+\underline{\hat{z}}_{t|t} + G_t\underline{\hat{u}}_{t|t}$, which, with (6.21) and by recognizing that $\underline{\hat{z}}_{t|t}$ and $\underline{\hat{u}}_{t|t}$ are uncorrelated, $\mathsf{C}(\underline{\hat{z}}_{t|t}, \underline{\hat{u}}_{t|t}) = 0$, can be written, together with its error-variance matrix, in the update form

$$\begin{array}{rcl} \underline{\hat{x}}_{t|t} & = & F_t^+\underline{\hat{z}}_{t|t} + G_t^x(\underline{y}_t - A_t F_t^+\underline{\hat{z}}_{t|t}) \\ P^x_{t|t} & = & M_t F_t^+ P^z_{t|t} F_t^{+T} M_t^T + G_t^x R_t G_t^{xT} \end{array} \tag{6.28}$$

with $M_t = I_n - G_t^x A_t$ and $G_t^x = G_t(A_t^{uT}R_t^{-1}A_t^u)^{-1}A_t^{uT}R_t^{-1}$. Note that the error-variance $P^x_{t|t}$ is the sum of two terms. In the first term, we recognize $P^z_{t|t} \leq P^z_{t|t-1}$, thus showing the improvement in precision that $\underline{y}_t$ brings through $\underline{\hat{z}}_{t|t}$. The addition of the positive semi-definite second term $G_t^x R_t G_t^{xT}$, however, reflects the increase in uncertainty due to the presence of the additional state-vector components for which no dynamic model is available. Also note the flexibility in formulation (6.28). In contrast to (6.26), the continuation of the filter is not affected, whether one decides to compute $\underline{\hat{x}}_{t|t}$ or not. Finally, note that the variance form of (6.26) is obtained if (6.25) is substituted into (6.28). For a summarizing flowchart and a comparison of the x-filter and z-filter, see Figure 6.2.

6.4 State-vector error-variance matrices

In this section, we consider some of the basic stochastic assumptions of the Kalman filter misspecified. This will affect the precision description of the Kalman filter, and in particular, it will make the P-matrices fail to be the error-variance matrices of the executed

filter. We determine the correct error-variance matrices and show how they can still be computed in recursive form.

6.4.1 Recursive error-variance matrices

We assume the vc-matrices R_i and S_i^z of the measurement and system noise, $\underline{n}_i$ and $\underline{d}_i^z$, to be misspecified. Their correct vc-matrices are denoted with an overbar, $\bar{R}_i$ and $\bar{S}_i^z$. Thus, we assume

$$\begin{array}{lcl} \mathsf{C}(\underline{n}_i, \underline{n}_j) \neq R_i \delta_{ij} & \Rightarrow & \mathsf{C}(\underline{n}_i, \underline{n}_j) = \bar{R}_i \delta_{ij} \\ \mathsf{C}(\underline{d}_i^z, \underline{d}_j^z) \neq S_i^z \delta_{ij} & \Rightarrow & \mathsf{C}(\underline{d}_i^z, \underline{d}_j^z) = \bar{S}_i^z \delta_{ij}. \end{array} \tag{6.29}$$

With this assumption, the generalized Kalman filter of the previous section is executed using the wrong vc-matrices, namely R_i and S_i^z, and will thus provide a precision description through its P-matrices that is incorrect. We denote the correct error-variance matrices using an overbar as $\bar{P}_{t|t-1}^z$, $\bar{P}_{t|t}^z$ and $\bar{P}_{t|t}^x$. The following lemma shows how they can be computed in recursive form, thereby making use of the information provided by the filter.

Lemma 1 (*Error-variance matrix recursion*) The error-variance matrices of the generalized Kalman filter, having misspecified vc-matrices for its measurement and system noise (cf. 6.29), are given in recursive form as

$$\begin{array}{lllcl} (a) & \bar{P}_{t|t-1}^z & = & \Phi_{t,t-1}^z \bar{P}_{t-1|t-1}^z \Phi_{t,t-1}^{zT} + \bar{S}_t^z \\ (b) & \bar{P}_{t|t}^z & = & L_t^z \bar{P}_{t|t-1}^z L_t^{zT} + K_t^z \bar{R}_t K_t^{zT} \\ (c) & \bar{P}_{t|t}^x & = & L_t^x \bar{P}_{t|t-1}^z L_t^{xT} + K_t^x \bar{R}_t K_t^{xT} \\ (d) & \bar{P}_{t|t}^z & = & F_t^T \bar{P}_{t|t}^x F_t \\ (e) & \bar{P}_{t|t}^x & = & H_t^x \bar{P}_{t|t}^z H_t^{xT} + G_t^x \bar{R}_t G_t^{xT} \end{array} \tag{6.30}$$

for $t = 1, \ldots$, with $L_t^z = [I_{p_t} - K_t^z A_t^z]$, $L_t^x = [I_n - K_t^x A_t] F^+$ and $H_t^x = [I_n - G_t^x A_t] F^+$. The initial error-variance matrix is given as $\bar{P}_{0|0}^z = F_0^T A_0^+ \bar{R}_0 A_0^{+T} F_0$, with $A_0^+ = (A_0^T R_0^{-1} A_0)^{-1} A_0^T R_0^{-1}$.

Proof For the proof, see "Appendix". □

Note, in (6.30), that the gain matrices K_t^z and K_t^x are to be computed by the assumed (and not correct) variance matrices. The above result provides a very useful tool for the efficient precision analysis of Kalman filters. In many practical applications, one may either be not too sure about the vc-matrices that one needs to specify or one may be forced, for instance, because of numerical constraints, to oversimplify the model, thereby neglecting particular stochastic contributions. With the above lemma, one has an easy-to-use tool available to do an online recursive sensitivity analysis of the generalized Kalman filter, whereby the computations can be done in parallel to the recursion of the filter itself.

It depends on the mechanization of the generalized Kalman filter which of the above error variances are used in the recursion. In case of only the z-filter, only (6.30) (a)+(b) are needed, giving the recursion $\bar{P}_{t-1|t-1}^z \rightarrow \bar{P}_{t|t-1}^z \rightarrow \bar{P}_{t|t}^z$. Would $\underline{\hat{x}}_{t|t}$ be included based on (6.26) and (6.27), then (6.30) (a)+(c)+(d) are needed, giving the recursion $\bar{P}_{t-1|t-1}^z \rightarrow \bar{P}_{t|t-1}^z \rightarrow \bar{P}_{t|t}^x \rightarrow \bar{P}_{t|t}^z$. For $\underline{\hat{x}}_{t|t}$ based on (6.28), however, the recursion is that of the z-filter, while (6.30) (e) is used to tap off $\bar{P}_{t|t}^x$ from $\bar{P}_{t|t}^z$.

In case of the standard Kalman filter, we have $F_t = I_n$ and G_t absent, and the results of Lemma 1 reduce to

$$\begin{array}{lll} (a) & \bar{P}_{t|t-1} & = \Phi_{t,t-1}\bar{P}_{t-1|t-1}\Phi_{t,t-1}^T + \bar{S}_t \\ (b) & \bar{P}_{t|t} & = L_t\bar{P}_{t|t-1}L_t^T + K_t\bar{R}_tK_t^T \end{array} \tag{6.31}$$

with $L_t = [I_n - K_tA_t]$.

When comparing $\bar{P}_{t|t}$ of (6.31) with $P_{t|t}$ of (6.10) or (6.11), and knowing that $P_{t|t}$ is an incorrect error-variance matrix when $\bar{R}_i \neq R_i$ and/or $\bar{S}_i \neq S_i$, for some $i \leq t$, one should be careful not to draw the automatic conclusion that $P_{t|t}$ gives a too optimistic precision description and that the actual precision is poorer. Only in two extreme cases can one make a definite statement concerning the relation between the assumed error variance $P_{t|t}$ and the actual error variance $\bar{P}_{t|t}$. When comparing $P_{t|t}$ with $\bar{P}_{t|t}$, one is comparing the error-variance of the same linear estimator $\underline{\hat{x}}_{t|t}$ under two different stochastic regimes. The assumed error variance is therefore too optimistic ($P_{t|t} \leq \bar{P}_{t|t}$) if the assumed stochastic model is too optimistic. Likewise, the assumed error variance is too pessimistic ($P_{t|t} \geq \bar{P}_{t|t}$) if the assumed stochastic model is too pessimistic. In all other cases, the assumed error variance $P_{t|t}$ can be either too optimistic or too pessimistic.

Next to the assumed and actual error variance, we may also consider the optimal error variance $\bar{\bar{P}}_{t|t}$, which is the error-variance when the Kalman filter is based on the correct stochastic model, $\bar{R}_i$ and $\bar{S}_i$. Based on the filter's 'best' property, we have $\bar{\bar{P}}_{t|t} \leq \bar{P}_{t|t}$. And when we compare $P_{t|t}$ with $\bar{\bar{P}}_{t|t}$, we can make use of the property that the error-variance of a Kalman filter improves if its stochastic model improves. Therefore, $P_{t|t} \leq \bar{\bar{P}}_{t|t}$, if the stochastic model under which $P_{t|t}$ is computed can be seen as an improvement of that under which $\bar{\bar{P}}_{t|t}$ is computed, and vice versa. This is summarized in Table 6.1. Similar conclusions hold for the error-variance matrices of the generalized Kalman filter.

Table 6.1: Assumed ($P_{t|t}$), actual ($\bar{P}_{t|t}$) and optimal ($\bar{\bar{P}}_{t|t} \leq \bar{P}_{t|t}$) Kalman filter error variances in dependence of actual and assumed measurement and system noise

Assumed vs actual error variance	**Assumed vs optimal error variance**
If $\forall i \leq t\ (R_i \leq \bar{R}_i, S_i \leq \bar{S}_i)$: $P_{t\|t} \leq \bar{P}_{t\|t}$	If $\exists i \leq t\ (R_i \leq \bar{R}_i, S_i \leq \bar{S}_i)$; $\forall j \neq i : (R_j = \bar{R}_j, S_j = \bar{S}_j)$: $P_{t\|t} \leq \bar{\bar{P}}_{t\|t}$
If $\forall i \leq t\ (R_i \geq \bar{R}_i, S_i \geq \bar{S}_i)$: $P_{t\|t} \geq \bar{P}_{t\|t}$	If $\exists i \leq t\ (R_i \geq \bar{R}_i, S_i \geq \bar{S}_i)$; $\forall j \neq i\ (R_j = \bar{R}_j, S_j = \bar{S}_j)$: $P_{t\|t} \geq \bar{\bar{P}}_{t\|t}$

Example 1 *(Assumed and actual precision compared)* To illustrate the characteristics of the assumed ($P_{t|t}$), actual ($\bar{P}_{t|t}$) and optimal ($\bar{\bar{P}}_{t|t}$) error variances, we consider a simple Kalman filter based on one-dimensional position observables with a constant-velocity model, i.e. a model in which the velocity fluctuations are treated as zero-mean system noise. Then, the state vector consists of position and velocity, $\underline{x}_k = [\underline{s}(t_k), \dot{\underline{s}}(t_k)]^T$, and the

design matrix, transition matrix and vc-matrix of the system noise vector are given as [4]

$$A_k = [1\ 0], \quad \Phi_{k,k-1} = \begin{bmatrix} 1 & \Delta t \\ 0 & 1 \end{bmatrix}, \quad S_k = q_{\ddot{s}} \begin{bmatrix} \frac{1}{3}\Delta t^3 & \frac{1}{2}\Delta t^2 \\ \frac{1}{2}\Delta t^2 & \Delta t \end{bmatrix} \tag{6.32}$$

with $q_{\ddot{s}}$ being the spectral density given and Δt the measurement interval. Figure 6.3 shows in a qualitative sense how the actual error variances $\bar{P}_{t|t}$, computed using the recursions of Lemma 1, can differ from the assumed $P_{t|t}$. Only in the strict case, when one knows that the assumed stochastic model is either too optimistic or too pessimistic, can one predict the relation between $P_{t|t}$ and $\bar{P}_{t|t}$ beforehand, as shown in Figure 6.3 (top-left and top-right). In the general case, however, this is not possible, as shown in Figure 6.3 (bottom). As this general case usually prevails in practice (in particular in regard to the settings of the system noise), one cannot rely on *a-priori* formulated bounds on the relation between $P_{t|t}$ and $\bar{P}_{t|t}$. This therefore underlines the practical usefulness of having the recursions of Lemma 1 available for an online and parallel precision analysis.

Example 2 *(Designing for precision)* The error-variance matrices of a (generalized) Kalman filter can be computed already in a designing phase, i.e. before the actual measurements and experiment are executed. Such computations only require knowledge about the design and transition matrices and the measurement and system noise vc-matrices. Hence, when for an application certain requirements are specified for the error-variance matrices, one can design a corresponding functional and stochastic model so as to meet these requirements. Such would then imply an analysis of the dependence of the error variances on changes in the assumed stochastic model. This can be done rather straightforwardly with the standard $P_{t|t}$ output of the Kalman filter and Figure 6.4 (left) shows such example based on (6.32).

However, in case of a misspecified stochastic model, such an analysis may give a seriously wrong picture, since the behaviour of the *actual* error-variance $\bar{P}_{t|t}$ for changes in the assumed stochastic model can be quite different from the dependence that $P_{t|t}$ exhibits. As a case in point, assume that the designer for his/her current application has a properly designed filter, i.e. one for which the assumed stochastic model is identical to the actual stochastic model and thus $P_{t|t} = \bar{P}_{t|t} = \bar{\bar{P}}_{t|t}$. Now, a new application comes up and the designer believes that for this new application, a more optimistic stochastic model can be used and thus designs the filter accordingly to reach a smaller $P_{t|t}$. But if in fact the actual stochastic model would have remained unchanged, the choice of taking a more optimistic stochastic model will lead to an actual precision that is poorer. Hence, the designer is then confronted with the case that $P_{t|t} \downarrow$ (designer believes to get a better precision), while $\bar{P}_{t|t} \uparrow$ (the actual precision gets poorer). The reason for this unwanted change is that the designer unknowingly replaced a best filter with one that is not best in the minimum mean squared error (MMSE) sense and therefore to one that provides a poorer precision. This will happen, irrespective of whether the assumed stochastic model was chosen to be an improvement or a deterioration relative to the correct stochastic model, and Figure 6.4 (right) shows such example based on (6.32).

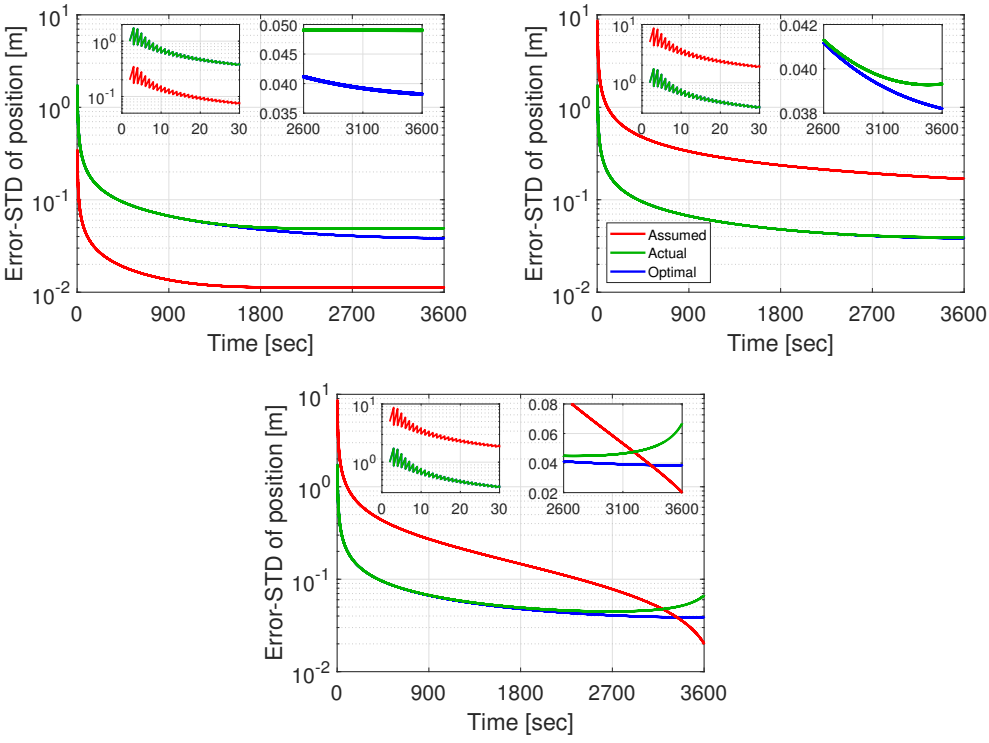


Figure 6.3: Relation between assumed ($P_{t|t}$), actual ($\bar{P}_{t|t}$) and optimal ($\bar{\bar{P}}_{t|t} \leq \bar{P}_{t|t}$) Kalman filter error-variances: (top-left) $P_{t|t} \leq \bar{P}_{t|t}$ since too optimistic assumed stochastic model; (top-right) $P_{t|t} \geq \bar{P}_{t|t}$ since too pessimistic assumed stochastic model; (bottom) $P_{t|t} \leq\geq \bar{P}_{t|t}$ mixture of pessimistic and optimistic stochastic model

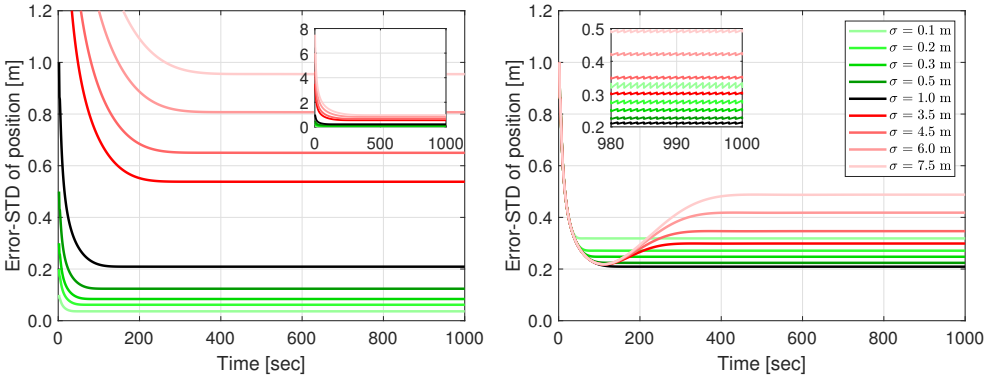


Figure 6.4: Square root of assumed ($P_{t|t}$; left) and actual ($\bar{P}_{t|t}$; right) error variances for different choices of assumed stochastic model ($R_i = \sigma^2$, with half of them smaller than $\bar{R}_i = \bar{\sigma}^2$ and the other half larger than $\bar{\sigma}^2$)

6.5 Predicted residuals

Predicted residuals play an important role in the quality control of Kalman filters [10, 15–21]. In this section, we generalize the concept of predicted residuals, show how their properties are affected by the stochastic misspecification (6.29) and discuss its consequences.

6.5.1 The predicted residual defined

The predicted residual of the standard Kalman filter at epoch t is defined as $\underline{y}_t - A_t\underline{\hat{x}}_{t|t-1}$. It derives its name from the fact that $A_t\underline{\hat{x}}_{t|t-1}$ is a prediction of the observable $\underline{y}_t$. In the case of the generalized Kalman filter, however, $\underline{y}_t = A_t\underline{x}_t + \underline{n}_t = A_t^z\underline{z}_t + A_t^u\underline{u}_t + \underline{n}_t$ cannot be predicted, since $\underline{\hat{u}}_{t|t-1}$, and therefore $\underline{\hat{x}}_{t|t-1}$, does not exist. The residual $\underline{y}_t - A_t^z\underline{\hat{z}}_{t|t-1}$ is therefore not a predicted residual. We can generalize the concept of the predicted residual however by considering functions of $\underline{y}_t$ that can be predicted. These must be functions that annihilate the contribution of $\underline{u}_t$. This leads therefore to the following definition.

Definition 1 (*Predicted residual*) Let $\underline{w}_t = \underline{y}_t - A_t^z\underline{\hat{z}}_{t|t-1}$ and let $U_t \in \mathbb{R}^{m\times(m_t-n+p_t)}$ be any basis matrix of the null space of A_t^{uT} (i.e. $U_t^T A_t^u = 0$). Then,

$$\underline{v}_t = U_t^T\underline{w}_t \tag{6.33}$$

is a (generalized) predicted residual of epoch t. □

Note that for the standard Kalman filter (i.e. $F_t = I_n$), we have $F_t^+ = I_n$, $A_t^u = 0$, $\underline{\hat{z}}_{t|t-1} = \underline{\hat{x}}_{t|t-1}$ and $U_t = I_{m_t}$, from which it follows that (6.33) will then reduce back to the standard predicted residual $\underline{v}_t = \underline{y}_t - A_t\underline{\hat{x}}_{t|t-1}$. Also note, since $U_t^T A_t^u = 0$, that $U_t^T A_t^z = U_t^T A_t F^+$ and that therefore $\underline{w}_t = \underline{y}_t - A_t^z\underline{\hat{z}}_{t|t-1}$ in (6.33) may be replaced by $\underline{y}_t - A_t F^+\underline{\hat{z}}_{t|t-1}$, which is the residual that occurs in all mechanizations of the generalized Kalman filter (cf. 6.24, 6.25, 6.26, 6.28).

6.5.2 Statistical testing

In standard Kalman filtering, the predicted residuals play an important role in the *recursive* execution of statistical tests for detecting and identifying potential biases in the underlying functional model (measurement and dynamic model). Their importance in executing such tests stems from their properties of being zero-mean and being uncorrelated in time, thereby making recursive testing possible. These same properties also hold true for the predicted residual (6.33),

$$\mathsf{E}(\underline{v}_t) = 0 \text{ and } \mathsf{C}(\underline{v}_t, \underline{v}_s) = Q_{v_t v_t}\delta_{ts} \tag{6.34}$$

with $Q_{v_t v_t} = U_t^T Q_{w_t w_t} U_t$ and $Q_{w_t w_t} = R_t + A_t^z P_{t|t-1}^z A_t^{zT}$. This implies that the same recursive testing algorithms that are in use for the standard Kalman filter, can be applied to its generalized version as well. This is the case, for instance, with local and global overall model (LOM/GOM) testing. Their associated test statistics are given as [16, 22],

$$\underline{T}_t = \frac{\underline{v}_t^T Q_{v_t v_t}^{-1}\underline{v}_t}{r_t} \quad \text{(LOM)} \tag{6.35}$$

and

$$\underline{T}_{s,t} = \underline{T}_{s,t-1} + [\sum_{i=s}^{t} r_i]^{-1}[\underline{T}_t - r_t \underline{T}_{s,t-1}] \text{ (GOM)} \tag{6.36}$$

in which $r_i = m_i - n + p_i$ denotes the local redundancy. Under a correctly specified Kalman filter, these test statistics are centrally $\mathscr{F}$-distributed as

$$\underline{T}_t \sim \mathscr{F}(r_t, \infty, 0) \text{ and } \underline{T}_{s,t} \sim \mathscr{F}(\sum_{i=s}^{t} r_i, \infty, 0) \tag{6.37}$$

$\mathscr{F}(\sum_{i=s}^{t} r_i, \infty, 0)$ denotes $\mathscr{F}$-distribution with $\sum_{i=s}^{t} r_i$ and ∞ degrees of freedom, and non-centrality parameter 0. Local and global biases are then, respectively, considered detected when $T_t > \mathscr{F}_{\alpha_l}(r_t, \infty, 0)$ and $T_{s,t} > \mathscr{F}_{\alpha_g}(\sum_{i=s}^{t} r_i, \infty, 0)$. The notations $\mathscr{F}_{\alpha_l}(r_t, \infty, 0)$ and $\mathscr{F}_{\alpha_g}(\sum_{i=s}^{t} r_i, \infty, 0)$ are the critical values having α_l and α_g as levels of significance, respectively.

6.5.3 On the precision of the predicted residuals

The distributional properties, stated in (6.37), fail to hold, once the underlying assumed properties of the predicted residuals fail to hold. Although with the misspecified stochastic model (6.29), the predicted residuals will still be normally distributed and will still have a zero-mean, their second moments will change. The following result shows how (6.29) affects this change.

Lemma 2 (*Predicted residual variance and between-epoch covariance*) With the actual vc-matrices of the measurement and system noise (cf. 6.29), the variance matrix of the predicted residual (6.33) and its between-epoch covariance read

$$\begin{array}{lcl} \bar{Q}_{v_t v_t} & = & U_t^T \bar{Q}_{w_t w_t} U_t \,,\; \bar{Q}_{w_t w_t} = \bar{R}_t + A_t \bar{P}_{t|t-1} A_t^T \\ \mathsf{C}(\underline{v}_t, \underline{v}_{t+1}) & = & U_t^T \bar{Q}_{w_t w_t} \left(\bar{K}_t^z - K_t^z\right)^T \Phi_{t+1,t}^{zT} A_{t+1}^{zT} U_t \end{array} \tag{6.38}$$

with $\bar{K}_t^z = \bar{P}_{t|t-1}^z A_t^{zT} \bar{Q}_{w_t w_t}^{-1}$ and $K_t^z = P_{t|t-1}^z A_t^{zT} Q_{w_t w_t}^{-1}$.

Proof For the proof, see "Appendix". □

This result shows that next to the change in vc-matrix of the predicted residual also time correlation is introduced. Thus, while the measurement noise and system noise are still assumed to be uncorrelated in time, the mere misspecification of their vc-matrices already introduces time correlation in the predicted residuals.

The change in the second moments of the predicted residuals will directly impact the statistics of $\underline{T}_t$ as the example of Figure 6.5, based on (6.32) ($R_i = (0.5\,\mathrm{m})^2$, $q_{\ddot{u}} = 0\,\mathrm{m}^2/\mathrm{s}^3$, $\bar{R}_i = (1.0\,\mathrm{m})^2$, and $\bar{q}_{\ddot{u}} = 3 \cdot 10^{-8}\,\mathrm{m}^2/\mathrm{s}^3$), illustrates. In case of an incorrect stochastic model, the LOM statistic will fail to have a mean equal one, as shown in Figure 6.5 (top-left); will be time correlated, as shown in Figure 6.5 (top-right); and will fail to follow the Chi-squared distribution, as shown in Figure 6.5 (bottom).

The induced time correlation, $\mathsf{C}(\underline{v}_t, \underline{v}_{t+1}) \neq 0$, due to the incorrectly assumed stochastic model, also implies that the GOM test statistic (6.36) cannot be used anymore as such. It will not have the $\mathscr{F}(\sum_{i=s}^{t} r_i, \infty, 0)$ distribution and the assumed absence of time-correlation

under which it is constructed fails to hold. The situation with regard to the LOM test statistic is fortunately somewhat brighter. Although $\underline{T}_t$ of (6.35) will also fail to be $\mathscr{F}$-distributed, knowledge of the correct vc-matrix of the predicted residuals allows one to construct a new LOM test statistic with the same $\mathscr{F}$-distribution. If we replace $Q_{v_t v_t}$ in (6.35) by $\bar{Q}_{v_t v_t}$ of (6.38), we obtain

$$\bar{\underline{T}}_t = \frac{\underline{v}_t^T \bar{Q}_{v_t v_t}^{-1} \underline{v}_t}{r_t} \sim \mathscr{F}(r_t, \infty, 0). \tag{6.39}$$

Hence, with knowledge of this distribution one can execute rigorous testing again.

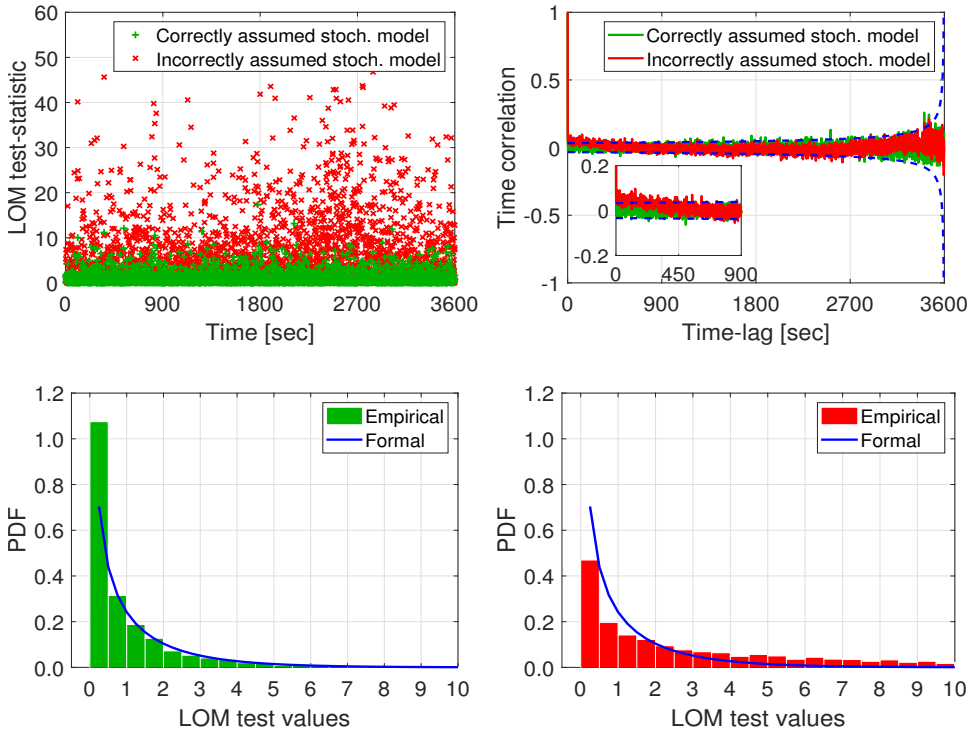


Figure 6.5: LOM test statistic $T_t = \underline{v}_t^T Q_{v_t v_t}^{-1} \underline{v}_t / r_t$ under correctly (green) assumed and incorrectly (red) assumed stochastic model: (*top-left*) T_t time-series; (*top-right*) T_t time correlation; (*bottom*) T_t histograms compared with $\chi^2(1,0)$-PDF

6.5.4 Reliability analysis

Although $\bar{\underline{T}}_t$ of (6.39) has the same distribution as $\underline{T}_t$ of (6.37), it is important to realize that the performance of the testing with $\bar{\underline{T}}_t$ will be different from that of testing with $\underline{T}_t$ under a correctly specified Kalman filter. To illustrate this, we consider the standard Kalman filter and assume that under the alternative hypothesis the mean of the observable $\underline{y}_t$ may be biased by $C_t b_t$, with matrix C_t known and b_t unknown. In a GNSS context, such may

represent the occurrence of outliers and/or slips in the GNSS-observables. We then have the following null and alternative hypotheses

$$\mathsf{E}(\underline{y}_t|\mathscr{H}_0) = A_t x_t \;\text{ versus }\; \mathsf{E}(\underline{y}_t|\mathscr{H}_a) = A_t x_t + C_t b_t. \tag{6.40}$$

Then, $\underline{v}_t|\mathscr{H}_a \sim \mathscr{N}(C_t b_t, Q_{v_t v_t})$ in case the stochastic model of the Kalman filter is correctly specified and $\underline{v}_t|\mathscr{H}_a \sim \mathscr{N}(C_t b_t, \bar{Q}_{v_t v_t})$ in case (6.29) is true. This implies that $\underline{T}_t \sim \mathscr{F}(m_t, \infty, \lambda)$ and $\underline{\bar{T}}_t \sim \mathscr{F}(m_t, \infty, \bar{\lambda})$, with noncentrality parameters

$$\lambda = b_t^T C_t^T Q_{v_t v_t}^{-1} C_t b_t \text{ and } \bar{\lambda} = b_t^T C_t^T \bar{Q}_{v_t v_t}^{-1} C_t b_t. \tag{6.41}$$

Hence, under the alternative hypothesis $\mathscr{H}_a$, the two test statistics, $\underline{T}_t$ and $\underline{\bar{T}}_t$, have different distributions. From a reliability analysis standpoint, it is then important to appreciate that the two noncentrality parameters of (6.41) have two very different usages. The noncentrality parameter λ can be used to analyse the *minimal detectable biases* (MDBs) in their dependence on the correctly specified vc-matrices R_i and S_i ($i \le t$). This is the usual way in which one studies the strength of the underlying model for detecting biases with the appropriate tests. The noncentrality parameter $\bar{\lambda}$, however, allows one to study the sensitivity of the MDBs in dependence of the *incorrectly* specified vc-matrices R_i and S_i ($i \le t$) and thus help answer questions like how well biases can still be detected even under the usage of a misspecified stochastic model.

In case of a single bias (i.e. $C_t \to c_t$) with (6.41), the corresponding MDBs are given as [23, 24]

$$|b_t| = \sqrt{\frac{\bar{\lambda}}{c_t^T Q_{v_t v_t}^{-1} c_t}} \text{ and } |\bar{b}_t| = \sqrt{\frac{\bar{\lambda}}{c_t^T \bar{Q}_{v_t v_t}^{-1} c_t}} \tag{6.42}$$

in which the reference value of the noncentrality parameter $\lambda = \bar{\lambda}$ is determined from the chosen level of significance and power of the test.

6.6 Summary and concluding remarks

In this contribution, we introduced a generalized Kalman filter with precision in recursive form when the stochastic model is misspecified. The filter allows for a relaxed dynamic model in which not all state vector elements are connected in time. The filter's flexibility stems from the property that its dynamic model is assumed to hold for only some functions of the state vector and that these functions are permitted to vary in time. Different mechanizations of the corresponding recursive filters were presented.

Just like the standard Kalman filter, its generalization has the property of being 'best' in the MMSE-sense. And just like with the standard Kalman filter, this property is lost in case the filter is based on an incorrectly specified stochastic model. Although losing this optimality property is a pitfall, we considered a far more serious problem the consequential lack of a proper quality description of the filter.

We therefore extended the filter with a recursion of its *actual* time-update and measurement-update error-variance matrices, to provide a tool for the efficient precision analysis of (generalized) Kalman filters. It allows for an easy-to-execute online recursive

sensitivity analysis, whereby the computations can be done in parallel to the recursion of the filter itself. The relevance of having such tool available was further underlined by illustrating through several examples that the behaviour of the actual filter precision, in response to changes in the assumed stochastic model, is difficult to predict a priori.

Next to the error-variance matrices, also the predicted residuals play an important role in the quality control of recursive filters. Due to the relaxation of the dynamic model, the concept of predicted residuals had to be generalized to predictable functions of the observables. It was thereby shown how their precision is affected by a misspecified stochastic model. It was hereby also shown that while the measurement noise and system noise are uncorrelated in time, the mere misspecification of their vc-matrices will already introduce time-correlation in the predicted residuals. This will therefore have its impact on the distributional properties of the test statistics used for the detection, identification and adaptation of the underlying models. In particular, the time correlation of the predicted residuals will affect the recursive global statistics as it invalidates the assumptions on which they are constructed. For the local statistics, fortunately the situation was shown to be brighter, as the usage of the given recursions of the actual vc-matrices still allows the construction of test statistics with known distributions. Finally, we demonstrated, differently from the traditional minimal detectable bias (MDB), which relies on a correctly specified model, how the recursive form of the affected precision of the predicted residuals can be used to study how well biases can still be detected even under the usage of a misspecified stochastic model.

Appendix

Proof of Lemma 1 The different error states can be written in their contributing factors as

$$\begin{array}{lll}
(a)\ \hat{\underline{z}}_{t|t-1}-\underline{z}_t &=& \Phi^z_{t,t-1}(\hat{\underline{z}}_{t-1|t-1}-\underline{z}_t)-\underline{d}^z_t \\
(b)\ \hat{\underline{z}}_{t|t}-\underline{z}_t &=& [I_{p_t}-K^z_tA^z_t](\hat{\underline{z}}_{t|t-1}-\underline{z}_t)+K^z_t(\underline{y}_t-A^z_t\underline{z}_t) \\
&=& L^z_t(\hat{\underline{z}}_{t|t-1}-\underline{z}_t)+K^z_t\underline{n}_t \\
(c)\ \hat{\underline{x}}_{t|t}-\underline{x}_t &=& [I_n-K^x_tA_t]F^+(\hat{\underline{z}}_{t|t-1}-\underline{z}_t)+K^x_t\underline{n}_t \\
&& +[K^x_tA_t-I_n](\underline{x}_t-F^+_t\underline{z}_t) \\
&=& L^x_t(\hat{\underline{z}}_{t|t-1}-\underline{z}_t)+K^x_t\underline{n}_t \\
(d)\ \hat{\underline{z}}_{t|t}-\underline{z}_t &=& F^T_t(\hat{\underline{x}}_{t|t}-\underline{x}_t) \\
(e)\ \hat{\underline{x}}_{t|t}-\underline{x}_t &=& [I_n-G^x_tA_t]F^+(\hat{\underline{z}}_{t|t}-\underline{z}_t)+G^x_t\underline{n}_t \\
&& +[G^x_tA_t-I_n](\underline{x}_t-F^+_t\underline{z}_t) \\
&=& H^x_t(\hat{\underline{z}}_{t|t}-\underline{z}_t)+G^x_t\underline{n}_t
\end{array} \tag{6.43}$$

where use has been made of $K^z_tA^u_t=0$, $F^T_t(\underline{x}_t-F^+_t\underline{z}_t)=0$ and the fact that the null space of both $[K^x_tA_t-I_n]$ and $[G^x_tA_t-I_n]$ are spanned by the columns of G_t. Application of the variance propagation law to the error states (6.43) gives the result. The error-variance matrix of the initial state follows from applying the variance propagation law to $\hat{\underline{z}}_{0|0}-\underline{z}_0=F^T_0A^+_0\underline{n}_0$. □

Proof of Lemma 2 For the predicted residuals $\underline{w}_t=\underline{y}_t-A^z_t\hat{\underline{z}}_{t|t-1}$ and $\underline{w}_{t+1}=\underline{y}_{t+1}-A^z_{t+1}\hat{\underline{z}}_{t+1|t}$, we may, with the help of $\underline{z}_{t+1}=\Phi^z_{t+1,t}\underline{z}_t+\underline{d}^z_t$, $\hat{\underline{z}}_{t+1|t}=\Phi^z_{t+1,t}\hat{\underline{z}}_{t|t}$, $\underline{y}_t=A^z_t\underline{z}_t+A^u_t\underline{u}_t+\underline{n}_t$, and $\hat{\underline{z}}_{t|t}=\hat{\underline{z}}_{t|t-1}+K^z_t[\underline{y}_t-A^z_t\hat{\underline{z}}_{t|t-1}]$, write

$$\begin{array}{lll}
\underline{v}_t &=& U^T_t[\underline{n}_t+A^z_t(\underline{z}_t-\hat{\underline{z}}_{t|t-1})] \\
\underline{v}_{t+1} &=& U^T_{t+1}[\underline{n}_{t+1}+A^z_{t+1}\Phi^z_{t+1,t}[L^z_t(\underline{z}_t-\hat{\underline{z}}_{t|t-1}) \\
&& -K^z_t\underline{n}_t]+A^z_{t+1}\underline{d}^z_{t+1}]
\end{array} \tag{6.44}$$

Application of the variance propagation law to the first equation gives $\bar{Q}_{v_tv_t}$. The covariance $\mathsf{C}(\underline{v}_t,\underline{v}_{t+1})$ follows from the above two equations by recognizing that only the random vectors that the two equations have in common, $\underline{n}_t$ and $\underline{z}_t-\hat{\underline{z}}_{t|t-1}$, contribute to this covariance. □

References

[1] R. E. Kalman, *A new approach to linear filtering and prediction problems,* Journal of Basic Engineering **82**, 35 (1960).

[2] K. R. Koch, *Parameter estimation and hypothesis testing in linear models* (Springer Verlag, Berlin, 1999).

[3] D. Simon, *Optimal State Estimation, Kalman, H-infinity and Nonlinear Approaches* (John Wiley and Sons, 2006).

[4] P. J. G. Teunissen, *Dynamic Data Processing: Recursive Least-Squares* (2nd Ed., Delft University Press, Delft, 2007).

[5] M. S. Grewal and A. P. Andrews, *Kalman Filtering; Theory and Practice Using MATLAB,* 3rd ed. (John Wiley and Sons, 2008).

[6] J. F. Zumberge, M. B. Heflin, D. C. Jefferson, M. M. Watkins, and F. H. Webb, *Precise point positioning for the efficient and robust analysis of GPS data from large networks.* Journal of Geophysical Research **102**, 5005 (1997).

[7] J. Kouba and P. Heroux, *Precise Point Positioning Using IGS Orbit and Clock Products.* GPS Solutions **5**, 12 (2001).

[8] T. Li, J. Wang, and D. Laurichesse, *Modeling and quality control for reliable precise point positioning integer ambiguity resolution with GNSS modernization,* GPS Solutions **18**, 429 (2014).

[9] P. J. G. Teunissen and A. Khodabandeh, *Review and principles of PPP-RTK methods,* Journal of Geodesy **89**, 217 (2015).

[10] M. Salzmann, *Least squares filtering and testing for geodetic navigation applications* (Netherlands Geodetic Commission, Publications on Geodesy 37, 1993).

[11] D. Odijk, B. Zhang, A. Khodabandeh, R. Odolinski, and P. J. G. Teunissen, *On the estimability of parameters in undifferenced, uncombined GNSS network and PPP-RTK user models by means of S-system theory,* Journal of Geodesy **90**, 15 (2016).

[12] X. Zhang, B. Zhang, Y. Yuan, and J. Zha, *Extending multipath hemispherical model to account for time-varying receiver code biases,* Advances in Space Research **65**, 650 (2020).

[13] A. Khodabandeh, P. J. G. Teunissen, and S. Zaminpardaz, *Consensus-based distributed filtering for GNSS,* Chapter 14 in Kalman Filters - Theory for Advanced Applications, InTech , 273 (2018).

[14] T. Kailath, *The innovations approach to detection and estimation theory,* Proceedings of the IEEE **58**, 680 (1970).

[15] P. J. G. Teunissen and A. Khodabandeh, *BLUE, BLUP and the Kalman filter: some new results.* Journal of Geodesy **87**, 461 (2013).

[16] P. J. G. Teunissen, *Quality control in integrated navigation systems,* IEEE Aerospace and Electronics System Magazine **5**, 35 (1990).

[17] I. Gillissen and I. A. Elema, *Test results of DIA: a real-time adaptive integrity monitoring procedure, used in an integrated navigation system,* The International Hydrographic Review **73**, 75 (1996).

[18] C. C. J. M. Tiberius, *Recursive data processing for kinematic GPS surveying* (Netherlands Geodetic Commission, Publications on Geodesy, 45, 1998).

[19] Y. Yang, H. He, and G. Xu, *Adaptively robust filtering for kinematic geodetic positioning,* Journal of Geodesy **75**, 109 (2001).

[20] N. Perfetti, *Detection of station coordinate discontinuities within the italian GPS fiducial network,* Journal of Geodesy **80**, 381 (2006).

[21] X. Zhang and X. Lu, *Recursive estimation of the stochastic model based on the Kalman filter formulation,* GPS Solutions **25** (2021), 10.1007/s10291-020-01060-4.

[22] P. J. G. Teunissen and M. Salzmann, *A recursive slippage test for use in state-space filtering,* Manuscripta Geodaetica **14**, 383 (1989).

[23] W. Baarda, *A testing procedure for use in geodetic networks,* Netherlands Geodetic Commission, Publ. on geodesy, New Series **2** (1968).

[24] P. J. G. Teunissen, *Distributional theory for the DIA method,* Journal of Geodesy **92**, 59 (2018).

7

Impact and mitigation of neglecting PPP-RTK correctional uncertainty

*The corrections needed to realize integer ambiguity resolution-enabled precise point positioning (PPP-RTK) at a single-receiver user are often treated **as if** they are deterministic quantities. The present contribution aims to study and analyze the effect the neglected uncertainty of these corrections, which are subject to time delay, has on the PPP-RTK user ambiguity resolution and positioning performance. Next to the analyses of the estimation results, we emphasize their quality information and show to what extent the assumed positioning precision, that the user is provided with, differs from the minimum-variance counterpart under an incorrectly specified user stochastic model. We develop and present two alternatives to the fully-populated error variance matrix of the PPP-RTK corrections that the user can reconstruct with limited information from the provider so as to properly weigh his corrected data and achieve close-to-optimal performance for high latencies. Supported by numerical results, our study demonstrates that the alternative variance matrices are sufficient enough for the user to obtain improved instantaneous PPP-RTK performance and a realistic precision description in the positioning domain.*

This chapter is based on the publication: Psychas, D., Khodabandeh, A. and Teunissen, P.J.G. (2021). Impact and mitigation of neglecting PPP-RTK correctional uncertainty. GPS Solutions, accepted for publication

7.1 Introduction

Integer ambiguity resolution-enabled precise point positioning (PPP-RTK) is the global navigation satellite system (GNSS) positioning mode that delivers single-receiver ambiguity-resolved parameter solutions. Its realization relies, next to satellite orbit and clock corrections, on the provision of satellite bias corrections which are often determined by a network of reference receivers [1–8]. Such corrections can also be computed and provided to positioning users via only one single reference receiver, the so-called *provider*. With such single-receiver PPP-RTK corrections [9], nearby positioning users are able to correct their code and phase data, recovering the integerness of their phase ambiguities, thereby achieving high-precision positioning solutions.

Despite their random nature, the PPP-RTK corrections are often treated *as if* they are nonrandom (deterministic) quantities either for implementation simplicity or because of the vast amount of information that needs to be transmitted to the user [10]. The justification behind this randomness is that the provider data used to generate these corrections is accompanied by an amount of uncertainty. Would the user, therefore, want to obtain minimum-variance positioning solutions, he needs to involve the true stochastic model of his corrected data so as to correctly incorporate their quality description into his estimation process. When the latter is characterized solely by the user data uncertainty, the weight matrices underlying the user model do not represent the inverse of the actual variance matrices. In such cases, the user's parameter solutions may lose their 'minimum-variance' property and become sub-optimal.

This becomes even more pronounced when one considers that, in real-time GNSS applications, the PPP corrections are not usually provided at an instant to the user, but with a certain time delay or latency (see, e.g., [11]). Therefore, the users have to predict the corrections in time, based on the information and methodology given by the provider (see, e.g., [12]), in order to bridge the gap between the corrections' generation time and the user positioning time, with a penalty on the achieved positioning accuracy as shown for PPP [13, 14] and PPP-RTK [15, 16]. Similar correction prediction approaches have been earlier developed for standard differential positioning applications [17]. A far more serious problem than the accuracy degradation is that the provided quality description of the user's parameters fails to represent the actual one, since the amount of uncertainty that lies in the corrections may get amplified as the time delay increases.

Based on a single-station framework for the generation and time-prediction of multi-epoch PPP-RTK corrections, Khodabandeh [18] showed the effect of high latency on the PPP-RTK user ambiguity resolution performance. The uncertainty involved in the time-predicted corrections is also expected to impact the user's ambiguity-resolved positioning performance and its accompanied precision description, for which an analysis is missing. This becomes especially relevant for peer-to-peer positioning applications that are enabled in such a single-station setup, without the need for instantaneous exchange of information, and are of great interest in light of the rapid development and utilization of low-cost GNSS devices [19–22].

In this contribution, we aim to demonstrate and analyze the user ambiguity resolution and positioning performance in case one neglects the uncertainty of the time-predicted single-station PPP-RTK corrections, and to show to what extent the per-

formance gets different from its true counterpart. Next to the user positioning estimation results, particular emphasis is given to the quality description that accompanies them. We develop and present two alternatives to the fully-populated variance matrix of the PPP-RTK corrections that the user optimally requires. While such alternative variance matrices can be fully structured at the user side via a limited amount of information from the provider, they are proven to be sufficient enough for the user to weigh his corrected data and achieve close-to-optimal results for high latencies.

This contribution is organized as follows. Section 7.2 introduces our underlying observation model and estimable parameters for both the single-station provider and the user setups. In Section 7.3, we first describe our processing strategy and show the importance of conducting a quality-judgement on the combined rather than the individual corrections. By considering various latencies and different strategies regarding the uncertainty of single-station PPP-RTK corrections, the single-epoch ambiguity resolution performance is then investigated based on GPS and Galileo dual-frequency observations through a formal and empirical success rate analysis. Afterwards, the corresponding positioning performance is analyzed for the ambiguity-float and -fixed cases, in terms of both the positioning accuracies and the precision description that goes along with them. Finally, concluding remarks are presented in Section 7.4.

7.2 Observation model

7.2.1 Single-station provider

Let us commence with the linearized observation equations of the observed-minus-computed, single-epoch, uncombined phase ($\Delta\phi^s_{r,j}$) and code ($\Delta p^s_{r,j}$) observables of a satellite s ($s = 1,\ldots,m$) on frequency j ($j = 1,\ldots,f$) that are collected by the provider r:

$$\begin{aligned} E(\Delta\phi^s_{r,j}) &= g_r^{s^{\mathrm{T}}}\Delta x_r + dt_r - dt^s + m^s_r\tau_r - \mu_j\iota^s_r + \lambda_j(\delta_{r,j} - \delta^s_{,j} + a^s_{r,j}) \\ E(\Delta p^s_{r,j}) &= g_r^{s^{\mathrm{T}}}\Delta x_r + dt_r - dt^s + m^s_r\tau_r + \mu_j\iota^s_r + (d_{r,j} - d^s_{,j}) \end{aligned} \tag{7.1}$$

where m and f denote the number of satellites and frequencies, respectively. Here and in the following, the observed-minus-computed observations are assumed to include the precise orbital corrections. The position increment Δx_r is linked to the observations through the receiver-satellite direction vector g^s_r. The common receiver and satellite clock parameters are denoted with dt_r and dt^s, respectively. The zenith tropospheric delay (ZTD) for receiver r, after removing the a priori (dry) value, and its mapping function for receiver r and satellite s are represented by τ_r and m^s_r, respectively. The first-order slant ionospheric delay experienced between the receiver r and satellite s on the first frequency is denoted by ι^s_r, and its linkage to the observations is done through the coefficient $\mu_j = \lambda_j^2/\lambda_1^2$ that depends on the wavelength λ_j. $\delta_{r,j}$ and $\delta^s_{,j}$ stand for the receiver and satellite phase biases, respectively, while $d_{r,j}$ and $d^s_{,j}$ denote those for the code observations, respectively. The integer phase ambiguity is represented by $a^s_{r,j}$. All parameters are expressed in units of range, apart from $\delta_{r,j}$, $\delta^s_{,j}$ and $a^s_{r,j}$ that are expressed in units of cycles. $E(\cdot)$ denotes the

expectation operator. Note that the receiver position is precisely known for the provider and therefore absent from (7.1), but unknown for the user receiver.

However, the lack of information content in the above system of GNSS observation equations does not allow us to unbiasedly determine all the individual parameters. By applying the *S*-system theory [23, 24] and by constraining a minimum set of parameters, namely the *S*-basis, we can remove the underlying model's rank deficiencies and determine, instead of the original, estimable functions of the original parameters.

As the *S*-basis is dependent not only on the measurement model but also on the assumptions regarding the dynamic model of the involved parameters, we need to make such models explicit. Some of the above parameters are known to behave constant in time, e.g., the phase ambiguities, while others may rapidly change in time, such as the satellite clocks. Therefore, to provide the user with the capability to time-predict the delayed corrections, one may take recourse to a minimum-mean-squared-error filtering technique such as the Kalman filter [25].

In this study, we choose a constant-state process for modeling the temporal behavior of the ionospheric delays, ambiguities and code/phase biases:

$$\alpha(i) = \alpha(i-1) + n_\alpha(i), \quad i = 2, \ldots, k \tag{7.2}$$

and a constant-velocity process to describe the temporal behavior of the satellite clocks:

$$\begin{aligned} \beta(i) &= \beta(i-1) + \Delta t\, \partial\beta(i-1) + n_\beta(i), \\ \partial\beta(i) &= \partial\beta(i-1) + n_{\partial\beta}(i), \quad i = 2, \ldots, k \end{aligned} \tag{7.3}$$

where α and β denote parameters the temporal behavior of which is modeled with a constant-state (random-walk) and a constant-velocity process, respectively. $\partial\beta$ denotes the 1st-order time derivative of β. i, k and Δt denote the epoch index, the total number of epochs and the sampling period, respectively. The system noises n_α, n_β and $n_{\partial\beta}$ are assumed to be zero-mean [26].

The reason behind the selection of the above processes for the time-variations of the parameters is justified as follows. The phase ambiguities are assumed to be time-constant unless cycle slips occur, while the receiver and satellite biases are reported to behave rather stable over time [27, 28]. Thus, their system noises are set to be identically zero. As for the ionospheric delays, it is known that they do not show significant time variations in short time spans, indicating that a constant-state process can sufficiently describe their temporal behavior. Such a process, though, seems not adequate to capture the temporal variation of the satellite clocks due to their rapid changes in time [15], which is the main reason for employing a constant-velocity model that has been reported to also improve the user positioning results. Finally, the receiver clocks are assumed to be completely unlinked in time, and therefore no dynamic model is assigned to them.

Based on the above assumptions, the full-rank version of the provider's model can be expressed as [18]:

$$\text{I}: \begin{cases} E(\Delta\phi^s_{r,j}(i)) & = d\tilde{t}_r(i) - d\tilde{t}^s(i) - \mu_j \tilde{t}^s_r(i) + \lambda_j(\tilde{\delta}_{r,j}(i) - \tilde{\delta}^s_{,j}(i)) \\ E(\Delta p^s_{r,j}(i)) & = d\tilde{t}_r(i) - d\tilde{t}^s(i) + \mu_j \tilde{t}^s_r(i) + (\tilde{d}_{r,j}(i) - \tilde{d}^s_{,j}(i)) \end{cases} \tag{7.4}$$

$$\text{II}: \begin{cases} d\tilde{t}^s(i) & = d\tilde{t}^s(i-1) + \Delta t\, \partial d\tilde{t}^s(i-1) + n_{dt^s}(i) \\ \partial d\tilde{t}^s(i) & = \partial d\tilde{t}^s(i-1) + n_{\partial dt^s}(i) \\ \tilde{t}^s_r(i) & = \tilde{t}^s_r(i-1) + n_{t^s_r}(i) \\ \tilde{\delta}_{r,j}(i) & = \tilde{\delta}_{r,j}(i-1) + n_{\delta_{r,j}}(i) \\ \tilde{d}_{r,j}(i) & = \tilde{d}_{r,j}(i-1) + n_{d_{r,j}}(i) \\ \tilde{\delta}^s_{,j}(i) & = \tilde{\delta}^s_{,j}(i-1) + n_{\delta^s_{,j}}(i) \\ \tilde{d}^s_{,j}(i) & = \tilde{d}^s_{,j}(i-1) + n_{d^s_{,j}}(i) \end{cases}$$

where the estimability and interpretation of the parameters, along with the S-basis, are listed in Table 7.1. Set I and II consist of the measurement and dynamic models, respectively.

The inclusion of the satellite clock velocity parameter $\partial d\tilde{t}^s(i)$ as unknown in the dynamic model brought an extra rank-deficiency, which was removed by considering the receiver clock at the second epoch as part of the S-basis. This is the reason why the receiver clock, the satellite clocks and their velocities are biased by the receiver clock velocity $\partial dt_r(2)$. As a consequence, two epochs of data are required to initialize the filter. Moreover, it is worth noting that the slant (residual) tropospheric delays are lumped into the estimable satellite clocks. Thus, for the users within the vicinity of the provider (e.g., with inter-station distances less than 5-10 km), the provision of the estimable satellite clocks $d\tilde{t}^s$ can also correct the user unknown tropospheric delays as $\tau_u \approx \tau_r$.

The stochastic model, as encapsulated in the variance-covariance (vc-) matrix of the phase and code measurements, is given as:

$$Q_{y_r y_r} = D\left(\begin{bmatrix} \Delta\phi_r(i) \\ \Delta p_r(i) \end{bmatrix}\right) = \text{blkdiag}(C_{\phi\phi}, C_{pp}) \otimes W_r^{-1}(i) \tag{7.5}$$

where $y_r = [\Delta\phi_r^{\mathrm{T}}(i), \Delta p_r^{\mathrm{T}}(i)]^{\mathrm{T}}$ and $\Delta\phi_r(i) = [\Delta\phi^1_{r,1}(i), \ldots, \Delta\phi^m_{r,1}(i), \ldots, \Delta\phi^1_{r,f}(i), \ldots, \Delta\phi^m_{r,f}(i)]^{\mathrm{T}}$ is the fm-vector containing the provider's phase measurements at epoch i. Similarly, $\Delta p_r(i)$ stands for the code measurements vector. The $f \times f$ matrices $C_{\phi\phi}$ and C_{pp} are, respectively, the covariance matrices of the phase and code observables at zenith. The $m \times m$ matrix $W_r(i) = \text{diag}(w^1_r(i), \ldots, w^m_r(i))$ contains the weights for every receiver-satellite link at epoch i. $D(\cdot)$ denotes the dispersion operator and $\otimes$ the Kronecker product. The notations diag and blkdiag represent a 'diagonal' and a 'block-diagonal' matrix, respectively.

Table 7.1: Estimable parameters and S-basis parameters of the single-system, multi-frequency, single-station provider model, in case of the constant-velocity setup for the satellite clocks.

Parameter	**Interpretation**
Rec. clocks	$d\tilde{t}_r(i) = dt_r(i) - dt_r(1) - [i-1]\Delta t\, \partial dt_r(2)$
Sat. clocks	$d\tilde{t}^s(i) = dt^s(i) + d^s_{,\mathrm{IF}}(1) - dt_r(1) - d_{r,\mathrm{IF}}(1) - [i-1]\Delta t\, \partial dt_r(2) - \tau^s_r(i)$
Ionospheric delays	$\tilde{\imath}^s_r(i) = \imath^s_r(i) + d_{r,\mathrm{GF}}(1) - d^s_{,\mathrm{GF}}(1)$
Rec. phase biases	$\tilde{\delta}_{r,j}(i) = \delta_{r,j}(i) - \delta_{r,j}(1)$
Sat. phase biases	$\tilde{\delta}^s_{,j}(i) = \delta^s_{,j}(i) + \frac{1}{\lambda_j}\left(\mu_j[d^s_{,\mathrm{GF}}(1) - d_{r,\mathrm{GF}}(1)] - [d^s_{,\mathrm{IF}}(1) - d_{r,\mathrm{IF}}(1)]\right) - \delta_{r,j}(1) - a^s_{r,j}$
Rec. code biases	$\tilde{d}_{r,j}(i) = d_{r,j}(i) - d_{r,j}(1)$
Sat. code biases	$\tilde{d}^s_{,j}(i) = \begin{cases} d^s_{,j}(i) - d^s_{,j}(1);\ j = 1,2 \\ [d^s_{,j}(i) - (d^s_{,\mathrm{IF}}(1) + \mu_j d^s_{,\mathrm{GF}}(1))] - [d_{r,j}(1) - (d_{r,\mathrm{IF}}(1) + \mu_j d_{r,\mathrm{GF}}(1))];\ j > 2 \end{cases}$
Sat. clock velocities	$\partial d\tilde{t}^s(i) = \partial dt^s(i) - \partial dt_r(2)$
S-basis parameters	$dt_r(1)$, $d_{r,j}(1)$, $\delta_{r,j}(1)$, $d^s_{,j=1,2}(1)$, $a^s_{r,j}$, $\partial dt_r(2)$

$(\cdot)_{,\mathrm{IF}} = \frac{1}{\mu_2-\mu_1}[\mu_2\,(\cdot)_{,1} - \mu_1\,(\cdot)_{,2}]$; $(\cdot)_{,\mathrm{GF}} = -\frac{1}{\mu_2-\mu_1}[(\cdot)_{,1} - (\cdot)_{,2}]$.

In case of the dynamic model, the receiver and satellite biases are assumed constant in time, and thus their system noises are set to be identically zero. As stated previously, the temporal behavior of the satellite clocks and slant ionospheric delays is modeled by a constant-velocity and a constant-state process, respectively. Therefore, the resulting covariance matrix S of their associated system noises, linking the parameters at two successive epochs, reads as [15]:

$$S = D\left(\begin{bmatrix} n_{dt^s} \\ n_{\partial dt^s} \\ n_{\imath^s_r} \end{bmatrix}\right) = \mathrm{blkdiag}\left(q^2_{dt^s}\begin{bmatrix} \frac{\Delta t}{2} & 0 \\ 0 & \frac{1}{2\Delta t} \end{bmatrix},\, q^2_{\imath^s_r}\Delta t\right) \otimes I_m \tag{7.6}$$

where $q^2_{dt^s}$ and $q^2_{\imath^s_r}$ denote the spectral density (in units of m^2/s) of the clock and ionosphere velocity parameters, respectively. I_m denotes an $m \times m$ unit matrix.

7.2.2 PPP-RTK user

Given that the correction generation time, say k, differs from the user positioning time, say l ($l > k$), the user needs to time-predict the PPP-RTK corrections using the individual corrections $d\hat{\tilde{t}}^s(k)$, $\partial d\hat{\tilde{t}}^s(k)$, $\hat{\tilde{\imath}}^s_r(k)$, $\hat{\tilde{\delta}}^s_{,j}(k)$, $\hat{\tilde{d}}^s_{,j}(k)$. Although the provided satellite code and phase biases are characterized by higher time stability than the other parameters and could be provided with a lower transmission rate, we assume here that all the PPP-RTK corrections are provided at the same epoch k for notational convenience. The

time-prediction of the corrections at the user positioning time follows as:

$$\begin{aligned} d\hat{\tilde{t}}^s(l) &= d\hat{\tilde{t}}^s(k) + [l-k]\Delta t\, \partial d\hat{\tilde{t}}^s(k) \\ \hat{\tilde{t}}^s_r(l) &= \hat{\tilde{t}}^s_r(k) \\ \hat{\tilde{\delta}}^s_{,j}(l) &= \hat{\tilde{\delta}}^s_{,j}(k) \\ \hat{\tilde{d}}^s_{,j}(l) &= \hat{\tilde{d}}^s_{,j}(k) \end{aligned} \tag{7.7}$$

where $[l-k]\Delta t$ is referred to hereafter as latency. Collecting the corrections at epoch k in a vector, $\hat{c}_k = [d\hat{\tilde{t}}^1(k),\ldots,d\hat{\tilde{t}}^m(k),\partial d\hat{\tilde{t}}^1(k),\ldots,\partial d\hat{\tilde{t}}^m(k),\hat{\tilde{t}}^1_r(k),\ldots,\hat{\tilde{t}}^m_r(k),\hat{\tilde{\delta}}^1_{,j}(k),\ldots,\hat{\tilde{\delta}}^m_{,j}(k),$ $\hat{\tilde{d}}^1_{,j}(k),\ldots,\hat{\tilde{d}}^m_{,j}(k)]^{\mathrm{T}}$, and their corresponding variance matrix $Q_{c_kc_k}$, the time-prediction of the corrections in matrix-vector notation reads as:

$$\hat{c}_l = \Phi_{l|k}\,\hat{c}_k, \quad Q_{c_lc_l} = \Phi_{l|k}\,Q_{c_kc_k}\,\Phi^{\mathrm{T}}_{l|k} + S_l \tag{7.8}$$

where S_l is the system noise variance matrix after replacing Δt with $[l-k]\Delta t$ in (7.6), and $\Phi_{l|k}$ the state transition matrix:

$$\Phi_{l|k} = \mathrm{blkdiag}\left(\begin{bmatrix} 1 & [l-k]\Delta t \\ 0 & 1 \end{bmatrix}, 1, I_f, I_{f-2}\right) \otimes I_m \tag{7.9}$$

It is reasonably implied here that the provider's dynamic model settings are given to the user either in real-time or through an offline accessible database. The user is then able to obtain the applicable PPP-RTK corrections in their combined form $\hat{c}_{u,l} = [\hat{c}^{\mathrm{T}}_{\phi,l}, \hat{c}^{\mathrm{T}}_{p,l}]^{\mathrm{T}} = [\hat{c}^{\mathrm{T}}_{\phi,1,l},\ldots,\hat{c}^{\mathrm{T}}_{\phi,f,l},\hat{c}^{\mathrm{T}}_{p,1,l},\ldots,\hat{c}^{\mathrm{T}}_{p,f,l}]^{\mathrm{T}}$ as:

$$\hat{c}_{u,l} = H\,\hat{c}_l, \quad Q^u_{c_lc_l} = H\,Q_{c_lc_l}\,H^{\mathrm{T}} \tag{7.10}$$

with

$$H = \begin{bmatrix} e_f & 0 & +\mu & \Lambda & 0 \\ e_f & 0 & -\mu & 0 & E_f \end{bmatrix} \otimes I_m \tag{7.11}$$

where Λ is an $f \times f$ diagonal matrix holding the frequency-specific wavelengths as its entries, μ is an f-vector with the ionospheric coefficients as its entries, and E_f is an $f \times f$ identity matrix with its first two columns removed. Note that E_f is structured in this way because the satellite code biases are estimable only from the third frequency onwards in the S-basis choice given here (cf. Table 7.1).

Given the correction component (7.10), the user's single-epoch, corrected phase and code observation equations are expressed as:

$$\begin{aligned} E(\Delta\phi^s_{u,j}(l) + \hat{c}^s_{\phi,j,l}) &= g^{s^{\mathrm{T}}}_u\,\Delta x_u(l) + d\tilde{t}_u(l) - \mu_j\tilde{\imath}^s_u(l) + \lambda_j(\tilde{\delta}_{u,j}(l) + \tilde{a}^s_{u,j}(l)) \\ E(\Delta p^s_{u,j}(l) + \hat{c}^s_{p,j,l}) &= g^{s^{\mathrm{T}}}_u\,\Delta x_u(l) + d\tilde{t}_u(l) + \mu_j\tilde{\imath}^s_u(l) + \tilde{d}_{u,j}(l) \end{aligned} \tag{7.12}$$

with the interpretation of the user's estimable parameters shown in Table 7.2. In this study, we focus on the impact of time-predicted corrections on the user positioning performance. We confine our study to a single-epoch user setup as it is the ultimate goal of

real-time applications and, at the same time, provides a lower bound for the precision of the corresponding user's multi-epoch solutions. It is worth mentioning that the user ambiguities are of double-differenced form, and therefore integer-valued. In the table, we have provided the interpretation of the user's slant ionospheric delays in case the distance between the provider and the user is either long or short. In the latter case, one can reasonably assume that the slant ionospheric delays experienced at both receivers are almost identical, which increases the model's strength through a $m-1$ gain in redundancy.

Table 7.2: Estimable parameters and S-basis parameters of the single-system, multi-frequency user model, in case of single-station provider corrections

Parameter	**Interpretation**
Rec. clock	$d\tilde{t}_u(l) = dt_u(l) + d_{u,\mathrm{IF}}(l) - dt_r(1) - d_{r,\mathrm{IF}}(1) - [l-1]\Delta t\, \partial dt_r(2)$
Ionospheric delays	$\tilde{\imath}^s_u(l) = \begin{cases} \imath^s_{ru}(l) + d_{ru,\mathrm{GF}}(1), & \text{if } \imath^s_u \neq \imath^s_r \\ d_{ru,\mathrm{GF}}(1), & \text{if } \imath^s_u = \imath^s_r \end{cases}$
Rec. phase biases	$\tilde{\delta}_{u,j}(l) = \delta_{u,j}(l) - \delta_{r,j}(1) + \frac{1}{\lambda_j}(\mu_j[d_{u,\mathrm{GF}}(l) - d_{r,\mathrm{GF}}(1)] - [d_{u,\mathrm{IF}}(l) - d_{r,\mathrm{IF}}(1)]) + a^1_{ru,j}$
Rec. code biases	$\tilde{d}_{u,j}(l) = d_{u,j}(l) - d_{r,j}(1) - [d_{u,\mathrm{IF}}(l) - d_{r,\mathrm{IF}}(1)] - \mu_j(d_{u,\mathrm{GF}}(l) - d_{r,\mathrm{GF}}(1)];\ j > 2$
Ambiguities	$\tilde{a}^s_{u,j} = a^s_{ru,j} - a^1_{ru,j};\ s \neq 1$
S-basis parameters	$d_{u,j=1,2}(l),\ a^1_{u,j}$,

$(\cdot)_{,\mathrm{IF}} = \frac{1}{\mu_2-\mu_1}[\mu_2\,(\cdot)_{,1} - \mu_1\,(\cdot)_{,2}];\ (\cdot)_{,\mathrm{GF}} = -\frac{1}{\mu_2-\mu_1}[(\cdot)_{,1} - (\cdot)_{,2}];\ (\cdot)_{ij} = (\cdot)_j - (\cdot)_i$.

Similar to the provider's stochastic model, the vc-matrix of the user's phase and code measurements, is given as:

$$Q_{y_u y_u} = D\left(\begin{bmatrix}\Delta\phi_u(l)\\ \Delta p_u(l)\end{bmatrix}\right) = \underbrace{\mathrm{blkdiag}(C_{\phi\phi}, C_{pp}) \otimes W_u^{-1}(l)}_{Q^0_{y_u y_u}} + Q^u_{c_l c_l} \tag{7.13}$$

where $\Delta\phi_u(l)$ and $\Delta p_u(l)$ are the fm-vectors containing the user's phase and code measurements at epoch l, respectively. We remark here that the phase $C_{\phi\phi}$ and code C_{pp} covariance matrices are not necessarily the same for the provider and the user but depend on the employed receivers. Note that the user's measurement vc-matrix (7.13) takes into account the uncertainty of the time-predicted PPP-RTK corrections. This is usually ignored in most PPP-RTK studies since the corrections are assumed to be sufficiently precise so that they can be treated *as if* they are deterministic.

An additional reason is that the provider needs to transmit, apart from the correction estimates, their associated vc-matrix, the vast information of which makes it impossible to transmit due to the large bandwidth required, and neglects the whole purpose of the state-space-representation (SSR). It has been shown, though, that the user-assumed ambiguity vc-matrix can unboundedly deviate from its optimal version in case of high latency [18]. In addition, we expect that the formal measures of the user ambiguity-resolved positioning results will deviate from their optimal counterparts and will not be representative of the empirical results. In this study, we analyze the user performance when one neglects the uncertainty of the single-station, time-predicted PPP-RTK corrections, and

present two solutions to the user's data weighting in order to obtain close-to-optimal results.

7.3 Experimental results and analysis

7.3.1 Data selection and processing strategy

In this study, 1 Hz GPS L1/L2 and Galileo E1/E5a code and phase data were collected at the stations CUBS and UWA0 (Perth, Australia) on DOY 218 of 2018. The 8 km distance between the stations allows to reasonably assume that the ionospheric delays experienced at both receivers are almost identical. Both stations are equipped with Septentrio PolaRx5 receivers. The cut-off elevation mask for the data analysis in this work is set to be 10° with 8 GPS and 6 Galileo satellites being tracked on average.

In our numerical analysis, the Multi-GNSS Experiment (MGEX; [29]) GPS and Galileo satellite orbits calculated by the Centre for Orbit Determination in Europe (CODE) were utilized as known parameters for both the provider and the user. The ground-truth coordinates of the stations were a priori precisely known and were used as known parameters in the single-station correction generation, while in the user processing they served only for the evaluation of the positioning errors. Moreover, the Saastamoinen model [30] with the Ifadis tropospheric mapping function [31] was used to obtain a priori tropospheric corrections. It has also been assumed that the residual troposphere has been lumped to the generated satellite clock offset and, due to the short distance between the employed stations, the differential tropospheric delays have been neglected, i.e. $\tau_u \approx \tau_r$. The receiver and satellite phase center offsets and variations, tidal and ocean loading effects, phase windup, relativistic effects have been corrected with standard models [32].

Table 7.3: Estimated zenith-referenced standard deviations of the code (cm) and phase (mm) observables for GPS L1/L2 and Galileo E1/E5a for the baseline CUBS-UWA0.

	Code [cm]	**Phase [mm]**
GPS	19.2 / 15.2	2.0 / 2.0
Galileo	16.4 / 13.5	2.0 / 2.0

To estimate the zenith-referenced code and phase standard deviations (STDs), we applied the least-squares variance component estimation (LS-VCE) method [33, 34] to the code and phase residuals computed for the baseline CUBS-UWA0 with fixed coordinates. Table 7.3 lists the estimated zenith-referenced STDs for both GPS and Galileo frequencies. The observation weights were computed based on the elevation-dependent exponential function [35].

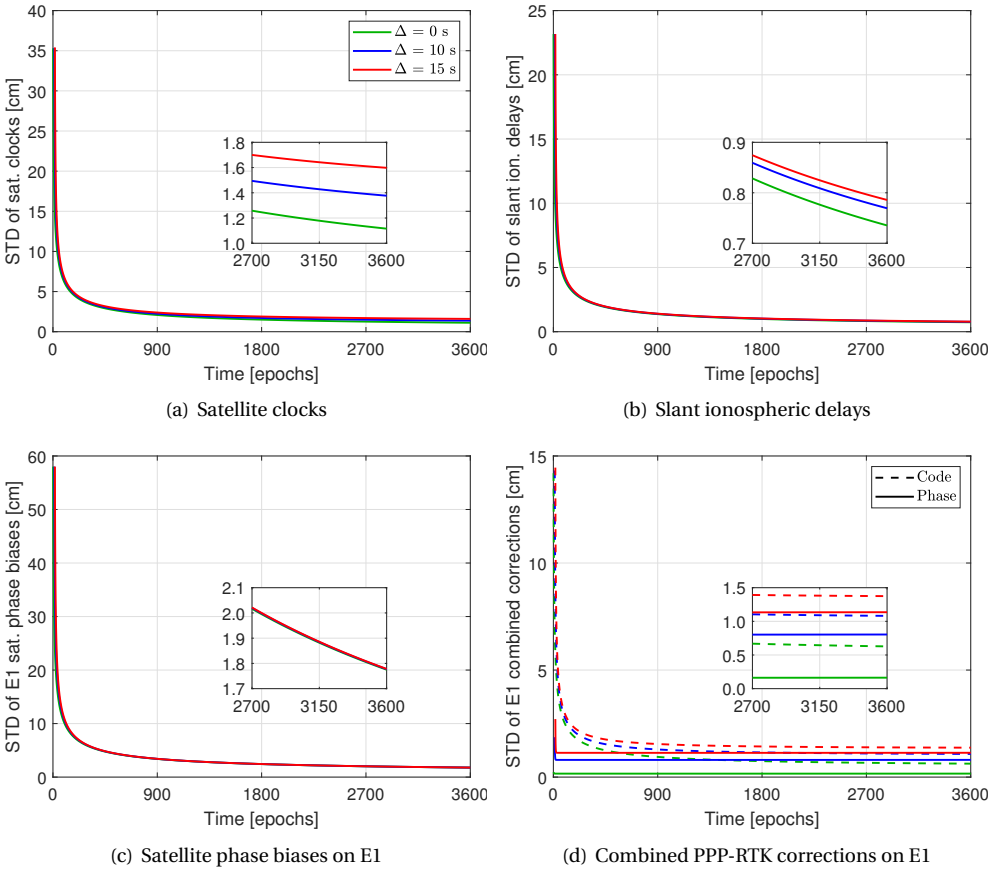
In carrying out our analysis, we considered the station CUBS as the provider and computed the single-station PPP-RTK corrections under the multi-epoch full-rank model (7.4) based on a Kalman filter. To initialize the filter, we performed a standard least-squares estimation based on two epochs of data. For the clock and ionospheric system noise standard deviations, we used the following values [15, 36]: $q^G_{dt^s} = 1\,\text{mm}/\sqrt{\text{s}}$, $q^E_{dt^s} = 0.3\,\text{mm}/\sqrt{\text{s}}$ and $q_{t^s_r} = 0.5\,\text{mm}/\sqrt{\text{s}}$. We empirically selected a system-specific clock system noise as it is known that Galileo, due to the use of very precise passive hydrogen maser clocks in the majority of the constellation, has a larger percentage of satellites with smaller clock noise compared to GPS [37, 38], which has also been shown through signal-in-space clock error analysis [39].

The recursively estimated corrections were then provided to the user station UWA0 with a latency of 10 and 15 seconds. Then, the user time-predicted the corrections based on (7.8) and (7.10), and performed single-epoch positioning on the basis of (7.12) using about 10,000 epochs of data. The user's double-differenced float-estimated ambiguities were decorrelated and fixed to their integers with the integer least-squares (ILS) estimator, which is efficiently mechanized in the LAMBDA (Least-squares AMBiguity Decorrelation Adjustment) method [40]. In this case, we did not make use of any ambiguity validation method to evaluate the empirical success rate and also the impact of both the latency and the correction uncertainty on it.

7.3.2 Quality of individual and combined corrections

In the attempt to evaluate the quality of the estimated corrections, one is usually inclined to inspect the formal standard deviations of the individual PPP-RTK corrections, see, e.g., [41]. However, it has to be reminded that the high correlation existing between them dictates that such a quality judgement should only be based on the combined version of these corrections [9].

To highlight the role of the stated correlation, we show the time-series of the formal standard deviation (STD) of both the individual and the combined PPP-RTK corrections during the first 3600 epochs for latencies up to 15 sec in Figure 7.1. Since the PPP-RTK corrections are effective at the between-satellite level for user positioning [9], the aforementioned values are expressed for a representative satellite-pair. One can observe from the figure that, even though the individual corrections are characterized by a code-precision level, especially at the beginning, the precision of the combined phase corrections is at the phase-noise level. For latencies up to 15 sec, the precision of both code and phase combined corrections is better than 2 cm after only a few minutes. Although the correlation between the code and phase combined corrections that becomes relevant for increasing latencies is not visualized here, it is properly taken into account in the user's performance analyses of the next subsections.



(a) Satellite clocks

(b) Slant ionospheric delays

(c) Satellite phase biases on E1

(d) Combined PPP-RTK corrections on E1

Figure 7.1: Formal standard deviations of the estimated between-satellite **(a)** clocks, **(b)** slant ionospheric delays, **(c)** phase biases, and **(d)** combined code/phase PPP-RTK corrections with a latency of 0 (green), 10 (blue) and 15 (red) seconds. The results correspond to the E1 data of a Galileo satellite pair (PRNs 5 and 30).

7.3.3 PPP-RTK user performance

This section presents and analyzes the user single-epoch ambiguity resolution and positioning performance for various scenarios regarding the error vc-matrix of the time-predicted corrections.

Let us first distinguish the assumptions that these scenarios are based on, for which a summarizing flowchart is given in Figure 7.2. As a starting point, we take the **'correct variance matrix'** case (scenario I) where the user takes the uncertainty of the single-station PPP-RTK corrections into account and performs a best linear unbiased estimation (BLUE). Although this is a stringent assumption because it means that the error vc-matrix of the corrections ($Q_{c_k c_k}$) is made available to the user, this result will serve later on in analyzing the performance loss due to the inconsideration of the correctional un-

certainty.

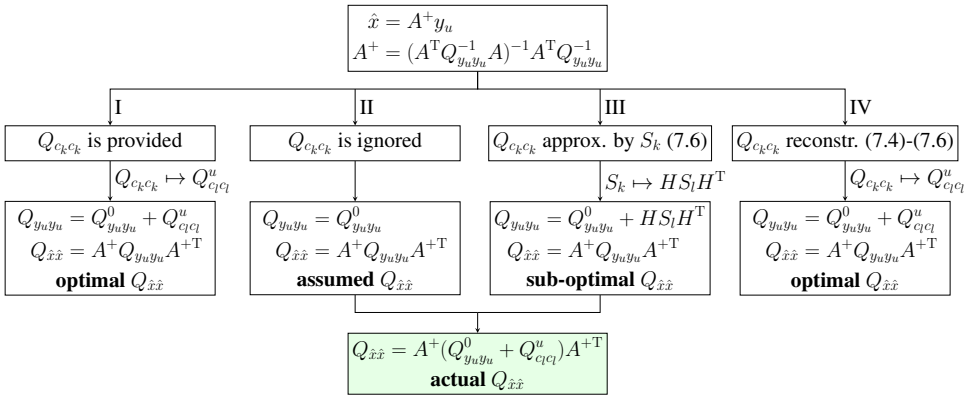


Figure 7.2: Flowchart of the steps for obtaining the weighted least-squares user parameter solutions $\hat{x}$ based on the strategy employed for the corrections error vc-matrix $Q_{c_k c_k}$. y_u is the vector of corrected observations, $Q^{0}_{y_u y_u}$ is the user's data vc-matrix, $Q_{y_u y_u}$ is the user's corrected data vc-matrix, A is the user design matrix, A^{+} is the least-squares inverse, $Q^{u}_{c_l c_l}$ is the error vc-matrix of the time-predicted combined corrections, S_k and S_l are the system noise vc-matrices at epochs k and l. The steps inside the green box are optionally performed by an analyzer (e.g. the provider).

Then, we have the **'incorrect variance matrix'** case (scenario II) which is the one used in practice, since the error vc-matrix of the corrections is often not provided to the users [10]. In this case, the user assumes that the corrections may be precise enough to be considered deterministic and, thus, weighs his corrected data based only on the uncertainty of his un-corrected data ($Q^{0}_{y_u y_u}$). As a consequence, his weighted least squares parameter solutions may lose their minimum-variance property, although he *assumes* that he performs BLUE-estimation. This will have an effect not only on the parameter solutions but also on their quality description. In fact, the variance matrices reported by the *incorrectly assumed* BLUE become incorrect and fail to provide the actual quality of the estimates. In such a case, we assume that an analyzer (e.g. the provider) exists who, given that the user's data uncertainty and the provider's correctional uncertainty are known, can perform a variance propagation law to obtain the *actual* quality of the user's positioning solutions.

As a first solution to mimic the information content within the fully-populated error vc-matrix of the corrections, we consider the **'sub-optimal variance matrix'** case (scenario III). In this case, the user attempts to approximate the stated error vc-matrix based only on the system-noise-variance part ($HS_l H^{\mathrm{T}}$) of the corrections' error vc-matrix. The realization of this approximation is based on the fact that the provider's dynamic model settings have been made available to the user either in real-time or through an external database the user has access to. Even though the user is still not in a position to obtain BLUE solutions, we investigate whether this approximation is sufficient enough so that the PPP-RTK user achieves close-to-optimal results. Also in this case, we consider an analyzer who, given the user's data uncertainty is known, is able to apply the variance propagation law and obtain the *actual* precision description.

Finally, we have the **'reconstructed variance matrix'** case (scenario IV), in which we propose a second solution to the aforementioned issue. Although the error vc-matrix of the time-predicted PPP-RTK corrections is not made available to the user, he attempts to fully reconstruct it based on a *model-driven recursive engine* he is equipped with. Given that the provider shares with the user information about the dynamic model settings, measurement precision, filter starting time and the approximate receiver location, the user is able to mimic the correctional error vc-matrix by resursively estimating it, based on (7.4)-(7.6), *as if* he would be the provider. Having such a tool available, which runs in parallel to the user's single-epoch processing, we investigate whether he is able to achieve (almost) identical results *as if* the error vc-matrix of the corrections would be made available directly by the provider.

Ambiguity resolution results

As a measure to analyze the instantaneous user ambiguity resolution performance for the selected scenarios, we utilize the easy-to-compute integer-bootstrapped (IB) success rate, which lower bounds that of the optimal ILS estimator [42]. The formal IB success rate is computed as [43]:

$$P(\check{a}_{\mathrm{ILS}} = a) = P(\check{z}_{\mathrm{ILS}} = z) \geq P(\check{z}_{\mathrm{IB}} = z) = \prod_{i=1}^{f(m-1)} \left(2\Phi\left(\frac{1}{2\sigma_{\hat{z}_{i|I}}} \right) - 1 \right) \tag{7.14}$$

with $\Phi(x) = \int_{-\infty}^{x} \frac{1}{\sqrt{2\pi}} \exp\{-\frac{1}{2}x^2\} dx$, and $P(\check{z}_{\mathrm{ILS}})$ and $P(\check{z}_{\mathrm{ILS}})$ being the ILS and IB success rates of the decorrelated ambiguities z, respectively. $\sigma_{\hat{z}_{i|I}}$ denote the conditional standard deviations of the ith decorrelated ambiguities, with $i = 1,\ldots,f(m-1)$ and $I = 1,\ldots,i-1$, which are given as the square roots of the entries of the diagonal matrix D after and $L^{\mathrm{T}}DL$-decomposition of the user's decorrelated ambiguity vc-matrix.

Table 7.4 presents the user empirical and formal ambiguity success rates for all scenarios and for latencies of 0, 5 and 15 sec. The formal values are computed by taking an average of the formal success rates of all the processing epochs, while the empirical success rate is given as the ratio of the number of processing epochs with correctly fixed ambiguities to the total number of the processing epochs. To validate whether the double-difference ambiguities are correctly fixed, we compared their ILS solution with the reference integer ambiguities computed from a geometry-fixed multi-epoch model.

The results in Table 7.4 show that, when the corrections are provided at an instant, the user achieves a 100% success rate in all scenarios for both single- and multi-system solutions. However, when the user ignores the correction uncertainty for nonzero latencies, there is a drop in the empirical success rates that becomes more pronounced the longer the latency becomes. Reducing the number of used GPS satellites to obtain a coverage similar to that of Galileo showed that the ambiguity success rate further reduces from 77.5% to 70.9%, indicating the impact the number of satellites has on the ambiguity resolution performance. The dual-system integration pushes the success rate to 96.8% due to the increased number of used satellites as observed by Khodabandeh [18].

Table 7.4: Instantaneous empirical and formal success-rate (%) at station UWA0 for the four precision description scenarios (I, II, III, IV) as a function of the latency Δ. The results refer to the GPS-only L1/L2, Galileo-only E1/E5a and GPS-plus-Galileo L1/L2+E1/E5a solutions obtained with 1 Hz data collected on DOY 218 of 2018.

System(s)/	$\Delta = 0$ sec		$\Delta = 10$ sec		$\Delta = 15$ sec	
Scenario	Empirical	Formal	Empirical	Formal	Empirical	Formal
GPS-only						
I	100	100	99.8	99.9	99.2	99.8
II	100	100	93.5	100	77.5	100
III	100	100	99.5	100	96.3	100
IV	100	100	99.8	100	99.2	99.9
Galileo-only						
I	100	100	100	100	100	100
II	100	100	96.0	100	94.1	100
III	100	100	99.9	100	99.9	100
IV	100	100	100	100	100	100
GPS-plus-Galileo						
I	100	100	100	100	99.7	100
II	100	100	99.5	100	96.8	100
III	100	100	99.9	100	99.1	100
IV	100	100	100	100	99.6	100

In addition, the results in the same table state that, upon employing the two proposed strategies for obtaining (part of) the error vc-matrix of the time-predicted corrections, the success rate increases dramatically, with the second method (scenario IV) bringing identical results to the case that the user is provided with the full error vc-matrix. This is an indicator that a user equipped with such a model-driven recursive engine is able to achieve optimal performance. Finally, the formal and empirical ambiguity success rates are in good agreement when (part of) the error vc-matrix of the corrections is utilized, confirming the consistency between data and model.

Positioning results

The ambiguity resolution performance analysis is followed by an investigation of the user single-epoch ambiguity-float and ambiguity-fixed positioning performance. Table 7.5 lists the single-epoch empirical and formal standard deviations of user's position components for both the ambiguity-float and -fixed cases, considering scenarios I-IV and delays up to 15 sec. The formal values are obtained from taking the average of the single-epoch position vc-matrices for all processing epochs, while the empirical values are determined by comparing the estimated positions to the ground-truth coordinates. The ambiguity-fixed outcomes are computed based on the correctly-fixed solutions.

Table 7.5: Instantaneous empirical and formal position standard deviations (mm) of station UWA0 for the four precision description scenarios (I, II, III, IV) as a function of the latency Δ, for both the ambiguity-float and -fixed cases. The results refer to the GPS-only L1/L2, Galileo-only E1/E5a and GPS-plus-Galileo L1/L2+E1/E5a solutions obtained with 1 Hz data collected on DOY 218 of 2018. For each case two values per coordinate components are given, which are the empirical (left) and formal (right) position standard deviations.

System(s) /		$\Delta = 0$ sec			$\Delta = 10$ sec			$\Delta = 15$ sec		
Scenario		North	East	Height	North	East	Height	North	East	Height
GPS-only										
I	float	149, 152	87, 112	390, 401	150, 153	88, 113	391, 402	151, 154	88, 113	393, 404
	fixed	5, 2	3, 2	11, 6	14, 12	8, 9	23, 28	19, 18	12, 13	33, 41
II	float	149, 152	87, 112	390, 400	150, 152	88, 112	391, 400	151, 152	88, 112	393, 404
	fixed	5, 2	3, 1	11, 5	12, 2	8, 1	24, 5	16, 2	11, 1	33, 5
III	float	149, 152	87, 112	390, 400	150, 152	88, 112	391, 400	151, 152	88, 112	393, 401
	fixed	5, 2	3, 1	11, 5	13, 3	8, 2	22, 8	18, 4	12, 3	32, 9
IV	float	150, 153	87, 112	390, 402	150, 153	88, 113	392, 404	151, 154	88, 113	393, 405
	fixed	5, 2	3, 2	11, 6	14, 12	8, 9	23, 28	19, 18	12, 13	33, 41
Galileo-only										
I	float	119, 135	96, 108	349, 407	119, 135	96, 108	349, 408	120, 135	96, 109	350, 408
	fixed	5, 2	3, 2	31, 7	6, 6	3, 5	29, 17	6, 8	3, 7	29, 23
II	float	119, 134	96, 108	349, 407	119, 134	96, 108	349, 407	120, 134	96, 108	350, 407
	fixed	5, 2	3, 1	31, 5	6, 2	4, 1	33, 5	6, 2	4, 1	33, 5
III	float	119, 134	96, 108	349, 407	119, 134	96, 108	349, 407	120, 134	96, 108	350, 407
	fixed	5, 2	3, 1	31, 5	6, 3	3, 2	29, 8	6, 3	3, 3	30, 9
IV	float	119, 135	96, 108	350, 407	119, 135	96, 108	350, 408	120, 135	96, 109	350, 408
	fixed	5, 2	3, 2	31, 7	6, 6	3, 5	29, 17	6, 8	3, 7	29, 23
GPS-plus-Galileo										
I	float	88, 94	63, 76	240, 257	88, 94	63, 77	241, 258	88, 95	64, 77	242, 259
	fixed	4, 1	2, 1	15, 4	5, 5	3, 4	20, 14	6, 7	4, 6	21, 19
II	float	88, 94	63, 76	240, 257	88, 94	63, 76	241, 257	88, 94	63, 76	242, 257
	fixed	4, 1	3, 1	15, 3	8, 1	5, 1	20, 3	10, 1	7, 1	25, 3
III	float	88, 94	63, 76	240, 257	88, 94	63, 76	241, 257	88, 94	63, 76	242, 257
	fixed	4, 1	3, 1	15, 3	6, 2	4, 2	19, 5	8, 2	6, 2	21, 6
IV	float	88, 94	63, 76	241, 258	88, 94	64, 77	242, 258	88, 95	64, 77	243, 259
	fixed	4, 1	2, 1	15, 4	5, 5	3, 4	20, 14	6, 7	4, 6	21, 19

Starting from the GPS-only results in scenario I, it can be observed that the ambiguity-float empirical and formal values remain almost invariant for increasing latency. This is due to the lower noise-level of the time-predicted corrections compared to the one of the code data for the investigated time delays (cf. Figure 7.1). Also, the empirical and formal solutions are in overall in good agreement, validating the stochastic model used for the processing.

Compared to the ambiguity-float results with dm-level precision for zero latency, one can observe two orders of magnitude improvement after successful ambiguity resolution. However, the same improvement is not present for increased latency due to an increase in the ambiguity-fixed empirical and formal STDs. This is due to the fact that the phase data are affected by the uncertainty of the time-predicted PPP-RTK corrections, thereby restricting the range of improvement.

Despite the closeness between the fixed formal and empirical values for scenario I, in which the error vc-matrix of corrections is made available to the user, this agreement tends not to hold when the user assumes the corrections to be of nonrandom nature (scenario II) for nonzero latencies. In these cases, the larger the latency becomes, the difference between the two values increases. Therefore, although precise positioning can still be achieved with an incorrect measurement noise, it becomes clear that the estimation results are not accompanied by a realistic precision description. With an incorrectly specified stochastic model, the BLUE-reported position standard deviations are incorrect and overoptimistic.

In case the user approximates the error vc-matrix of corrections with only their system-noise-variance part (scenario III), we observe only a slight improvement in terms of the difference between the formal and empirical values for the fixed results. This result suggests that, upon using the system-noise-variance part of the correction vc-matrix, one can achieve close-to-optimal ambiguity resolution performance (cf. Table 7.4), but the precision description of position components is still not realistic enough. However, when the user is equipped with the proposed model-driven recursive engine (scenario IV) in an attempt to reconstruct the full error vc-matrix of the corrections, it can be observed that he obtains identical positioning performance as the one observed in scenario I. Therefore, one can expect to obtain optimal positioning performance even when the provider does not provide the corrections' uncertainty, given that the user has all the necessary information to reconstruct it.

Similar conclusions can be drawn for the Galileo-only solutions. The main difference compared to the GPS counterparts is that the former enjoy better performance, especially along the horizontal components, for nonzero latencies. This can be attributed to the higher quality of Galileo satellite clocks, which allows the user to more accurately time-predict them. The GPS-plus-Galileo integrations delivers, in general, better positioning results compared to the single-system solutions, which is expected as the satellite geometry is strengthened with a larger number of used satellites.

To gain a better understanding of the impact that the inconsideration of the correction uncertainty has on the user positioning precision description for nonzero latencies, the horizontal positioning errors of user station UWA0 are visualized and analyzed. Shown in Figure 7.3 are the scatter plots of 10,000 single-epoch horizontal component estimation errors based on GPS L1/L2 data for increased corrections' latency (looking from left to right) and the aforementioned scenarios (looking from top to bottom). Since the use of the model-driven recursive engine (scenario IV) delivered identical results to the optimal case, we do not present the scatter plots of the former for brevity.

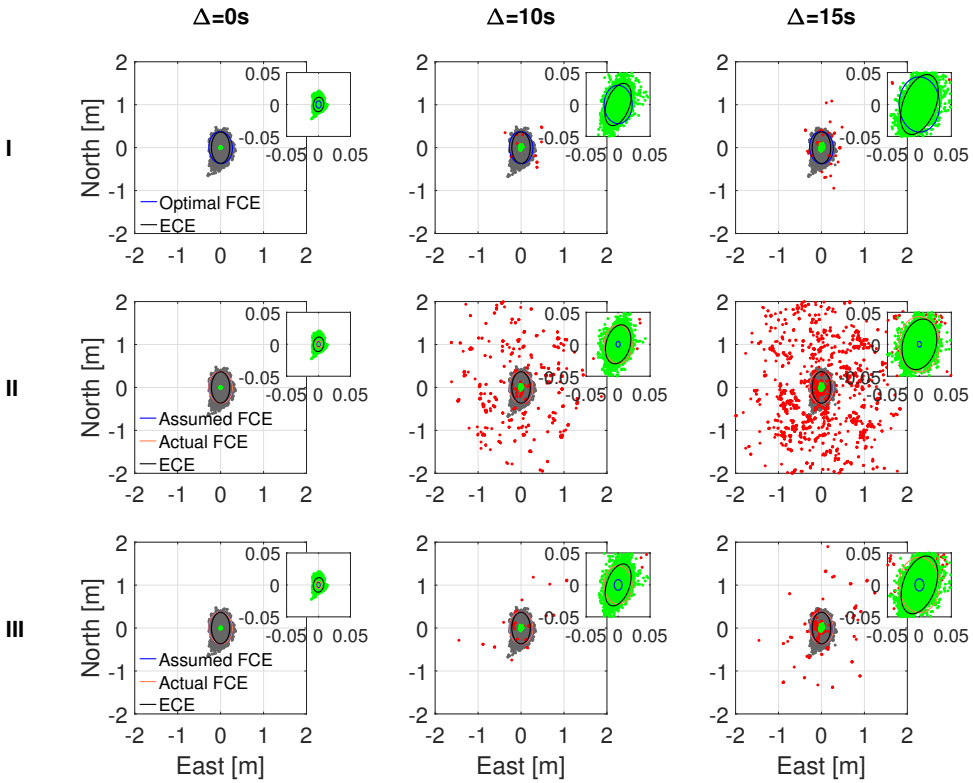


Figure 7.3: GPS L1/L2 single-epoch user east-north position error scatterplots of station UWA0 using multi-epoch single-station PPP-RTK corrections with latencies Δ of 0 (left column), 10 (middle column) and 15 (right column) seconds. From top to bottom, the first three figures refer to the 'correct variance matrix' case (scenario I) where the user considers the correctional uncertainty, thus producing the optimal minimum-variance results. The middle row figures refer to the 'incorrect variance matrix' case (scenario II) where the user ignores the correctional uncertainty but the analyzer is able to obtain the actual formal measures based on correct variance propagation. The last row figures refer to the 'sub-optimal variance matrix' case (scenario III) where the user considers only the system-noise-part of the correctional uncertainty but the analyzer is able to obtain the actual formal measures based on correct variance propagation. The gray, green and red dots represent the solutions with float, correctly-fixed and wrongly-fixed ambiguities, respectively. The 95% empirical confidence ellipses (ECE) are shown in black, while the 95% formal confidence ellipses (FCE) are shown in blue (assumed FCE) and orange (actual FCE).

The solutions shown in each panel are categorized into three types; ambiguity-float solutions as gray dots, correctly-fixed solutions as green dots, and wrongly-fixed solutions as red dots. The provided 95% confidence ellipses are derived from the empirical and formal vc-matrices of the position solutions. The empirical vc-matrix is determined by the positioning errors derived from comparing the estimated and the ground-truth positions. The formal vc-matrix is given from the mean of the single-epoch position vc-matrices of all considered epochs. Note that in the panels of the second and third rows we provide the assumed confidence ellipse (blue), which is the one reported by the *incorrectly-assumed* BLUE-estimation, and the actual confidence ellipse (orange), which is the one computed with correct variance propagation law from an analyzer.

In the unrealistic case that the user has access to the error vc-matrix of the corrections (top row), one can observe only a small number of incorrectly-fixed solutions, with the achieved empirical success rate being above 99% even for the 15-second latency case (see Table 7.4). Despite this fact, it is shown that as the latency increases, the success rate slightly decreases while the ambiguity-fixed position error scatter gets amplified. This is actually expected since the user's phase data are affected by the uncertainty of the time-predicted corrections, which increases as the latency gets higher. Most importantly, it can be observed that the formal confidence ellipse is in good agreement with the empirical one, indicating that one can expect a proper quality description when one considers the true uncertainty of one's corrected data.

When the user ignores the correctional uncertainty (middle row), a 100% success rate is achieved in the zero-latency case. However, the success rate experiences a significant reduction for increasing latencies. In the case of a 15-second latency, there are many incorrectly-fixed solutions (red dots), leading to a 77.5% success rate. Worse than that, the fixed precision description reported by the *incorrectly-assumed* BLUE is misleading as it provides a quite overoptimistic confidence ellipse with respect to the empirical one. After applying a correct variance propagation, the analyzer is able to obtain the *actual* precision description of the correctly-fixed solutions that nicely fits the empirical one.

As a solution to the above issue, we now investigate whether the error vc-matrix of the corrections can be sufficiently approximated by the system-noise-variance part of the former (bottom row), given that the provider's dynamic model settings are known to the user. One notices the considerable improvement in terms of the ambiguity resolution performance, which is also shown in Table 7.4. Therefore, given this easy-to-use approximation, the user is able to achieve close-to-optimal ambiguity-resolved positioning performance. However, the position precision description that comes along with these results, although more representative than the one in case of ignoring the correctional uncertainty, is still not good enough to describe the empirical positioning errors.

Although not shown in the figure for brevity, this is where the role of the model-driven recursive engine becomes prominent. Despite the various settings that need to be provided by the single-station provider and the engine the user needs to utilize in parallel, he is able to obtain optimal performance in terms of both ambiguity resolution and positioning, *as if* he would be provided with the error vc-matrix the provider computed.

The user's corresponding solutions based on Galileo E1/E5a and dual-system data are shown in Figure 7.4 and Figure 7.5, respectively. Similar conclusions can be drawn as in the GPS-only case. The major difference between the single-system solutions is the re-

markably larger success rate that can be achieved with Galileo for high latencies even if the user completely ignores the correctional uncertainty. In particular, the user is able to achieve a 94.1% success rate for a 15-second latency, compared to the 77.5% achieved for GPS. Moreover, the Galileo-only solutions show a smaller fixed position error scatter compared to GPS, despite the increased latency. We consider these to be results of the highly time-stable clocks of the Galileo satellites, which allows the user to more accurately time-predict the clocks. It is interesting to note that incorporating only the system-noise-variance part of the error vc-matrix of the corrections, rather than the full part, leads to almost-optimal results even for 15-second latency where the success rate is 99.9%.

Finally, it is obvious that, compared to the single-system solutions, the dual-system integration delivers better positioning results and shows smaller sensitivity to the inconsideration of the correctional uncertainty. However, the lack of the actual stochastic model of user's measurements still leads to an over-optimistic quality description.

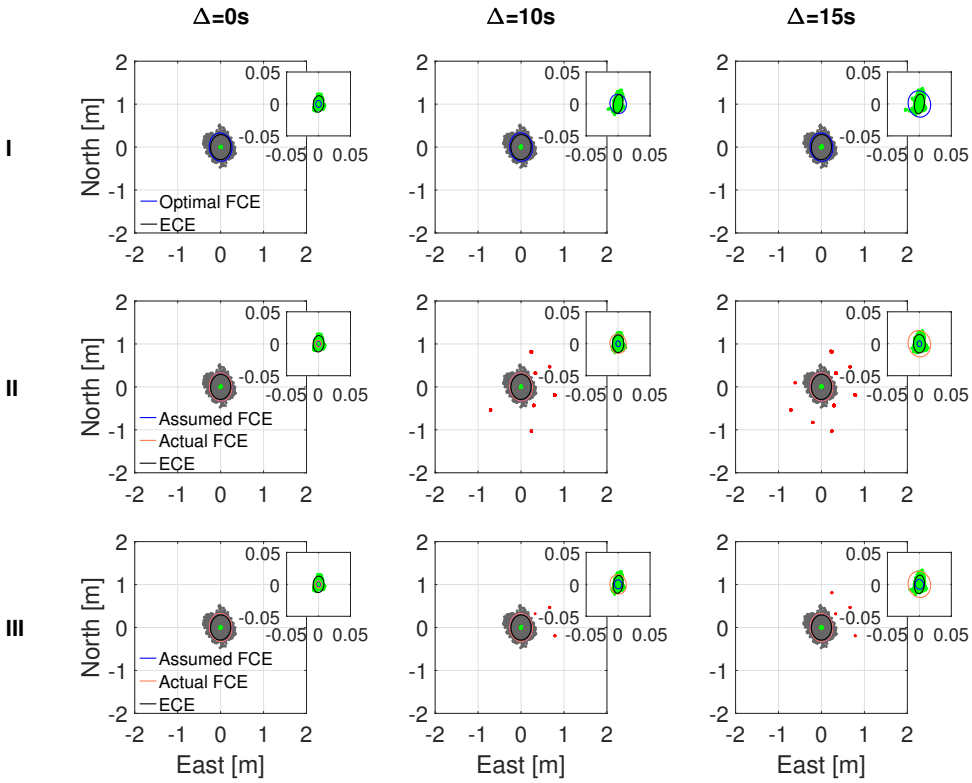


Figure 7.4: Galileo E1/E5a single-epoch user east-north position error scatterplots of station UWA0 using multi-epoch single-station PPP-RTK corrections (cf. Figure 7.3).

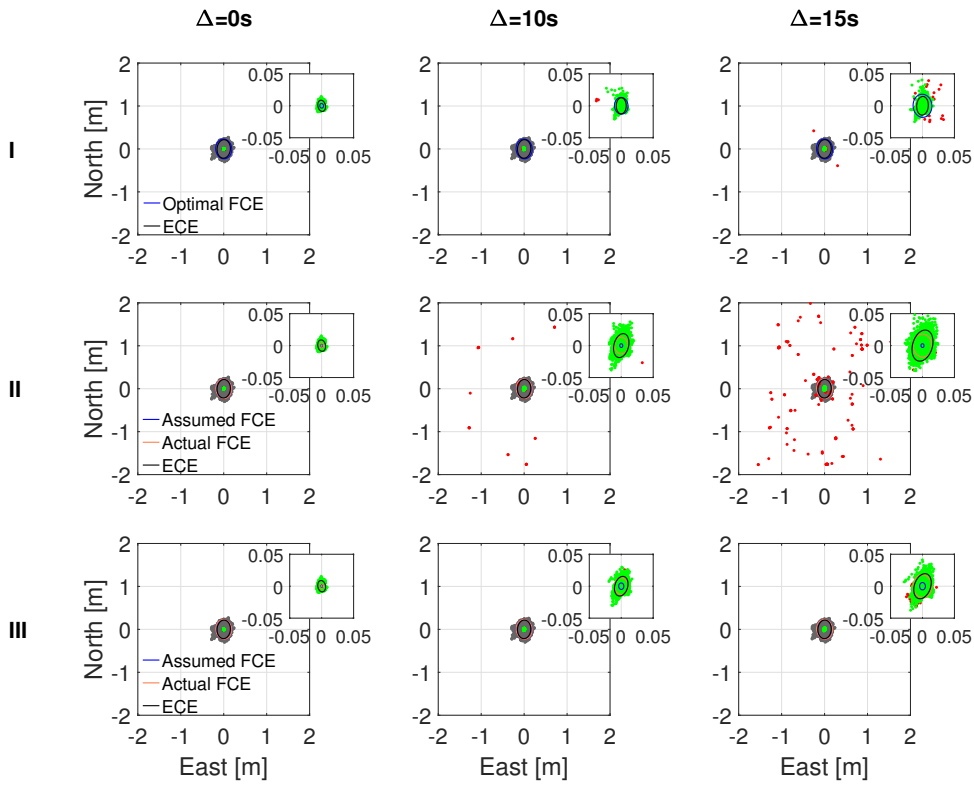


Figure 7.5: GPS L1/L2 + Galileo E1/E5a single-epoch user east-north position error scatterplots of station UWA0 using multi-epoch single-station PPP-RTK corrections (cf. Figure 7.3).

7.3.4 Relevance to multi-station PPP-RTK

Despite the fact that our numerical analysis is focused on the single-station PPP-RTK corrections, this does not affect the generality of our analysis as it can also be applied for when corrections from a multi-station (or network) setup are utilized. The advantage of the network approach over the single-station setup is that the area of coverage of the corrections is enlarged, which is especially important for the ionospheric component. Given that the error vc-matrix of the network-derived corrections is not made available to the user, he may take recourse to the strategies discussed in the previous section (cf. Figure 7.2), with the optimal one being the use of a model-driven recursive engine to reconstruct the error vc-matrix based on the information of the employed network receivers. In this case, the provider needs to share more information with the user, regarding the location of all network receivers and the measurement precision each one of them employs.

One could, instead, make use of the fact that the network PPP-RTK corrections are formed as a weighted average of the multiple single-station corrections [9], thereby requiring less information from the provider to reconstruct the error vc-matrix of the corrections. This, however, implies that the employed receivers collect measurements of the

same precision level, which might not hold true in case of receivers of different types.

7.4 Conclusions

In this contribution, we studied and presented the impact that the single-station time-predicted corrections have on the PPP-RTK user ambiguity resolution and positioning performance when the error variance matrix of the corrections is neglected. In a single-epoch user setup, we numerically demonstrated whether and to what extent the user's parameter solutions differ from their minimum-variance counterpart. Next to the user positioning estimation results, our focus was also placed on their precision description.

We started off with a detailed presentation of the single-station PPP-RTK provider's measurement and dynamic models using uncombined GNSS measurements. It was then shown how a subset of the single-receiver estimable parameters, provided as PPP-RTK corrections to the user with a certain time delay, is translated into the combined code and phase corrections that enable single-receiver user ambiguity resolution. The pitfall of analyzing the quality of individual corrections was addressed, for which we demonstrated that such an analysis is far from sufficient as it is the high correlation between the corrections that needs to be taken into account so that a proper quality judgment is done.

Further, the instantaneous PPP-RTK user performance was assessed with real GPS and Galileo dual-frequency 1-s data collected at two stations in Australia. It was shown that the user ambiguity success rate exceeds 99% even for a latency of 15 s when the uncertainty of the corrections is properly taken into account. When the corrections were assumed to be nonrandom, the success rate experienced a reduction for nonzero latencies, that was more pronounced the longer the latency became. Despite the low success rate of 77.5% that was achieved with GPS-only data, the Galileo-only solution delivered a success rate above 94%, that is due to the higher time-stability of the Galileo satellite clocks.

In both the ambiguity-float and -fixed cases, the empirical and formal positioning results showed a good agreement, thus validating the stochastic model used for the processing. Single-receiver ambiguity resolution resulted in two orders of magnitude precision improvement compared to the dm-level float solutions. This was shown not to hold for increased latency due to the fact that the phase data were affected by the uncertainty of the time-predicted corrections. It was then demonstrated that the inconsideration of the PPP-RTK correctional uncertainty led to a discrepancy between the formal and empirical results that was enlarged the longer the time delay. As a result, one cannot expect to obtain a realistic precision description in the positioning domain when the uncertainty of the corrections is not considered, and is thus misled by the incorrectly-assumed BLUE-reported standard deviations. Next to the user-estimated quality information, our illustrations included the actual precision description in the user positioning domain, as estimated with a correct variance propagation from an external analyzer (e.g. the provider), who is aware of the uncertainties of the corrections and of the user's data. Our findings revealed that the actual formal precision matched well with the empirical one, indicating the extent to which the user-assumed quality information differs from the user-actual one.

Finally, to circumvent these limitations, we developed and presented two alternatives to the fully-populated error variance matrix of the PPP-RTK corrections that can be structured from the user via a limited amount of information from the provider. With the first strategy considering the system noise variance matrix as an approximation to the error variance matrix of the time-predicted corrections, it was numerically shown that the user can achieve close-to-optimal ambiguity resolution performance, with the success rate exceeding 95%, in both single- and dual-system models for latencies up to 15 s. However, the positioning precision description proved to be not sufficient enough to realistically describe the empirical position errors.

Our second alternative encompasses using a model-driven recursive engine that can recursively estimate, at the user side, the error variance matrix of the provider's corrections using information shared by the provider. In this case, we showed that the user is able to obtain optimal performance for both ambiguity resolution and positioning, even for high latencies, *as if* the user would be provided with the original error variance matrix estimated by the provider. With the above real-data results, we believe that the proposed strategies enable a wide variety of applications that can make use of corrections with high latency and at the same time meet high accuracy and reliability requirements.

References

[1] G. Wubbena, M. Schmitz, and A. Bagge, *PPP-RTK: Precise Point Positioning Using State-Space Representation in RTK Networks.* in *Proceedings of the 18th International Technical Meeting of the Satellite Division of The Institute of Navigation, ION GNSS 2005* (Long Beach, CA, USA, 2005) pp. 2584–2594.

[2] M. Ge, G. Gendt, M. Rothacher, C. Shi, and J. Liu, *Resolution of GPS carrier-phase ambiguities in Precise Point Positioning (PPP) with daily observations.* Journal of Geodesy **82**, 389 (2005).

[3] P. Collins, *Isolating and Estimating Undifferenced GPS Integer Ambiguities.* in *Proceedings of the 2008 National Technical Meeting of The Institute of Navigation.* (San Diego, CA, 2008) pp. 720–732.

[4] L. Mervart, Z. Lukes, C. Rocken, and T. Iwabuchi, *Precise Point Positioning with Ambiguity Resolution in Real-Time.* in *Proceedings of the 21st International Technical Meeting of the Satellite Division of The Institute of Navigation, ION GNSS 2008* (Savannah, GA, 2008).

[5] D. Laurichesse, F. Mercier, J. P. Berthias, P. Broca, and L. Cerri, *Integer Ambiguity Resolution on Undifferenced GPS Phase Measurements and its Application to PPP and Satellite Precise Orbit Determination.* Journal of The Institute of Navigation **56**, 135 (2009).

[6] P. J. G. Teunissen, D. Odijk, and B. Zhang, *PPP-RTK: Results of CORS network-based PPP with integer ambiguity resolution,* Journal of Aeronautics, Astronautics and Aviation A, **42**, 223 (2010).

[7] J. Geng, C. Shi, M. Ge, A. H. Dodson, Y. Lou, Q. Zhao, and J. Liu, *Improving the estimation of fractional-cycle biases for ambiguity resolution in precise point positioning.* Journal of Geodesy **86**, 579 (2012).

[8] D. Odijk, B. Zhang, A. Khodabandeh, R. Odolinski, and P. J. G. Teunissen, *On the estimability of parameters in undifferenced, uncombined GNSS network and PPP-RTK user models by means of S-system theory,* Journal of Geodesy **90**, 15 (2016).

[9] A. Khodabandeh and P. J. G. Teunissen, *An analytical study of PPP-RTK corrections: precision, correlation and user-impact,* Journal of Geodesy **89**, 1109 (2015).

[10] D. Odijk, P. J. G. Teunissen, and A. Khodabandeh, *Single-Frequency PPP-RTK: Theory and Experimental Results.* in *Earth on the Edge: Science for a Sustainable Planet. International Association of Geodesy Symposia, Vol. 139*, edited by C. Rizos and P. Willis (Springer, Berlin, Heidelberg, 2014).

[11] R. Leandro, H. Landau, M. Nitschke, M. Glocker, S. Seeger, X. Chen, A. Deking, M. BenTahar, F. Zhang, K. Ferguson, R. Stolz, N. Talbot, G. Lu, T. Allison, M. Brandl, V. Gomez, W. Cao, and A. Kipka, *RTX positioning: The next generation of cm-accurate real-time GNSS positioning.* in *Proceedings of the 24th International Technical Meeting of the Satellite Division of The Institute of Navigation, ION GNSS 2011* (Portland, OR, 2011).

[12] IGS, *IGS State Space Representation (SSR) Format Version 1.00 (accessed on 13/10/2021),* (2020).

[13] A. Martin, T. Hadas, A. Dimas, A. B. Anquela, and J. L. Berne, *Influence of real-time products latency on kinematic PPP results.* in *Presented at the 5th International Colloquium Scientific and Fundamental Aspects of the Galileo Programme.* (Braunschweig, Germany, 2015).

[14] H. Yang, C. Xu, and Y. Gao, *Analysis of GPS satellite clock prediction performance with different update intervals and application to real-time PPP.* Survey Review **51**, 43 (2017).

[15] K. Wang, A. Khodabandeh, and P. J. G. Teunissen, *A study on predicting network corrections in PPP-RTK processing,* Advances in Space Research **60**, 1463 (2017).

[16] N. Nadarajah, A. Khodabandeh, K. Wang, M. Choudhury, and P. J. G. Teunissen, *Multi-GNSS PPP-RTK: From Large- to Small-Scale Networks,* Sensors **18**, 1078 (2018).

[17] P. Teunissen, *Differential GPS: Concepts and Quality Control,* Invited lecture for the Netherlands Institute of Navigation (NIN), Amsterdam, September 27 1991 (1991).

[18] A. Khodabandeh, *Single-station PPP-RTK: correction latency and ambiguity resolution performance,* Journal of Geodesy **95** (2021), 10.1007/s00190-021-01490-z.

[19] M. Gill, S. Bisnath, J. Aggrey, and G. Seepersad, *Precise Point Positioning (PPP) using Low-Cost and Ultra-Low-Cost GNSS Receivers.* in *Proceedings of the 30th International Technical Meeting of the ION Satellite Division, ION GNSS+ 2017* (Portland, Oregon, 2017).

[20] S. Banville, G. Lachapelle, R. Ghoddousi-Fard, and P. Gratton, *Automated processing of low-cost GNSS receiver data.* in *Proceedings of the 32nd International Technical Meeting of the ION Satellite Division, ION GNSS+ 2019* (Miami, Florida, 2019).

[21] D. Psychas, J. Bruno, L. Massarweh, and F. Darugna, *Towards Sub-meter Positioning using Android Raw GNSS Measurements.* in *Proceedings of the 32nd International Technical Meeting of the ION Satellite Division, ION GNSS+ 2019* (Miami, Florida, 2019).

[22] L. Wang, Z. Li, N. Wang, and Z. Wang, *Real-time GNSS precise point positioning for low-cost smart devices,* GPS Solutions **25** (2021), 10.1007/s10291-021-01106-1.

[23] W. Baarda, *S-transformations and criterion matrices.* in *Publications on Geodesy, 18*, Vol. 5 (Netherlands Geodetic Commission, Delft, The Netherlands, 1973).

[24] P. J. G. Teunissen, *Zero Order Design: Generalized Inverses, Adjustment, the Datum Problem and S-Transformations.* in *Optimization and Design of Geodetic Networks.*, edited by E. Grafarend and F. Sanso (Springer, Berlin, Heidelberg, 1985) pp. 11–55.

[25] R. E. Kalman, *A new approach to linear filtering and prediction problems.* ASME Journal of Basic Engineering **82**, 35 (1960).

[26] P. J. G. Teunissen, *Dynamic Data Processing: Recursive Least-Squares* (2nd Ed., Delft University Press, Delft, 2007).

[27] A. Komjathy, L. Sparks, B. D. Wilson, and A. J. Mannucci, *Automated daily processing of more than 1000 ground-based GPS receivers for studying intense ionospheric storms.* Radio Science **40** (2005), 10.1029/2005RS003279.

[28] B. Zhang, T. Liu, and Y. Yuan, *GPS receiver phase biases estimable in PPP-RTK networks: dynamic characterization and impact analysis.* Journal of Geodesy **92**, 659 (2018).

[29] O. Montenbruck, P. Steigenberger, L. Prange, Z. Deng, Q. Zhao, F. Perosanz, I. Romero, C. Noll, A. Sturze, G. Weber, R. Schmid, K. MacLeod, and S. Schaer, *The Multi-GNSS Experiment (MGEX) of the International GNSS Service (IGS) - Achievements, prospects and challenges.* Advances in Space Research **59**, 1671 (2017).

[30] J. Saastamoinen, *Contributions to the theory of atmospheric refraction.* Bulletin Geodesique **105**, 279 (1972).

[31] I. I. Ifadis, *The atmospheric delay of radio waves: modelling the elevation dependence on a global scale. Technical report no 38L,* Tech. Rep. (Chalmers University of Technology, Gothenburg, 1986).

[32] J. Kouba, *A guide to using International GNSS Service (IGS) products,* (2015).

[33] P. J. G. Teunissen and A. R. Amiri-Simkooei, *Least-squares variance component estimation,* Journal of Geodesy **82**, 65 (2008).

[34] A. R. Amiri-Simkooei, P. J. G. Teunissen, and C. C. J. M. Tiberius, *Application of Least-Squares Variance Component Estimation to GPS Observables.* Journal of Surveying Engineering **135**, 149 (2009).

[35] H. J. Euler and C. C. Goad, *On optimal filtering for GPS dual-frequency observations without using orbit information,* Bulletin Geodesique **65**, 130 (1991).

[36] A. Khodabandeh, J. Wang, C. Rizos, and A. El-Mowafy, *On the detectability of mis-modeled biases in the network-derived positioning corrections and their user impact.* GPS Solutions **23** (2019), 10.1007/s10291-019-0863-x.

[37] T. Hadas, K. Kazmierski, and K. Sosnica, *Performance of Galileo-only dual-frequency absolute positioning using the fully serviceable Galileo constellation.* GPS Solutions **23** (2019), 10.1007/s10291-019-0900-9.

[38] L. Carlin, A. Hauschild, and O. Montenbruck, *Precise point positioning with GPS and Galileo broadcast ephemerides.* GPS Solutions **25** (2021), 10.1007/s10291-021-01111-4.

[39] A. Hauschild and O. Montenbruck, *Precise real-time navigation of LEO satellites using GNSS broadcast ephemerides.* NAVIGATION **68**, 419 (2021).

[40] P. J. G. Teunissen, *The least-squares ambiguity decorrelation adjustment: a method for fast GPS integer ambiguity estimation.* Journal of Geodesy **70**, 65 (1995).

[41] X. Zhang, P. Li, and G. Guo, *Ambiguity resolution in precise point positioning with hourly data for global single receiver.* Advances in Space Research **51**, 153 (2013).

[42] P. J. G. Teunissen, *An Optimality Property of the Integer Least-Squares Estimator,* Journal of Geodesy **73**, 587 (1999).

[43] P. J. G. Teunissen, *Success probability of integer GPS ambiguity rounding and bootstrapping,* Journal of Geodesy **72**, 606 (1998).

8

Conclusions and recommendations

This chapter outlines the main conclusions that can be drawn from the work discussed in the previous chapters and provides recommendations for further research.

8.1 Conclusions

The research objective of this PhD thesis was to develop a framework for evaluating and improving the single-receiver PPP-RTK user positioning convergence time and reliability. The conclusions of this thesis are organized along the main objectives (see Section 1.3), which are all covered by Chapters 2-7, and can be briefly summarized as follows.

- *Regional network-derived ionospheric corrections are utilized from multi-scale network configurations for rapid PPP-RTK convergence.*

First, the quality of ionospheric corrections needed to accelerate PPP-RTK convergence was analyzed in a formal analysis setup, and it was found that such correction information is needed at a precision level better than 5 cm to allow for faster ambiguity resolution. An ionosphere representation was then developed for modelling ambiguity-fixed slant ionospheric delays in a regional network setup. Although the estimated receiver and satellite differential code biases showed sufficient time-stability, it was found that a function-based two-dimensional ionosphere model was not able to provide sufficiently precise ionospheric information, due to the multitude of simplifying assumptions (single-layer model, mapping function) that are usually considered.

A strategy was then introduced to spatially predict, by means of best linear unbiased prediction, the unobservable random slant, instead of vertical, ionospheric signals at the user side, per satellite and per epoch, based on the observable random network-derived slant ionospheric delays and their spatial coherence. Near-instantaneous convergence to the sub-decimeter level was shown to be feasible when the corrections are provided from a

68 km spaced network. The impact the network density has on the GPS-only ionosphere-weighted user performance was measured, for the first time in terms of PPP-RTK, and it was found that the user convergence time bears a linear relationship with the mean inter-station distance. Sub-decimeter positioning accuracy was achieved in 1.0 (5.5), 1.5 (10.5), 4.0 (16.5) and 7.0 (20.0) min for networks with density 68, 115, 174 and 237 km, respectively, at 50% (90%) during a day with medium ionospheric disturbance.

- *Integration of multi-GNSS and multi-frequency data is explored as an alternative to ionospheric information in order to improve the convergence performance.*

Due to the dependence of the ionosphere-corrected version of PPP-RTK on the existence of dense network infrastructure, that is not available everywhere, the integration of multi-GNSS and multi-frequency data was investigated as an alternative to achieve rapid positioning convergence. As such, a formal analysis was conducted based on a simulated global dataset in order to provide insight to the ambiguity resolution and positioning performance that can be expected with an increased number of satellites and frequencies. It was numerically shown that the satellite and frequency redundancy work in tandem in improving the PPP-RTK user performance, with the former being the main contributor for speeding up convergence due to the improved geometry strength. The dual- and triple-frequency GPS+Galileo+BeiDou solutions were shown to achieve a time-to-fix-ambiguities of 6.5 and 4.5 min, respectively, at 90%. Numerical evidence also showed that the sensitivity of the user's performance for varying measurement precision becomes less pronounced when data from multiple constellations and frequencies are employed.

The role of the number and spacing of frequencies in speeding up the user convergence were then explored, for the first time in the PPP-RTK sense, for multi-frequency Galileo-based positioning in the absence of ionospheric information. It was formally shown that frequency separation plays a key role in ambiguity resolution in that, the further the third frequency is from the starting two ones, the higher the success rate and the position precision gain are. In addition, it was presented that the spacing of frequencies aids ambiguity resolution to a larger extent than the number of frequencies, which was evidenced by the fact that the E1+E5a+E6 solutions had a better performance than the E1+E5a+E5b+E5 counterparts, while the former had an almost identical performance with the five-frequency solutions. The formal analysis findings were confirmed with real-data experiments, the results of which showed that it suffices to use the three widely-spaced frequencies (E1, E5a, E6) to achieve optimal Galileo-based performance, with the convergence time being equal to 15.0 min at 90%. The role of the estimable satellite code biases from the third frequency onwards in speeding up convergence was also highlighted, with the improvement ranging up to 4.0 min. The integration of multi-frequency Galileo and GPS data was shown to achieve a convergence time of 3.0 min on average and 5.0 min at 90%.

- *The impact of an incorrectly-specified stochastic model on the user's performance is analyzed and mitigation methods are considered.*

Further, the generalized Kalman-filter was introduced that is capable of, first, rigorously processing dynamic systems when only a subset of the state-vector elements are linked in time and, second, recursively providing the actual precision in case of a misspecified stochastic model as is the case when neglecting the uncertainty of PPP-RTK corrections. Through several examples, it was illustrated that the behavior of the actual filter-precision, in response to changes in the assumed stochastic model, is difficult to predict a priori. It was also proved and presented that, despite the assumptions of time-uncorrelated measurement and system noise, the incorrect specification of their variance matrices introduces time correlation in the predicted residuals. The presence of such time correlation alters the distributional properties of the test-statistics used for the detection, identification and adaptation of model errors.

The thesis was concluded by an analysis of the impact the neglected PPP-RTK correctional uncertainty has on the user single-epoch ambiguity resolution and positioning performance for non-zero correction latencies. Focus was placed not only on the estimation results, but also on their associated precision description, since these are the measures the user would rely on to judge his real-time performance. Experimental results, using real GPS and Galileo dual-frequency data, showed that the neglected uncertainty leads to reduced ambiguity success rate for non-zero latencies, that was more obvious with increasing latency (77.5% for GPS and 94% for Galileo with 15 s latency). Further, the inconsideration of the PPP-RTK correctional uncertainty led to significant discrepancies between the formal and empirical results, thereby indicating that a realistic precision-description cannot be expected and that the users are misled by the standard deviations reported by the incorrectly-assumed best linear unbiased estimation. To tackle these limitations, two alternatives to the fully-populated error variance matrix of the corrections were developed and presented that can aid the user in achieving nearly optimal ambiguity resolution performance even for high latencies. It was further demonstrated that the provided positioning precision-description realistically describes the empirical position errors only when the user is equipped with a model-driven recursive engine that is able to recursively estimate the error variance matrix of the PPP-RTK corrections.

8.2 Recommendations

Based on this dissertation, a number of recommendations for further research can be given, which are summarized below:

- The almost instantaneous PPP-RTK centimeter-level convergence relies on ionospheric corrections, the quality description of which is typically based on empirically derived measures. Although such empirical precision description may be sufficient for this scope, its determination requires, next to the reference stations used for the correction's generation, additional validation stations, thereby increasing the cost and operation requirements. A methodology combining the network-derived ionospheric formal measures and the location- and time-dependent ionospheric

conditions shall be explored to determine the a priori ionospheric standard deviation that a user applies in his ionosphere-weighted processing, thereby reducing the above network requirements.

- More research is needed on the estimation of a global precise ionosphere model for rapid PPP-RTK convergence. Compared to the regional network-derived slant ionospheric corrections per satellite that require dense infrastructure for their determination and high bandwidth for their transmission, a precise function-based ionosphere model, in which a subset of model coefficients may be sufficiently stable over time, would circumvent these limitations. In addition, improvements may also be expected from an augmentation of GNSS with LEO satellites due to the improved global coverage, see e.g. [1, 2].

- The emergence of smartphones that provide access to GNSS data suggests that such low-cost receivers can be used, instead of costly high-grade geodetic receivers, in a network setup for the estimation of PPP-RTK corrections. An extensive analysis of these corrections is needed to confirm whether they can be used for achieving successful PPP-RTK ambiguity resolution and positioning.

- The feasibility of achieving near-instantaneous PPP-RTK user convergence shall be explored by incorporating multi-frequency data, in addition to GPS and Galileo, from BeiDou, QZSS and GLONASS.

- The utilization of one pivot satellite in overlapping frequencies across systems, instead of one per system, leads to a user model strengthening after applying proper inter-system bias corrections [3]. As such, the multi-system PPP-RTK user ambiguity resolution and positioning performance shall be assessed with real-world data.

- In this dissertation, it was shown that, while the measurement and system noise are assumed to be uncorrelated in time, the misspecification of their variance matrices delivers Kalman-filtered predicted residuals that are correlated in time. The impact of these affected predicted residuals on the data quality control shall be analyzed with real-world GNSS data.

- In case of a high sampling rate or when network corrections are correlated in time, the user's GNSS measurements may also be subject to time correlation. This implies that the Kalman-filter formulas are not applicable anymore and need to be modified in such a way that the time-correlation is incorporated in the stochastic model in order to compute the correct error-variance matrix of the states.

References

[1] X. Ren, X. Zhang, M. Schmidt, Z. Zhao, J. Chen, J. Zhang, and X. Li, *Performance of GNSS Global Ionospheric Modeling Augmented by LEO Constellation,* Earth and Space Science **7**, e2019EA000898 (2020).

[2] X. Ren, J. Zhang, J. Chen, and X. Zhang, *Global Ionospheric Modeling Using Multi-GNSS and Upcoming LEO Constellations: Two Methods and Comparison,* IEEE Transactions on Geoscience and Remote Sensing , 1 (2021).

[3] A. Khodabandeh and P. J. G. Teunissen, *PPP-RTK and inter-system biases: the ISB look-up table as a means to support multi-system PPP-RTK.* Journal of Geodesy **90**, 837 (2016).

Acknowledgements

This thesis is the result of my PhD research conducted in the Mathematical Geodesy and Positioning group of the Department of Geoscience and Remote Sensing at the Delft University of Technology, in collaboration with the GNSS R&D group of Fugro Innovation & Technology B.V. within the framework of the TREASURE project. TREASURE has received funding from the European Union's Horizon 2020 research and innovation program under the Marie Skłodowska-Curie Grant Agreement No 722023. This result would have not been possible without the support of many individuals, to whom I feel the need to express my gratitude.

First and foremost, I would like to express my sincere gratitude to my promotor Prof.dr.ir Peter J.G. Teunissen, for his scientific support and sharp supervision throughout the course of my PhD research. Peter, your analytical thinking and scientific rigor have been instrumental in my formation as a researcher, while your strong views on estimation theory and your first-class research on GNSS theory, models, and algorithms have inspired me to conduct scientific research in these fields.

I would like to equally thank my copromotor Dr.ir. Sandra Verhagen, who has been my daily supervisor during the last four years. Sandra, your friendly behavior, continued support and scientific guidance were invaluable to all the challenges I faced as a PhD candidate at TU Delft. Thank you for your constructive criticism on my work and your motivation to keep enhancing the quality of my research.

I am also very grateful to Fugro for providing me the opportunity to work in the GNSS R&D team, and also for partially supporting me during my research. I would like to thank my former colleagues, Dr. Xianglin Liu, Dr. Dennis Odijk, Dr. Yahya Memarzadeh, Ir. Hans Visser, and Dr. Javier Tegedor for their support and for being such a good team to work with. Particular thanks go to Xianglin who has been an incredible mentor and GNSS team leader, and has played a pivotal role in shaping my GNSS algorithm development skills.

Further, I would like to express my appreciation to all fellows, researchers, supervisors, institutes and industrial partners involved in the TREASURE project. In particular, I would like to thank Dr. Hongyang Ma, Ir. Lotfi Massarweh, Dr. Francesco Darugna, and Dr. Jon Bruno. Hongyang, thanks for all the chats, scientific discussions and collaboration over the years, and most importantly for your pure friendship. I really hope we can meet again somewhere. To Lotfi, Francesco and Jon: I have enjoyed very much our time together, and the professional and social interaction with you have helped me grow in many ways. Thanks for your excellent collaboration during the ESA Galileo App Competition 2018/19, for putting up with my rigorousness, and for all the hard work we put in winning the first prize with GADIP3. Moreover, I would like to thank Prof.dr.ir Peter J.G. Teunissen and Prof. Manuel Hernández-Pajares for hosting me during my TREASURE research visits at Curtin University and Universitat Politècnica de Catalunya, respectively.

I would also like to thank Dr. Amir Khodabandeh for the fruitful collaboration during the last phase of my research, for his valuable advice and support, and for broadening my understanding of some complex aspects of the PPP-RTK mechanics through his work and our discussions. Amir, I really look forward to our future collaboration.

Many more people have directly or indirectly contributed to this work, all of whom I cannot name and thus I apologize in advance. In particular, I would like to express my sincere gratitude to all members of my doctoral committee for their assessment and useful comments on my thesis. I would also like to thank the anonymous reviewers who improved my journal publications through their constructive comments. My appreciation is also forwarded to the researchers at TU Delft I have interacted with and also to all secretaries of the department. Special thanks go to my friend and researcher Christos Gatidis for the enjoyable discussions we had during coffee breaks at the university. Further, I would like to thank Elena Sotiri for designing the cover of my thesis.

In addition, I would like to thank my dear friends Christos Platias and Aleksandar Belberov for their warm friendship and encouragement despite the distance between us.

Finally, and most of all, I would like to express my deepest gratitude to my family for supporting me in all of my endeavours. Special thanks go to three people who have played an important role in my life. Rania, thank you for being there for me at every single step of this journey, for enduring my bottomless stubbornness and never-ending monologues on GNSS, for your selfless support and encouragement when I needed it the most. Christoforos, thank you for your endless support since I can remember and for being the best brother I could ever have. Mother, thank you for all the sacrifices you've made for us, for your unconditional love, and for all the lessons you've taught me that made me the man I am today.

Curriculum Vitæ

Dimitrios Vasileios PSYCHAS

07-08-1992 Born in Mytilini, Lesvos, Greece.

Education

2017–2021 **Ph.D. in Geodesy and GNSS**
Delft University of Technology, The Netherlands
Thesis: Fast and reliable multi-GNSS precise point positioning with integer ambiguity resolution
Promotors: Prof.dr.ir. P.J.G. Teunissen
Dr.ir. A.A. Verhagen

2015–2017 **M.Sc. in Earth Oriented Space Science and Technology**
Technische Universität München, Germany
Thesis: Estimation of GNSS satellite phase biases using a global network of reference stations

2010–2015 **Diploma (Integrated Master's) in Rural and Surveying Engineering**
National Technical University of Athens, Greece
Thesis: Investigation and analysis of accuracy improvement techniques in Precise Point Positioning (PPP) method using multiple GNSS constellations

2007–2010 **Lyceum Apolytirio**
5th General Lyceum of Mytilini, Greece

2004–2007 **Gymnasium Apolytirio**
5th General Gymnasium of Mytilini, Greece

Work experience

Current	**Radio Navigation Engineer** European Space Research and Technology Centre, European Space Agency, The Netherlands
2017–2021	**Geodesist - GNSS R&D Engineer** Fugro Innovation & Technology B.V., The Netherlands
2017	**Teaching assistant** Institute for Astronomical and Physical Geodesy, Technische Universität München, Germany
2016–2017	**Research assistant** Institute for Astronomical and Physical Geodesy, Technische Universität München, Germany

Awards

2019	**1st Prize at the ESA Galileo App Competition 2018/19** awarded by the European Space Agency for developing a GNSS Android-based dual-frequency positioning smartphone app with the best positioning performance and availability
2018	**2nd Prize at the GSA Farming by Satellite Contest 2018** awarded by the European GNSS Agency for the proposal of a Galileo PPP-RTK positioning framework for economically viable automated transplanting
2017	**European Union's Horizon 2020 Marie Skłodowska-Curie Grant** awarded by the European Commission
2016	**Thomaidio Prize** awarded by the National Technical University of Athens for ranking 3rd among all 500 students of School of Rural and Surveying Engineering for the academic year 2014/15

List of publications

This PhD thesis by publication comprises 5 first-author peer-reviewed journal publications and 1 third-author peer-reviewed journal publication, the details of which can be found below and are referred to as *main* publications. These articles have been published/accepted in the following journals. The list of publications also contains *secondary* peer-reviewed journal and conference publications that are not assigned to individual chapters, because they have been a product of collaborative work out of the framework and/or the initial scope of this PhD thesis.

Main peer-reviewed journal publications

1. **Psychas, D.**, Khodabandeh, A. and Teunissen, P.J.G. (2021). *Impact and mitigation of neglecting PPP-RTK correctional uncertainty*, GPS Solutions, accepted for publication.

2. Teunissen, P.J.G., Khodabandeh, A. and **Psychas, D.** (2021). *A generalized Kalman-filter with its precision in recursive form when the stochastic model is misspecified,* Journal of Geodesy, 95(9):108.

3. **Psychas, D.**, Teunissen, P.J.G. and Verhagen, S. (2021). *A Multi-Frequency Galileo PPP-RTK Convergence Analysis with an Emphasis on the Role of Frequency Spacing*, Remote Sensing, 13(16):3077.

4. **Psychas, D.**, Verhagen, S. and Teunissen, P.J.G. (2020). *Precision analysis of partial ambiguity resolution-enabled PPP using multi-GNSS and multi-frequency signals*, Advances in Space Research, 66(9):2075-2093.

5. **Psychas, D.** and Verhagen, S. (2020). *Real-Time PPP-RTK Performance Analysis Using Ionospheric Corrections from Multi-Scale Network Configurations*, Sensors, 20(11):3012.

6. **Psychas, D.**, Verhagen, S., Liu, X., Memarzadeh, Y. and Visser, H. (2019). *Assessment of ionospheric corrections for PPP-RTK using regional ionosphere modelling,* Measurement Science and Technology, 30(1):014001.

Secondary peer-reviewed journal publications

1. Ma, H., Verhagen, S., **Psychas, D.**, Monico, J.F.G. and Marques, H.A. (2021). *Flight-Test Evaluation of Integer Ambiguity Resolution Enabled PPP*, Journal of Surveying Engineering, 147(3):04021013.

2. Ma, H., **Psychas, D.**, Xing, X., Zhao, Q., Verhagen, S. and Liu, X. (2021). *Influence of the inhomogeneous troposphere on GNSS positioning and integer ambiguity resolution*, Advances in Space Research, 67(6):1914-1928.

3. Ma, H., Zhao, Q., Verhagen, S., **Psychas, D.** and Dun, H. (2020). *Kriging Interpolation in Modelling Tropospheric Wet Delay*, Atmosphere, 11(10):1125.

4. Ma, H., Zhao, Q., Verhagen, S., **Psychas, D.** and Liu, X. (2020). *Assessing the Performance of Multi-GNSS PPP-RTK in the Local Area*, Remote Sensing, 12(20):3343.

Peer-reviewed conference publications

1. **Psychas, D.**, Bruno, J., Massarweh, L. and Darugna, F. (2019). *Towards Sub-meter Positioning using Android Raw GNSS Measurements*, Proceedings of the 32nd International Technical Meeting of the Satellite Division of The Institute of Navigation (ION GNSS+ 2019), Miami, Florida, September 2019, pp. 3917-3931.

2. Massarweh, L., Darugna, F., **Psychas, D.** and Bruno, J. (2019). *Statistical Investigation of Android GNSS Data: Case Study Using Xiaomi Mi 8 Dual-Frequency Raw Measurements*, Proceedings of the 32nd International Technical Meeting of the Satellite Division of The Institute of Navigation (ION GNSS+ 2019), Miami, Florida, September 2019, pp. 3847-3861.

Oral and poster presentations

1. **Psychas, D.** (2020). *Fast and reliable multi-GNSS PPP with integer ambiguity resolution, Speaker*, TREASURE final conference: The Ultimate Real Time EGNSS Solution: achievements and the near future, Session 3: High accuracy GNSS positioning algorithms to support real time PPP and RTK.

2. **Psychas, D.** and Verhagen, S. (2020). *Analysis of the network dimension impact on the performance of ionosphere-weighted single-receiver integer ambiguity resolution-enabled PPP, Online Display*, 33rd International Technical Meeting of the Satellite Division of The Institute of Navigation (ION GNSS+ 2020).

3. **Psychas, D.** (2020). *Fast and reliable multi-GNSS PPP with integer ambiguity resolution, Speaker*, Third TREASURE Workshop: Appraisal of scientific and technological output, Session 3: High accuracy GNSS positioning algorithms to support real time PPP and RTK.

4. **Psychas, D.** (2019). *Fast and reliable multi-GNSS PPP with integer ambiguity resolution, Speaker*, Second TREASURE Workshop: A response to user needs in PPP and RTK, Session 3: High accuracy GNSS algorithms.

5. **Psychas, D.**, Verhagen, S. and Liu, X. (2019). *Preliminary analysis of the ionosphere-corrected PPP-RTK user performance, Poster*, EGU2019, Session: G1.3 High-precision GNSS: methods, open problems and Geoscience applications.

6. **Psychas, D.**, Verhagen, S. and Liu, X.(2018). *Assessment of ionospheric corrections for PPP-RTK using S-system theory, Speaker*, NCG Symposium 2018, Session: GNSS and SDI/Governance.

7. **Psychas, D.**, Verhagen, S., Liu, X., Memarzadeh, Y., Visser, H. and Teunissen, P.J.G. (2018). *Assessment of ionospheric corrections for PPP-RTK using regional ionosphere modeling, Speaker*, First TREASURE Workshop: Initial Developments and Interaction with Academia and Industry, Session 3: Expectations in PPP and RTK.

8. **Psychas, D.**, Verhagen, S., Liu, X., Memarzadeh, Y., Visser, H. and Teunissen, P.J.G. (2018). *Assessment of ionospheric corrections for PPP-RTK using regional ionosphere modeling, Speaker*, EGU2018, Session: G1.3 High-precision GNSS: methods, open problems and Geoscience applications.

Manual

1. **Psychas, D.**, Verhagen, S. and Teunissen, P.J.G. (2019). LAMBDA - Python implementation, version 1.0, Delft University of Technology.